TABLE OF CONTENTS

Volume 3, Number 10, October 2010

The figure on the front cover shows the Pathophysiology of Parkinson's disease. (Courtesy Miriam Kammerer *et al*)

Journal of Biomedical Science and Engineering (JBiSE)

Journal Information

SUBSCRIPTIONS

The *Journal of Biomedical Science and Engineering* (Online at Scientific Research Publishing, www.SciRP.org) is published monthly by Scientific Research Publishing, Inc., USA.

Subscription rates:

Print: $50 per issue.
To subscribe, please contact Journals Subscriptions Department, E-mail: sub@scirp.org

SERVICES

Advertisements
Advertisement Sales Department, E-mail: service@scirp.org

Reprints (minimum quantity 100 copies)
Reprints Co-ordinator, Scientific Research Publishing, Inc., USA.
E-mail: sub@scirp.org

COPYRIGHT

PRODUCTION INFORMATION

For manuscripts that have been accepted for publication, please contact:
E-mail: jbise@scirp.org

J. Biomedical Science and Engineering, 2010, 3, 931-942 **JBiSE**
doi:10.4236/jbise.2010.310124 Published Online October 2010 (http://www.SciRP.org/journal/jbise/).

Comparative analysis of various modularization algorithms and species specific study of VEGF signaling pathways

Namrata Tomar, Losiana Nayak, Rajat K. De

Machine Intelligence Unit, Indian Statistical Institute, Kolkata, India
Email: namrata_t@isical.ac.in; losiana_t@isical.ac.in; rajat@isical.ac.in

Received 24 August 2009; received 9 September 2009; accepted 30 August 2010.

ABSTRACT

In biology, signal transduction refers to a process by which a cell converts one kind of signal or stimulus into another. It involves ordered sequences of biochemical reactions inside the cell. These cascades of reactions are carried out by enzymes and activated by second messengers. Signal transduction pathways are complex in nature. Each pathway is responsible for tuning one or more biological functions in the intracellular environment as well as more than one pathway interact among themselves to carry forward a single biological function. Such kind of behavior of these pathways makes understanding difficult. Hence, for the sake of simplicity, they need to be partitioned into smaller modules and then analyzed. We took VEGF signaling pathway, which is responsible for angiogenesis for this kind of modularized study. Modules were obtained by applying the algorithm of Nayak and De (Nayak and De, 2007) for different complexity values. These sets of modules were compared among themselves to get the best set of modules for an optimal complexity value. The best set of modules compared with four different partitioning algorithms namely, Farhat's (Farhat, 1998), Greedy (Chartrand and Oellermann, 1993), Kernighan-Lin's (Kernighan and Lin, 1970) and Newman's community finding algorithm (Newman, 2006). These comparisons enabled us to decide which of the aforementioned algorithms was the best one to create partitions from human VEGF signaling pathway. The optimal complexity value, on which the best set of modules was obtained, was used to get modules from different species for comparative study. Comparison among these modules would shed light on the trend of development of VEGF signaling pathway over these species.

Keywords: Signal Transduction Pathway, VEGF Pathway, Complexity Value, KEGG Database, Modularization, Newman's Community Finding Algorithm, Kernighan-Lin's Algorithm, Farhat's Algorithm, and Greedy Algorithm.

1. INTRODUCTION

The ability of cells to receive and act on signals from beyond the plasma membrane is fundamental to life. This ability of cells to respond correctly to their microenvironment is the basis of development, tissue repair, immunity and normal tissue homeostasis. Cells respond to their environment by recognizing their structure, regulating the activity of proteins and finally by altered gene expression. The stimulus for such type of responses is known as signal. Signals interact with the responding cell through molecules, called receptors [1]. For example, cells receive constant input from membrane proteins that act as information receptors, sampling the surrounding medium for pH, osmotic strength, and the availability of food, oxygen and light and the presence of noxious chemicals, predators or competitors for food. These signals elicit appropriate responses like motion towards food or away from toxic substances [2]. In multi-cellular organisms, cells with different functions, exchange a wide variety of signals. For example, plant cells respond to growth hormones and to variations in sunlight. Animal cells exchange information through the concentrations of ions and glucose in extra-cellular fluids, the interdependent metabolic activities, taking part in different tissues, and in an embryo, the correct placement of cells during development. So, we can get the concept that in all the cases, signal represents information that is detected by specific receptors and converted to a chemical process. This conversion of information into a chemical change or signal transduction is a universal property of living cells. Errors in cellular information processing are responsible for diseases such as cancer, autoimmunity and diabetes. By understanding cell signaling, diseases may be treated effectively. Systems biology research helps us to understand the underlying structure of cell

signaling networks and how changes in these networks may affect the transmission and flow of information.

Signal transduction is specific and exquisitely sensitive [2]. In unicellular organisms, signals are of environmental origin and diffusible in nature. Signals, in metazoans, are paracrine (*e.g*. neurotransmitters); they release from the nearby cells and diffuse over short distances. In the case of endocrine signals (*e.g*. hormones), they may be released from distant cells and vascular system sends them to their targets. Macromolecular signals are associated with the extra-cellular matrix or on the surface of the neighboring cells, and they are called juxtacrine signals. It requires two adjacent cells to make physical contact in order to communicate. Some cells require direct cell-cell contact; others form gap junctions to connect to the cytoplasm of other cells' cytoplasm for communication. A molecular signal that binds to a receptor is a ligand. As signaling pathway is made up of many different input and output nodes that make it, complex network, it is difficult to study and analysis. So the idea to divide it into small bio-significant modules, through the process called modularization came into light. A module is a subset of the original pathway, which has minimal dependency on the rest part of the network [3]. Here, the idea is to divide a pathway in such a way that the complexity of resulting modules is much less than that of the entire pathway, which provides an easier way to study the entire pathway. Many methods are developed to divide a network into smaller divisions.

Here, we considered Vascular Endothelial Growth Factor (VEGF) pathway for applying different partitioning algorithms. It has a receptor, *i.e.*, VEGFR, which is activated by ligand. Ligand binding to the receptor leads to receptor homodimerization or heterodimerization. Dimerization of receptors leads to their activation and subsequent autophosphorylation on certain tyrosine residues. It has many types of receptors. The receptors for vascular epithelial growth factor (VEGF) and related ligands are VEGFR-1 (Flt-1), VEGFR-2 (KDR/Flk-1), VEGFR-3 (Flt-4), neuropilin-1 and neuropilin-2. The interaction of VEGFR with either neuropilin-1 (NRP-1) or heparan sulfate proteoglycan helps in binding VEGF to its receptor. These receptors have multiple immunoglobulin G-like extra-cellular domains and intracellular tyrosine kinase activity. The human gene for VEGF resides on chromosome 6p21. The coding region spans 14 kb and contains eight exons. Alternative splicing of a single pre-mRNA generates several distinct VEGF species. There are several splice variants of VEGF, like VEGF 121, 145, 165, 189, and 206. Among them, VEGF 165 is the predominant form [4]. VEGF family has other members also. These are VEGF -B, -C, and -D, and Placental Growth Factor (PlGF). VEGF binds to VEGFR-1 and 2, and triggers angiogenesis.

PlGF is localized to the placenta and binds only to VEGFR-1. VEGF-B also binds only to VEGFR-1, and has function in coronary vascularization and growth. VEGF-C and VEGF-D activate VEGFR-2 and -3 but not VEGF-1. VEGF-C is involved in lymphangiogenesis. The function of VEGF-D is unknown [5]. For activation of the signaling pathway, VEGF binds to at least two transmembrane Flt-1 (VEGF receptor-1) and Flk-1/KDR (VEGF receptor-2). Both these are tyrosine kinase receptors. This results in tyrosine phosphorylation, and activation of phosphatidylinositol 3-kinase (PI3K) and phospholipase Ca^{2+} (PLC-γ). PLC-γ forms two molecules, Diacylgylcerol (DAG) and Inositol (1, 4, 5)-trisphosphate (IP3). These two further activate PKC and release Ca^{2+}. PI3K activates Akt. PKC, calcium and Akt activate endothelial Nitric Oxide Synthase (eNOS). It releases NO that is responsible for vasodilation and increased vascular permeability. The role for PLC-γ, PKC, calcium and NO in VEGF-induced hyper permeability has been confirmed in isolated coronary venules, and the involvement of PI3K/Akt and NO was demonstrated in human umbilical vein endothelial cell (HUVEC) monolayer [6]. Further, it also triggers intracellular signaling cascade that are able to recognize and dock at phosphorylated tyrosine residues of the activated receptors. These interactions are mediated by Src, phosphatidylinositol 3-kinase (PI3K), Shc, Grb2, and the phosphates SHP-1 and SHP-2 and other domains of the signaling proteins.

VEGF receptor activation can induce activation of the MAPK cascade via Raf stimulation. It leads to gene expression and cell proliferation. Activation of PI3K leads to PKB activation and cell survival; activation of PLC-γ leads to cell proliferation, vasopermeability and angiogenesis. VEGF regulates several endothelial cell functions, including proliferation, differentiation, permeability, vascular tone and the production of vasoactive molecules [5]. *H. sapiens* VEGF pathway taken from KEGG database is given in **Figure 1**.

The organization of this article is as follows. The next section describes the methodology of algorithm of Nayak and De in detail, and then introductory description of Kernighan-Lin's, Farhat's, Greedy and Community finding algorithms has been given. After that, we provide results in which we analyzed output got through implementing different partitioning algorithms. Species' evolution based comparison has also been done over the modules got through applying the algorithm of Nayak and De.

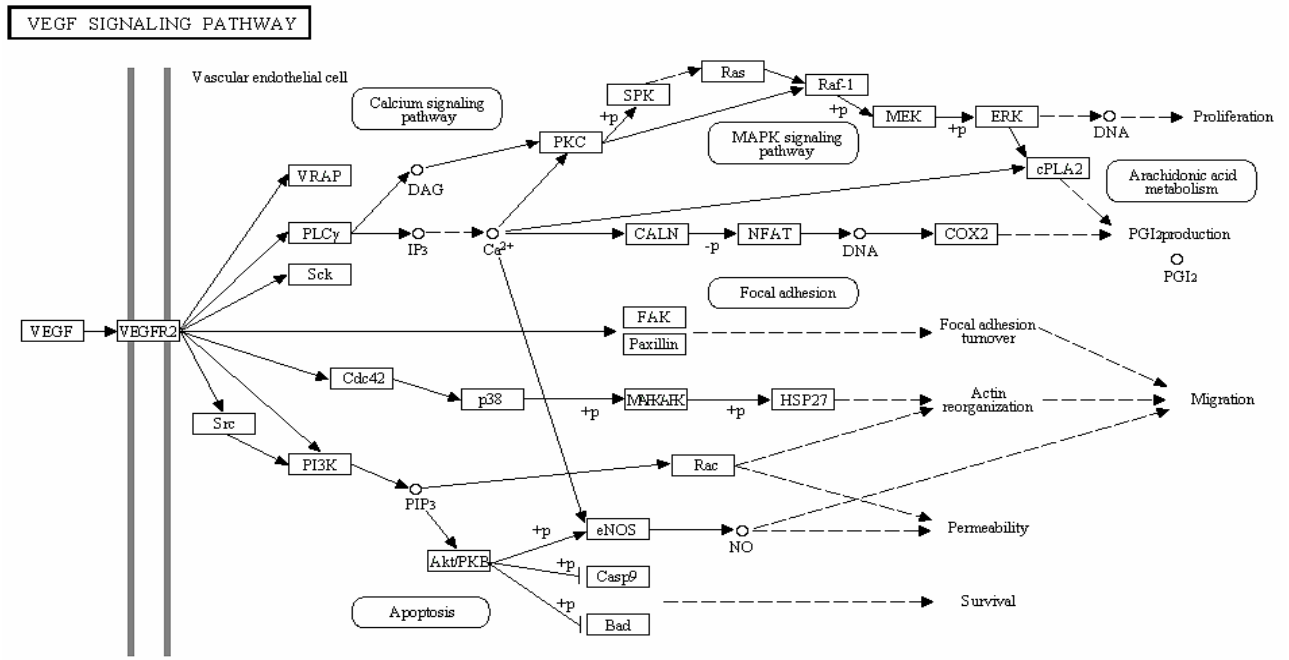

Figure 1. VEGF signaling pathway of *H. sapiens* present in KEGG pathway database.

2. METHODOLOGY

Many algorithms are proposed for the partition of a network. We compared the algorithm of Nayak and De [3] with community finding algorithm of Newman, Farhat's, Greedy and Kernighan-Lin's algorithms. Farhat's, Greedy and Kernighan-Lin's algorithms are graph partitioning algorithms and they need cut size and cut number for partitioning a network. Newman's community finding algorithm has been applied to one category of biochemical networks (metabolic pathways). The chosen set provided a good mix of algorithms that belong to atleast three categories. They provide a uniform platform for the comparative study. But by no means, this set of chosen algorithms is an exhaustive one.

Algorithm of Nayak and De works on a biochemical pathway which has gene products and chemical compounds. Here, the pathway is considered as a graph, gene products and chemical compounds are nodes. Edges show protein-protein interaction, protein-compound interaction or link to another map. The total number of relations with *n* as either a preceding or succeeding node is given by $Tn = Rnp+Rns$, where *Rnp* and *Rns* are outdegree and indegree, respectively, of a node *n*. The term *Tn* is the total degree of the node. According to algorithm, a node is detected which has maximum number of relations in the node pool *E* for a given network. This detected node is considered as a "starting node". This is always considered as a "permanent member". Permanent member is removed from the pool *E*. By defining the starting node, an initial module is created for relation *r*. Here, *n* may be a predecessor or a successor. After initialization of the module, the total number of relations of every individual member is considered.

Now, a node is checked for its permanency. If the number of relation lying inside the module is equal to the total number of relation associated with the node, then, it is permanent member. If a node in a module has more than *c* relations lying outside the module, it is excluded from the module with decreasing the previous non permanent nodes' total relation by one. This certain number of relations is known as complexity level *c* which can be set by the user. This process is continued until we have no new immediate neighboring node to be included or no node is left to be declared permanent. One important fact is that if a member *X* is present four times in a network, it will be considered four times like *X*1, *X*2, *X*3 and *X*4. After formation of a module, it searches for another starting point and repeat all above mentioned steps. This process will terminate when all the nodes of node pool *E* are exhausted.

This algorithm had been applied for different *c*-values for VEGF KEGG pathway database http://www.genome.jp/kegg/pathway.html#environmental. Then, appropriate *c*-value had been selected for comparative analysis of different species present in KEGG. KEGG has KGML layout which has XML files. These XML files' coding was used to give input for the algorithm.

Species of which KGML layout and XML coding were present in KEGG were considered for the comparative study of VEGF pathway. The species were *H. sapiens* (human), *P. troglodytes* (Chimpanzee), *M. musculus* (mouse), *R. norvegicus* (rat), *C. familiaris* (dog), *B. taurus* (cow), *S. scrofa* (pig).

Kernighan-Lin's algorithm is a heuristic algorithm applied for graph partitioning problems. It has important applications in the layout of digital circuits and components in VLSI. B. W. Kernighan and S. Lin has proposed an heuristic method in paper [7] to partition of the graph in such a way that it would be effective in finding optimal partitions. They deal with a combinatorial problem and partition of a graph *G* into subsets those would be no larger than a given maximum size. In this way, total cost of the edge cut is minimized.

Greedy algorithm [8] works well when a problem has greedy choice property and optimal substructure. It makes local optimal choice at each stage and tries to find global optimum. Farhat in 1988 has presented an algorithm which is an efficient non-numerical algorithm for the automatic decomposition of an arbitrary finite element domain into a specified number of balanced subdomains [9]. It is found to be effective for the implementation of concurrent solution strategies on high performance architectures.

Community structure detection is used for social networks, internet and web data, biochemical networks or gene network. Here, it is assumed that the network of interest divides naturally into subgroups, and the researchers find those groups. So, we can say that the number and size of the subgroups are determined by the network itself and not by the researcher. It has been applied to metabolic pathways. It divides a network in which good modules are not present. So, we can say that it is based on the properties of the network. Modularity score is directly dependent on the network architecture, adjacency matrix and eigenvalues of a symmetric matrix calculated from the adjacency matrix. Positive value of modularity means there is presence of modules in a network and a negative value shows that division is not possible [10].

3. RESULTS AND COMPARATIVE ANALYSIS

Species those were available in KEGG database had been considered for the comparative study. They are *H. sapiens* (human), *P. troglodytes* (Chimpanzee), *M. musculus* (mouse), *R. norvegicus* (rat), *C. familiaris* (dog), *B. taurus* (cow), *S. scrofa* (pig). The gradual development of this pathway in some species had been studied with respect to VEGF pathway of *H. sapiens* using the algorithm of Nayak and De. We applied all selected algorithms to VEGF signaling pathway of *H. sapiens* as obtained from KEGG database and compared their performances.

3.1. Modularization of VEGF Signaling Pathway of *H. Sapiens* using Different Algorithms

We took different *c*-values and studied various modules obtained by the algorithm of Nayak and De. Then, by analyzing all the modules for different *c*-values, we chose a particular *c*-value for the comparative study of organisms. VEGF signaling pathway of *H. sapiens* has 40 nodes and 34 relations. Modules were created for c = 1, 2, 3, 4 and 5.

For c = 1, we had 12 modules shown in **Table 1**. Number of modules was reduced, as complexity level was increased. For c = 2, node MAK1 merged with central node (PLCG1, PLC1) as shown in **Table 2**. Now, this node had function of cell survival and migration of vesicular endothelial cell [11]. For the same complexity value, another central node, MAPK14 merged into central node KDR. KDR has role in cell proliferation and growth function along with previous function of focal adhesion turnover and cell migration. It had paxillin and FAK as node members. Paxillin acts as a focal adhesion adaptor in focal adhesion dynamics and cell migration. Paxillin-FAK interaction is involved in Erk activation [12]. For c = 2, we had 6, and for c = 3, we had 4 modules as shown in **Table 3**. The node AKT3 was present as central node for c = 2 but it combined with PIK3R5 as we changed complexity to c = 3. It resulted in having multiple functions for the node AKT3. For c = 3, PIK3R5 functioned for permeability, vasodilatation as well as for cell survival and nitric oxide release [13]. For c = 2, there was a central node called CHP that had members (NFAT5), (PTGS2). But for c = 3, it merged with central node (PLCG1, PLC1). CHP, a central node for c = 2, had NFAT as a member, which is a family of transcription factors. It has at least four structurally similar members, *e.g.*, NFATp (NFAT1), NFATc (NFAT2), NFAT3 and NFAT4. NFATc is present in endocardium, and is involved in morphogenesis of cardiac valves, septum and also in heart organization during development [14]. It regulates the properties of reserve cells. SMC uses NFAT signaling for adaptation. Calcineurin (CHP) is a Ca^{2+}/CAM dependent phosphatase that regulates the process of dephosphorylation and nuclear import of NFAT. Another member PTGS2 is a target of NFAT and is involved in prostaglandin synthesis during angiogenesis. It is necessary for the migration of endothelial cells to allow the proper formation of endothelial

tubes and postnatal angiogenesis *in vivo* [15]. For c = 2, (PRKCA) was a central node which had members (RAF1), (SPHK 2) and (HRAS, HRAS1), but for c = 3, the same central node had no members and as complexity was increased, it became a single node. For c = 4 and c = 5, the number of modules created were the same but this number was less as many central nodes merged. These modules were large enough to study and analysis.

Table 1. Modularization for c = 1 for *H. sapiens* VEGF signaling pathway.

S. No.	Central Node	Other Nodes
1	(KDR)	(VEGFA,VEGF),(SHC2), (PTK2), (PXN)
2	(PLCG1, PLC1)	(SH2D2A)
3	(AKT3)	(NOS3), (CASP9), (BAD)
4	(PRKCA)	-
5	(CHP)	-
6	(PIK3R5)	(RAC1),(SRC)
7	(RAF1)	-
8	(MAPK1)	(PLA2G2D), (MAP2K1)
9	(MAPK14)	(CDC42)
10	(HRAS, HRAS1)	(SPHK2)
11	(MAPKAPK3)	(HSPB1)
12	(NFAT5)	(PTGS2)

Table 2. Modularization for c = 2 for *H. sapiens* VEGF signaling pathway.

S. No.	Central Node	Other Nodes
1	(KDR)	(VEGFA, VEGF), (SH2D2A), (SHC2), (PTK2), (PXN), (CDC42), (SRC), (MAPK14), (MAPKAPK3), (HSPB1)
2	(PLCG1, PLC1)	(PLA2G2D), (NOS3), (MAPK1), (MAP2K1)
3	(PRKCA)	(RAF1), (SPHK2), (HRAS, HRAS1)
4	(PIK3R5)	(RAC1)
5	(CHP)	(NFAT5), (PTGS2)
6	(AKT3)	(CASP9), (BAD)

Table 3. Modularization for c = 3 for *H. sapiens* VEGF signaling pathway.

S. No.	Central Node	Other Nodes
1	(KDR)	(VEGFA, VEGF), (SH2D2A), (SHC2), (PTK2), (PXN), (CDC42), (SRC), (MAPK14), (MAPKAPK3), (HSPB1)
2	(PLCG1, PLC1)	(CHP), (PLA2G2D), (NOS3), (NFAT5), (MAPK1), (PTGS2), (MAP2K1), (RAF1), (HRAS,HRAS1), (SPHK2)
3	(PRKCA)	-
4	(PIK3R5)	(RAC1), (AKT3), (CASP9), (BAD)

3.2. Changes Found with the Increased Complexity Values

We found that different c-values gave different number and complexity of modules. Number of modules was decreased as we increased the c-value. This resulted in over splitting. Many different modules were combined and increased in size with increase in c-value. With increase in c-value, new members were inserted in a certain module or changed its earlier central node. As we took the case of VEGF signaling pathway of *H. sapiens*, we found just half number of modules with decrease in c-value by one, *i.e.*, for c-value of two, we had six modules whereas, the number was 12 for c = 1. But, for c = 4 and 5, size and number of modules, and the number of their members became static (in **Tables 4** and **5** respectively). The names of central nodes and their members for different c-values are given in **Tables 1-5**.

3.3. Fixing the Complexity Values

Now, by assigning different c-values, we had different sets of modules. So, by analyzing all the modules thoroughly, we understood that for c = 5, we should have stopped modularization process. Because for c = 4 and c = 5, we had the same set of modules. Even for c = 3, number of modules were less and they were merged, and thereby, it was unworthy to proceed. As per above analysis, it was clear that for higher c-values, number of nodes and relations were greater than that we got for c = 1 as nodes started merging with other nodes. For c = 1, we

Table 4. Modularization for c = 4 for *H. sapiens* VEGF signaling pathway.

S. No.	Central Node	Other Nodes
1	(KDR)	(VEGFA, VEGF), (SH2D2A), (SHC2), (PTK2), (PXN), (CDC42), (PIK3R5), (SRC),(MAPK14), (RAC1), (AKT3), (MAPKAPK3), (NOS3), (CASP9), (BAD), (HSPB1)
2	(PLCG1, PLC1)	(CHP), (PRKCA), (PLA2G2D), (NFAT5), (RAF1), (SPHK2), (MAPK1), (PTGS2), (HRAS,HRAS1), (MAP2K1)

Table 5. Modularization for c = 5 for *H. sapiens* VEGF signaling pathway.

S. No.	Central Node	Other Nodes
1	(KDR)	(VEGFA, VEGF), (SH2D2A),(SHC2), (PTK2), (PXN), (CDC42), (PIK3R5), (SRC), (MAPK14), (RAC1), (AKT3), (MAPKAPK3), (NOS3), (CASP9), (BAD), (HSPB1)
2	(PLCG1, PLC1)	(CHP), (PRKCA), (PLA2G2D), (NFAT5), (RAF1), (SPHK2), (MAPK1), (PTGS2), (HRAS, HRAS1), (MAP2K1)

had sufficient nodes, and relations for most of the nodes of this pathway. By analysis of all the modules for different *c*-values, we assumed that increase in *c*-value gave almost similar output as nodes got merged. Module names, their number of nodes and relations for different *c*-values for *H. sapiens* VEGF signaling pathway are shown in **Table 6**. We were getting a simplified and biologically significant network for $c = 1$. We found $c = 1$ to be an optimal one, because for this *c*-value, network was modularized properly and not too much over splitting was occurred. This made us to fix *c*-value to 1 for VEGF signaling pathway of *H. sapiens*.

3.4. Comparison of Algorithm of Nayak and De with Newman's Community Finding Algorithm

For the algorithm of Nayak and De, we got modules where central nodes were defined but it was not the case with Newman's algorithm. By applying Newman's algorithm, we got four modules while it was 12 for the algorithm of Nayak and De for $c = 1$. Thus, we found less

Table 6. Module names and their number of nodes and relations for *H. sapiens* VEGF signaling pathway. `N' represents number of nodes and `R' stands for number of relations.

S.No	Module Name	*c* = 1		*c* = 2		*c* = 3		*c* = 4		*c* = 5	
		N	R	N	R	N	R	N	R	N	R
1	(KDR)	5	4	11	10	11	10	17	16	17	16
2	(PLCG1, PLC1)	2	1	5	4	11	11	11	10	11	10
3	(AKT3)	4	3	3	2	1	0	1	0	1	0
4	(PRKCA)	1	3	4	4	1	0	0	0	0	0
5	(CHP)	1	2	3	2	1	0	0	0	0	0
6	(PIK3R5)	3	2	2	1	5	4	0	0	0	0
7	(RAF1)	1	3	1	0	0	0	0	0	0	0
8	(MAPK1)	3	2	1	0	0	0	0	0	0	0
9	(MAPK14)	2	1	1	0	0	0	0	0	0	0
10	(HRAS, HRAS1)	2	1	1	0	0	0	0	0	0	0
11	(MAP-KAPK3)	2	1	1	0	0	0	0	0	0	0
12	(NFAT5)	2	1	1	0	0	0	0	0	0	0

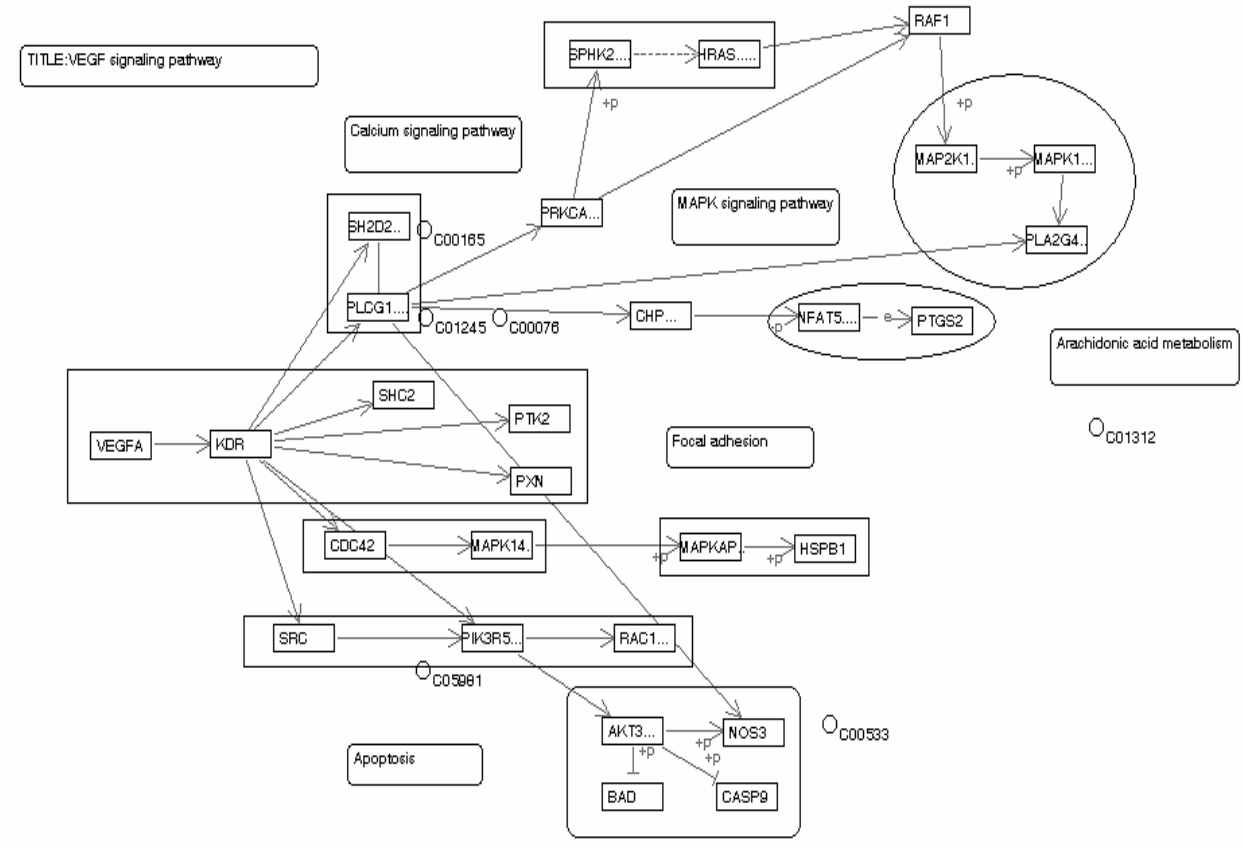

Figure 2. Modules of human VEGF signaling pathway created by the algorithm of Nayak and De for *c*-value of 1.

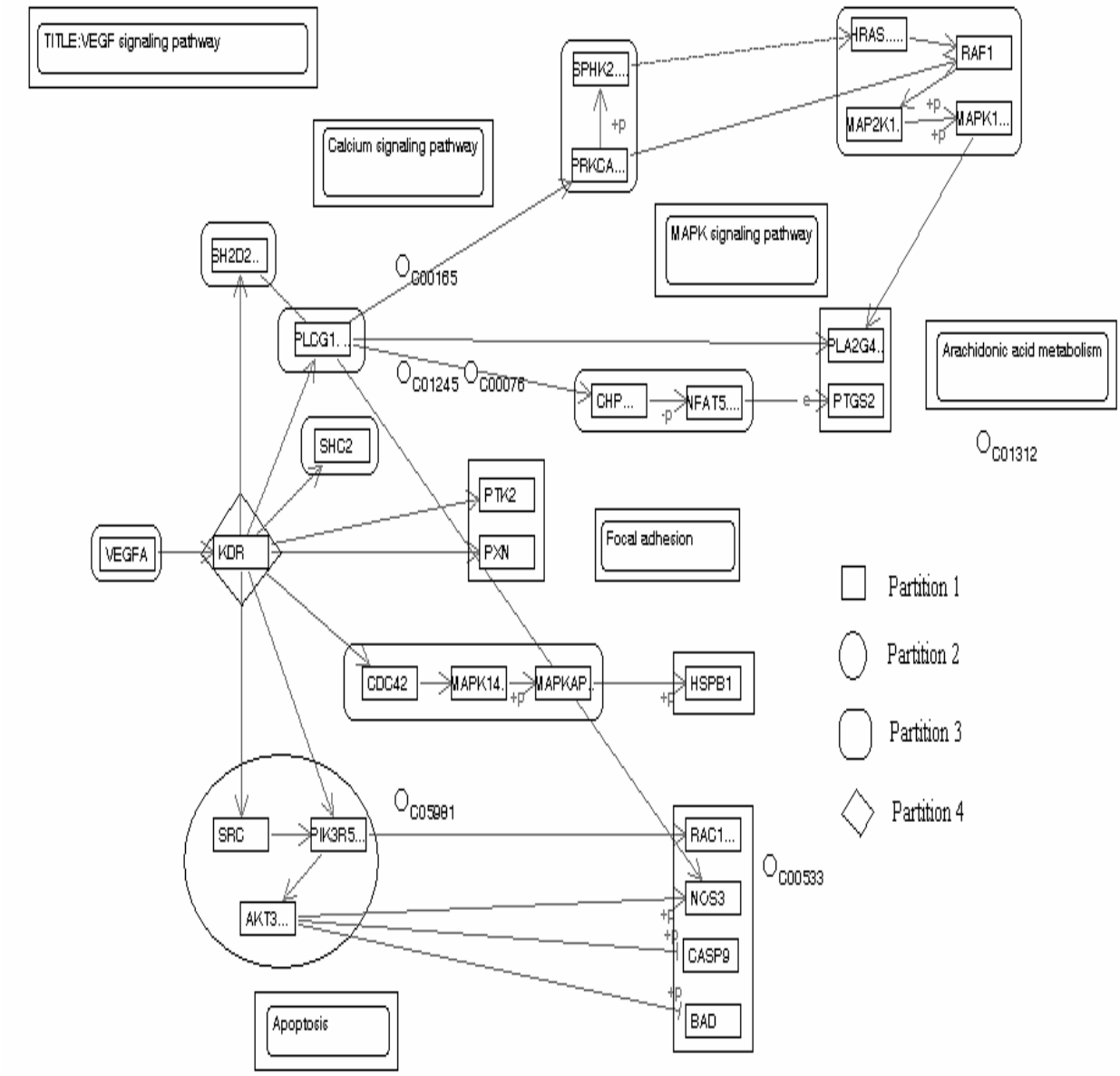

Figure 3. Modules of human VEGF signaling pathway created by Newman's algorithm.

number of modules by Newman's algorithm. Hence, the complexity of the modules obtained by Newman's algorithm was quite high compared to those generated by the algorithm of Nayak and De. This may defeat the objective of modularizing a signal transduction pathway. Nodes of a created module obtained by Newman's algorithm were placed at very much distance, so assigning functions for these types of modules, was difficult. Moreover, as we know that signaling networks work on the basis of interaction between the input signaling node and output signaling node, most of the nodes present in the modules created by Newman's community finding algorithm had no such interaction. So, we can say that function and behavior of a modules generated by Newman's community finding algorithm were not clearly revealed as shown in **Figure 3**.

By analyzing the modules obtained by both the algorithms, we found that MAPK1 includes MAP2K1, RAF1 and HRAS by implementing Newman's algorithm while in algorithm of Nayak and De; MAPK1 had PLA2G2 instead of RAF1 and HRAS. Here, RAF1 and HRAS formed a separate module. The module MAPK1, as generated by the algorithm of Nayak and De, had 2 functions regarding cell proliferation and PGI2 production. But in Newman's algorithm, function of this module had

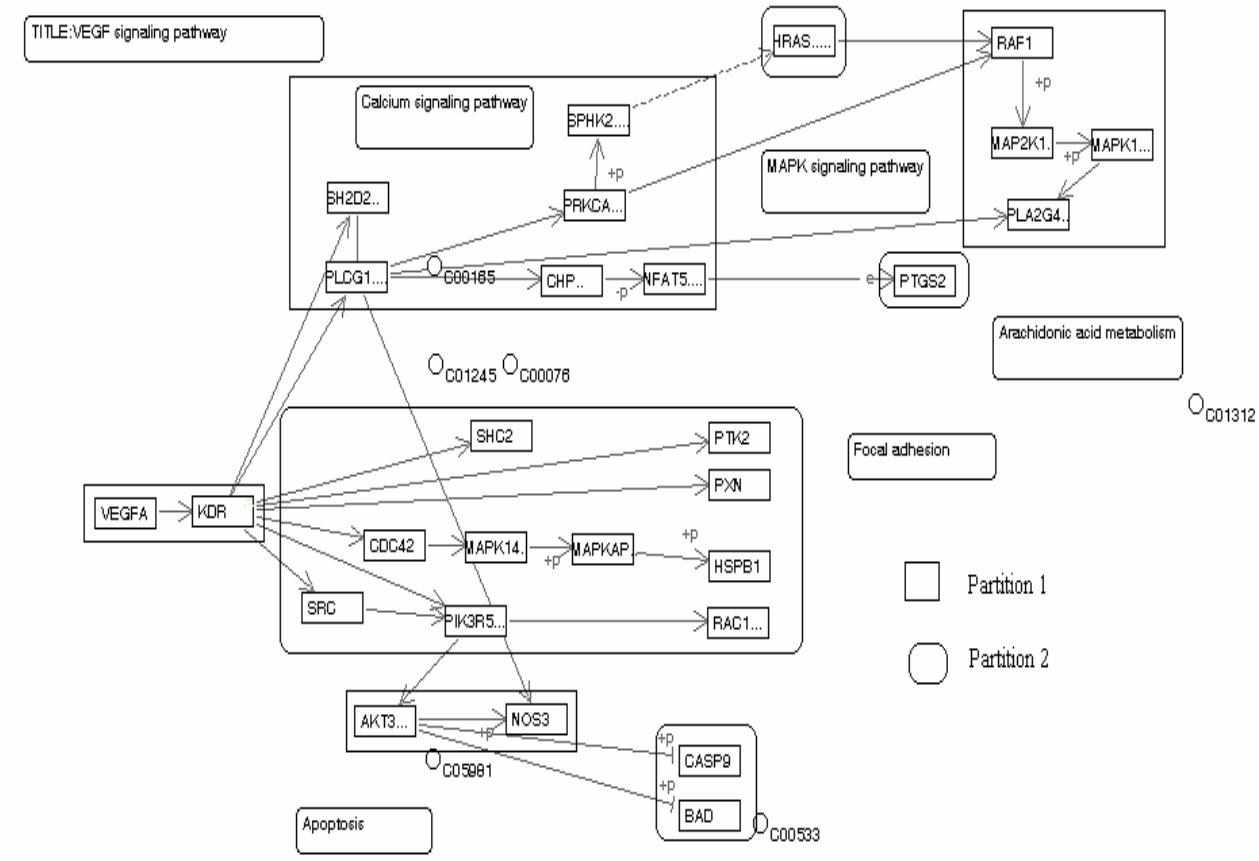

Figure 4. Modules created by Farhat's algorithm of *H. sapiens* VEGF signaling pathway.

been changed as this module was merged with RAF1 and HRAS. Now, PLA2G2 was involved only in PGI2 production. Another functionally important node PLC-γ was with SH2D2 through the algorithm of Nayak and De, while by Newman's algorithm, it was included in module 3 and had SPHK2 as a different member. In Newman's algorithm, KDR emerged as a singleton node in module 4 (**Figure 3**), while through the algorithm of Nayak and De, it was with VEGF and three other members. So we can say that KDR acts as a receptor for VEGF and functions in focal adhesion, as it has PTK2 and PXN as its members. In Newman's algorithm, node RAC was with NOS and other apoptotic signaling pathway components, functions for cell permeability as well as cell survival. But for this, the algorithm of Nayak and De, it was with PI3K and SRC having only one function, *i.e.*, of cell migration.

3.5. Comparison of Algorithm of Nayak and De with Farhat's and Greedy Algorithms

Applying Farhat's and Greedy algorithms to this problem, we got two partitions. AKT3 appeared as a central node and had 3 other members by the algorithm of Nayak and De but both Farhat's and Greedy algorithms had divisions in members of AKT3. These members were present in 2 different partitions. The node KDR had different members obtained by Farhat's and Greedy algorithms. Even the members of MAPK signaling pathway were present in different modules created by the algorithm of Nayak and De but through implementation of Greedy and Farhat's algorithms all the members were in the same partition. The modularized diagram through Farhat's algorithm and Greedy algorithm are shown in **Figures 4** and **5** respectively.

3.6. Comparison of the algorithm of Nayak and De with the combined Farhat's, Greedy and Kernighan-Lin's algorithms

Kernighan-Lin's algorithm had been implemented in two ways. It was implemented by taking output of Farhat's and Greedy algorithms as its input. These outputs are shown in **Figures 6** and **7** respectively. It also gave two

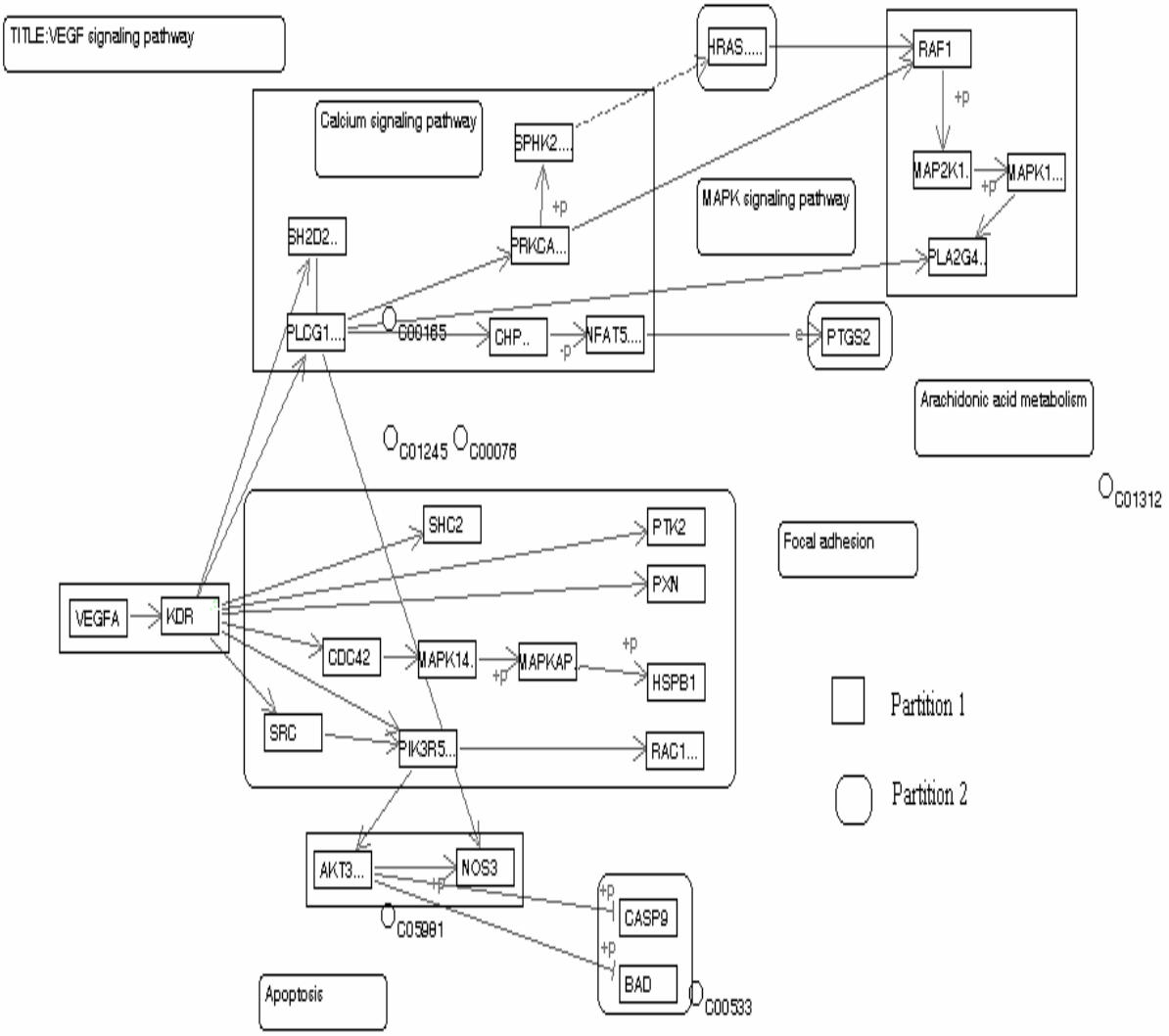

Figure 5. Modules created by Greedy algorithm of *H. sapiens* VEGF signaling pathway.

partitions that were different from the algorithm of Nayak and De. Module AKT3 had four members obtained by the algorithm of Nayak and De, while this particular module had two different partitions through Farhat's and Greedy algorithms. AKT3 and NOS3 were present in one partition, and CASP9 and BAD were found in different partitions as shown in **Figures 6** and **7** respectively.

3.7. Comparative Study of the Modules of VEGF Signaling Pathways for Different Species for $c = 1$

For $c = 1$, we had applied the algorithm to seven different species present in KEGG database. In the case of *H. sapiens*, 12 modules were created which were the same for *M. musculus* (mouse) where all the modules were same in number and characteristics. **Figure 2** shows a modularized pathway for $c = 1$ of *H. sapiens*. As we further compared these two species with *R. norvegicus* (rat), we found difference in only one module and it was Plc –1. This module appeared as a single node in *R. norvegicus* (rat) whereas in *H. sapiens* (human being) and *M. musculus* (mouse), it had one member SH2D2A. So this kind of comparison gives an idea that the VEGF pathway of these three species is developed almost in a similar manner.

For *B. taurus* (cow), we had 10 modules. The module MAPK was fully developed and had other members. MAPKAP and MAP14 were present as two different modules in *H. sapiens*, which were combined in *B. tau-*

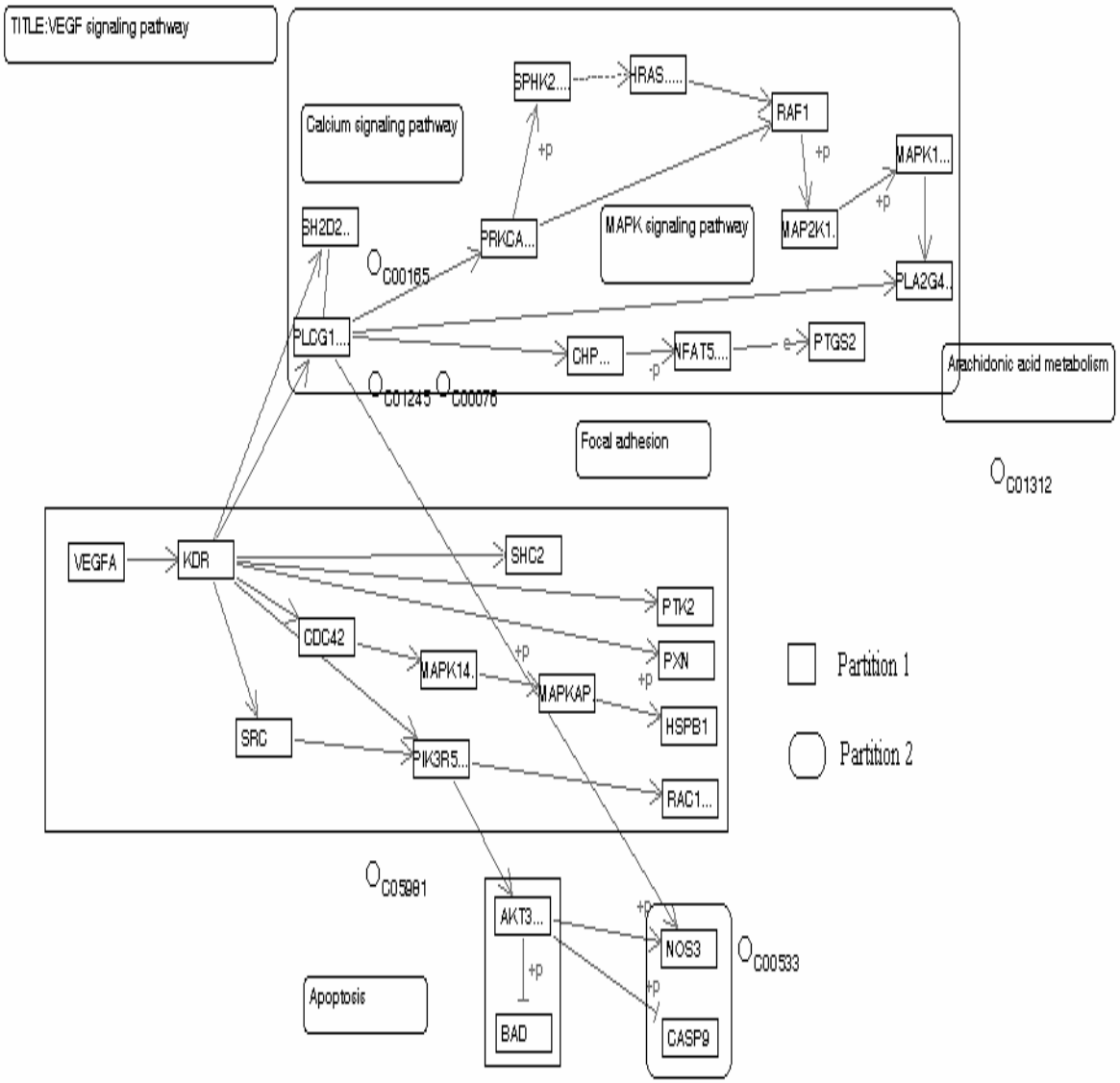

Figure 6. Modules created by combined Kernighan-Lin's and Farhat's algorithms for *H. sapiens* VEGF signaling pathway.

rus(cow). The module LOC534LOC511224 and had a member COX which was absent in *H. sapiens*. Here the module AKT3, named as AKT1, had a member MGC 127164 that made it different from others because in other species, it had all the three members. Even, PRKCA was present as a single node. For *P. troglodytes* (Chimpanzee), we had 8 modules. As in the previous species' modules, MAPK, PI3K were fully developed and even node RAF1 was a central node and had two members. It was not present as a single node as we had seen earlier. In *C. familiaris* (dog), we found 7 modules. The modules KDR, MAPK and AKT3 were fully developed but PLC-γ, PRKCA and PIP3K were absent. In *H. sapiens*, the node Src was included in module PIK3R5 but it was in module KDR in *C. familiaris* (dog). But for *S. scrofa* (pig), it was the least developed and had only one module for NFAT [13]. **Table 7** provides the details of the modules obtained, for $c = 1$, from VEGF pathways of these species. So, from this comparison, we can say that, KDR and MAPK are said to be consistent in most of the studied species.

4. CONCLUSIONS

In this paper, different partitioning algorithms were applied to human VEGF signaling pathway in order to divide it into smaller meaningful modules for analysis purpose. The applied partitioning algorithms are: modularization algorithm of Nayak and De, Newman's com-

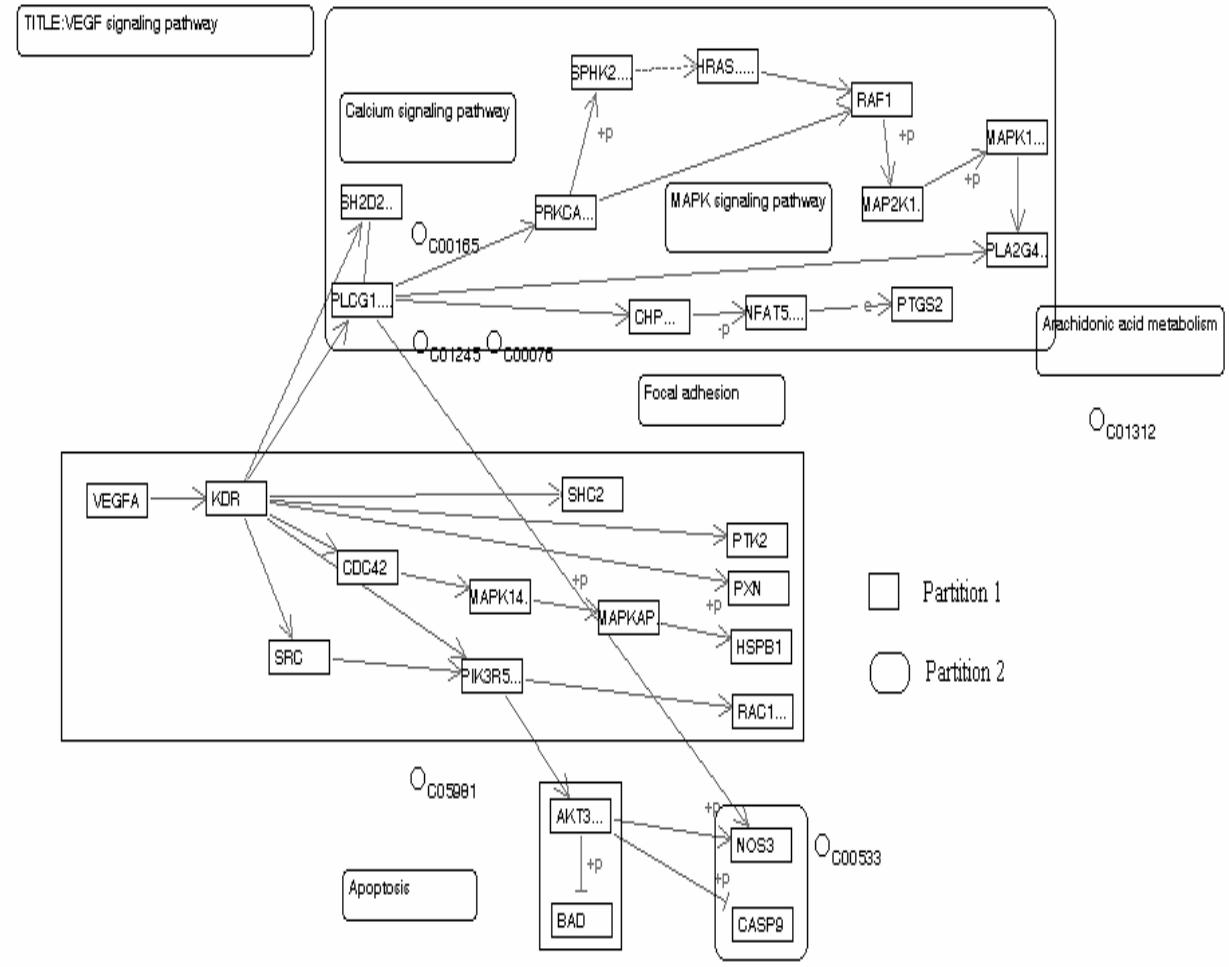

Figure 7. Modules created by combined Kernighan-Lin's and Greedy algorithms for *H. sapiens* VEGF signaling pathway.

Table 7. Created modules and nodes for VEGF signaling pathway of seven species for c = 1. (M- Modules names; (N) - Number of Nodes present in a module).

Human and Mouse	Rat	Cow	Chimpanzee	Dog	Pig
M(N)	M(N)	M(N)	M(N)	M(N)	M(N)
KDR(5)	Kdr(5)	PLCG1(1)	LOC461315(3)	LOC460400(2)	NFATC1(3)
PLCG, PLC1(0)	Plcg1(1)	PIK3CA(2)	LOC455085(3)	KDR(3)	-
AKT3(4)	Akt1(4)	flk-1(3)	RAF1, LOC460182(3)	LOC484648(3)	-
PRKCA(0)	Prkca(1)	LOC521196(2)	LOC453202(3)	AKT3(3)	-
CHP(0)	Ppp3cc(1) LOC454037(3)	PPP3R1(0) LOC477575(3)	MAPK3,	-	-
PIK3R5(3)	Pik3ca(3)	MAPK1(3)	MAPK14(2)	MAPK14(3)	-
RAF1(0)	Raf1(1)	LOC534492(3)	LOC452821(3)	LOC479678(2)	-
MAPK1(3)	Mapk1(3)	PRKCA(1)	LOC460400(2)	-	-
MAPK14(2)	Mapk13(2)	AKT1(2)	-	-	-
HRAS,HRAS1(2)	Kras(2)	LOC511224(2)	-	-	-
MAPKAPK3(2)	Mapkapk2(2)	-	-	-	-
NFAT5(2)	Nfatc4(2)	-	-	-	-

munity finding algorithm, Graph partitioning algorithm of Kernighan-Lin's, Farhat's and Greedy algorithms. First of all, algorithm of Nayak and De was applied to human VEGF signaling pathway for different *c*-values. The best set of modules were found for $c = 1$. The comparison of human VEGF signaling pathway modules for $c = 1$ was done with those obtained by some other partitioning algorithms. We got four modules by applying Newman's algorithm, while it was 12 for the algorithm of Nayak and De for $c = 1$. We got only two partitions by applying Farhat's, Greedy and Kernighan-Lin's algorithms. The number of partitions and their members were kept the same while applying Farhat's and Greedy algorithms. So again, our objective was not fulfilled of getting smaller biological meaningful modules. All the modules got through applying algorithm of Nayak and De are self-sufficient and have minimal dependency on the rest part of the network. This property works behind the idea of modularization of a biological signaling pathway. Through the result analysis, we can say that the algorithm of Nayak and De is superior over considered existing partitioning algorithms here, and better in reducing the complexity of the signaling pathway.

Moreover, the species specific modules were obtained for the same optimal *c*-value through the algorithm of Nayak and De. Their comparison proved that the trend of development, in ascending order, was "*S. scrofa* (pig), *C. familiaris* (dog), *P. troglodytes* (chimpanzee), *B. taurus* (cow), *M. musculus* (mouse), *R. norvegicus* (rat) and *H. sapiens* (human being)." This trend shows that signaling pathways become more complex in higher organisms. We found that the modules KDR and PLC-γ were consistent in *H. sapiens* for all *c*-values and were functional in all studied species. So, we can say, as per comparative analysis that modules KDR and PLC-γ are conserved in all the studied species. Even the module AKT3 was found in all the studied species except in *S. scrofa* (pig) and *B. Taurus* (cow).

This analysis makes one to study a conserved or consistent module rather than considering the complex signaling pathway as a whole. It is easier to determine underlying mechanism of normal development as well as in certain disorders or diseased conditions. In a certain disease, only one molecule or a small group of molecules gets deregulated, so modularized study makes one to concentrate over a few modules containing responsible molecules only. This type of implementation also saves time and cost for experimental analysis.

REFERENCES

[1] Twyman, R.M. (2000) Advanced molecular biology. Garland/BIOS Scientific Publishers, UK.

[2] David, L.N. and Cox, M.M. (2008) Lehninger principles of biochemistry. 5th Edition, W. H. Freeman & Company, New York.

[3] Nayak, L. and De, R. (2007) An algorithm for modularization of MAPK and calcium signaling pathways: Comparative analysis among different species. *Journal of Biomedical Informatics*, **40(6)**, 726-749.

[4] Robinson, C.J. and Stringer, S.E. (2001) The splice variants of vascular endothelial growth factor (VEGF) and their receptors. *Journal of Cell Science*, **114(5)**, 853-865.

[5] Kowanetz, M. and Ferrara, N. (2006) Vascular endothelial growth factor signaling pathways: Therapeutic perspective. *Clinical Cancer Research*, **12(17)**, 5018-5022.

[6] Breslin, J.W., Pappas, P.J., Cerveira, J.J., Hobson, R.W. and Durn, W.N. (2002) VEGF increases endothelial permeability by separate signaling pathways involving ERK-1/2 and nitric oxide. *American Journal of Physiologic Heart Circ Physiology*, **284(1)**, H92-H100.

[7] Kernighan, B.W. and Lin, S. (1970) An efficient heuristic procedure for partitioning graphs. *The Bell System Technical Journal*, **49**, 291-307.

[8] Chartrand, G. and Oellermann, O.R. (1993) Applied and algorithmic graph theory. *International Series in Pure and Applied Mathematics*. McGraw Hill, New York.

[9] Farhat, C.G. (1988) A simple and efficient automatic fem domain decomposer. *Computers & Structures*, **28(5)**, 579-602.

[10] Newman, M.E.J. (2006) Modularity and community structure in networks. *PNAS*, **103(23)**, 8577-8582.

[11] McLaughlin, A.P. and Vries, G.W.D. (2001) Role of PLCg and Ca^{2+} in VEGF and FGF-induced choroidal endothelial cell proliferation. *American Journal of Physiologic Cell Physiology*, **281(5)**, C1448-C1456.

[12] Hunag, C., Jacobson, K. and Schallerl, M.D. (2004) MAP Kinases and cell migration. *Journal of Cell Science*, **117**, 4619-4628.

[13] Blum, S., Issbrucker, K., Willuweit, A., Hehlgans, S., Lucerna, M., Mechtcheriakova, D., Walsh, K.V.D., Ahe, D., Hofer, E. and Clauss, M. (2001) An inhibitory role of the phosphatidylinositol 3-kinase-signaling pathway in vascular endothelial growth factor-induced tissue factor expression. *The Journal of Biochemistry*, **276(36)**, 33428-33434.

[14] Horsley, V. and Pavlath, G.K. (2002) NFAT: Ubiquitous regulator of cell differentiation and adaptation. *The Journal of Cell Biology*, **156(5)**, 771- 774.

[15] Armesilla, A.L., Lorenzo, E., Arco, P.G.D., Martinez S., Alfranca, A. and Redondo, J.M. (1999) Vascular endothelial growth factor activates nuclear factor of activated T cells in human endothelial cells: A role for tissue factor gene expression. *Molecular and Cellular Biology*, **19(3)**, 2032-2043.

J. Biomedical Science and Engineering, 2010, 3, 943-955 **JBiSE**
doi:10.4236/jbise.2010.310125 Published Online October 2010 (http://www.SciRP.org/journal/jbise/).

Characteristic sites in the internal proteins of avian and human influenza viruses

David King, Zachary Miller, Wesley Jones, Wei Hu*

Department of Computer Science, Houghton College, Houghton, USA
Email: wei.hu@houghton.edu

Received 8 July 2010; revised 19 July 2010; accepted 18 August 2010.

ABSTRACT

The capacity of zoonotic influenza to cross species boundaries to infect humans poses a global health threat. A previous study identified sites in 10 influenza proteins that characterize the host shifts from avian to human influenza. Here, we used seven feature selection algorithms based on machine learning techniques to generate a novel and extensive selection of diverse sites from the nine internal proteins of influenza based on statistically importance to differentiating avian from human viruses. A set of 131 sites was generated by processing each protein independently, and a selection of 113 sites was found by analyzing a concatenation of sequences from all nine proteins. These new sites were analyzed according to their annual mutational trends. The correlation of each site with all other sites (one-to-many) and the connectivity within groups of specific sites (one-to-one) were identified. We compared the performance of these new sites evaluated by four classifiers against those recorded in previous research, and found our sites to be better suited to host distinction in all but one protein, validating the significance of our site selection. Our findings indicated that, in our selection of sites, human influenza tended to mutate more than avian influenza. Despite this, the correlation and connectivity between the avian sites was stronger than that of the human sites, and the percentage of sites with high connectivity was also greater in avian influenza.

Keywords: Connectivity, Correlation, Feature Selection, Host Specificity, Influenza, Machine Learning, Mutation

1. INTRODUCTION

The genetic shift and recombination of influenza have resulted in a virus that is an annually recurring health problem [1,2]. In addition to infecting humans, the viruses are also able to infect a number of other hosts, including swine and birds. While these species-specific strains typically remain within their species of origin, there is a potential for them to cross over to human hosts, with the outbreak of H1N1 (swine) Flu in 2009 being the most recent example [1,3,4]. Because these strains of host-shifted viruses have the potential for increased virulence and mortality rate in humans, study of these crossover pandemic shifts is critical. In particular, identification of key amino acid sites that have significant impact on the biological functions of the viruses, especially those sites that potentially affect host shifts, is crucial in influenza research.

The genome of influenza can be divided into eight gene segments which encode 11 proteins. Of these, nine are internal proteins (M1, M2, NP, NS1, NS2, PA, PB1, PB1-F2, PB2) while two are surface glycoproteins (HA, NA) [1,2,5]. Information from the HA gene was utilized in a predictive analysis of evolutionary trends [6], in which a five step process was used to create a mutual information matrix that could be used to characterize evolutionary paths and to make predictions on future genetic shifts based on previous data. Given quality input, the process was able to predict historical trends with 70% accuracy [6]. Co-mutation of amino acids has also been used in order to track antigenic shifts in the viruses [2,7]. Metrics have been created to reduce the background information in the protein sequences, furthering the ability to identify co-evolving amino acid sites [8].

A study [1] conducted in 2009 by Asif U. Tamuri *et al.* analyzed sequences from 10 influenza proteins using a phylogenic analysis on each individual protein, which resulted in a large number of specific sites in each protein being found to have different selection constraints in human and avian viruses. There were 172 amino acid sites found with strong support and 346 sites with moderate support. In [1], each site was treated as a completely independent attribute, but the authors suggested that a pair-wise analysis might yield further interesting results.

In addition to the phylogenic analysis conducted in [1], a paper [3] published in 2009 by Jonathan Allen *et. al.* reported the use of linear support vector machines (SVMs), a machine learning technique, to evaluate human and avian influenza protein sites as markers for high mortality rate and host specificity. Combined, these two characteristics were indicators of potential pandemic outbreak of avian influenza in human hosts. A set of 34 amino acid markers associated with both of these traits was found. Further, the study demonstrated that current recombinations of avian and H1N1 strains of human and swine influenza could attain these pandemic markers with a double reassortment and two amino acid mutations.

A project [2] conducted by Xiangjun Du, *et. al.* focused on the relationships between nucleotide positions in the eight gene segments comprising the entire influenza genome. A value $C_{i,j}$ was used to calculate the co-occurrence of a pair of nucleotides occurring at sites i and j. Another value, the K-Value, made use of $C_{i,j}$ to evaluate the connectivity within a gene sequence ($C_{i,j}$ and a modified version of the K-Value are defined in Subsection 2.3). The averaged K-Values of different influenza gene sequences were evaluated according to year, which showed the trends of nucleotide substitution co-occurrence against the passing of flu-seasons. The analysis in [2] showed that the methodology of generating co-occurrence networks was an effective tool for tracking influenza's evolutionary patterns. Interestingly, the study implied that there was a correlation between nucleotide co-occurrence and virus antigenicity, where 86% of the pairs shared both connectivity clusters and antigenicity clusters.

The design of our study was inspired by the work of [1,2,3]. It was our intention in this project to use seven feature selection algorithms based on machine learning techniques to discover a diverse set of widely distributed sites in each of the nine internal proteins of avian and human influenza, as well as a set selected competitively from a concatenation of all nine sequences. The mutational trends of these sites were analyzed, as was the site correlation using the connectivity and co-occurrence metrics described in [2]. Finally, connectivity networks of related sites within each individual protein and between all nine internal proteins were generated.

2. MATERIALS AND METHODS

2.1. Protein Sequence Data

Three sets of avian and human influenza protein sequences were used in the current study, all selected from the National Influenza Virus Database, managed by The National Center for Biotechnology Information.

In order to establish a baseline of comparison with previous studies, the first sequence set, hereafter referred to as sequence set A, was the same as that used in [1]. Sequence set A included aligned full-length sequences from 10 influenza proteins (HA, NA, M1, M2, NP, NS1, NS2, PA, PB1, PB2). Near-duplicate sequences (those 95% similar to already-included sequences), were not included. This resulted in each protein having around 400 to 500 sequences.

A second set, hereafter referred to as sequence set B, was formed to evaluate comparatively the connectivity across all nine internal proteins. Sequences from each protein (M1, M2, NP, NS1, NS2, PA, PB1, PB1-F2 and PB2) were aligned using the MAFFT multi-sequence alignment tool (available at http://mafft.cbrc.jp/alignment/server/index.html), and divided according to host species. Protein sequences with common identifiers were concatenated in the order given above to create a set of protein sequences spanning all nine internal proteins. Positions that contained gaps in the majority of sequences were eliminated, leaving a set of 2286 concatenated sequences of length 3520.

Lastly, a third sequence set, hereafter referred to as sequence set C, was included to allow for time- dependant analysis. Because sequence set B was constructed based on common sequence identifiers among all nine proteins, there were not enough sequences from each year to conduct a statistically reliable analysis. Sequence set C included roughly 3000 to 5000 full length sequences from each internal protein.

2.2. WEKA Feature Selection

In order to identify the sites significant to species distinction, a feature selection was performed. To reduce the bias from a particular feature selection algorithm, seven algorithms from the data mining utility WEKA [9] were employed in our analysis. The algorithms used were: Chi-Squared, Information Gain, Information Gain Ratio, 1R, Relief, Symmetrical Uncertainty and Filtered Attribute Evaluation. In the current study, the features to be selected were the amino acid sites in the protein sequences.

Chi-Squared feature selection uses the Chi-Squared test to select the best discriminating features between positive and negative examples [10]. Both Information Gain and Information Gain Ratio construct decision trees to determine their selections. Information Gain decision trees use the Kullback-Leibler divergence (often called information gain) to build the tree, while Information Gain Ratio decision trees use a slight modification of the Kullback-Leibler divergence that keeps the selection from focusing on features with large pools of potential values [11].

The 1R algorithm is different than most other feature selection algorithms because it ranks the features ac-

cording to the error rate rather than using entropy-based measures. The algorithm chooses the most informative feature and interprets the rest of the data based on this one features [12]. Relief ranks features by their ability to discriminate between neighboring patterns [13]. Symmetric Uncertainty evaluates the weighted mutual information of two features. Filtered Attribute Evaluation simply allows for an arbitrary filter to be used to evaluate features; in this instance, the Ranker filter, provided by WEKA, was used.

2.3 Co-Occurrence and K-Value

The evaluation of co-occurrence and connectivity between amino acid sites was performed through two measurements. The original versions of these metrics were used in [2], however one of them has been modified slightly to better serve the purposes of this analysis. $C_{i,j}$, which measures the co-occurrence between two amino acids x and y at a pair of sites i and j respectively, can be defined as

$$C_{i,j} = \frac{f(x_i, y_j)^2}{f(x_i) * f(y_j)}$$

where $f(x_i)$ is the frequency of amino acid x occurring at position i, $f(y_j)$ is the frequency of amino acid y occurring at position j, and $f(x_i,y_j)$ is the frequency of both occurring in the same sequence. The range of the value produced is, where 1 means perfect co-occurrence of x_i and y_j. While [2] used these values to construct connectivity matrices, wherein only pairs of sites with perfect co-occurrence would receive an edge between them, all pairs are utilized in this study, and the $C_{i,j}$ value is used as a weight, such that those pairs with greater co-occurrence contribute more to the total connectivity.

The K-Value, K_i, which measures the average co-occurrence value of all amino acid pairs involving site i can be given as:

$$K_i = \frac{1}{l * m} \sum_{j=1}^{m} C_{i,j} * n(x_i, y_j)$$

where l is the sequence length, m is the number of sequences, and $n(x_i,y_j)$ is the number of occurrences of both amino acids x and y at the sites i and j occurring together. In [2], the K-Value was used to represent the average connectivity of all sites within a single sequence, however in this study; the formula was modified to represent the connectivity of a single site to all other sites in all sequences in a given sequence set.

3. RESULTS AND DISCUSSION

3.1 Important Sites for Distinguishing Avian from Human Viruses

The original selection of sites important to distinguishing host species was the critical foundation for the subsequent work in this study. Using amino acid sites as features for the seven WEKA feature selection algorithms (Subsection 2.2), two selections of sites were generated: one based on sequence set A and one based on sequence set B.

For the selection based on sequence set A, the intersection of the top 25 sites generated by each algorithm was taken for each protein. The number of sites selected by the different algorithms varied; on average, 15 sites were selected from each protein, for a total of 131 sites over all the proteins. This selection will subsequently be referred to as the individually selected sites (**Table 1**).

In order from most to least, the number of sites selected from each protein was as follows: NP(22), PB2(19), M2(18), PA(17), NS1(12), PB1(12), PB1-F2(11), M1(10), NS2(10). The frequency of amino acid substitution at these sites (**Table 1**) showed the avian strains generally had less amino acid variation than the human strains: the avian and human proteins maintained site conservation averages of 94.2 and 80.9 respectively. The avian protein with the most conserved sites was NP with a site conservation average of 99.8, compared to human NP, with a conservation average of 87.2. PB1-F2 sites showed the lowest site conservation average for avian (76.8). The proteins that contained the highest and lowest site conservation averages for human influenza were M2 with a site conservation average of 89.1, and PB1 with a site conservation average of 60.2 respectively.

The same process was followed for the selection of sites for sequence set B, which contained full-length concatenated sequences. The intersection of the top 150 sites selected by the seven algorithms yielded 113 significant sites in sequence set B. Of these 113, 89 were also part of the individually selected sites (marked in Table 1). Those that were distinct from the individually selected sites included: NP:136, NP:535, NP:450, NS1:59, NS1:70, NS1:84, NS1:166, NS1:171, PA:142, PA:184, PA:272, PA:277, PA:231, PA:383, PA:385, PA:387, PA:400, PA:668, PB1-F2:73, PB1-F2:76, PB1-F2:79, PB1-F2:87, PB2:67 and PB2:292. This selection will be hereafter referred to as the concatenated selected sites.

Because the concatenated selected sites were based on full-length concatenated sequences, all sites were treated equally, regardless of which protein they were located in. When selected competitively, we found some proteins to be more essential to determining host species than others. The number of sites selected from each individual protein was: PA(25), NP(21), PB2(20), M2(14), NS1(13), PB1-F2(8), M1(5), PB1(4) and NS2(3). In addition to the raw number of sites each protein contributed, the total percentage of the sites in each protein selected was

also considered. The percentages selected from each protein, in order from greatest to least, were: M2(14.4%), PB1-F2(8.9%), NS1(5.7%), NP(5.0%), PA(2.9%), PB2 (2.6%), NS2(2.5%), M1(2.0%) and PB1(0.5%), suggesting

Table 1. Important Sites for distinguishing avian from human viruses.

Site	Avian	Freq.	Human	Freq.	Site	Avian	Freq.	Human	Freq.	Site	Avian	Freq.	Human	Freq.
M1		**99(Avg)**		**81.9(Avg)**	375*^	D	100	E(G,V,D)	66(22,10,2)	552*^	M	100	S(T)	99(1)
115*^	V(M)	98(2)	I(V)	99(1)	421	E	100	D(E)	66(34)	**PB1**		**99.7**		**60.2**
121*	T	100	A	100	422*	R	100	K(R)	87(13)	212*	L	100	L(V)	51(49)
137*^	T	100	A(T)	99(1)	423*	A	100	S(T,P,A)	45(34,18,3)	327*	R	100	R(K)	51(49)
147	V	100	V(I)	90(10)	442*	T	100	A(T)	87(13)	336*	V	100	I(V)	62(38)
167	T(A)	98(2)	T(A)	57(43)	455*	D	100	E(D)	87(13)	361	S	100	S(R)	59(41)
205	V	100	V(I)	71(29)	**NS1**		**90.1**		**84.9**	473	V	100	V(L)	66(34)
218*	T	100	A(T,V)	82(17,1)	21*	R(L)	85(15)	Q(R)	85(15)	486	R	100	R(K)	70(30)
227*	A	100	A(T)	73(27)	22*	F(L)	85(15)	V(I,F)	95(3,2)	576	L(I)	98(2)	L(I)	62(38)
231^	D(N)	96(4)	D(N)	84(16)	23	A(S)	85(15)	V(A)	58(42)	581*	E	100	E(D)	63(37)
239	A(T)	98(2)	A(T)	64(36)	53	D	100	D(N)	54(46)	584^	R(H)	98(2)	R(Q,H)	65(34,1)
M2		**95.1**		**89.1**	60*	A(E)	75(25)	V(A)	91(9)	645	V	100	V(M,I)	68(28,4)
11*	T(I)	98(2)	I(T)	97(3)	81*^	I(-,T)	94(4,2)	M(-)	99(1)	654	S	100	S(N,I)	66(32,2)
14*	G(E)	96(4)	E	100	98	M(I)	85(15)	L(M)	57(43)	768	A	100	S(T,A)	39(31,30)
16*	E(G)	96(4)	G(E)	96(4)	114*	S(G)	79(21)	P	100	**PB1-F2**		**76.8**		**67**
18*	K(R,S)	64(34,2)	R	100	125	K(R)	99(1)	K	100	3	Q(R,-)	53(44,3)	Q(-)	98(2)
20*	S(N)	98(2)	N	100	196*	E(-)	98(2)	K(E)	84(16)	6	D(G,-)	85(13,2)	G(D,-)	79(19,2)
28*	I(V,F,T)	78(18,2,2)	V(I)	90(10)	215*^	P(-)	98(2)	T	100	23	N(S,-,D)	59(38,2,1)	S(D,-,N)	67(29,2,2)
36	L	100	L(V)	96(4)	227*^	E(-)	98(2)	R(-,E)	96(3,1)	27*	T(I,-)	94(4,2)	I(T,-)	78(20,2)
43	L	100	L(I)	96(4)	**NS2**		**89**		**82**	29*	R(K,-)	66(31,3)	K(R,-)	95(3,2)
48	F	100	F(S)	96(4)	14	M(Q,T,V)	77(19,2,2)	L(M,V)	60(37,3)	59*	K(R)	97(3)	R(-,K)	62(29,9)
50	C	100	C(S)	96(4)	26	E(V,A)	87(11,2)	E(G)	94(6)	60*	Q(R,-,P)	95(2,2,1)	L(-,P,Q)	55(29,8,8)
54*	R(C)	98(2)	L(F,R,I)	53(36,7,4)	37	S(R)	87(13)	S	100	62	L(P,-)	95(4,1)	P(-,L)	52(30,18)
55*	L(F,I)	93(5,2)	F(L)	96(4)	55	L(F)	98(2)	L(I,F)	96(2,2)	66	S(N,-,I)	57(41,1,1)	N(-,S)	69(30,1)
57*	Y	100	H(Y,R)	90(9,1)	57	S	100	S(L)	59(41)	70	G(E,V)	53(44,3)	G(-,V,E)	39(30,27,4)
78*	Q	100	K(E,T)	89(10,1)	60	S(N,I)	79(13,8)	N(S,H,T,I)	92(3,3,1,1)	82	L(S,-)	91(7,2)	S(-,P,L)	43(31,14,12)
82*	S(N)	95(5)	N(S)	51(49)	70*	S	100	G(S)	97(3)	**PB2**		**98.9**		**88**
86*	V	100	A(V)	97(3)	86	R(I)	87(13)	R(K)	80(20)	9*	D	100	N(D,T)	96(3,1)
89*	G(S)	96(4)	S(G,D)	79(18,3)	89*	I(K,V,M)	75(19,4,2)	T(I,V)	56(43,1)	44*^	A	100	S(A)	90(10)
93*^	N	100	S(N)	81(19)	107*	L	100	F(L)	86(14)	64*	M(I)	96(4)	T(M,I)	96(2,2)
NP		**99.8**		**87.2**	**PA**		**99.1**		**88.4**	81*	T	100	M(V,T,I)	91(4,3,2)
16*	G	100	D	100	28*	P(T)	95(5)	L(P)	96(4)	105*^	T	100	V(M,T,I)	60(36,3,1)
31*	R	100	K(R)	94(6)	55*	D	100	N(D)	96(4)	114	V	100	V(I)	57(43)
33*	V	100	I(V)	96(4)	57*	R	100	Q(R)	97(3)	199*^	A	100	S(A)	99(1)
61*	I	100	L	100	65*	S(F)	95(5)	L(P,S,F)	87(9,3,1)	271*	T(A)	96(4)	A(T)	94(6)
100*	R	100	V	100	66*	G	100	D(G,E)	76(17,7)	368*	R(Q)	98(2)	K(R)	86(14)
109*	I(T)	95(5)	V(I)	84(16)	100*	V(I)	95(5)	A	100	453*	P(S,T)	96(2,2)	H(P,S)	71(27,1)
127	E	100	D(E)	81(19)	225*	S	100	C(S)	90(10)	475*^	L	100	M(L)	99(1)
146	A	100	T(A)	79(21)	241	C	100	Y(C)	51(49)	567*	D(V)	98(2)	N(D)	99(1)
214*	R	100	K(R)	97(3)	268*	L	100	I(L)	86(14)	588*	A(T)	98(2)	I(A,V)	94(3,3)
283*^	L	100	P(S)	99(1)	312	C	100	R(K)	83(17)	613*^	V	100	T(A,V,I)	90(6,3,1)
293*	R	100	K(R)	84(16)	337*	L	100	S(A)	97(3)	627*^	E(K)	98(2)	K	100
305*^	R	100	K(R)	91(9)	356*^	K	100	R(K)	87(13)	661*^	A	100	T(A,V)	90(9,1)
313*	F	100	Y(F)	99(1)	382*	V	100	D(E)	94(6)	674*	A	100	T(A,P)	96(3,1)
351	R	100	K(R)	93(7)	404*	R	100	S(A)	90(10)	684*^	A	100	S(A,D)	67(31,2)
357*^	Q	100	K(R,Q)	94(5,2)	409*	W	100	N(S)	97(3)	702*^	K	100	R(K)	97(3)
372*	E	100	D(E)	90(10)	421*	T	100	I(V,S,T)	76(11,9,4)	**Average**		**94.2(Avian)**		**80.9(Human)**

The table contains the individually selected sites, with those sites that are also in the concatenated selected sites marked with a "*". The avian and human columns show the consensus amino acids and their frequencies. Sites marked with a "-" signify a gap in the protein sequence alignment and "^" shows that the selected sites also occur in [1].

certain proteins contained more sites informative to host origin. Notably, the proteins containing the highest percentage of sites critical to host differentiation were those with the shortest sequence length (M2 and PB1-F2), and the protein with the longest sequence length had the lowest percentage of sites (PB1).

3.2 Performance of Classification of the Individually Selected Sites

To validate the statistical significance of our individually selected sites, we compared them with the sites reported in [1]. Four classifiers provided by WEKA were used to assess the ability of these two sets of sites to differentiate avian from human viruses: Support Vector Machine, Naive Bayes, Random Forest and Rotation Forest. Protein sequences from sequence set A were used in this comparison, as both our individually selected sites and the sites reported in [1] were generated using this sequence set.

Support Vector Machines are machine learning techniques which, in binary classification, calculate the optimal separating hyperplane between two data sets [14,15]. The Naive Bayes classifier uses probability to associate each independent feature with a particular class. The classifier then takes the product of the individual probabilities and classifies the instance [16]. The Random Forest constructs a number of decision trees, using a random subset of the training dataset for each. The resulting forest of decision trees represents the final ensemble classifier where each decision tree votes for the final classification, and the majority decision wins [17]. The Rotation Forest classifier randomly splits the entire data set into *N* training subsets, and applies the Principle Component Analysis (PCA) to each. A N axis rotation is used to select the new features for a base classifier [18].

The performance of the classifiers was calculated by the sensitivity, specificity, overall accuracy (*Q2*) and the Matthews correlation coefficient (MCC) expressions, defined as:

$$Sensitivity = \frac{TP}{TP + FN}, \quad Specificity = \frac{TN}{TN + FP},$$

$$Q2 = \frac{TP + TN}{TP + FP + TN + FN},$$

$$MCC = \frac{TP * TN - FP * FN}{\sqrt{(TN + FN) * (TN + FP) * (TP + FN) * (TP + FP)}}$$

where *TP* is the number of true positives, *TN* is the number of true negatives, FP is the number of false positives, and *FN* is the number of false negatives. The results of these calculations for all four classifiers were averaged (**Table 2**), attesting that our individually selected sites were, with the exception of those from the *NP* protein, better able to determine the host species than those reported in [1]. Because [1] did not provide a selection of sites for NS2 and PB1-F2, these two proteins could not be compared.

3.3 Annual Mutational Trends of Individually Selected Sites

In order to determine the mutational trends of the individually selected sites, the amino acids at these sites in sequence set B were concatenated based on protein to form nine sets of subsequences with equal size. Sequence set A was not used because there were not enough sequences per year. These subsequences were grouped and a consensus sequence was taken with respect to each year. The annual consensus sequences were then used to generate a consensus of all the years for each protein. The percentage of sites in each annual consensus that differed from the all-year consensus was recorded.

Table 2. Performance metrics of WEKA classifiers on individually selected sites vs. sites in [1].

Performance Metrics for Sites Published in [1].									
	M1(4)	M2(2)	NP(13)	NS1(4)	NS2(0)	PA(2)	PB1(3)	PB1-F2(0)	PB2(13)
Sensitivity	0.9890	0.9269	0.9992	0.9897		0.9930	0.9059		0.9954
Specificity	0.9827	0.9751	1.0000	0.9830	No Data	0.9951	0.8640	No Data	1.0000
Q2	0.9873	0.9433	0.9994	0.9886		0.9933	0.8961		0.9963
MCC	0.9668	0.8807	0.9986	0.9580		0.9723	0.7311		0.9883
Performance Metrics for Our Individually Selected Sites									
	M1(10)	M2(18)	NP(15)	NS1(9)	NS2(10)	PA(17)	PB1(12)	PB1-F2(11)	PB2(19)
Sensitivity	0.9958	0.9928	0.9976	0.9960	0.9870	0.9978	0.9643	0.9154	0.9969
Specificity	0.9926	0.9985	1.0000	0.9877	0.9729	1.0000	0.9924	0.9870	1.0000
Q2	0.9949	0.9949	0.9983	0.9946	0.9835	0.9981	0.9713	0.9610	0.9975
MCC	0.9868	0.9893	0.9957	0.9804	0.9546	0.9927	0.9280	0.9154	0.9922

These tables display the accuracy of the WEKA classification in comparison to the sites recorded in [1] by performing the calculations for sensitivity, specificity, overall accuracy (Q2) and the Matthews correlation coefficient (MCC).

As can be seen in the plots of **Figure 1**, avian influenza tended to have very low deviation values, often differing from year to year by only a single site's worth of variance. Additionally, within the avian proteins, many years displayed no deviation whatsoever. This lead to curves that tended to be constant with occasional spikes of deviation. On average, 58.9% of the annual avian consensus sequences matched the all-year consensus perfectly. The avian proteins which produced the lowest deviation values on average were PB1 with 0.5%, followed by PB2, PA, and M1 with 1.0%, 0.9%, and 0.9% respectively. The proteins with the highest deviation values were NS1, NS2, and PB1-F2: they averaged 13.6%, 7.9%, and 9.4% respectively.

Human influenza produced curves that were more varied, with distinctly higher deviation values. On average there was 13.7 times more deviation in human influenza than there was in avian. The proteins with the lowest deviation were M2 with 7.3% and NS2 with 8.7%, and the proteins that displayed the highest were PB1-F2, NS1 and PB1, with 29.1%, 25.5% and 25.4% respectively. Human influenza also had far fewer annual consensus sequences that matched the all-year consensus perfectly: only 7.5%.

A comparative analysis of avian and human trends was also performed. While both PB1-F2 and NS2 were highly varied in both, other proteins showed distinct patterns. PB1 was one of the most varied proteins in human influenza, but one of the least in avian, with the human having 44.1 times the deviation of the avian, compared to only 1.2 times for NS2. Human influenza was clearly more varied: in no protein was the average deviation for avian greater than it was for human. There were, however, specific annual consensuses wherein the deviancy of the avian was greater than that of the human. For instance in 1971 the avian deviation of NS1 was 89.3%, the highest deviation for any one protein at any one year, while the human deviation was 3.6%. This occurred rarely, and the dramatic disparity in NS1 in 1971 was the extreme case.

3.4 Correlation of Sites in Proteins According to Year

In Subsection 3.3, the annual mutational trends of the individually selected sites were analyzed. The current section analyzes the correlation patterns of amino acid pairs according to year. Because the correlation metrics used require a greater number of sequences than our mutational trends, sequence set B was not used for this analysis, despite the benefit of having the same number of sequences in each protein. The protein sequences in sequence set C were separated according to year. If the two sites i and j are conserved, $C_{i,j}$ is an value of 1.0. Thus, all sites that were conserved in a given year were removed from the sequences from that year, leaving only those sites that were variable. The K-Value K_i was calculated for each variable site i for each year, using all other variable sites in the K-Value formula. The averaged K-Values of these sites in each protein were used as the K-Value of that protein for that year. We standardized the K-Values according to the mean and standard deviation.

The contrast between avian and human influenza can be seen in **Figure 2**, Plot A. Human influenza had higher K-Values than avian influenza across all years except 1986. Further, the patterns of correlation in each of the human influenza proteins were very similar to one another (**Figure 2**, Plot B), while those of avian influenza were much more diverse. In human influenza, when the K-Value of one protein was high, the others tended to be high, and vice versa. The proteins of avian influenza produced much more varied K-Value distributions. While there were few similarities between all nine proteins, we found three groups of proteins that had K-Value distributions similar to one another, these being [PA, PB1, PB2], [M1, M2, NP] and [NS1, NS2, PB1-F2]. These can be seen in **Figure 2**, Plots C through E. The [PA, PB1, PB2] group was especially interesting, as these three proteins make up the polymerase complex of influenza, which is essential for the replication and transcription of the influenza viruses.

3.5. Correlation of Sites in Proteins for All Years

To expand the year-dependant study of the patterns of correlation of sites within each protein in Subsection 3.4, the patterns were also analyzed for all years. Unlike in Subsection 3.4, where all variable sites were used, in this analysis only a certain percentage of variable sites in each protein were included. Because of the different mutation rates of avian and human influenza (**Figure 1**), a different cutoff was applied to each. For the avian selection, the 33% most variable sites were selected from the individually selected sites, while the top 20% were used for the human. These selections were subsets of the individually selected sites and from hereafter will be referred to as the I-sites. Correlation was evaluated both for I-site pairs exclusively within individual proteins as intra-protein K-Values, and for I-site pairs between proteins as inter-protein K-Values. Both calculations of K-Value were performed using the I-sites from sequence set B (**Table 1**).

There were significant distinctions between both the intra- and inter-correlation of avian and human I-sites. While correlation in human influenza was fairly uniform in all proteins, with K-Values predominantly remaining between 0.5 and 0.6, avian influenza tended to be more variable, with values commonly ranging as low as 0.4 and as high as 0.8. Further, sites within avian proteins typically had similar correlation values; for instance, PA, PB1, and M1 ha consistently high K-Values for all sites,

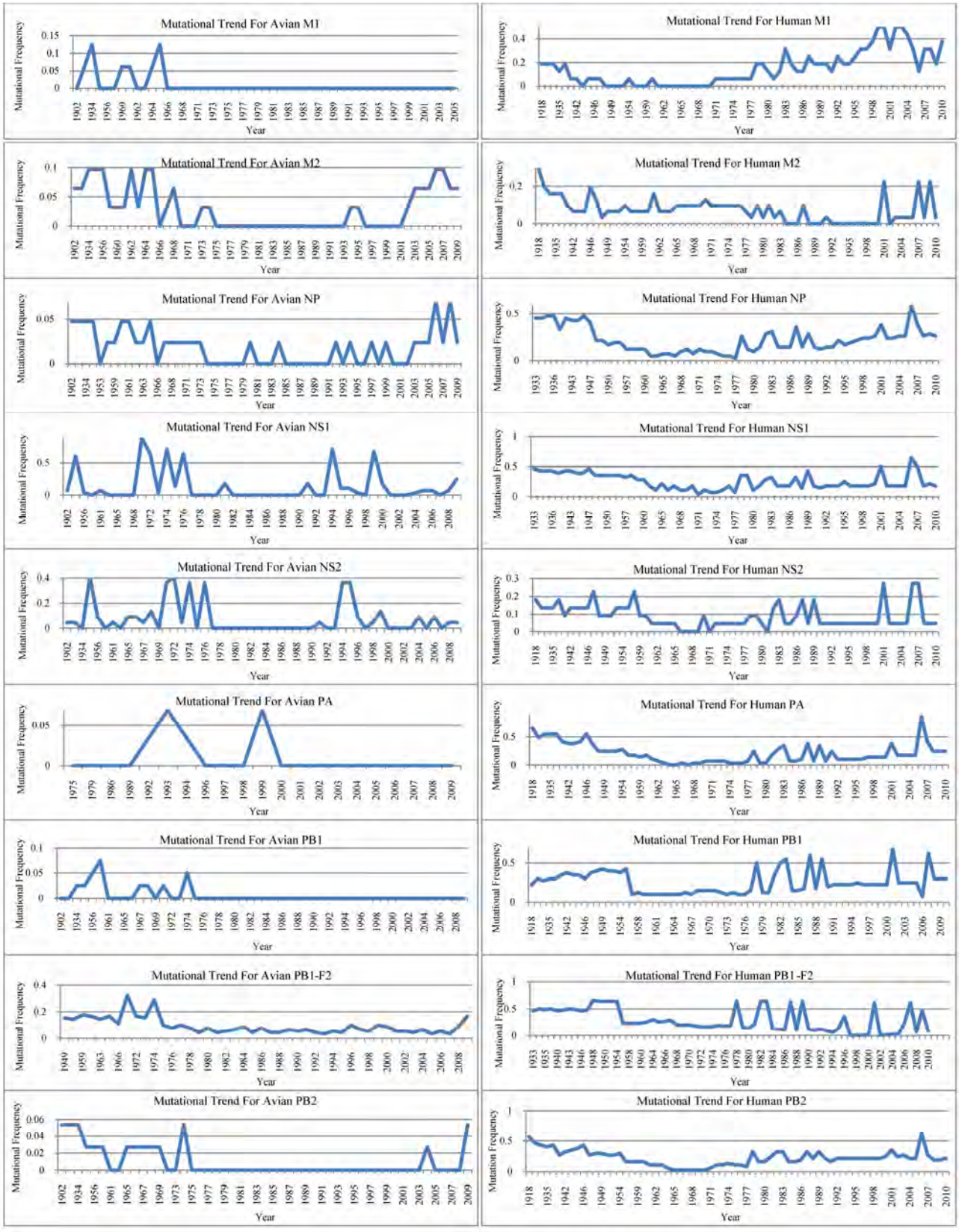

Figure 1. Annual mutational trend of individually selected sites.

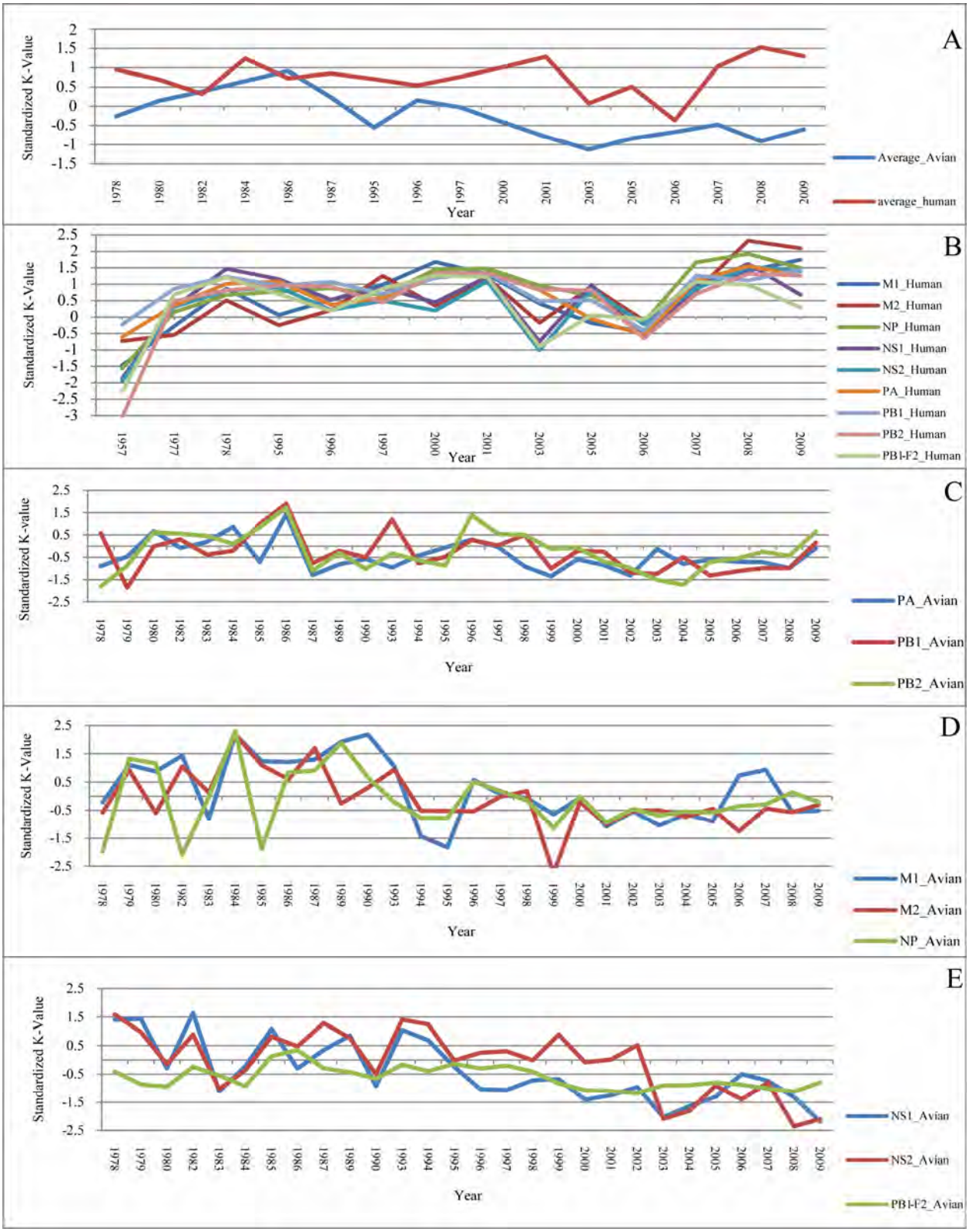

Plot A shows the average K-Values of all the proteins for both avian and human-host influenza. Plots B through E show the K-Values for the specific proteins of both human and avian hosts. Plot B shows all human-host proteins, which had similar patterns of K-Value distribution. Avian proteins yielded K-Value curves less similar to one another, and have been split into three different plots (C through E) for clarity.

Figure 2. Average standardized K-Value of proteins according to year.

while PB1-F2 had low values. On the other hand, while there were individual sites that deviated from the norm in human influenza, these tended to not be grouped by protein; for example, the PB1 protein in human housed both the site with the second highest K-Value (PB1:336 with an average value of 0.688) and the site with the lowest K-Value (PB1:79 with an average value of 0.386).

Although both the intra- and inter-protein correlations are similar in all proteins for both avian and human influenza, the average distance between the inter- and intra-protein K-Values varied: 0.060 for avian, and only 0.024 for human. The K-Value gain from intra- to inter-K-Values was calculated such that positive numbers would represent an increase, and negative numbers a decrease; then the average was taken for each protein (**Figure 3**). Human K-Value gain was typically positive, indicating that human influenza tended to have higher correlation between proteins than within proteins. In contrast, avian inter-protein K-Value gain was typically negative, indicating that correlation was stronger within specific proteins than between proteins. Despite this, avian influenza had higher K-Values, indicating higher correlation, than human influenza, in both inter- and intra-proteins. This was different from the results reported in 3.4, where it was observed that annual correlation, which was measured by the K-Value of the sequences in a particular year, was higher in human influenza than in avian (**Figure 2**). This indicated that the contribution of correlation between sequences in different years was significant.

In both human and avian, an exception to this trend was the PB1-F2 protein, where the trend of human-positive and avian-negative K-Value gain was reversed: the averaged K-Value gain for PB1-F2 was 0.016, while the averaged human K-Value gain was –0.088, indicating that in PB1-F2 avian influenza had greater correlation outside the protein than within, and vice versa for human influenza. Averaged human K-Value gain was negative in NS1 and PB1 as well. These three proteins were also found to have the highest annual variability of any of the human proteins, as seen in **Table 2**.

3.6. Site-Connectivity Networks

In the previous several sections, the correlations between one site and other related sites (one-to-many) were detected. In this section, specific associations between one site and another single site (one-to-one) from sequence set A, the set of individual-protein sequences, were ana-

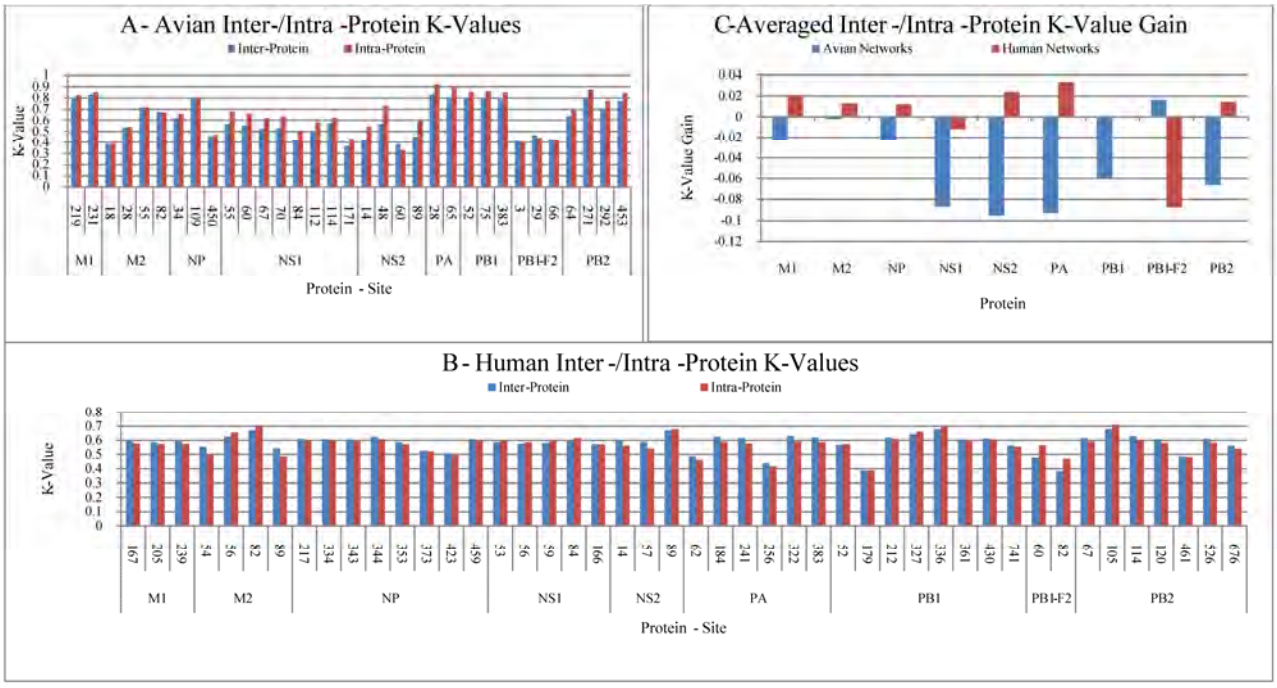

Plots A and B were generated by calculating K-Values for each of the I-sites. The inter-protein K-Values were calculated using pairings with all I-sites from all nine proteins, while the intra-protein K-Values include only pairings within a single protein - for instance, the site M1:167 would only be paired with amino acid sites that are also in M1. All site positions are given relative to the starting position in their containing protein. Plot C shows the K-Value gain per protein from plots A and B, such that positive values indicate that the inter-protein K-Values are higher than the intra-protein K-Values, and negative vice versa. Avian K-Value gain is consistently lower than human, with the exception of PB1-F2.

Figure 3. Avian and human K-Values produced by inter- and intra-protein analysis.

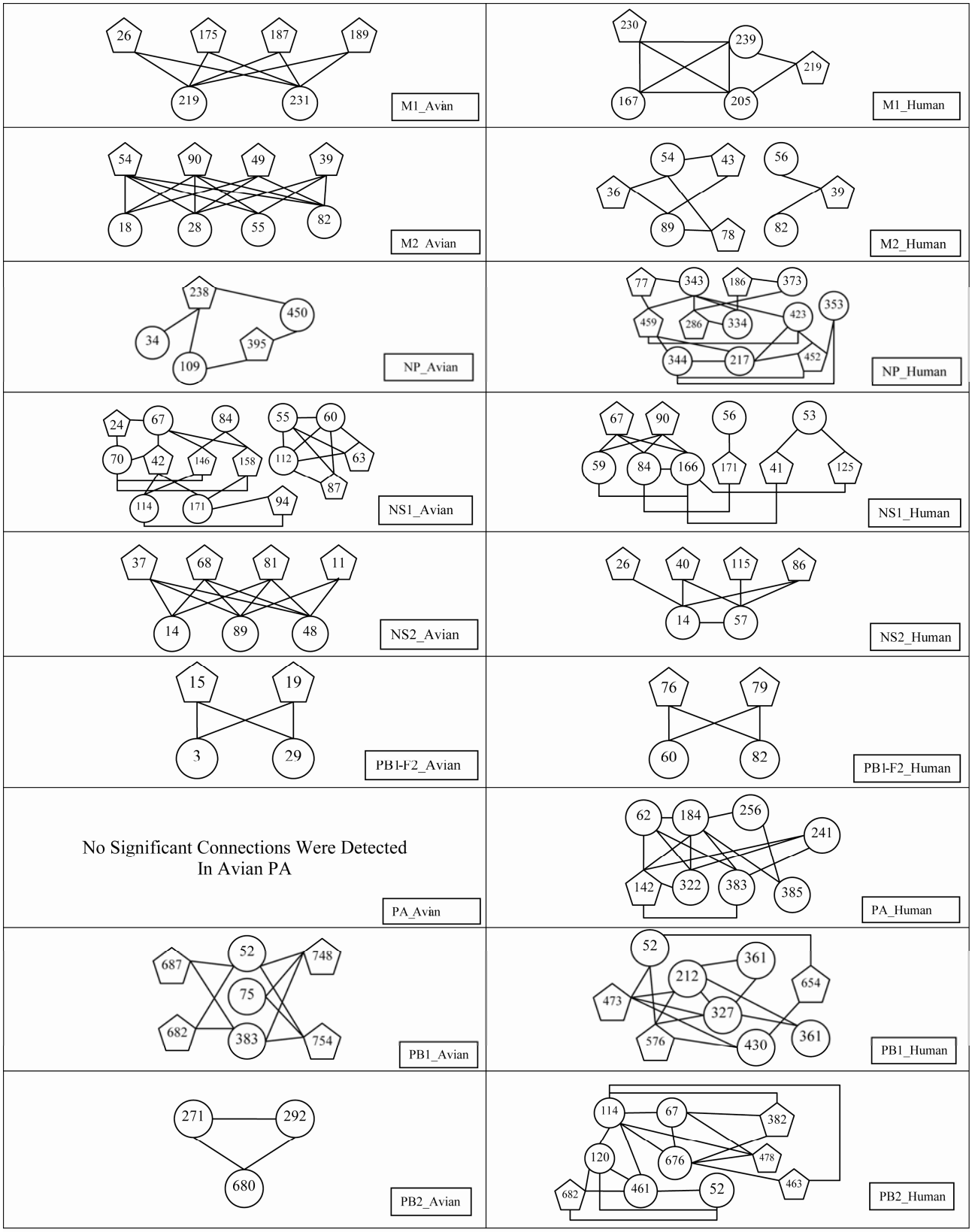

Figure 4. Amino acid connectivity networks.

lyzed. Connectivity networks between correlated sites were generated by calculating the co-occurrence $C_{i,j}$ between two different sets of amino acid sites. The first consisted of the I-sites described in Subsection 3.5. The second set acted as a baseline of comparison, containing all sites in each protein that displayed any variation whatsoever, hereafter referred to as B-sites. This allowed connections to be formed not only between two sites deemed to be important (between two I-Sites), but also between an important site and a variable site that had not been previously selected by WEKA (between an I-site and a B-site).

Co-occurrence values were calculated for all amino acid pairs such that one site of the pair belonged to the first set, and the other site belonged to the second. The connection strength between the site-pairs was the summation of the co-occurrence values of all amino acid pairs occurring at those sites. To retain the most significantly connected sites, only the sites associated with the four strongest connections to each of the I-sites were included. Further, any B-sites that had only a single connection within the network were removed.

As seen in **Figure 1**, human influenza tended towards higher variance, leading to a greater number of sites being selected by our procedure despite the more rigorous cutoff limit, as described in Subsection 3.5. The network graphs in **Figure 4** indicated that while human influenza had more variable positions than avian, the average number of sites in each graph was almost equal: 7.625 sites per graph for human, and 7.429 for avian. The reason for this was that the human connectivity networks tended to be more reflexive, having more connections between the I-sites. The avian, on the other hand, tended to be less reflexive, having more connections to B-sites, those not found by WEKA. In other words, human I-sites tended to co-mutate among themselves, while the avian I-sites tended to co-mutate with sites that, while still variable, were not statistically important to host differentiation.

3.7. Protein-Connectivity Networks

A process similar to that of Subsection 3.6 was also applied to the concatenated sequences of sequence set B. The connectivity between the nine internal proteins was our goal in this section, rather than the one-to-one connectivity between sites. Three sets of sites were used in this portion of the study: the I-sites from Subsection 3.5, the B-sites from Subsection 3.6, and a set of all variable sites in the concatenated selected sites, hereafter referred to as C-sites. Two sets of networks were generated: one connecting the I-sites and B-sites, and another connecting the C-sites and B-sites. Because the B-sites included all variable sites, both the I- and C-sites were subsets of the B-sites.

All B-sites were retained in sequence set B by removing those sites that were conserved. Then, networks were generated by calculating $C_{i,j}$ for all pairs such that site i was part of the contributing set I or C, and site j was part of the set of B-sites. For each pair of amino acid sites, the summation of all $C_{i,j}$ values was taken, and a cutoff (the average of these summations) was applied such that the resulting value was 1 if greater than or equal to the cutoff, and 0 otherwise. Then the average value of all site pairs within a pair of proteins was taken, giving each pair of proteins a connectivity value between 0 and 1.

The plots in **Figure 5** represent the protein-connectivity networks. The vertical axis indicates the B-sites, while the horizontal axis indicates the I- or C-sites. The columns, then, display the connectivity of the I- or C-sites to the B-sites, while the rows show the connectivity of the B-sites to the I- or C-sites. Because the B-sites were different than the I- and C-sites, these graphs are not symmetric. Lists of the I- and C-sites are provided in **Table 3**.

The connectivity of the different sets of selected sites in these networks varied. Avian PB1-F2-I sites, for instance, had no connectivity whatsoever, while the avian PB1-F2-C sites showed high connectivity. The opposite

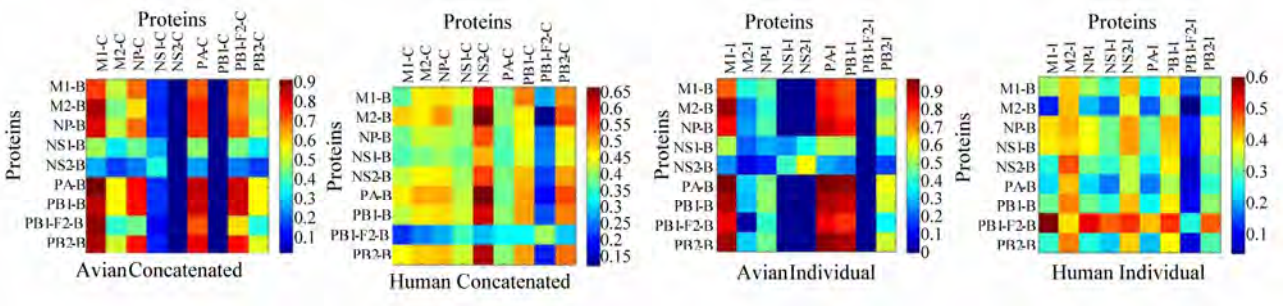

Figure 5. Protein connectivity heat maps.

Table 3. I-sites and C-sites used in Figure 5.

	Human (I)	Human(C)	Avian (I)	Avian (C)
M1	167, 205, 239	115^, 137, 227	219, 231	115^
M2	54^, 56, 82*, 89^	11, 16, 28, 54^, 55^, 57, 78, 82*, 86, 89^, 93	55^, 82*	14, 16, 20, 54^, 55^, 82*, 89^
NP	217, 334, 343, 344, 353^, 373, 423^, 459	31, 33^, 109^, 214, 283, 293, 305, 313, 353^, 357, 372, 375, 422, 423^, 442, 450, 455	34, 109^	33^, 109^
NS1	53, 56, 59, 84*, 166, 244	21, 22, 59, 60, 70, 81, 84*, 171, 196, 227	55, 60, 67, 70, 84*	21, 22, 59, 60, 70, 81, 84*, 166, 196, 215, 227
NS2	57, 89^	89^, 107	48	
PA	62, 184^, 241, 256, 322, 383^	28^, 55^, 57, 65^, 66^, 142^, 184^, 268^, 272, 277^, 321^, 337, 356^, 382^, 383^, 385^, 387, 400, 404^, 409, 552^, 668^	28^, 65^	28^, 55^, 65^, 66^, 142^, 184^, 225, 268^, 277^, 321^, 356^, 382^, 383^, 385^, 404^, 421, 552^, 668^
PB1	52^, 212^, 327^, 336^, 361, 430, 741	212^, 327^, 336^, 581	52^, 75, 383	
PB1-F2	60*, 82	27^, 29, 59^, 60*, 73, 76^, 79, 87		27^, 59^, 60*, 76^
PB2	67^, 105^, 114, 120, 461, 526, 676	9, 44, 64^, 67^, 81, 105^, 199, 271^, 292^, 368^, 453^, 475, 567^, 588^, 613, 661, 674, 684, 702	64^, 271^, 292^, 453^	64^, 271^, 292^, 368^, 453^, 567^, 588^, 627

This table shows the I- and C-sites for both human and avian influenza. Those sites marked with a "*" occur in all four instances, those marked with a "^" occur in two or three.

was true for PB1, with PB1-C sites displaying no connections, and high connectivity in the PB1-I. There were commonalities between avian I- and C- sites, also: NS1 and NS2 sites yielded very low connectivity in both, while M1 and PA had very high connectivity.

Similarly, in human influenza, both I- and C-sites of PB1-F2 displayed extremely low, and only mild connectivity for PA and NS1. NS2-C sites, on the other hand, displayed much higher connectivity than NS2-I. Otherwise, both I- and C-sites for human influenza were fairly normative, with typical connectivity values ranging between 0.3 and 0.5.

There were also differences between the avian and the human networks. While both NS1 and NS2 sites had very low connectivity in avian, the connectivity of human NS1 and NS2 sites was moderate to high, with a very high connectivity value for NS2-I sites. In the same fashion, PB1-F2 sites were in general poorly connected, but the avian PB1-F2-C sites showed exceptionally high connectivity.

In general, both avian I- and C-sites tended to have higher connectivity between proteins than human, which was consistent with the trend of avian influenza having more widespread connectivity within individual proteins noted in Subsection 3.6. Both of these findings were interesting in light of avian influenza's relatively lower mutation rate, noted in Subsection 3.2.

4. CONCLUSIONS

There were five main components in our findings. First, a diverse and extensive set of sites in nine internal proteins of avian and human influenza was identified through the use of seven feature selection algorithms. The validity of these sites was justified by the capability to differentiate between avian and human protein sequences using four machine learning classifiers. Second, the mutational trends of these sites were analyzed, which signified that in general human influenza displayed higher mutation rates than avian. Third, by calculating the K-Values of these sites, it was found that in contrast to the higher mutation rate, the patterns of correlation in each of the human influenza proteins were very similar to one another, while those of avian influenza were much more diverse. When considered for all years, K-Values illustrated that avian site-correlation was on average higher than human site-correlation. Further, while the correlation of most individual human sites was very similar with occasional outliers, the correlation of avian sites was much more varied. Fourth, networks of correlated sites from each protein were generated, not only showing that avian connectivity tended to be higher, but also that the sites selected in avian networks tended to be more evenly distributed over the entire protein. Finally, connectivity heat maps were generated from the sites selected from concatenated sequences of all nine internal proteins, exhibiting the global trends of connection across all the proteins.

These findings suggest that in our site selection there is an inverse relationship between variability and connectivity within the nine internal proteins of avian and human influenza. Avian influenza showed consistently higher correlation and connectivity, reflected by co-occurrence and K-Value, than human, despite the significantly lower rate of mutation. Within individual proteins, there is a higher percentage of variable sites with high connectivity in avian than in human. The con-

tribution of connectivity between proteins to the overall connectivity of the nine proteins, however, is greater in human influenza than it is in avian. In conclusion, the sites we selected were significant in distinguishing avian and human viruses, and revealed the signatures of correlation and connectivity of the nine internal proteins, which reflected the characteristics of avian and human influenza viruses.

5. ACKNOWLEDGEMENTS

We would like to thank the Summer Research Institute at Houghton College for the funding of this study. Additionally, we would like to thank Asif Tamuri for providing the data used in his previous study [1] as well as his helpful discussions.

REFERENCES

[1] Tamuri, A.U., Reis, M., Hay, A.J. and Goldstein, R.A. (2009) Identifying changes in selective constraints: Host shifts in influenza. *PLoS Comput Biol*, **5(11)**, e1000564.

[2] Du, X., Wang, Z. and Wu, A., *et al*. (2008) Networks of genomic co-occurrence capture characteristics of human influenza A (H3N2) evolution. *Genome Res*, **18(1)**, 178-187.

[3] Allen, J., Gardner, S., Vitalis, E. and Slezak, T. (2009) Conserved amino acid markers from past influenza pandemic strains. *BMC Microbiol*, **9**, 77.

[4] Furuse,Y., Suzuki, A., Kamigaki, T. and Oshitani, H. (2009) Evolution of the M gene of the influenza A virus in different host species: Large-scale sequence analysis. *Virology*, **6**, 67.

[5] Suzuki, Y. (2006) Natural selection on the influenza virus genome. *Molecular Biology and Evolution*, **23(10)**, 1902.

[6] Xia, Z., Jin, G., Zhu, J.and Zhou, R. (2009) Using a mutual information-based site transition network to map the genetic evolution of influenza A/H3N2 virus. *Bioinformatics*, **25(28)**, 2309-2317.

[7] Huang, J., King, C. and Yang, J. (2009) Co-evolution positions and rules for antigenic variants of human influenza A/H3N2 viruses. *BMC Bioinformatics*, **10(1)**, S41.

[8] Dunn, S.D., Wahl, L.M. and Gloor, G.B. (2008) Mutual information without the influence of phylogeny or entropy dramatically improves residue contact prediction. *Bioinformatics*, **24(3)**, 333-340.

[9] Witten, I.H. and Frank, E. (2005) Data mining: Practical machine learning tools and techniques. 2nd Edition, Morgan Kaufmann Publishers, Massachusetts.

[10] Cohen, A., Bhupatiraju, R. and Hersh, W. (2004) Feature generation, feature selection, classifiers, and conceptual drift for biomedical document triage. *Proceedings of the Thirteenth Text Retrieval Conference*.

[11] Quinlan, J.R. (1993) C4.5: Programs for machine learning. Morgan Kaufmann Publishers, Massachusetts.

[12] Holte, R.C. (1993) Very simple classification rules perform well on most commonly used data sets. *Machine Learning*, **11(1)**, 63-90.

[13] Kononenko, I. (1994) Estimating attributes: analysis and extensions of relief. *Machine Learning: ECML-94*, **784**, 171-182.

[14] Platt, J. (1999) Fast training of support vector machines using sequential minimal optimization, Advances in kernel methods: support vector learning. MIT Press, Cambridge, Massachusetts, 185-208.

[15] Cortes, C. and Vapnik, V. (1995) Support-vector network. *Machine Learning*, **20(3)**, 273-297.

[16] Domingos, P. and Pazzani, M. (1997) On the optimality of the simple Bayesian classifier under zero-one loss. *Machine Learning*, **29(2)**, 103-137.

[17] Breiman, L. (2001) Random Forests. *Machine Learning*, **45(1)**, 5-32.

[18] Rodriguez, J.J., Kuncheva, L.I. and Alonso, C.J. (2006) Rotation forest: A new classifier ensemble method. *IEEE Transactions on Pattern Analysis and Machine Intelligence*, **28(10)**, 1619-1630.

J. Biomedical Science and Engineering, 2010, 3, 956-963 **JBiSE**
doi:10.4236/jbise.2010.310126 Published Online October 2010 (http://www.SciRP.org/journal/jbise/).

A PQAS-containing glass-ionomer cement for improved antibacterial function

Yiming Weng[1], Xia Guo[1], Jun Zhao[1], Richard L. Gregory[2], Dong Xie[1*]

[1]Department of Biomedical Engineering, Purdue School of Engineering and Technology, Indiana University-Purdue University, Indianapolis, USA;
[2]Department of Oral Biology, School of Dentistry, Indiana University, Indianapolis, USA.
Email: dxie@iupui.edu

Received 5 August 2010; revised 18 August 2010; accepted 26 August 2010.

ABSTRACT

The novel non-leachable poly (quaternary ammonium salt) (PQAS)-containing antibacterial glass-ionomer cement has been developed. Compressive strength (CS) and S. mutans viability were used as tools for strength and antibacterial activity evaluations, respectively. All the specimens were conditioned in distilled water at 37˚C prior to testing. Commercial glass-ionomer cement Fuji II LC was used as control. With PQAS addition, the studied cements showed a reduction in CS with 25-95% for Fuji II LC and 13-78% for the experimental cement and a reduction in S. mutans viability with 40-79% for Fuji II LC and 40-91% for the experimental cement. The experimental cement showed less CS reduction and higher antibacterial activity as compared to Fuji II LC. The long-term aging study indicates that the cements are permanently antibacterial with no PQAS leaching. It appears that the experimental cement is a clinically attractive dental restorative that can be potentially used for long-lasting restorations due to its high mechanical strength and permanent antibacterial function.

Keywords: PQAS; Antibacterial; Glass-Ionomer Cement; CS; Aging

1. INTRODUCTION

In dental clinics, secondary caries is found to be the main reason to the restoration failure of either composite resins or glass-ionomer cements (GICs) [1-4]. Secondary caries that often occurs at the interface between the restoration and the cavity preparation is mainly caused by demineralization of tooth structure due to invasion of plaque bacteria (acid-producing bacteria) such as *StreptococcuS. mutans* (*S. mutans*) in the presence of fermentable carbohydrates [4]. Among all the dental restoratives, GICs are found to be the most cariostatic and somehow antibacterial due to release of fluoride, which is believed to help reduce demineralization, enhance remineralization and inhibit microbial growth [5,6]. However, annual clinical surveys found that secondary caries was still the main reason for GIC failure [1-4], indicating that the fluoride-release from GICs is not potent enough to inhibit bacterial growth or combat bacterial destruction. Although numerous efforts have been made on improving antibacterial activities of dental restoratives, most of them have been focused on release or slow-release of various incorporated low molecular weight (MW) antibacterial agents such as antibiotics, zinc ions, silver ions, iodine and chlorhexidine (CHX) [6-10]. However, release or slow-release can lead or has led to reduction of mechanical properties of the restoratives over time, short-term effectiveness, and possible toxicity to surrounding tissues if the dose or release is not properly controlled [6-10].

Macromolecules containing quaternary ammonium (QAS) or phosphonium salt (QPS) groups have been studied extensively as an important antimicrobial material and used for a variety of applications due to their potent antimicrobial activities [11-15]. These polymers are found to be capable of killing bacteria that are resistant to other types of cationic antibacterials [16]. The examples of polyQAS or PQAS used as antibacterials for dental restoratives include incorporation of a methacryloyloxydodecyl pyridinium bromide (MDPB) as an antibacterial monomer into composite resins [13], use of DMAE-CB as a component for antibacterial bonding agents [17,18], and incorporation of quaternary ammonium polyethylenimine (PEI) nanoparticles into composite resins [19]. All these studies found that PQAS did exhibit significant antibacterial activities. So far there have been no reports on using PQAS as an antibacterial

agent for GICs.

The objective of this study was to synthesize a new poly (acrylic acid-co-itaconic acid) with pendent quaternary ammonium salt (PQAS) and explore the effects of this PQAS on mechanical strength and antibacterial activity of commercial Fuji II LC and recently developed experimental high-strength cements.

2. MATERIALS AND METHODS

2.1. Materials

2-dimethylaminoethanol (DMAE), bromotetradecane (BT), dipentaerythritol, 2-bromoisobutyryl bromide (BIBB), acrylic acid (AA), itaconic acid (IA), 2,2'-azobisisobutyronitrile (AIBN), triethylamine (TEA), CuBr, N, N, N', N'', N'' -pentamethyldiethylenetriamine (PMDETA), dl-camphoroquinone (CQ), 2-(dimethylamino) ethyl methacrylate (DMAEMA), pyridine, tert-butyl acrylate (t-BA), glycidyl methacrylate (GM), hydrochloric acid (HCl, 37%), N, N'-dicyclohexylcarbodiimide (DCC), pyridine, diethyl ether, dioxane, N,N-dimethylformamide (DMF), methanol (MeOH), ethyl acetate (EA), hexane and tetrahydrofuran (THF) were used as received from VWR International Inc (Bristol, CT) without further purifications. Light-cured glass-ionomer cement Fuji II LC and Fuji II LC glass powders were used as received from GC America Inc (Alsip, IL). Z100 resin composite was used as received from 3M ESPE (St. Paul, MN).

2.2. Synthesis and Characterization

2.2.1. Synthesis of the Quaternary Ammonium Salt (QAS)

The hydroxyl group-containing quaternary ammonium salt (QAS) was synthesized following the procedures described elsewhere with a slight modification [12]. Briefly, to a flask containing DMAE (0.056 mol) in methanol (100 ml), BT (0.062 mol) was added. The reaction was run at room temperature overnight. After most of methanol was removed, the mixture was washed with hexane 3 times. The formed 2-dimethyl-2-tetradecanyl-1-hydroxyethyl ammonium bromide (DTHAB) was then dissolved in 10% HCl aqueous solution containing a small amount of MeOH. After the solution was stirred at 110˚C for 3 h, MeOH, HBr and water were removed via a rotary evaporator. The formed 2-dimethyl -2-tetradecanyl-1-hydroxyethyl ammonium chloride (DT HAC) was purified by washing with hexane several times before drying in a vacuum oven. The synthesis scheme is shown in **Figure 1**.

2.2.2. Synthesis of the Poly (Acrylic Acid-co-Itaconic acid) with Pendent QAS

The linear poly (acrylic acid-co-itaconic acid) or poly (AA-co-IA) was prepared following our published procedures [20]. Briefly, to a flask containing a solution of AA (0.08 mol) and IA (0.04 mol) in 40 ml THF, AIBN (0.5 mmol) in 10 ml THF was added. After the reaction was run under N_2 purging at 60˚C for 18 h, poly (AA-co-IA) was precipitated with ether, followed by drying in a vacuum oven. Then DTHAC was tethered onto the purified poly (AA-co-IA) [21]. Briefly, to a solution of poly (AA-co-IA) in DMF, DTHAC was added with DCC and pyridine. The reaction was kept at room temperature overnight. After the insoluble dicyclohexyl urea was filtered off, the formed poly(AA-co-IA) with pendent QAS or PQAS was purified by precipitation from ether, washing with ether and drying in a vacuum oven prior to use (see **Figure 1**).

2.2.3. Synthesis of the GM-Tethered Star-Shape Poly (Acrylic Acid)

The GM-tethered 6-arm star-shape poly (acrylic acid) (PAA) was synthesized similarly as described in our previous publication [22]. Briefly, dipentaerythritol (0.06 mol) in 200 ml THF was used to react with BIBB (0.48 mol) in the presence of TEA (0.35 mol) to form the 6-arm initiator. t-BA (0.078 mol) in 10 ml dioxane was then polymerized with the 6-arm initiator (1% by mole) at 120˚C in the presence of CuBr (3%)-PMDETA (3%) catalyst complex via ATRP. The resultant 6-arm poly (t-BA) was hydrolyzed with HCl and dialyzed against distilled water. The purified star-shape PAA was obtained via freeze-drying, followed by tethering with GM (50% by mole) in DMF in the presence of pyridine (1% by weight) [22]. The GM-tethered star-shape PAA was recovered by precipitation from diethyl ether, followed by drying in a vacuum oven at room temperature. The synthesis scheme for the 6-arm star-shape PAA is also shown in **Figure 1**.

2.2.4. Characterization

The chemical structures of the synthesized QAS and PQAS were characterized by Fourier transform-infrared (FT-IR) spectroscopy and nuclear magnetic resonance (NMR) spectroscopy. The proton NMR (^{1}HNMR) spectra were obtained on a 500 MHz Bruker NMR spectrometer (Bruker Avance II, Bruker BioSpin Corporation, Billerica, MA) using deuterated dimethyl sulfoxide and chloroform as solvents and FT-IR spectra were obtained on a FT-IR spectrometer (Mattson Research Series FT/IR 1000, Madison, WI).

2.3. Evaluation

2.3.1. Sample Preparation for Strength Tests

The experimental cements were formulated with a two-component system (liquid and powder) [22]. The liquid was formulated with the light-curable star-shape poly (acrylic acid), water, 0.9% CQ (photo-initiator, by

weight) and 1.8% DC (activator). The polymer/water (P/W) ratios (by weight) = 70:30. Fuji II LC glass powder was either used alone or mixed with the synthesized PQAS to formulate the cements, where the PQAS mixing ratio (by weight) = 1, 3, 5, 10, or 30% of the glass. The detailed formulations are shown in **Table 1**. Fuji II LC and Z100 were used as controls and prepared per manufacturers' instructions, where the P/L ratio = 3.2 for Fuji II LC and premixed paste for Z100.

Specimens were fabricated at room temperature according to the published protocol [22]. Briefly, the cylindrical specimens were prepared in glass tubing with dimensions of 4 mm in diameter by 8 mm in length for compressive strength (CS), 4 mm in diameter by 2 mm in length for diametral tensile strength (DTS) and 4 mm in diameter by 2 mm in depth for antibacterial tests. All the specimens were exposed to blue light (EXAKT 520 Blue Light Polymerization Unit, EXAKT Technologies, Inc., Oklahoma City, OK) for 2 min, followed by conditioned in 100% humidity for 15 min, removed from the mold and conditioned in distilled water at 37˚C for 24 h unless specified, prior to testing.

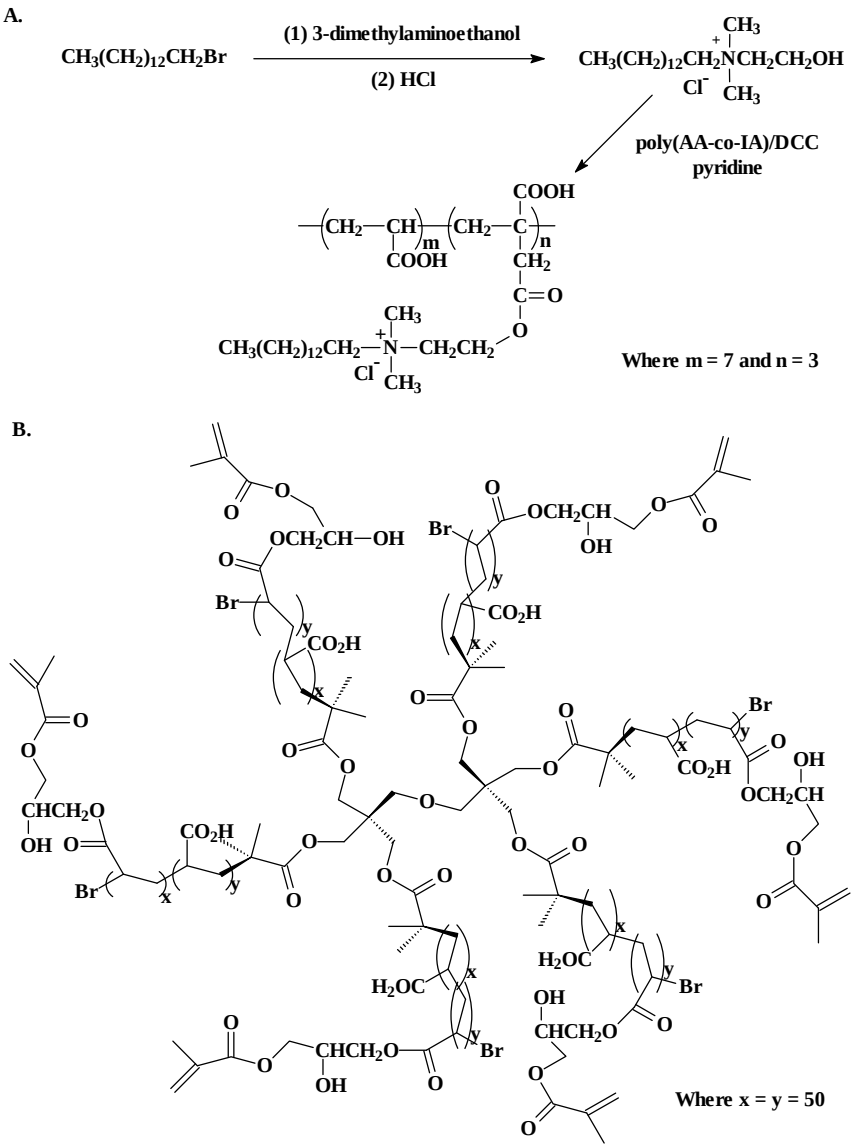

Figure 1. Schematic diagrams for synthesis of poly(AA-co-IA) with pendent QAS or PQAS and chemical structure of the 6-arm star-shape poly(acrylic acid) tethered with methacylate groups: (A): synthesis of PQAS; (B) chemical structure of the 6-arm star-shape poly(acrylic acid) tethered with polymerizable methacrylates.

Table 1. Materials and formulations used in the study.

Code	Liquid formulation[1]	PQAS % (by weight)[2]	P/L ratio (by weight)[3]
FIILC	N/A	0	3.2
FIILC (1%)	N/A	1	3.2
FIILC (3%)	N/A	3	3.2
FIILC (5%)	N/A	5	3.2
FIILC (10%)	N/A	10	3.2
FIILC (30%)	N/A	30	3.2
EXP	70/30	0	2.7
EXP (1%)	70/30	1	2.7
EXP (3%)	70/30	3	2.7
EXP (5%)	70/30	5	2.7
EXP (10%)	70/30	10	2.7
EXP (30%)	70/30	30	2.7

[1]Liquid formulation: N/A = not available; Liquid for EXP = 6-arm star-shape poly (acrylic acid) vs. water (by weight); [2]PQAS = poly (AA-co-IA) with pendent QAS; PQAS was mixed with Fuji II LC filler; 0 = only Fuji II LC filler was used; [3]P/L ratio = a total amount of glass filler powder (Fuji II LC glass + PQAS) vs. polymer liquid.

2.3.2. Strength Measurements

CS and DTS tests were performed on a screw-driven mechanical tester (QTest QT/10, MTS Systems Corp., Eden Prairie, MN), with a crosshead speed of 1 mm/min. Six to eight specimens were tested to obtain a mean value for each material or formulation in each test. CS was calculated using an equation of $CS = P/\pi r^2$, where P = the load at fracture and r = the radius of the cylinder. DTS was determined from the relationship $DTS = 2P/\pi dt$, where P = the load at fracture, d = the diameter of the cylinder, and t = the thickness of the cylinder.

2.3.3. Antibacterial Test

The antibacterial test was conducted following the published procedures [23]. S. mutans (oral bacterial strain) was used for evaluation of antibacterial activity of the studied cements. Briefly, colonies of S. mutans (UA159) were suspended in 5 ml of Tryptic soy Broth (TSB), supplemented with 1% sucrose. Specimens pretreated with ethanol were incubated with S. mutans in TSB at 37˚C for 48 h under anaerobic condition with 5% CO_2. After equal volumes of the red and the green dyes were combined in a microfuge tube and mixed thoroughly for 1 min, 3 µl of the dye mixture was added to 1 ml of the bacteria suspension, mixed by vortexing for 10 sec, sonicating for 10 sec as well as vortexing for another 10 sec, and kept in dark for about 15 min, prior to analysis. Then 20 µl of the stained bacterial suspension was analyzed using a fluorescent microscope (Nikon Microphot-FXA, Melville, NY, USA). Triple replica was used to obtain a mean value for each material.

2.3.4. Statistical analysis

One-way analysis of variance (ANOVA) with the post hoc Tukey-Kramer multiple-range test was used to determine significant differences of both CS and antibacterial tests among the materials in each group. A level of $\alpha = 0.05$ was used for statistical significance.

3. RESULTS

3.1. Characterization

Figure 2 shows the ^{1}HNMR spectra for BT, DMEA, DTHAC, poly (AA-co-IA) and poly (AA-co-IA) with pendent QAS or PQAS. The characteristic chemical shifts (ppm) are shown below: BT: 3.35 ($-CH_2Br$), 1.80 ($-CH_2CH_2Br$), 1.38 ($-CH_2-$, all) and 0.89 ($-CH_3$); DMEA: 4.40 (-OH), 3.42 ($-CH_2OH$), 2.30 ($-CH_2N-$) and 2.10 (H_3CN-); DTHAC: 5.30 (-OH), 3.82 ($-CH_2OH$), 3.35-3.45 ($-CH_2N(CH_3)_2$), 3.10 (H_3CN-), 1.65 ($-CH_2CH_2N(CH_3)_2$), 1.25 ($-CH_2-$ all) and 0.89 ($-CH_3$); poly (AA-co-IA): 12.2 (-COOH), 3.45 (-CH(COOH)-) and 1.2-2.5 ($-CH_2-$, all); PQAS: 3.80 ($-CH_2(COOH)-$), 3.30-3.45 ($-CH_2N-$), 3.10 (H_3CN-), 1.65 ($-CH_2CH_2N(CH_3)_2$), 1.25 ($-CH_2-$ all) and 0.89 ($-CH_3$). The appearance of all the new peaks in the spectrum at the top of **Figure 2** confirmed the successful attachment of DTHAC onto the poly (AA-co-IA).

Figure 3 shows the FT-IR spectra for BT, DMEA, DTHAC, poly (AA-co-IA) and PQAS. The characteristic peaks (cm^{-1}) are listed below: BT: 2924 (C-H stretching on $-CH_2-$), 2853 (C-H stretching on $-CH_3$), 1466, 1377 and 1251 (C-H deformation on $–CH_2-$), 721 and 647 (C-Br deformation); DMEA: 3399 (O-H stretching), 2944 (C-H stretching on $-CH_2-$), 2861 (C-H stretching on $-CH_3$), 2820 and 2779 (C-H stretching on $–N(CH_3)_2$), 1459, 1364 and 1268 (C-H deformation on $–CH_2-$), 1090 (O-H deformation), 1040 and 776 (C-N deformation); DTHAC: 3349 and 3248 ($= N^+ =$ stretching), 2917 (C-H stretching on $-CH_2-$), 2850 (C-H stretching on $-CH_3$), 1470 (C-H deformation on $–CH_2-$), 1090 and 730 (O-H deformation); poly(AA-co-IA): 3800-2400 (O-H stretching on –COOH), 1716 (-C=O stretching), 1196-1458 (C-H deformation on $–CH_2-$); PQAS: 3353 ($= N^+ =$ stretching), 3800-2400 (O-H stretching on –COOH), 2923 (C-H stretching on $-CH_2-$), 2853 (C-H stretching on $-CH_3$), 1732 (-C = O stretching), 1167-1466 (C-H deformation on $–CH_2-$) and 776 (C-N deformation). The significant peaks at 3353 for $= N^+ =$ group, 2923 and 2853 for $–CH_2-$ group and 1736 for carbonyl group confirmed the formation of PQAS.

3.2. Evaluation

Table 1 shows the codes, materials and formulations

used in this study. Both Fuji II LC and experimental (EXPGIC) cements with and without PQAS were evaluated. PQAS was incorporated in a ratio of 1, 3, 5, 10 and 30% (by weight) of the total glass fillers.

Figure 4 shows the mean CS values of Fuji II LC and EXPGIC cements with and without PQAS addition. The CS value (MPa) was in the decreasing order of EXPGIC > EXPGIC (1%) > EXPGIC (3%) > Fuji II LC > EXPGIC (5%) > Fuji II LC (1%) > Fuji II LC (3%) > EXPGIC (10%) > Fuji II LC (5%) > Fuji II LC (10%) > EXPGIC (30%) > Fuji II LC (30%). There were no statistically significant differences between EXPGIC (3%) and Fuji II LC and between Fuji II LC (3%) and EXPGIC (10%) ($p > 0.05$). Increasing PQAS decreased the CS values of both cements. However, the decreasing rate for Fuji II LC was much faster than that for EXPGIC. With 1 to 10% PQAS addition, Fuji II LC decreased 25 to 78% of its original CS whereas EXPGIC only decreased 12 to 57%. **Table 2** shows the results of yield strength (YS), compressive modulus, CS and DTS. The same trend was observed in **Table 2** as shown in **Figure 4**. With 1 to 10% PQAS addition, Fuji II LC showed a decrease of 26-82% in YS, 22-78% in modulus and 12-70% in DTS, which decreased much faster than EXPGIC (1.9-43% in YS, 2.7-34% in modulus and 1.5-43% in DTS). **Figure 5** shows the effect of the cement aging on CS. After one month of aging in water, all the cements showed an increase in CS, especially from 1 h to 1 day. There was a slight increase (statistically no difference) for each formulation tested from 1 day to 1 week and from 1 week to 1 month.

Figure 6 shows the mean S. mutans viability values after culturing with Fuji II LC and EXPGIC with and without PQAS addition. The mean S. mutans viability was in the decreasing order of Z100 > Fuji II LC >

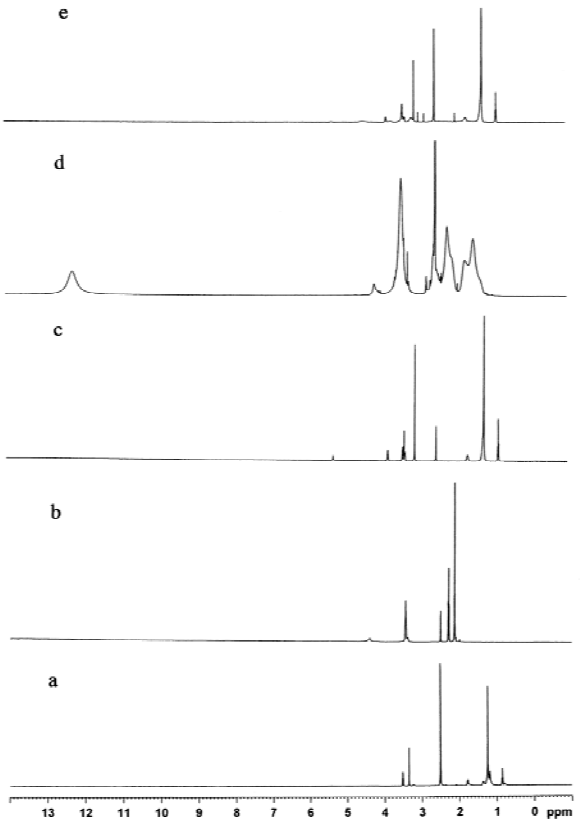

Figure 2. ^{1}HNMR spectra for BT, DMEA, DTHAC, poly(AA-co-IA) and PQAS: (a) BT; (b) DMEA; (c) DTHAC; (d) poly(AA-co-IA) and (e) PQAS.

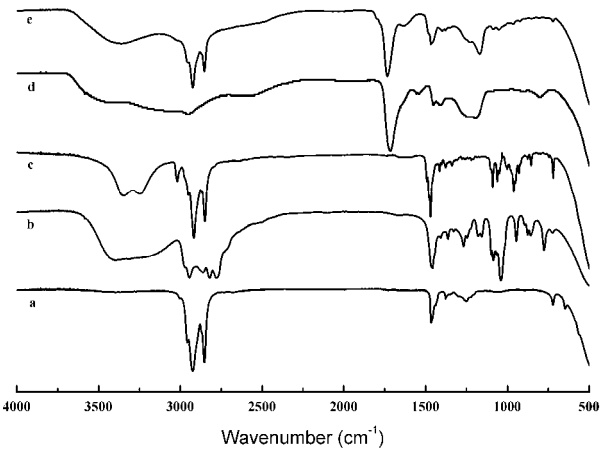

Figure 3. FT-IR spectra for BT, DMEA, DTHAC, poly (AA-co-IA) and PQAS: (a) BT; (b) DMEA; (c) DTHAC; (d) poly(AA-co-IA) and (e) PQAS.

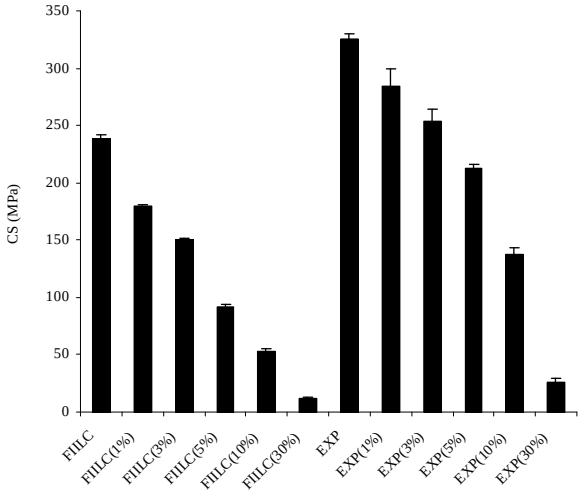

Figure 4. CS of Fuji II LC and experimental cements with and without PQAS addition: FIILC = Fuji II LC; EXP = EXPGIC; For Fuji II LC cements, P/L = 3.2; Filler = Fuji II LC or Fuji II LC + PQAS. For experimental cements, MW of the 6-arm poly (acrylic acid) = 17,530 Daltons; Filler = Fuji II LC or Fuji II LC + PQAS; Grafting ratio = 50%; P/L ratio = 2.7; P/W ratio = 70:30. Specimens were conditioned in distilled water at 37˚C for 24 h prior to testing.

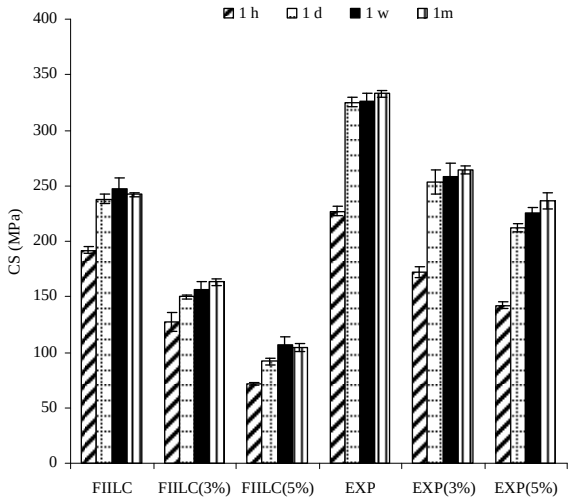

Figure 5. Effect of aging on CS: The formulations were the same as those described in **Figure 4**. Specimens were conditioned in distilled water at 37˚C for 1 h, 1 day, 1 week and 1 month prior to CS testing.

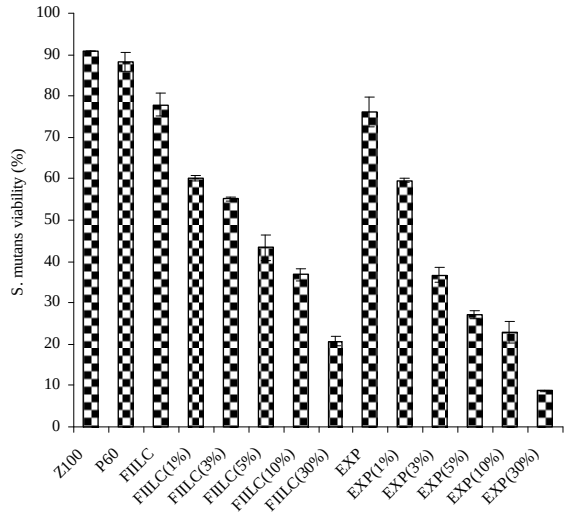

Figure 6. The S. mutans viability after culturing with Fuji II LC and experimental cements with and without PQAS addition: The formulations were the same as those described in **Figure 4**. Specimens were conditioned in distilled water at 37 ˚C for 24 h, followed by incubating with S. mutans before antibacterial testing.

EXPGIC > Fuji II LC (1%) > EXPGIC (1%) > Fuji II LC (3%) > Fujii II LC (5%) > Fuji II LC (10%) = EXPGIC (3%) > EXPGIC (5%) > EXPGIC (10%) > Fuji II LC (30%) > EXPGIC (30%). There were no statistically significant differences among Z100, Fuji II LC and EXPGIC, among Fuji II LC (1%), Fuji II LC (3%) and EXPGIC (1%), among Fuji II LC (5%), Fuji II LC (10%) and EXPGIC (3%), and among Fuji II LC (30%), EXPGIC (5%) and EXPGIC (10%) (10%) ($p > 0.05$). Increasing PQAS decreased the S. mutans viability. With 3 to 30% PQAS addition, Fuji II LC killed 45 to 79% of S. mutans whereas EXPGIC killed 63 to 91%, indicating that the killing power of EXPGIC was much higher than that for Fuji II LC. **Figure 7** shows the effect of the cement aging on the S. mutans viability. No significant changes in the S. mutans viability were found for each formulation tested except Fuji II LC and EXP, where the S.mutans viability was significantly higher in 1 day than in either 3 days or 1 week ($p > 0.05$).

4. DISCUSSION

Currently there is a growing interest in preventing or reducing biofilm formation in many biomedical areas. In preventive restorative dentistry, secondary caries is a critical issue and prevention of secondary caries plays a key role in long-lasting restorations [1-4]. PQAS represents a new trend of antimicrobial agents in biomedical applications [11,14]. PQAS can be incorporated in many ways, including mixing with fillers, copolymerizing with other monomers and grafting onto the polymer skeletons [11-15]. The beauty of using QAS is that they can kill the microorganism by touch or simple contact. The mechanism of QAS to kill bacteria is believed to disrupt the surface membrane of bacteria by changing membrane permeability or surface electrostatic balance [12,19]. Unlike other leachable antibacterial agents such as silver ions, antibiotics, CHX and low MW QAS, PQAS are not leachable due to their high MW [15]. In this regard, we purposely synthesized the new PQAS, incorporated it into both Fuji II LC and our experimental high-strength cements and evaluated the CS and antibacterial function of the formed cements.

Table 2. YS, modulus, CS and DTS of Fuji II LC and EXP cements.

Material	YS[1] [MPa]	Modulus [GPa]	CS[2] [MPa]	DTS[3] [MPa]
FIILC	138.4 (2.2)[a, 4]	6.91 (0.42)[d]	237.9 (4.5)[g]	43.4 (4.5)
FIILC (1%)	101.3 (2.9)[b]	5.40 (0.09)[e]	179.6 (1.2)	38.3 (4.6)
FIILC (3%)	86.4 (5.2)[b]	4.53 (0.01)	149.8 (1.4)[h]	29.6 (1.8)[i]
FIILC (5%)	50.4 (2.6)	3.22 (0.24)	91.6 (2.7)	24.3 (1.5)
FIILC (10%)	24.4 (2.6)	1.54 (0.09)	52.3 (2.9)	12.9 (0.3)
EXP	173.9 (7.1)[c]	7.74 (0.04)[f]	325.3 (4.2)	58.8 (0.2)[j]
EXP (1%)	170.6 (5.5)[c]	7.53 (0.16)[f]	284.4 (15)	57.9 (2.2)[j]
EXP (3%)	173.9 (10)[c]	7.25 (0.13)[d, f]	253.7 (11)[g]	50.3 (1.7)[k]
EXP (5%)	137.7 (12)[a]	6.68 (0.08)[d]	212.0 (4.1)[g]	49.9 (3.8)[k]
EXP (10%)	98.8 (2.6)[b]	5.09 (0.09)[e]	136.9 (6.7)[h]	33.7 (2.2)[i]

[1]YS = CS at yield; [2]CS = ultimate CS; [3]DTS = diametral tensile strength; [4]Entries are mean values with standard deviations in parentheses and the mean values with the same superscript letter were not significantly different ($p > 0.05$). Specimens were conditioned in distilled water at 37˚C for 24 h prior to testing.

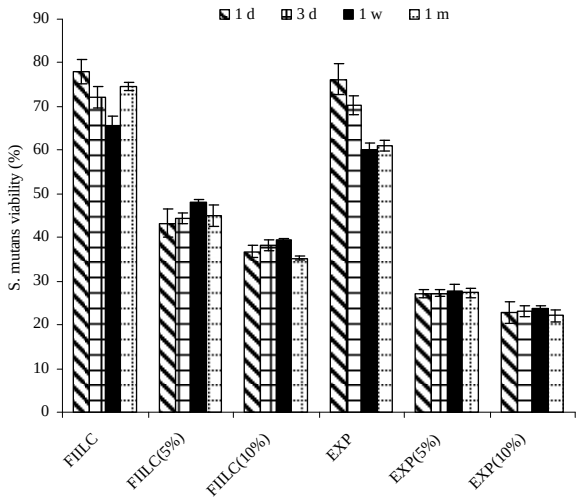

Figure 7. Effect of aging on the S. mutans viability after culturing with Fuji II LC and experimental cements with and without PQAS addition: The formulations were the same as those described in **Figure 5**. The specimens were conditioned in distilled water for 1 day, 3 days, 1 week and 1 month, followed by incubating with S. mutans before antibacterial testing.

From the results in **Figure 4** and **Table 2**, apparently both Fuji II LC and EXPGIC cements showed a decrease in CS, YS, modulus and DTS with increasing PQAS. This can be attributed to the reason that the incorporated QAS contains a 14 carbon long chain that does not contribute to any strength enhancement. On the other hand, EXPGIC showed a slower decreasing pace with nearly 30% less in CS decrease as compared to Fuji II LC (see **Figure 4**). This result implies that there may be some strong intermolecular interactions between PQAS and star-shape polymers. Furthermore, EXPGIC still kept its CS above 200 MPa at PQAS = 5% or less, which may be attributed to its original high strength (325 MPa).

Regarding the antibacterial activity, we also tested a commercial dental composite resin Z100 for comparison. We found that Z100 hardly killed S. mutans. After 48 h incubation with S. mutans, Z100 only killed 10% S. mutans (see **Figure 5**). Composite resins usually do not have antibacterial functions [5,6]. Both Fuji II LC and EXPGIC cements without PQAS addition killed about 20% S. mutans, which can be attributed to the release of fluoride. It is known that GICs have inhibitory effects on bacteria due to its fluoride release [6]. With PQAS addition, both Fuji II LC and EXPGIC increased their antibacterial function significantly. More interestingly, EXP GIC showed an even stronger antibacterial activity than Fuji II LC with 3 to 30% PQAS addition. The possible reason may be explained below. Since PQAS is composed of 50% carboxylic acid and 50% QAS and both components are very hydrophilic, they like to have interactions with other hydrophilic components from the cement in the presence of water. EXPGIC contains only hydrophilic GM-tethered poly (acrylic acid) (70%) and water (30%), whereas Fuji II LC contains a substantial amount (approximately 25-35%) of 2-hydroxyethyl methacrylate (partially hydrophilic) and dimethacrylaye/ oligomethacrylte (very hydrophobic), except for the linear poly (acrylic acid) (20-30%) and water (20-30%) [24]. Therefore, the components in EXPGIC may help the PQAS chains better extend on the surface of the cements but dimethacrylaye/oligomethacrylte and 2-hydroxyethyl methacrylate in Fuji II LC may restrict or interfere with the extension of the PQAS chains on the surface. Obviously, the more the QAS exposed the higher the antibacterial activity anticipated. The results imply that to reach the same or similar antibacterial results less PQAS might be required for EXPGIC than Fuji II LC. This outcome is very encouraging because it will allow us to use the minimum amount of PQAS in EXPGIC to obtain the maximum antibacterial activity without significantly reducing mechanical strengths.

As previously discussed, most antibacterial dental materials rely on the release of chemicals or antibacterial agents including antibiotics, silver ions, zinc ions, *etc* [6-10]. However, release or slow-release can lead or has led to reduction of mechanical properties of the restoratives over time, short-term effectiveness, and possible toxicity to surrounding tissues if the dose or release is not properly controlled [6-10]. Our hypothesis was to develop an antibacterial glass-ionomer cement without leachable. To confirm if the incorporated PQAS was not leachable, we examined both CS and antibacterial function of EXPGIC (containing 5% PQAS) after aging in water for 1 day, 3 days, 1 week and 1 month. The result in **Figure 5** showed that there was a slight increase in CS for all the formulations tested after one month of aging, indicating no PQAS leaching. The result in **Figure 7** showed that there was no change or reduction in antibacterial function for all the formulations tested, also suggesting no leaching. Otherwise, both strength and antibacterial function would decrease with aging. The reason can be attributed to the fact that the PQAS is the polyacid-containing polymer. It is known that the carboxylic acid group is the key to GIC setting and salt-bridge formation. The PQAS polymer synthesized in the study not only provided QAS for antibacterial function but also supplied carboxyl groups for salt-bridge formation. The latter helped the PQAS polymer firmly attached to the glass fillers.

5. CONCLUSIONS

We have developed novel antibacterial glass-ionomer cement containing non-leachable PQAS. With PQAS

addition, both Fuji II LC and experimental cements showed a reduction in CS with 25-95% for Fuji II LC and 13-78% for the experimental cement and a reduction in S. mutans viability with 40-79% for Fuji II LC and 40-91% for the experimental cement. The experimental cement showed less CS reduction and higher antibacterial activity as compared to Fuji II LC. The result also indicates that the cements are permanently antibacterial with no PQAS leaching. It appears that the experimental cement is a clinically attractive dental restorative that can be potentially used for long-lasting restorations due to its high mechanical strength and permanent antibacterial function.

REFERENCES

[1] Mjor, I.A., Dahl, J.E. and Moorhead, J.E. (2002) Placement and replacement of restorations in primary teeth. *Acta Odontologica Scandinavica*, **60(1)**, 25-28.

[2] Forss, H. and Widstrom, E. (2004) Reasons for restorative therapy and longevity of restorations in adults. *Acta Odontologica Scandinavica*, **62(2)**, 82-86.

[3] Manhart, J., Godoy, F.G. and Hickel, R. (2002) Direct posterior restorations: clinical results and new developments. *Dental Clinics of North America*, **46(2)**, 303-339.

[4] Deligeorgi, V., Mjor, I.A. and Wilson, N.H. (2001) An overview of reasons for the placement and replacement of restorations. *Primary Dental Care: Journal of the Faculty of General Dental Practitioners*, **8(1)**, 5-11.

[5] Craig, R.G. and Power, J.M. (2002) Restorative dental materials. 11th Edition, Mosby-Year Book, Inc., St. Louis.

[6] Wiegand, A., Buchalla, W. and Attin, T. (2007) Review on fluoride-releasing restorative materials—Fluoride release and uptake characteristics, antibacterial activity and influence on caries formation. *Dental Materials*, **23(3)**, 343-362.

[7] Osinaga, P.W., Grande, R.H., Ballester, R.Y., Simionato, M.R., Rodrigues, C.R.D. and Muench, A. (2003) Zinc sulfate addition to glass-ionomer-based cements: Influence on physical and antibacterial properties, zinc and fluoride release. *Dental Materials*, **19(3)**, 212-217.

[8] Takahashi, Y., Imazato, S., Kaneshiro, A.V., Ebisu, S., Frencken, J.E. and Tay, F.R. (2006) Antibacterial effects and physical properties of glass-ionomer cements containing chlorhexidine for the ART approach. *Dental Materials*, **22(7)**, 647-652.

[9] Yamamoto, K., Ohashi, S., Aono, M., Kokybu, T., Yamada, I. and Yamauchi, J. (1996) Antibacterial activity of silver ions implanted in SiO2 filler on oral streptococci. *Dental Materials*, **12(4)**, 227-229.

[10] Syafiuddin, T., Hisamitsu, H., Toko, T., Igarashi, T., Goto, N., Fujishima, A. and Miyazaki, T. (1997) In vitro inhibition of caries around a resin composite restoration containing antibacterial filler. *Biomaterials*, **18(15)**, 1051-1057.

[11] Gottenbos, B., Mei, H.C., Klatter, F., Nieuwenhuis, P. and Busscher, H.J. (2002) *In vitro* and *in vivo* antimicrobial activity of covalently coupled quaternary ammonium silane coatings on silicone rubber. *Biomaterials*, **23(6)**, 1417-1423.

[12] Thebault, P., Givenchy, E.T., Levy, R., Vandenberghe, Y., Guittard, F. and Geribaldi, S. (2009) Preparation and antimicrobial behavior of quaternary ammonium thiol derivatives able to be grafted on metal surfaces. *European Journal of Medicinal Chemistry*, **44(2)**, 717-724.

[13] Imazato, S., Russell, R.R. and McCabe, J.F. (1995) Antibacterial activity of MDPB polymer incorporated in dental resin. *Journal of Dentistry*, **23(3)**, 177-181.

[14] Murata, H., Koepsel, R.R., Matyjaszewski, K. and Russell, A.J., (2007) Permanent, non-leaching antibacterial surfaces—2: How high density cationic surfaces kill bacterial cells. *Biomaterials*, **28(32)**, 4870-4879.

[15] Lu, G., Wu, D. and Fu, R. (2007) Studies on the synthesis and antibacterial activities of polymeric quaternary ammonium salts from dimethylaminoethyl methacrylate. *Reactive and Functional Polymers*, **67(4)**, 355-366.

[16] Lee, S.B., Koepsel, R.R., Morley, S.W., Matyjaszewski, K., Sun, Y. and Russell, A.J. (2004) Permanent, nonleaching antibacterial surfaces. 1. Synthesis by atom transfer radical polymerization. *Biomacromolecules*, **5(3)**, 877-882.

[17] Li, F., Chai, Z.G., Sun, M.N., Wang, F., Ma, S., Zhang, L., Fang, M. and Chen, J.H. (2009) Anti-biofilm effect of dental adhesive with cationic monomer. *Journal of Dental Research*, **88(4)**, 372-376.

[18] Li, F., Chen, J., Chai, Z., Zhang, L., Xiao, Y., Fang, M. and Ma, S. (2009) Effects of a dental adhesive incorporating antibacterial monomer on the growth, adherence and membrane integrity of Streptococcus mutans. *Journal of Dentistry*, **37(4)**, 289-296.

[19] Beyth, N., Farber, I.Y.Y., Bahir, R., Domb, A.J. and Weiss, E.I. (2006) Antibacterial activity of dental composites containing quaternary ammonium polyethylenimine nanoparticles against Streptococcus mutans. *Biomaterials*, **27(21)**, 3995-4002.

[20] Wu, W., Xie, D., Puckett, A. and Mays, J. (2003) Synthesis and formulation of vinyl-containing polyacids for improved light-cured glass-ionomer cements. *European Polymer Journal*, **39(4)**, 663-670.

[21] Xie, D., Weng, Y. and Zhao, J. (2008) Alternative methacrylate-tethering methods for resin-modified glass- ionomer cements. *Journal of Applied Polymer Sciences*, **111(2)**, 869-875.

[22] Xie, D., Yang, Y., Zhao, J., Park, J.G. and Zhang, J.T. (2007) A novel comonomer-free light-cured glass-ionomer system for reduced cytotoxicity and enhanced mechanical strength. *Dental Materials*, **23(8)**, 994-1003.

[23] Kim, Y., Farrah, S. and Baney, R.H. (2007) Membrane damage of bacteria by silanols treatment. *Electronic Journal of Biotechnology*, **10(2)**, 252-259.

[24] Momoi, Y., Hirosaki, K., Kohno, A. and McCabe, J.F. (1995) Flexural properties of resin-modified "hybrid" glass-ionomers in comparison with conventional acid-base glass-ionomers. *Dental Materials Journal*, **14(2)**, 109-119.

J. Biomedical Science and Engineering, 2010, 3, 964-977 **JBiSE**
doi:10.4236/jbise.2010.310127 Published Online October 2010 (http://www.SciRP.org/journal/jbise/).

Computer system for simulation of human perception. Some implications for the pathophysiology of the schizophrenic syndrome

Bernhard J. Mitterauer

Bernhard Mitterauer, MD Volitronics-Institute for Basic Research, Psychopathology and Brain Philosophy, Gotthard Guenther Archives, Wals (Salzburg), Austria.
Email: mitterauer@wasi.tv

Received 16 June 2010; revised 25 June 2010; accepted 29 June 2010.

ABSTRACT

After the description of a brain model based on glial-neuronal interactions, a computer system for simulation of human perception, called clocked perception system, is proposed. The computer system includes a receptor field with sensors, each of which receives data with specific characteristics. These data are passed to processors, whereby only those connections between sensors and processors are released that are suited for an evaluation of the data according to a combination of specific data dictated by a phase program circuit. The computer system also includes a selector circuit that discards those dictated program commands that lead to a "senseless" computation result. A motor program circuit for the control of effectors may be connected to the computer system which at least contributes to the movement of the receptor field in order to bring the receptor field closer to suitable data with specific characteristics for better execution of the program. From disorders of the computer system implications are deduced for the pathophysiology of the schizophrenic syndrome. Finally, a novel treatment approach to this syndrome is proposed.

Keywords: Glial-Neuronal Interactions; Clocked Perception System; Technical Implementation; schizophrenic Syndrome

1. INTRODUCTION

The construction of artificial perception systems dates back to the 1960s [1]. Over the years, far better learning algorithms were developed and much more powerful hardware provided, hence rendering neural networks, or neurocomputing, the method of choice for most pattern-recognition applications or robotics [2,3]. Sophisticated pattern-recognition systems are now available in all perception qualities.

The present paper is one of a series investigating the time-coding principle from a biological and formal-technical point of view [4-8]. Here, the biological and formal background is further elaborated and some implications for the pathophysiology of schizophrenia are deduced from disorders of the mechanism.

2. CLOCKED PERCEPTION SYSTEM

2.1. Brain biological background

The biological brain model for the proposed clocked perception system is based on glial-neuronal interactions [5,7]. The nervous tissue of the brain consists of the neuronal systems (neurons, axons, dendrites) and the glial system (astrocytes, oligodendrocytes with myelin sheaths enfolding axons, radial glia, and microglia). Experimental results are inspiring a major reexamination of the role of glia in the regulation of neural integration in the central nervous system [9,10]. **Figure 1** shows a schematic diagram of the glial-neuronal interaction: two astrocytes ($Ac_{1,2}$) are shown in this very simple model, whereby in each case only one neuron ($N_{1,2}$) belonging to an astrocyte is taken into consideration. Halassa *et al*. [11] identified how a single astrocyte contacts only four to eight neurons, but 300 to 600 synapses via its processes. The glial network (syncytium) consists in this schema of two astrocytes and two oligodendrocytes ($Oc_{1,2}$) interconnected via gap junctions (g.j.). The neuronal system shows two neurons ($N_{1,2}$) with two afferent axons ($Ax_{i,j}$) and two afferent axodendritic synapses ($Sa_{i,j}$), two efferent axons ($Ax_{1,2}$) with myelin sheaths (Ms) and a node of Ranvier (N.R.), as well as two dendro-dendritic synapses ($Sd_{1,2,3,4}$) with the corresponding dendrites (D_1, D_2, D_3, D_4).

Although a true understanding of how the astrocyte, the dominant glial cell type, interacts with neurons is

still missing, several models have been published. Here, I focus on a modified model proposed by Newman [12]. **Figure 2** depicts a schematic diagram of possible glial-neuronal interactions at a glutamatergic tripartite synapse. Release of glutamate (GLU) from the presynaptic terminal activates glial receptors (glR) and postsynaptic receptors (poR) (1) (for the sake of clarity only one receptor is shown). The occupancy of glial receptors evokes a Ca^{2+} increase (2) and the release of glutamate from the astrocyte. Glutamate excitation of presynaptic receptors (prR) (3) modulates glutamate release while activation of postsynaptic receptors (4) directly depolarizes the postsynapse. Activation of the astrocyte also elicits the release of adenosine-triphosphat (ATP), which depolarizes the postsynaptic neuron (5) and inhibits the presynaptic terminal (6) via occupancy of the cognate receptors [13]. Hence, glia may exert a temporal boundary-setting function in synaptic information processing [5].

For understanding the clock mechanism of the perception system, the rhythmic contraction waves of glial cells (astrocytes and oligodendrocytes) are decisive. Glial cells, when they get swollen and/or depolarized, can potentially release accumulated K^+, neurotransmitters, neuromodulators (*e.g.* taurine), and water into interstitial fluid in a pulsatile manner. Such discharge processes represent mechanisms by which glial cell networks could influence neuronal firing in a coordinated fashion [14]. In addition to modulating synaptic transmission in neuronal cells, astrocytes and oligodendrocytes may play a direct role in generating pacemaker rhythms [15].

This originally speculative assumption has already been verified. Parri *et al.* [16] showed that astrocytes in situ could act as a primary source for generating neuronal activity in the mammalian central nervous system. Slow glial calcium oscillations (every 5 to 6 minutes) occur spontaneously and can cause excitations in nearby neurons. Although experimental evidence shows that neuronal-glia interactions also occur in the millisecond range [17], until now spontaneous rapid glial oscillations within a second are not found. However, slow rhythmic pulsations of glial cells, especially of astrocytes, could influence cognitive processes such as thinking and could also play a role in neuronal pacemaker circuits [18].

Since phase programming represents a basic mechanism in the clocked perception system that may be generated in the astrocytic syncytium, the underlying biological structure and function must be described. **Figure 3** shows a diagrammatic schema depicting an astrocytic syncytium composed of two astrocytes (Ac_1, Ac_2) interconnected via gap junctions (g.j.). Each astrocyte contacts four synapses (S_y) with four different qualities (a, b, c, d) building an astrocytic-neuronal compartment. A

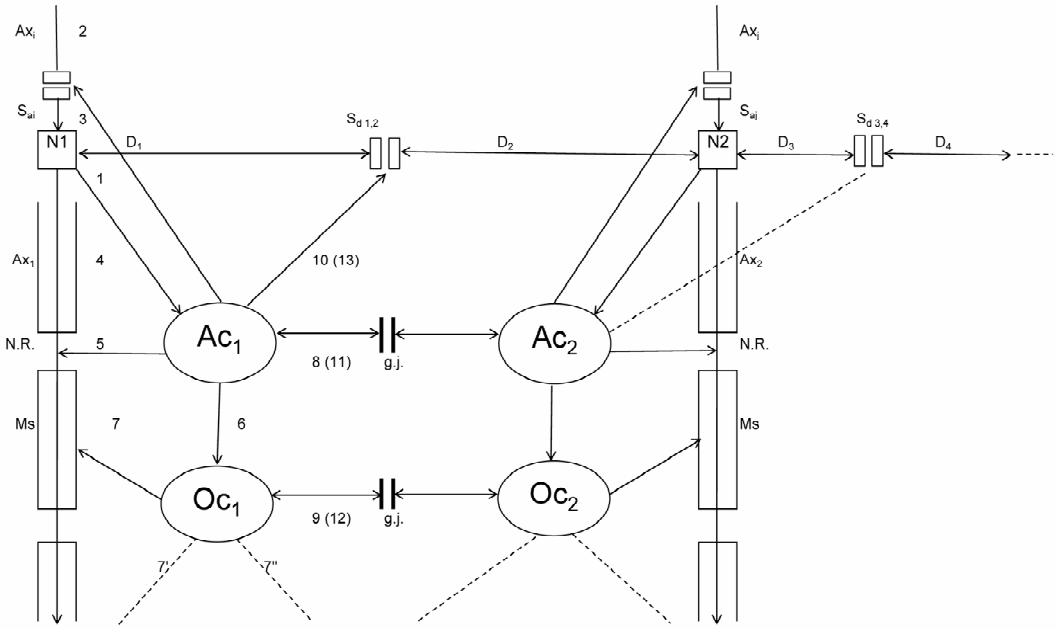

Two astrocytes ($Ac_{1,2}$) are shown in this very simple model, whereby in each case only one neuron belonging to an astrocyte is taken into consideration. The glial network (syncytium) consists of two astrocytes and two oligodendrocytes ($Oc_{1,2}$) belonging to them. Gap junctions (g.j.) exist between the astrocytes and the oligodendrocytes. The neuronal system shows two neurons ($N_{1,2}$) with two afferent axons ($Ax_{i,j}$) and two afferent axo-dendritic synapses ($Sa_{i,j}$), two efferent axons ($Ax_{1,2}$) with myelin sheaths (Ms) and a node of Ranvier (N.R.), as well as two dendro-dendritic synapses ($Sd_{1,2;3,4}$) with the corresponding dendrites (D_1, D_2, D_3, D_4).

Figure 1. Schematic diagram of the glial-neuronal interaction.

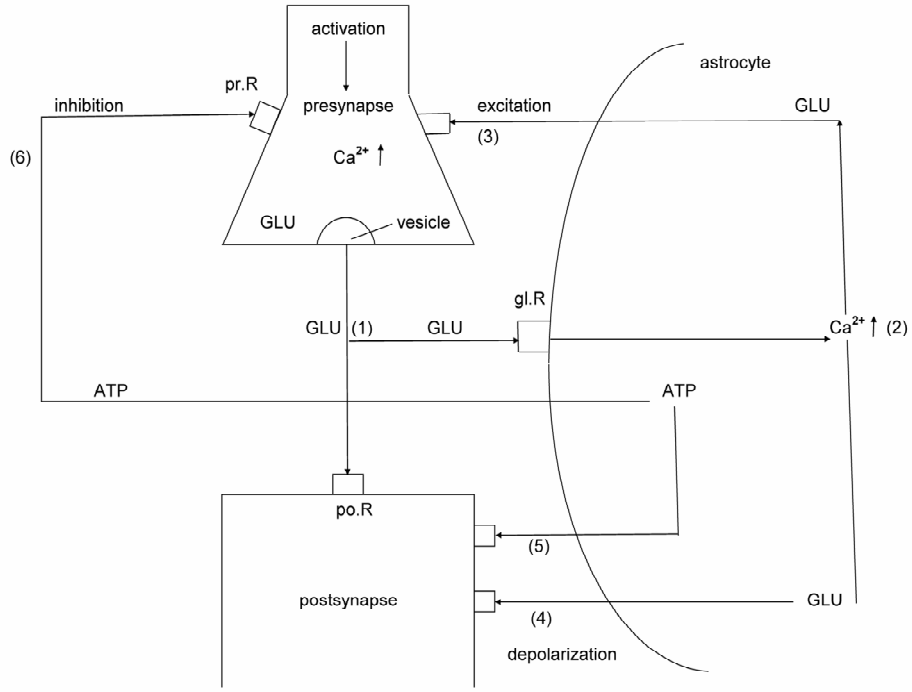

Release of glutamate (GLU) from the presynapse activates (arrows) glial receptors (glR) and postsynaptic receptors (poR) (1), (for the sake of clarity only one receptor is shown). The occupancy of glR evokes a Ca^{2+} increase (2) and the release of GLU from the astrocyte. GLU excitation of presynaptic receptors (prR) (3) modulates GLU-release while activation of prR (4) directly depolarizes the postsynapse. Activation of the astrocyte also elicits the release of adenosine-triphosphat (ATP), which depolarizes the postsynapse (5) and inhibits the presynapse (6) via occupancy of the cognate receptors.

Figure 2. Schematic diagram of possible glial-neuronal interactions at the glutamatergic tripartite synapse (modified after Newman, 2005).

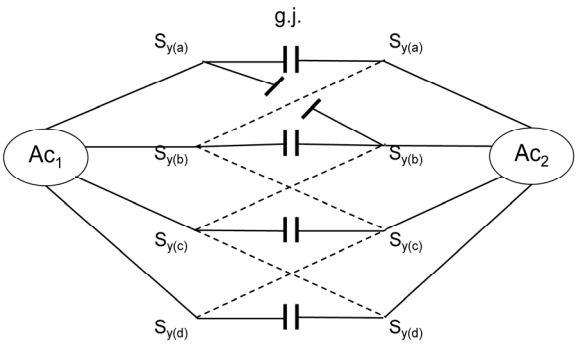

Two astrocytes (Ac_1, Ac_2) are interconnected via gap junctions (g.j.). Each astrocyte contacts four synapses (S_y) with four different qualities (a, b, c, d) building two astrocytic-neuronal compartments. Since these two compartments are interconnected via gap junctions, a network is generated, called syncytium.

Figure 3. Diagrammatic schema of an astrocytic syncytium.

quality is defined as the specific neurotransmitter type that mainly operates in synaptic neurotransmission, say glutamate (a), acetylcholine (b), serotonin (c), and dopamine (d). The gap junctions consist of the four identified astrocytic connexins Cx43, Cx30, Cx26, and Cx45, forming homotypic and heterotypic gap junction channels (for the sake of clarity not shown in the figure).

Moreover, astrocytes are also connected with oligodendrocytes via gap junctions (g.j.), as shown in **Figure 4**. One speaks of a panglial syncytium [19]. Importantly, astrocytes may activate or inhibit the axonal information flux on the nodes of Ranvier (N.R.). In addition to "traditional" myelin formation oligodendrocytes may influence synaptic regulation and signaling of the nodes of Ranvier [20]. There is growing experimental evidence that oligodendrocytes co-determine axonal information processing via myelin sheaths, by ions and transmitters. Since oligodendrocytes are interconnected with astrocytes via gap junctions, the processes in the astrocytic syncytium may determine the function of the oligodendrocytes [21]. This functional interplay between glial cells represents a basic mechanism in the implementation of the clocked perception system. The special functions of the neuronal system will be described and interpreted below. Let me now attempt to show how the double structure of the neuronal and glial networks can be implemented as a spatio-temporal mechanism, termed clocked perception system [7].

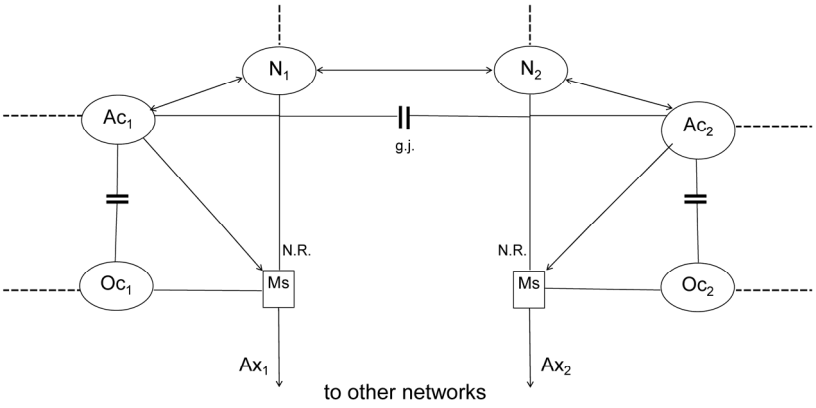

Two astrocytes ($Ac_{1,2}$) contact two neurons ($N_{1,2}$). The astrocytes are interconnected via gap junctions (g.j.) building an astrocytic syncytium. In addition, the astrocytes ($Ac_{1,2}$) are interconnected with oligodendrocytes ($Oc_{1,2}$) via gap junctions (g.j.) forming a general glial network, called panglial syncytium. Only two axons ($Ax_{1,2}$), two myelin sheaths (Ms) and nodes of Ranvier (N.R.) are shown (see Figure 1).

Figure 4. Schematic diagram of the panglial syncytium.

3. CLOCKED PERCEPTION SYSTEM

3.1. Description of the Preferred Embodiments

Figure 5 shows a computer system for the simulation of human perception via sense organs that contains a large number of sensors R_n, namely R_1, R_2, R_3,…R_{10}, R_{11},…R_n in a receptor field 2. These sensors are sensitive to data a, b, or c, which are represented here by different configurations of the sensors; thus, the sensors, such as R_1, R_4, etc. which have a triangular receptor surface, are sensitive to specific data that are simulated in the illustration by STa. Correspondingly, sensors R_2, R_5, R_{11}, etc. are sensitive to specific data b supplied by stimuli ST_b, which here are shown to have a semi-circular receptor surface and a similar stimulus. Further sensors such as sensors R_3, R_6, …R_n are sensitive to specific data c, which here are shown to have a quadrilateral receptor surface or correspondingly quadrilateral stimuli ST_c. All stimuli are compiled in a stimulus field 3. It is clear that the stimuli are not produced by an arranged stimulus field as shown in the illustration; rather, they are presented to the computer system within the scope of a simulation of the environment in a non-arranged fashion. Each sensor R_i is connected with a processor P_i via a line L_i, whereby the index *i* progresses from 1 to n. Instead of a processor, an entire processor group PG, consisting of several processors P_i, as shown by dotted lines in **Figure 6** may be provided. Such a processor group consisting of processors $P_{6.1}$, $P_{6.2}$, to $P_{6.6}$ is shown in **Figure 6**. The results calculated by processors P_i are stored in a memory buffer 4.

A circuit configured as a line circuit 5 is provided that is controlled by a phase circuit 6. Lines A_1 to A_n proceed from the line circuit 5 to corresponding lines L_1 to L_n, where they affect switches S_1 in the lines L_1, of which only the switches S_1, S_6, S_7 and S_n are shown. These switches are pure on/off switches, so that the lines L_i are either interrupted or connected by the switches. Along with the control circuit C for the line switching 5, the phase circuit 6 includes a large number of output lines B, of which the lines B_1 to B_{11} and B_n are shown here. These lines B_i also lead to the connection lines L_i between the sensors R_i and the processors P_1, and control the switches SW_i located in the lines there, of which only switches SW_1, SW_6, SW_7, and SW_n are shown. As switch S_i, these switches SW_i are pure on/off switches, so that lines L_i are either interrupted or connected by the switches as they are controlled.

The central element of this computer system is a phase program circuit 7 in which an intended program for the total computer system is embedded and that controls the phase circuit 6 via control line C_2 and also the line switching directly via control line C_1. Cycles are dictated to phase circuit 6 via the phase program circuit 7, whereby a cycle corresponds to the time phase in which a certain switching applies. Depending on the programming, a primary, secondary, or tertiary analysis of the status of the sensors is performed, for example, by the phase circuit. Thus, the cycled programming has a sampling function in that all monographs, digraphs, or trigraphs are played through or intentionally implemented, so that a certain combination of sensor statuses is sought in the simulated environment. The processors are arranged such that exactly as many processors are assigned to each receptor as there are phases being processed by the phase program. In the simplified case represented in **Figure 6**, there are six processors per group PG_i that are connected with one of the sensors R_i

via lines L_i. In this case, only three characteristics for the stimuli, *i.e*. three specific data types a, b, and c are dictated; during simulation of optical perception these could be, for example, specific characteristics such as "flat ground" (a), "obstacle" (b), and "small objects on the floor" (c). Naturally, considerable more sensors and considerably more specific characteristics would be necessary for a complete simulation of optical perception.

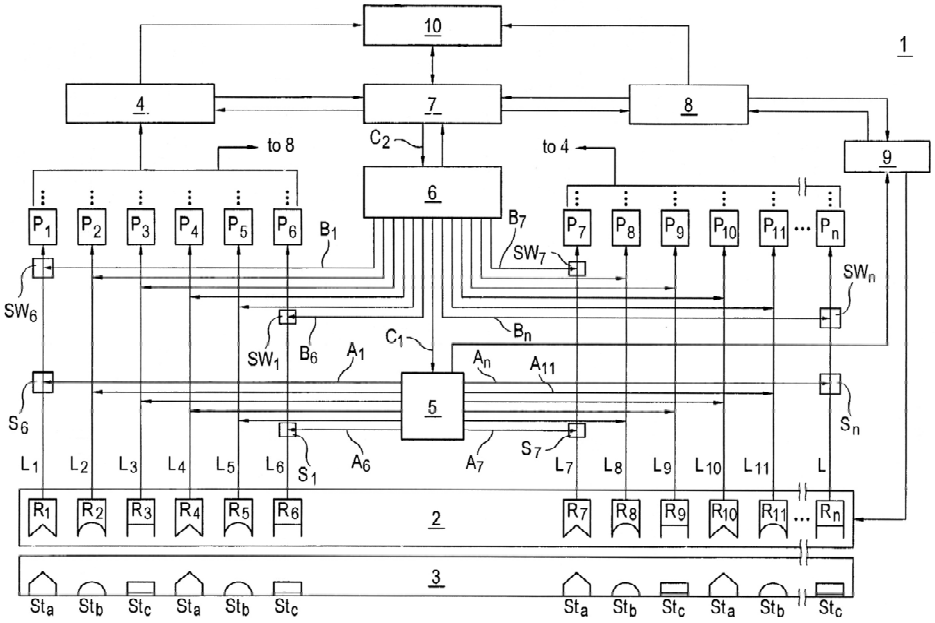

Figure 5. Circuit diagram of a clocked computer system for the simulation of human perception (see text).

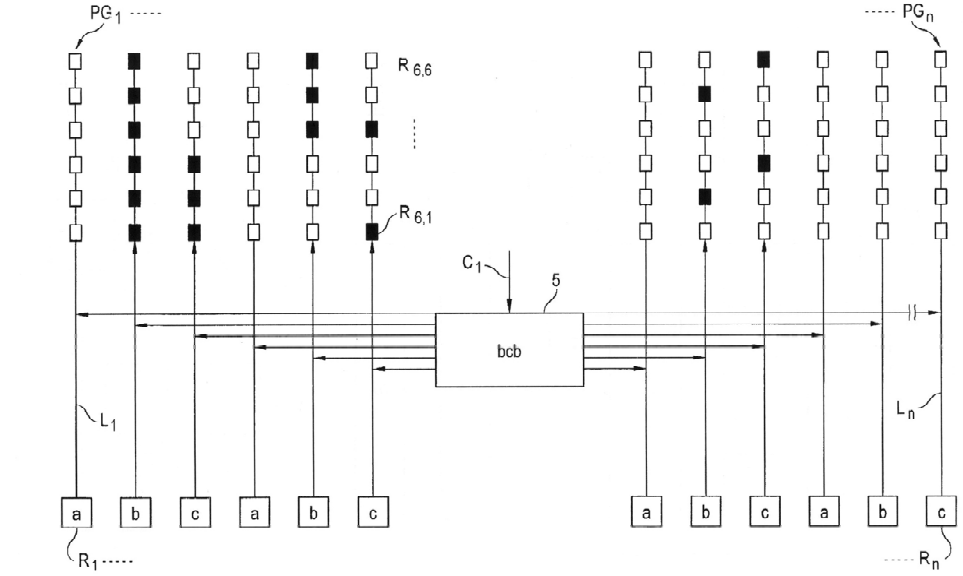

Figure 6. Schematic representation of the active elements of a part of the computer system in Figure 5 during simulation of a perception (see text).

In the simplified representation in **Figure 6**, only those sensors that may be assigned the named chracteristics R_1 to R_n are shown as small boxes, each connected to a processor group PG_1 to PG_n. Each processor group PG_i consists of six processors, whereby, as mentioned above, only those processors of the sixth group are designated as $P_{6.1}$ through $P_{6.6}$. **Figure 6** shows only the line circuit 5 from the computer system in the upper part of **Figure 5**, whereby a trigraph of the specific characteristics b, c, b are specified on the line circuit block, which are processed in six steps corresponding to the six processors based on the phase program. One may see from **Figure 6** that the sensors occupied by specific characteristics "b" and "c" are switched through, and that some processors are already acting in the pertinent processor groups (designated by black boxes). It is also clear that no processor is active in the processor group PG_n, which leads to the conclusion that the sensor R_n is not occupied. Since neither the sensors nor the processors executing the specific characteristics "a" are being queried by the trigraph, the corresponding processor groups are not active. During the processing of the distribution of specific characteristics specified by the trigraph, the line circuit 5 must perform the following number of switchings in the arrangement of sensors for the computer system shown:

- For primary analysis ("Is a suitable stimulation of the three specific characteristics occurring at all?"), two switchings;
- For secondary analysis ("What is the distribution of the specific characteristics queried?"), 24 switchings; and
- For tertiary analysis ("How many of the specific characteristics are present at the sensor?"), 12 switchings.

As may be derived from the diagram in **Figure 6**, only matching stimuli are accepted for the pre-determined phase program, while non-matching stimuli, *i.e.* those that do not correspond to the phase program, are discarded. This alternation between acceptance and rejection is a characteristic of subjective intentional systems. A system's ability to reject is an "index of its subjectivity", which means that the implementation of intentions requires not only the identification of matching objects, but also the simultaneous discarding of present objects not intended. In order to dynamically configure the statistical computer system described, and thus to optimally simulate perception, as mentioned above, a motor program circuit 8 is connected with the computer system that interacts with the phase program circuit 7 via bi-directional lines, and is controlled by it in accordance with each phase program step. This motor program circuit controls effectors 9 that affect the receptor field 2, for example, in order to display it, thus achieving a better reception of stimuli by the individual sensors. The effectors might also serve to reposition a complete robot. The line circuit 5 also acts directly on the effectors 9 or their control circuits, which report each phase program step to be processed to the effectors, so that these may be controlled correspondingly.

It must be mentioned for the sake of completeness that another comparator circuit 10 may be provided that contains data from the memory buffer 4, the motor program circuit 8, and the phase programming circuit 7, whereby communication with the phase program circuit 7 is bi-directional. The available data may be compared after suitable transformation in order to determine how well the intended phase program was processed. Based on this result, the phase program may be altered, or the computer system may be placed into another condition, *e.g.* by movement of the sensors or repositioning the robot. In this case, the decision is sent to the computer system whether it should continue to attempt to find the characteristics corresponding to the phase program, or whether it should alter the phase program with the help of the memory buffer 4.

The perception mechanism presented may be viewed as a guitarist who hears a melody in his head and wants to hear how it really sounds. He wants to perceive it. He picks up his guitar and with his left hand presses the strings at exactly those points that correspond to his desired melody. The melody therefore dictates where the strings must be pressed. Regarding the perception mechanism, this means that the phase program determines which lines must be released by the switching mechanism for a certain time period. Since the melody consists of varying combinations of sounds or notes, the grip on the guitar must be constantly changed, which correspond to a change in the phase program. Earlier, the guitar did not produce any sound by itself except for the minor sounds caused by placing the fingers on the strings. The guitar player must first strike the strings with his right hand (or guitar pick). This process corresponds to stimulation of the sensors. This takes into account the combination of how the guitarist uses the strings of his instrument. This mechanism of creating a melody requires no logical calculations, but rather takes advantage of the possibilities of use of the instrument in time cycles. However, from a biological point of view we are faced with the problem how and where these phase programs may be generated in the brain [22].

3.2. Generation of the Phase Programs within the Astrocytic Syncytium

First of all, if one speaks of intentional programs, one has to define the formalism on which these programs are based. According to Guenther [23], a negative language

can be formalized in an *n*-valent permutation system. Generally, a permutation of *n* things is defined as an ordered arrangement of all the members of the set taken all at a time according to the formula *n!* (*!* means factorial). **Table 1** shows a quadrivalent permutation system in a lexicographic order. It consists of the integers 1, 2, 3, 4. The number of permutations is 24 (4! = 1.2.3.4 = 24). The permutations of the elements

1		4
2	to	3
3		2
4		1

can be generated with three different NOT operators N_1 , N_2 , N_3 , that exchange two adjacent (neighbored) integers (values) by the following scheme:

1 ↔ 2; 2 ↔ 3; 3 ↔ 4
(N_1) (N_2) (N_3)

Generally, the number of negation operators (NOT) is dependent on the valuedness of the permutation system minus 1. For example, in a pentavalent permutation system four negation operators (N_1-N_4) (n = 5-1 = 4) are at work.

It is possible to form loops, each of which passes through all permutations of the permutation system once (Hamilton loop). In a quadrivalent system they are computable (44 Hamilton loops), but in higher valent systems they are not computable. **Table 2** shows an example of a Hamilton loop [23]. The first permutation (P = 1234) is permutated via a sequence of negation operators ($N_{1x2x3,...,2x1x2}$) generating all the permutations once until the loop is closed.

Such permutation systems can be mathematically formalized as negation networks, called permutographs [24]. **Figure 7** shows a quadrivalent permutograph. The individual NOT or negation functions N_1-N_3 are represented between the permutations (1,…,24). The various Hamilton loops differ in NOT or negation operator sequence. An example of a Hamilton loop is indicated in this permutograph by a dash-dotted line. It is defined by the following negation operator sequence:

N_1–N_2–N_3–N_2–N_3–N_2–N_1–N_2–N_1–N_2-N_3-N_2-N_3-N_2-N_1-N_2-N_1-N_2-N_3-N_2-N_3-N_2-N_1-N_2

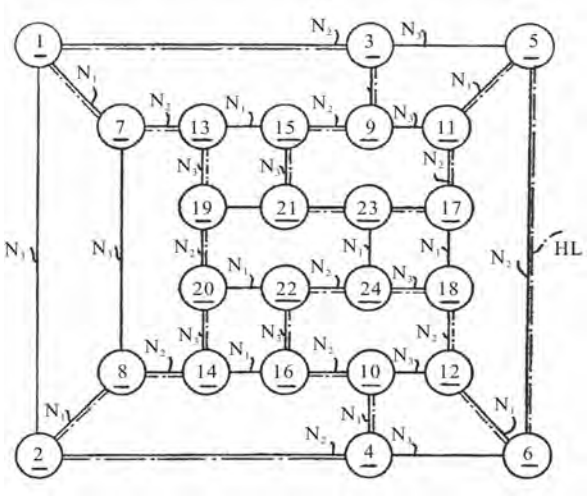

Figure 7. Example of a Hamilton loop in a quadrivalent permutograph.

Table 1. Quadrivalent (n = 4) permutation system arranged in a lexocographic order.

	1	1	1	1	1	1	2	2	2	2	2	2	3	3	3	3	3	3	4	4	4	4	4	4
	2	2	3	3	4	4	1	1	3	3	4	4	1	1	2	2	4	4	1	1	2	2	3	3
	3	4	2	4	2	3	3	4	1	4	1	3	2	4	1	4	1	2	2	3	1	3	1	2
	4	3	4	2	3	2	4	3	4	1	3	1	4	2	4	1	2	1	3	2	3	1	2	1
number of the permutation	1	2	3	4	5	6	7	8	9	10	11	12	13	14	15	16	17	18	19	20	21	22	23	24

This permutation system consists of 24 permutations (1 x 2 x 3 x 4, ….., 4 x 3 x 2 x 1) according to the formula n = 4! (factorial) = 1
The 24 permutations are lexicographically arranged.

Table 2. Example of a Hamilton loop generated by a sequence of negation operators (Guenther, 1980) and designation of a phase program.

Phase program in triplets:		a	b	c	b	c	b	a	b	a	b	c	b	c	b	a	b	a	b	c	b	c	b	a	b	
P	**N**	1.	2.	3.	2.	3.	2.	1.	2.	1.	2.	3.	2.	3.	2.	1.	2.	1.	2.	3.	2.	3.	2.	1.	2.	**P**
1		2	3	4	4	3	2	1	1	2	3	4	4	3	2	1	1	2	3	4	4	3	2	1	1	
2		1	1	1	1	1	1	2	3	3	2	2	3	4	4	4	4	4	4	3	2	2	3	3	2	
3		3	2	2	3	4	4	4	4	4	4	3	2	2	3	3	2	1	1	1	1	1	1	2	3	
4		4	4	3	2	2	3	3	2	1	1	1	1	1	1	2	3	3	2	2	3	4	4	4	4	

This first permutation (P = 1 x 2 x 3 x 4) is permutated via a sequence of negation operators (N1 x 2 x 3 …. 2 x 1 x 2) generating all the permutations once until it is closed (1234) in the sense of a Hamiltion loop. It represents a phase program consisting of triplets, where N1, N2, N3 stand for the characteristics a, b, c.

Already in the 1980ies we were able to show that the negative language may represent an appropriate formal model for a description of intentional programs generated in neuronal networks of biological brains. Based on this formalism, computer systems for robot brains have also been proposed [25,26]. Here, I will try to further elaborate on this possible intentional programming in our brains, focusing on glial-neuronal interaction.

3.2.1. Glial Gap Junctions Could Embody Negation Operators

In situ, morphological studies have shown that astrocyte gap junctions are localized between cell bodies, between processes and cell bodies, and between astrocytic end-feet that surround brain blood vessels. In vitro, junctional coupling between astrocytes has also been observed. Although less frequently observed than junctions between astrocytes, gap junctions also occur between oligodendrocytes, as observed in situ and in vitro. Moreover, astrocyte-to-oligodendrocyte gap junctions have been identified between cell bodies, cell bodies and processes, and between astrocyte processes and the outer myelin sheath. Thus, the astrocytic syncytium extends to oligodendrocytes, allowing glial cells to form a generalized glial syncytium, also called "panglial syncytium", a large glial network that extends radially from the spinal cord and brain ventricles, across gray and white matter regions, to the glia limitans and to the capillary epithelium. Ependymal cells are also part of the panglial syncytium. Additionally, activated microglia may also be interconnected with astrocytes via gap junctions. However, the astrocyte is the linchpin of the panglial syncytium. It is the only cell that interconnects to all other glia. Furthermore, it is the only one with perisynaptic processes.

Gap junctions are now recognized as a diverse group of channels that vary in their permeability, voltage sensitivities, and potential for modulation by intracellular factors; thus, heterotypic coupling may also serve to coordinate the activities of the coupled cells by providing a pathway for the selective exchange of molecules below a certain size. In addition, some gap junctions are chemically rectifying, favoring the transfer of certain molecules in one direction versus the opposite direction. The main gap junction protein of astrocytes is connexin Cx43, whereas Cx32 is expressed in oligodendrocytes in the CSN as well as another type of connexin, Cx45. Heterelogous astro-oligodendrocyte gap junctions may be composed of Cx43/Cx32, if these connexins form functional junctions [27]. Recent experimental results suggest roles of glial gap junction-mediated anchoring of signalling molecules in a wide variety of glial homeostatic processes [28].

Gap junctions are showing properties that differ significantly from chemical synapses [29]. The following enumeration of gap junctional properties in glial syncytia may support my hypothesis that gap junctions could embody negation operators in the sense of a generation of negative language in glial syncytia:

First, gap junctions communicate through ion currents in a bi-directional manner, comparable to negation operators defined as exchange relations. Bidirectional information occurs between astrocytes and neurons at the synapse. This is primarily chemical and based on neurotransmitters. It is not certain that all glial gap junction communications are bidirectional due to rectification. This is a poorly understood area because of extremely severe technical difficulties, especially in vivo [30]. Second, differential levels of connexin expression reflect region-to-region differences in functional requirements for different astrocytic gap junctional coupling states. The presence of several connexins enables different permeabilities to ions and molecules and different conductance regulation. Such differences of gap junctional functions could correspond to the different types of negation operators. Third, neuronal gap junctions do not form syncytia and are generally restricted to one synapse. Fourth, processing within a syncytium is driven by neuronal input and depends on normal neuronal functioning. The two systems are indivisible. It is important to emphasize that neuronal activity-dependent gap junctional communication in the astrocytic syncytium is long-term potentiated. This is indicative of a memory system as proposed in neuronal synaptic activity by Hebb over five decades ago [31]. Fifth, the diversity of astrocytic gap junctions results in complex forms of intercellular communication because of the complex rectification between such numerous combinatorial possibilities. Sixth, the astrocytic system normally functions to induce precise efferent (*e.g.* behaviorally intentional or appropriate motor) neuronal responses. Admittedly, the testing of this conjecture is also faced with experimental difficulties.

Now, let us tie junctional functions and negative language together. Negation operators represent exchange relations between adjacent values or numbers. So they operate like gap junctions bi-directionally. Dependent on the number of values (n) that constitute a permutation system, the operation of different negation operators (n–1) is necessary for the generation of a negative language. With concern to gap junctions, they also show functional differences basically influenced by the connexins. Therefore, different types of gap junctions could embody different types of negation operators. Furthermore, a permutation system represents — like the glial syncytium — a closed network generating a negative language. So we have a biomimetic interpretation of the negative language.

If it is supposed that Hamilton loops are generated in the astrocytic syncytium, how can these be interpreted as working phase programs in glial-neuronal interactions? Let us take the Hamilton loop shown in **Table 2** as an example. It consists of a sequence of 24 negation operators (N_1-N_3). In the computer system proposed, the phase programming is clocked and based on characteristic triplets (a, b, c) in various combinations [7]. If the negation operators N_1, N_2, N_3 stand for the characteristics a, b, and c, then a Hamilton loop consists of eight triplets representing a phase program (**Table 2**). Now, a phase programming in various combinations of triplets (*e.g.* aaa; baa, *etc.*) occurs [7]. Interestingly, in a quadrivalent permutation system all possible Hamilton loops (n = 44) are computable. In higher valued systems one is faced with a NP (non-deterministic polynomial time) problem so that the number of all possible Hamilton loops is uncomputable. What the implementation of this biomimetic model of phase programming concerns, we can expect promising biotechnical developments [32].

3.3. Coping with "Nonsense" Phase Programs

In undisturbed dynamics the perception system is capable of coping with "nonsense" phase programs. In order to shorten the time required to process the overall phase program, and to calculate sigificant results from the phase program quickly, the computer system includes a selection circuit that quasi "jumps over" such commands during readout of those individual program commands whose execution would lead to senseless or non-executable results, thereby discarding them. Such "nonsense" program commands are buffered, so that the meaningful commands are compared with the buffered "nonsense" program commands when the program commands are read out, and may thus be removed from program execution.

The computer system starts, for example, with any particular phase program and tests which program commands created significant perception images within a certain environment. The criterion for "meaningful" might be, for instance, that the computer system intentionally conducts an action corresponding to the perception. For example, the proper motor is actuated in a robot that leads to meaningful handling. The computer system determines over time that certain program commands corresponding to a time cycle in the phase program lead to "senseless" perception images which also evince themselves in purposeless, *i.e.* "nonsense" actions, *e.g.* motor processes. However, such program commands executed in another environment might cause meaningful actions, so that consideration of the current environment is significant. The computer system's learning process consists of having the phase programs created for a specific, targeted environment, and, based on system feedback, having program commands ignored that are unsuitable for each task in the current environment, and thereby creating a suitable action, *e.g.* movement of sensors.

The sensors address three different properties or data types, whereby the individual program commands are compiled as triplets, *i.e.* as a triple data set composed of a, b, and c. When triplets, for example, that have the property b in the first position are unsuitable for the creation of meaningful actions in the current environment, they are removed from the phase program. If, for example, the following phase program is present:

aaa/baa/cba/bcc/aca,

then the second and fourth triplets beginning with b will be cancelled, *i.e.* removed, so that the following implementable phase program remains:

aaa/cba/aca.

From this very brief example, one may see that the act of ignoring part of the phase program can significantly shorten it, so that the calculation time for the entire system is also shortened. Actions that are suitable and meaningful for the environment may be quickly calculated.

The function of this phase program circuit, which is modified by this selection circuit, is oriented to genetic code: a gene carries so-called codones, *i.e.* genetic words consisting of four (or possibly five) nucleotides A, T, C, and G (and possibly U), which represent a reading framework for amino acids from which in turn a certain protein is created. Comparable to this genetic mechanism, command programs are encoded as phase program triplets that represent the structure of a perception image. Note, a gene consists of sections of nucleotides which may factor a gene (so-called exons), and sections which cannot factor a protein (so-called introns). In order to create a functional protein at all, the introns must be "spliced out" of the nucleotide sequence. In science, one speaks of a so-called "splicing mechanism". As soon as this mechanism is destroyed in that introns are not actually cut out, non-functional "Chimera" proteins or only short-lived supported proteins (truncated proteins) come into existence. In the phase programming for the computer system based on the invention, this genetic principle means that program commands encode in the form of trigraphs, *e.g.* triplets of time cycles which encode unsuitable positions for a qualitative image construction for the objects of a certain environment, or tend to lead to sense deceptions within the meaning of false perceptions if these program commands are not spliced out.

4. IMPLICATIONS FOR THE PATHOPHYSIOLOGY OF THE SCHIZOPHRENIC SYNDROME

Since in schizophrenia various phenomenologies are

observed, it is more appropriate to speak of a schizophrenic syndrome [33]. From the perception system proposed three main disorders can be deduced that could play a role in the pathophysiology of the schizophrenic syndrome. First, a disorder of phase programming in the glial syncytium occurs. Second, phase programs cannot be transferred to the neuronal system in synapses. Third, the switching mechanism is defective so that the oligodendrocyte-axonic system is affected. These disorders can also be combined which determines the severity of the schizophrenic syndrome.

4.1. Incomplete Generation of Phase Programs Caused by a Loss of Gap Junctions

If the function of an amount of gap junctions in the glial syncytium is genetically or (and) by stress disturbed, the network is incomplete ("leaky") [34]. Hence, complete cycles of phase programs cannot be generated. Even if the synaptic glial-neuronal interactions would remain intact, phase programs cannot work, since incomplete triplets are unable to conduct analyses of the various object qualities in the environment. Hallucinations may be caused by this perception disorder. In visual hallucinations, for example, uncanny scenes arise where unreal objects are composed, corresponding to neologisms in the semantic domain. Such severe cognitive impairment also affects thinking, emotions and motor behaviour.

4.2. Phase Programs cannot be Transferred in Synapses Caused by Non-Functional Astrocytic Receptors

As shown in **Figure 2**, astrocytes exert a modulatory function in synaptic information transmission via their receptors accompanied by gliotransmission. As in **Figure 8** depicted, the glial receptors (glR) are non-functional (crosses) and cannot be occupied by neurotransmitters (NT), so that the activation of the gliotransmitters (GT) is impossible. Hence, they cannot negatively feedback to the receptors on the presynapse (prR). As a consequence, the glia lose their inhibitory or boundary-setting function and the neural transmitter flux is unconstrained, as the flux of thought on the phenomenological level [35].

The glial system in its interaction with the neuronal system generates glial-neuronal compartments in the sense of specific functional units or operational domains [5, 36]. The interactional structure of an astrocyte with n-neurons can be defined as an elementary compartment of nerve cells. By simultaneously activating and deactivating neurotransmission in all of the synapses enveloped by an astrocyte, the astrocyte calcium wave may coordinate synapses into synchronously firing groups, interpretable as harmonization [7,37].

A loss of the glial boundary-setting function is depicted in **Figure 9**. The astrocytes (Ac_i; Ac_j) of compartment x and compartment y have non-functional glial receptors (crosses), so that glia cannot influence neuronal information processing. This genetically determined disturbance results in a compartmentless neuronal network displayed as a group of eight neurons with 28 connecting lines (according to the formula $[n^2\text{-}n]$ 2).Such a brain is unable to structure the environmental information. One may argue that a glial determination of neuronal networks into functional units is not necessary because the neuronal system is compartmentalized per se [38]. However, there is a qualitative difference between the purely neuronal compartments and the glia-determined compartments. Neuronal compartments may be merely functional for information processing, whereas glial-neuronal compartments may in addition have an information-structuring potency that we need for recognizing the qualitative differences between objects and individuals in our environment. That capacity may be lost in schizophrenic patients. Therefore, one can also speak of a loss of conceptual boundaries in schizophrenia. This disorder can affect cognitive processes such as thinking. If a schizophrenic patient is unable to delimit conceptual boundaries among words, thoughts, or ideas with different meanings, then meaningless word constructs (neologisms) or disorganized speech are the typical phenomenological manifestations, called "thought disorder".

From an ontological point of view, delusions are the consequence of the loss of boundaries between the self and the others (nonselves). Here, the self is defined as a living system capable of self-observation. One could also say that our brain embodies a distinct ontological locus of self-observation. Everything taking place in the brains of schizophrenic patients is reality because they cannot differentiate between their inner world and the outer world. Therefore, they cannot see ontological differences between the selves and the nonselves. This loss of ontological boundaries may lead to a delusional misinterpretation of reality.

Hallucinations may be caused by the same disorder. However, the perception systems are phenomenologically affected. A schizophrenic who hears the voice of a person in his head is absolutely convinced that this person is really speaking to him. The loss of ontological boundaries or inner/outer confusion shows its phenomenological manifestation in the auditory system. Such a disorder can also occur in other sensory systems. The loss of the glial boundary-setting function may also be responsible for motoric and emotional symptoms in

schizophrenia as catatonia and affective flattening. Importantly, Kondziella *et al* [39] argued that astrocytes are important in controlling glutamate homeostasis and it is therefore necessary to assign a significant role to glial-neuronal interactions in the pathophysiology of schizophrenia. Moreover, there is extensive evidence suggesting glial impairment in the cerebral cortex of patients with schizophrenia [40].

Patients with schizophrenia have trouble distinguishing between expressions of emotions in the faces of people. Researchers' working hypothesis is that the brain of these patients cannot focus on a stimulus because they are unable to inhibit or gate irrelevant material [41]. This means that a schizophrenic brain has lost the capability to reject irrelevant information. The crucial function of rejection in undisturbed perception is described in Section 3.

4.3. Defective Switching Mechanism Caused by Decomposed Oligodendrocyte-Axonic Relations Leads to Incoherence of Information Processing

The processes of oligodendrocytes that envelop axons via myelin sheaths tie axons together in groups according to a combinational rule [42]. Axons conduct informations of various properties. These axonal properties are classified into categories by the processes of oligodendrocytes. By means of this mechanism the undisturbed brain is capable to compose informational qualities and can construct meaning from the many details of information. In the case of a decrease or loss of oligodendrocytes and their myelin sheaths (demyelination), the oligodendrocyte-axonic system decomposes so that it is incapable of generating categories of information. This incoherence may be responsible for symptoms of disorganization in schizophrenia like thought disorder, inappropriate affect and incommunicable motor behavior.

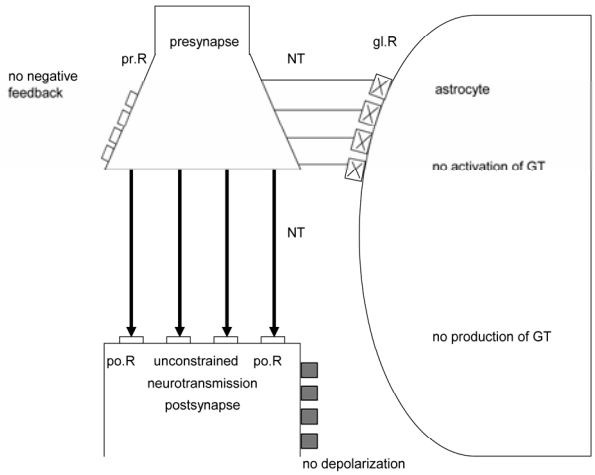

Non-functional glial receptors (glR), depicted by crosses, cannot be occupied by neurotransmitters (NT). Since the activation and production of gliotransmitters (GT) is not possible, glia do not negatively feed back to the presynaptic receptors (prR) and cannot depolarize the postsynaptic neuron. This severe synaptic disturbance leads to an unconstrained neurotransmission (fat arrows).

Figure 8. Unconstrained neurotransmission in tripartite synapses may cause schizophrenia.

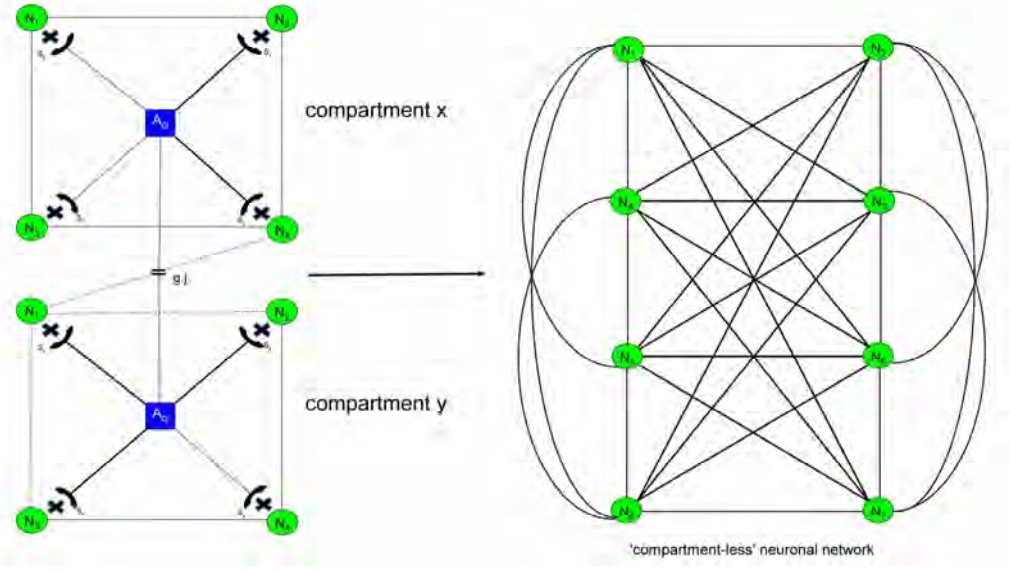

Two astrocytes ($Ac_{i,j}$) each form a compartment (x, y) via their synaptic processes (S_y) with four neurons (N_1-N_4). Since the astrocytic receptors are non-functional (crosses), synaptic information processing is unconstrained leading to a compartment-less neuronal network.

Figure 9. Loss of glial boundary-setting function. Generalization of neuronal information processing.

The research criteria for alternative dimensional descriptors for schizophrenia [43] differentiate between a psychotic (hallucinations, delusions) dimension, a disorganized dimension and a negative (deficit) dimension of schizophrenia. The disorganized dimension describes the degree to which disorganized speech, disorganized behaviour or inappropriate affect have been present. This kind of schizophrenic symptomatology can be deduced from the incoherence of brain functions that may be caused by decomposed oligodendrocyte-axonic relations.

Thought disorder is the main symptom of cognitive disorganization. This appears in incoherent words, termed neologisms, and in incoherent sentences (word salad) [44]. These symptoms of incoherence may be caused by decomposed oligodendrocyte-axonic relations, if the cognitive systems are affected. However, one may argue that multiple sclerosis is also based on a demyelinating disorder of the brain where oligodendroglia is decreased or lost, comparable to the mechanism that is hypothesized for symptoms of incoherence in schizophrenia. In addition, patients with multiple sclerosis show not only the typical motoric symptoms, but can also suffer from cognitive impairments, affective disorders, and even psychotic symptoms [45]. First of all, although the pathophysiology of schizophrenia is as yet unknown, there is a consensus that the core symptoms (delusions and hallucinations) of schizophrenia may be basically caused by a disorder in the synaptic information processing, so that the astrocyte-neuronal interaction in tripartite synapses must primarily be disordered, which is not the case in multiple sclerosis. In line with this argumentation all macroglial cells (astrocytes and oligodendrocytes) with their syncytia must be considered in their interaction with the neuronal system with regard to research of the pathophysiology of schizophrenia. Therefore, abnormalities of white matter in brains with schizophrenia may be mainly responsible for symptoms of incoherence and not for the whole schizophrenic syndrome.

Structural magnetic resonance imaging research suggests that schizophrenia is associated with grey matter reductions in a network of frontal, temporal, limbic, thalamic, and striatal areas [46]. In addition, abnormalities of cerebral white matter, oligodendrocytes and myelin have been observed in schizophrenia with in-vivo imaging and post-mortem biochemistry [47]. White matter abnormalities are also frequently associated with cognitive impairment in both healthy and diseased individuals, and cognitive dysfunction is an important component of schizophrenia [48,49].

Although the neurobiological origins of the abnormalities in white matter of brains with schizophrenia are unclear, gene studies involved in the maintenance of white matter structures may be particularly fruitful in schizophrenia. Recently, data gathered in a number of model systems indicated that axonal RNAs are synthesized in the surrounding glial cells. Experiments on the perfused squid giant axon have definitely proven that axoplasmic RNAs are transcribed on periaxonal glia. Their delivery to the axon occurs by a modulatory mechanism based on the release of neurotransmitters from the stimulated axon and on their binding to glial receptors [20,50].

5. FUTURE PROSPECTS

Since the computer system for simulation of human perception is implementable in a robot brain [8], an alternative approach to experimental biological brain research is available. Moreover, the underlying brain model is based on the structures and functions of both the neuronal and the glial system. The latter may generate intentional or phase programs that characterize subjective systems. Therefore, a robot brain endowed with intentions may show features of subjectivity in its behaviour. Importantly, the perception mechanism proposed does not primarily work as a pattern-recognition system but as a pattern-generation system.

What the so-called mental disorders concerns, we can also implement these disorders in a robot brain as described for schizophrenia. Then the robot could teach us what we know about these disorders, what we should further investigate and what probably remains unknown. The hypothesis that the schizophrenic syndrome may essentially be caused by non-functional astrocytic receptors is experimentally testable. Since the splicing code has recently been deciphered [51], the hypothesis that non-functional, truncated astrocytic receptors are caused by a non-splicing of introns can be investigated at least in post-mortem brains with schizophrenia. Should these non-functional receptors be identified, the substitution of proteins identical with astrocytic receptor types could represent a novel therapeutic approach to the schizophrenic syndrome.

REFERENCES

[1] Rosenblatt, F. (1962) Principles of neurodynamics: Perception and the theory of brain mechanisms. *Spartan Books*, Washington, D. C.

[2] Nolfi, S. and Floreano, D. (2000) Evolutionary robotics. *The Biology, Intelligence, and Technology of Self-Organizing Machines*, MIT Press, Cambridge.

[3] Sarhan, A.M. (2009) Iris recognition using discrete cosine transform and artificial neural networks. *Journal of Computer Science*, **5(5)**, 369-373.

[4] Mitterauer, B., Leitgeb, H. and Reitboeck, H.J. (1996) The neuro-glial synchronization hypothesis. *Recent Research Developments in Biological Cybernetics*, **1(1)**, 137-155.
[5] Mitterauer, B. (1998) An interdisciplinary approach towards a theory of consciousness. *Bio-systems*, **45(1**), 99-121.
[6] Mitterauer, B. (2000) Some principles for conscious robots. *Journal of Intelligent Systems*, **10(1)**, 27-56.
[7] Mitterauer, B. (2001) Clocked perception system. *Journal of Intelligent Systems*, **11(4)**, 269-298.
[8] Mitterauer, B. (2004) Computer system, particularly for simulation of human perception via sense organs. *United States Patent*, **6**, 697, 789B2.
[9] Kettenmann, H. and Ransom, B.R. (2005) Neuroglia. Oxford University Press, Oxford.
[10] . Halassa, M.M and Haydon, P.G. (2010) Integrated brain circuits: Astrocytic networks modulate neuronal activity and behaviour. *Annual Review of Physiology*, **72**, 335-355.
[11] Halassa, M.M., Fellin, T., Takano, H., Dong, J. and Haydon, P.G. (2007) Synaptic islands defined by the territory of a single astrocyte. *The Journal of Neuroscience*, **27(24)**, 6473-6477.
[12] Newman, E.A. (2005) Glia and synaptic transmission. In: H. Kettenmann and B. R. Ransom, Eds., *Neuroglia*, Oxford University Press, Oxford, 355-366.
[13] Haydon, P.G. and Carmignoto, G. (2006) Astrocyte control of synaptic transmission and neurovascular coupling. *Physiological Review*, **86(3)**, 1009-1031.
[14] Newman, E.A. and Zahs, K.R. (1997) Calcium waves in retinal glial cells. *Science*, **275(5301)**, 844-846.
[15] Mitterauer, B., Garvin, A.M. and Dirnhofer, R. (2000) The sudden infant death syndrome: A neuro-molecular hypothesis. *Neuroscientist*, **6(3)**, 154-158.
[16] Parri, H.R., Gould, T.M and Crunelli, V. (2001) Spontanous astrocytic Ca^{2+} oscillations in situ drive NMDAR-mediated neuronal excitation. *Nature Neuroscience*, **4(8)**, 803-812.
[17] Winship, I.R., Plaa, N. and Murphy, T.H. (2007) Rapid astrocyte calcium signals correlate with neuronal activity and onset of the hemodynamic response in vivo. *The Journal of Neuroscience*, **27(23**), 6268-6272.
[18] Mitterauer, B. (2010) Possible Role of Astrocytes in the Sudden Death Infant Syndrome. *Artificial Ingenuity*, http://www.artificialingenuity.com/BB/viewtopic.php?t=102
[19] Rash, J.E. (2010) Molecular disruptions of the panglial syncytium block potassium siphoning and axonal saltatory conduction: Pertinence to neuromyelitis optica and other demyelinating diseases of the central nervous system. *Neuroscience*, **168(4**), 982-1008.
[20] DeFelipe, J., Fields, R.D., Hof, P.R., Höstad, M., Kostovic, I., Meyer, G. and Rockland, K.S. (2010) Cortical white matter: Beyond the pale remarks, main conclusions and discussion. *Frontiers in Neuroanatomy*, **3(3)**.
[21] Fields, R.D. (2009) The other brain. Simon and Schuster, New York.
[22] Mitterauer, B. (2007) Where and how could intentional programs be generated in the brain? A hypothetical model based on glial-neuronal interactions. *BioSystems*, **88(3)**, 101-112.
[23] Guenther, G. (1980) Martin Heidegger und die Weltgeschichte des nichts. In: G. Guenther, Ed., *Beiträge zur Grundlegung einer operationsfähigen Dialektik*, Meiner, Hamburg, 260-296.
[24] Thomas, G.G. (1982) On Permutographs. *Supplemente ai Rendiconti del Circulo Matematico di Palermo*, **2(2)**, 275-286.
[25] Mitterauer, B. (1988) Computer system for simulating reticular formation operation. *United States Patent*, **4**, 783, 741.
[26] Thomas, G.G. and Mitterauer, B. (1989) Computer for simulating complex processes. *United States Patent*, **4**, 829, 451.
[27] Baumann, N. and Dinh, D.P. (2001) Biology of oligodendrocyte and myelin in the mammalian central nervous system. *Physiological Reviews*, **81(2**), 871-927.
[28] Giaume, C. and Theis, M. (2009) Pharmacological and genetic approaches to study connexin-mediated channels in glial cells of the central nervous system. *Brain Research Reviews*, doi:10.1016/ j.brainresrev.2009.11.005.
[29] Theis, M., Söhl, G., Elberger, J. and Willecke, K. (2005) Emerging complexities in identity and function of glial connexins. *Trends in Neurosciences*, **28(4)**, 188-195.
[30] Perea, G. and Araque, A. (2005) Glial calcium signalling and neuron-glia communication. *Cell Calcium*, **38(3-4)**, 375-382.
[31] Hebb, D.O. (1949) The organization of behaviour. Wiley, New York.
[32] Rambidi, N.G. and Yakovenchuk, D. (2001) Chemical reaction-diffusion implementation of finding the shortest paths in a labyrinth. *Physical Reviews*, E63.026607.
[33] Dean, B., Boer, S., Gibbons, A., Money, T. and Scarr, E. (2009) Recent advances in post-mortem pathology and neurochemistry in schizophrenia. *Current Opinion in Psychiatry*, **22(2)**, 154-160.
[34] Mitterauer, B. (2009) Loss of function of glial gap junctions may cause severe cognitive impairments in schizophrenia. *Medical Hypotheses*, **73(7)**, 393-397.
[35] Mitterauer, B. (2010) Synaptic imbalances in endogenous psychoses. *Bio-systems*, **100(1)**, 113-121.
[36] Mitterauer, B. (2003) The loss of self-boundaries: Towards a neuromolecular theory of schizophrenia. *Bio-systems*, **72(2)**, 209-215.
[37] Mitterauer, B. and Kopp, C. (2003) The self-composing brain: Towards a glial-neuronal brain theory. *Brain and Cognition*, **51(4)**, 357-367.
[38] Rall, W. (1995) Theoretical significance of dendritic trees for neuronal input-output relations. In: I. Segev, J. Rinzel, G.M. Shephard, Eds., *The Theoretical Foundation of Dendrite Function*, MIT Press, Cambridge, 122-146.
[39] Kondziella, D., Brenner, E., Eyjolfsson, E.M. and Sonnewald, U. (2007) How do glial-neuronal interactions fit into current neurotransmitter hypotheses of schizophrenia. *Neurochemistry International*, **50(3)**, 291-301.
[40] Rametti, G., Jungue, C., Falcon, C., Bargalló, N., Catalán, R., Penadés, R., Garzon, B. and Bernado, M. (2009) A voxel-based diffusion tensor imaging study of temporal white matter in patients with schizophrenia. *Psychiatry Research*, **171(3)**, 166-176.
[41] Holden, C. (2003) Deconstructing schizophrenia. *Science*, **299**, 333-335.
[42] Thomas, G.G. (1985) Introduction to kenogrammatics.

Proceedings of the 13th Winter School on Abstract Analysis, section of Topology, *Rendiconti del Circolo Matematico di Palermo*, **2(11)**, 113-123.

[43] Diagnostic and statistical manual of mental disorders. American Psychiatric Association, Washington, D. C., 1998.

[44] Frith, C.D. (1999) The cognitive neuropsychology of schizophrenia. Psychology Press, Sussex.

[45] Beatty, W.W. (1993) Cognitive and emotional disturbances in multiple sclerosis. *Neurologic Clinics*, **11(1)**, 189-204.

[46] Fornito, A., Yűcel, M. and Pantelis, C. (2009) Reconciling neuroimaging and neuropathological findings in schizophrenia and bipolar disorder. *Current Opinion in Psychiatry*, **22(3)**, 312-319.

[47] Kubicki, M., McCarley, R.W. and Shenton, M.E. (2005) Evidence for white matter abnormalities in schizophrenia. *Current Opinion in Psychiatry*, **18(2)**, 121- 134.

[48] Dwork, A.J., Mancevski, B. and Rosoklija, G. (2007) White matter and cognitive function in schizophrenia. *International Journal of Neuropsychopharmacology*, **10(4)**, 513-536.

[49] Wolf, R.C., Höse, A., Frasch, K., Walter, H. and Vasic, N. (2008) Volumetric abnormalities with cognitive deficits in patients with schizophrenia. *European Psychiatry*, **23 (8)**, 541-548.

[50] Giuditta, A., Chun, J.I., Eyman, M., Cefaliello, C., Bruno, A.P. and Crispino, M. (2008) Local gene expression in axons and nerve endings: The glia-neuron unit. *Physiological Reviews*, **88(5)**, 515-555.

[51] Barash, Y., Calarco, J.A., Gao, W., Pan, Q., Wang, X., Shai, O., Blencowe, B.J. and Frey, B.J. (2010) Deciphering the splicing code. *Nature*, **465(6)**, 53-59.

J. Biomedical Science and Engineering, 2010, 3, 978-986 **JBiSE**
doi:10.4236/jbise.2010.310128 Published Online October 2010 (http://www.SciRP.org/journal/jbise/).

Global pattern of pairwise relationship in genetic network

Ao Yuan, Qingqi Yue, Victor Apprey, George E. Bonney

National Human Genome Center, Howard University, Washington DC, USA.
Email: yuanao@hotmail.com; ayuan@howard.edu

Received 6 April 2010; revised 22 April 2010; accepted 10 May 2010.

ABSTRACT

In recent times genetic network analysis has been found to be useful in the study of gene-gene interactions, and the study of gene-gene correlations is a special analysis of the network. There are many methods for this goal. Most of the existing methods model the relationship between each gene and the set of genes under study. These methods work well in applications, but there are often issues such as non-uniqueness of solution and/or computational difficulties, and interpretation of results. Here we study this problem from a different point of view: given a measure of pair wise gene-gene relationship, we use the technique of pattern image restoration to infer the optimal network pair wise relationships. In this method, the solution always exists and is unique, and the results are easy to interpret in the global sense and are computationally simple. The regulatory relationships among the genes are inferred according to the principle that neighboring genes tend to share some common features. The network is updated iteratively until convergence, each iteration monotonously reduces entropy and variance of the network, so the limit network represents the clearest picture of the regulatory relationships among the genes provided by the data and recoverable by the model. The method is illustrated with a simulated data and applied to real data sets.

Keywords: Convergence, Gene-Gene relationship, Neighborhood, Pattern analysis, Relationship measure.

1. INTRODUCTION

A gene regulatory network (also called a GRN or genetic regulatory network) is a collection of DNA segments in a cell which interact with each other (indirectly through their RNA and protein expression products) and with other substances in the cell, thereby governing the rates at which genes in the network are transcribed into mRNA. From methodology point of view, genetic networks are models that, in a simplified way, describe some biological phenomenon from interactions between the genes. They provide a high-level view and disregard most details on how exactly one gene regulates the activity of another. The gene-gene pair wise relationships provide a special insight of the network and are of interest in the study.

Our work is closely related to that of genetic network analysis, and we first give a brief review of the methods. Some methods are deterministic, such as differential (difference) equation models [1-3], which may not be easy to solve nor have unique solutions. Since the genetic network is a complex system, any artificial model can only explain part of its mechanism; the unexplained parts are random noises, so we prefer a stochastic model. Existing stochastic methods for this problem including the linear models [4,5] or generalized linear models [6], the Bayesian network [7,8] *etc*. All these methods have their pros and cons, but have the common disadvantage that the solution may not be unique and the results are not easy to interpret. Also, when the network size exceeds that of the data, these methods break down. In genetic work the pair wise regulatory relationships among the genes are important. For such data, it is of interest to investigate the underlying patterns that may have biologic significance, in particular those arising from pair wises regulatory relationships among the genes. Here we study this problem from a different point of view. Given a measure of pair wise gene-gene relationship, we compute the measures from the data, and use the technique of pattern recognition and image restoration to infer the underlying network relationships. The pair wise regulatory relationships among the genes are inferred according to the principle that neighboring genes tend to share some common features, as neighboring genes tend to be co-regulated by some enhancers because of their close proximity [9]. In this method, the solution is unique and computationally simple, the results are easy to interpret and the network can be of any size. In the following we describe our method, study its

basic properties, and illustrate its application. This method is used to reveal the true relationships of structured high dimensional data array [10-12].

2. MATERIALS AND METHODS

The gene expression data are generally time dependent, as in Iyer *et al.* [14]. Let $X_{ij}(t)$ $(i=1,...,m; j=1,...,n; t=1,...k)$ be the observed gene expression response for subject *i*, gene *j* at time *t*. Denote $x_i(t)=(x_{i1}(t),...,x_{in}(t))'$ be the observations across all the genes for subject *i*, and we use $x(t)$ to denote a general sample of the $x_i(t)$'s. Often for this type of data, *m* and *k* are in the low tens, and *n* in the tens to thousands.

The commonly used differential equation model for genetic network analysis is a set of first order homogeneous differential equations with constant coefficients, in the simple case, has the form

$$\frac{dx(t)}{dt}=Wx(t),$$

where $W=(w_{ij})$ is the *n* × *n* matrix of unknown regulatory coefficients to be solved. This type of models and its more specific and complicated variations characterize well the dynamic of the network over time. The base solution of the above equation set is the matrix exponential $e^{tW}:=\sum_{r=0}^{\infty}t^rW^r/r!:=(v_1(t),...,v_n(t))'$, and the general solution of it has the form $x_i(t)=\sum_{j=1}^{n}c_jv_j(t)$ x_{i} (t), (*i* = 1,...,*m*), where the c_j's are constants to be determined by initial conditions from the data. So there are in total $n^2+n=n(n+1)$ coefficients, n^2 of them from *W* and *n* from the c_j's, to be determined from a total of *mnk* data points. When $mnk<n(n+1)$ these coefficients can not be determined; when $mnk\geq n(n+1)$ they may be uniquely or non-uniquely determined, or may still be not determined. For differential (difference) equation models more complicated than this, solutions are more difficult to get.

The commonly used stochastic model is the multivariate linear model

$$x_i(t+1)=Wx_i(t)+\varepsilon_i,\quad E(\varepsilon_i)=0,\quad (i=1,\ldots,m;\ t=1,\ldots,k\text{-}1)$$

where $\varepsilon=(\varepsilon_{i1},...,\varepsilon_{in})'$ is the random deviations unexplained by the model. Denote $X(t)=(x_{ij}(t))$, if $X'(t)X(t)$ is non-singular, the least-squares solution of the above model is $W=X'(t+1)X(t)(X'(t)X(t))^{-1}$, and it may have multiple solutions for different t. For $X'(t_r)X(t_r)$ to be non-singular, one must have $n\leq m$. Even for $n<m$, $X'(t_r)X(t_r)$ may not necessarily be non-singular. This puts an immediate restriction on the size of the network to be analyzed. Also, the solution of the above model may not be unique due to different time points.

For these reasons, we study the problem from a different point of view; by analyze the pair wise gene-gene relationships in the network. In the following we describe our model in which there is always an unique solution, the result is easy to interpret, and there is no restriction on the size of the network. Since the pattern in the genetic network is based on the principle of neighboring similarity, the order of the genes matters in the study, and generally we assume the genes are arranged in their chromosome order.

First we need a measurement for the relationship between any pair of genes, and the network can be represented by the matrix of the pair wise relationships. For large network, linear relationship is not adequate to use, as most of the coefficients will be very small. Also, as mentioned above, such model in this case has no solution because of the small sample size. Pearson's correlation is a good choice for this purpose, other choices including Kendal's tau and Spearman's rho, *etc*. Here we illustrate the method with Pearson's correlation, and our goal is to infer the triangular correlation matrix $R=(r_{ij})_{1\leq i<j\leq n}$ from the observed data, where r_{ij} is the Pearson's correlation coefficient between genes *i* and *j*. As usually the number m of individuals is small (sometimes as few as 2), estimate the correlations using the data at each time point alone is inadequate. So we use all the data to estimate them. An empirical initial version of these correlations are

$$r_{ij}^{(o)}=\frac{1}{mk}\sum_{r=1}^{m}\sum_{s=1}^{k}\frac{(x_{ri}(t)-x_i(t))(x_{sj}(t)-x_j(t))}{\sqrt{Var(x_i(t))Var(x_j(t))}},$$

$$((1\leq i<j\leq n)\qquad(1)$$

where $x_i(t)=\frac{1}{m}\sum_{r=1}^{n}x_{ri}(t)$,

$$Var(x_i(t))=\frac{1}{m}\sum_{r=1}^{n}(x_{ri}(t)-x_i(t))^2,\quad (i=1,...,n;\ s=1,...,k).$$

here the $x_{ri}(t)$'s are not i.i.d. over the time *t*'s, and the sample size *mk* is often not large, so the above empirical correlations are very crude evaluations of the true correlations r_{ij}'s. The initial table $R^{(0)}=(r_{ij}^{(0)}:1\leq i<j\leq n)$ is used as the raw data for the next step analysis. For each fixed *i* the observations $x_i(t)$ s at different time conditions reduced the common features in the data, this table is biased as an estimate of *R*. We need to restore their values according to the basic property of the genetic regulatory system. Many reports have shown that nearby genes tend to have similar expression profiles [13-16], thus nearby pairs of genes tend to have similar relationships, and their correlations tend to be close. This

is just the same principle as used in image restoration of data arrays of any size. In the following we use this technique to reduce the bias and improve the estimate of R based on the observation $R^{(0)}$.

Meloche and Zammar [10] considered a method for image restoration of binary data, here we adopt their idea and revise their method to gene expression analysis for continuous data. We assume the following model

$$r_{ij}^{(0)} = r_{ij} + \varepsilon_{ij}, \quad \varepsilon_{ij} \sim N(0,\sigma^2), (1 \le i < j \le n) \tag{2}$$

for some unknown $\sigma^2 > 0$, where the ε_{ij}'s represent the part of measurements unexplained by the true regulatory relationships in the model. Define the neighbor $R_{ij}^{(0)}$ of $r_{ij}^{(0)}$ to be the collection of the nine immediate members of $R_{ij}^{(0)}$ of $r_{ij}^{(0)} = \{ r_{ab}^{(0)} : |a-i| \le 1, |b-j| \le 1 \}$, which includes $r_{ij}^{(0)}$ itself at the center. For $r_{ij}^{(0)}$'s on the boundary of $R^{(0)}$ the definition is modified accordingly. For example, $R_{1,2}^{(0)}$ and $R_{n-1,n}^{(0)}$ has only three members, $R_{1,j}^{(0)}$ $(3 < j < n\text{-}1)$ has six members, *etc*. Larger neighbors of different shapes can also be considered; here we only illustrate using the above neighbor systems. We assume the $r_{ij}^{(0)}$'s only depend on their neighbors $R_{ij}^{(0)}$'s. The aim is to provide estimates $\hat{r}_{ij}$'s for the true r_{ij}'s based on the records $R^{(0)}$. We assume the estimates have the form for some function $h(\cdot)$ to be specified. The performance of the estimates will be measured by the average conditional mean squared error.

$$r_{ij} = h(R_{ij}^{(0)}), (1 \le i < j \le n), \tag{3}$$

$$\frac{2}{n(n-1)} \sum_{1 \le i < j \le n} E[(\hat{r}_{ij} - r_{ij})^2 \mid R^{(0)}] \tag{4}$$

The optimal set of estimates is the one which minimizes (4). Although r_{ij} is deterministic, we may view it as a realization of the random variable r_{IJ} with *(I, J)* uniformly distributed over the integer set $S = \{(i, j) : 1 \le i < j \le n\}$. So (4) can be rewritten as

$$EE_{IJ}[(\hat{r}_{IJ} - r_{IJ})^2 \mid R^{(0)}] = E[(\hat{r}_{IJ} - r_{IJ})^2 \mid R^{(0)}]$$
$$= E[(h(R^{(0)}) - r_{IJ})^2 \mid R^{(0)}]$$

Thus by (3), the minimizer of (4) is achieved by

$$\hat{r}_{IJ} := h^*(R_{IJ}^{(0)}) = E(r_{IJ} \mid R^{(0)}) = E(r_{IJ} \mid R_{IJ}^{(0)}), \text{ and so}$$
$$\hat{r}_{ij} = h^*(R_{ij}^{(0)}) = E(r_{IJ} \mid R^{(0)}).$$

To evaluate the above conditional expectation, we need a bit more preparation. Note σ^2 is estimated by

$$\hat{\sigma}^2 = \frac{2}{n(n-1)} \sum_{(i,j) \in S} (r_{ij}^{(0)} - \bar{r})^2, \quad \bar{r} = \frac{2}{n(n-1)} \sum_{(i,j) \in S} r_{ij}^{(0)}.$$

Denote $\varphi(t \mid \sigma^2)$ the normal density function with mean 0 and variance σ^2. Denote S_{ij} as the collection of indices for $R_{ij}^{(0)}$. Given $R_{ij}^{(0)}$, for $(I, J) \in S_{ij}$, view $r_{IJ}^{(0)}$ as a random vector over indices *(I,J)*. We define the conditional distribution of $r_{IJ}^{(0)}$ as

$$P(r_{IJ}^{(0)} = r_{uv}^{(0)} \mid R_{ij}^{(0)}) = \frac{\{\#member \ldots in \ldots R_{ij}^{(0)} = r_{uv}^{(0)}\}}{|S_{ij}|} = \frac{1}{|S_{ij}|}$$

In the above we used the fact that the $r_{uv}^{(0)}$ are continuous random variables, so the collection {members in $R_{ij}^{(0)} = r_{uv}^{(0)}$} = {$r_{uv}^{(0)}$} almost surely. The corresponding conditional probability is defined as

$$P((I, J) = (u, v) \mid R_{ij}^{(0)}) = \frac{\varphi(r_{uv}^{(0)} - r_{ij}^{(0)} \mid \sigma^2) P(r_{uv}^{(0)} \mid R_{ij}^{(0)})}{\sum_{(u,v) \in S_{ij}} \varphi(r_{uv}^{(0)} - r_{ij}^{(0)} \mid \sigma^2) P(r_{uv}^{(0)} \mid R_{ij}^{(0)})}, (u,v) \in S_{ij}$$

By (2), we deduce $E(r_{IJ} \mid R_{IJ}^{(0)}, (I, J) = (u, v)) = r_{uv}^{(0)}$, so we have

$$\hat{r}_{ij} = E(r_{IJ} \mid R_{ij}^{(0)}) = \sum_{(u,v) \in S_{ij}} E(r_{IJ} \mid R_{ij}^{(0)}, (I, J) = (u, v)) P((I, J) = (u, v) \mid R_{ij}^{(0)})$$
$$= \frac{\sum_{(u,v) \in S_{ij}} r_{uv}^{(0)} \varphi(r_{uv}^{(0)} - r_{ij}^{(0)} \mid \sigma^2) P(r_{uv}^{(0)} \mid R_{ij}^{(0)})}{\sum_{(u,v) \in S_{ij}} \varphi(r_{uv}^{(0)} - r_{ij}^{(0)} \mid \sigma^2) P(r_{uv}^{(0)} \mid R_{ij}^{(0)})}$$
$$= \frac{\sum_{(u,v) \in S_{ij}} r_{uv}^{(0)} \varphi(r_{uv}^{(0)} - r_{ij}^{(0)} \mid \sigma^2)}{\sum_{(u,v) \in S_{ij}} \varphi(r_{uv}^{(0)} - r_{ij}^{(0)} \mid \sigma^2)} \approx \frac{\sum_{(u,v) \in S_{ij}} r_{uv}^{(0)} \varphi(r_{uv}^{(0)} - r_{ij}^{(0)} \mid \hat{\sigma}^2)}{\sum_{(u,v) \in S_{ij}} \varphi(r_{uv}^{(0)} - r_{ij}^{(0)} \mid \hat{\sigma}^2)},$$
$$(i, j) \in S_{ij} \tag{5}$$

The matrix $\hat{R} = (\hat{r}_{ij})$ is our one-step restored estimate of the genetic correlation network R, we also denote it by $R = R^{(1)} = (r_{ij}^{(1)})$.

Denote $F(\cdot)$ the operator given in (5), as $r_{ij}^{(1)} = F(R_{ij}^{(1)})$, and denote $r_{ij}^{(1)} = F(R_{ij}^{(1)})$ $R^{(1)} = F(R^{(0)}) = E(R \mid R^{(0)})$. We view $F(\cdot)$ as a filter for the noises, so $R^{(1)}$ is a smoothed version of $R^{(0)}$. Let $R = r_{IJ}$ be the random variable of the r_{ij}'s over the random index *(I,J)* and the variation of possible values of the r_{ij}'s, with density $p(\cdot)$, its uncertainty can be characterized by variance and entropy, which is defined as

$$H(p) = -E[\log p(R)] = -\int p(r) \log p(r) dr.$$

It is maximized or most uncertain when R is uniformly distributed, and has smaller value when the distribution of r is more certain. It has some relationship with variance. The former depends on more innate features, such as moments, of the distribution than the latter, which only measures the disparity from the mean. When

$p(\cdot)$ is a normal density with variance σ^2, then $H(p)=1+\sqrt{2\pi\sigma^2}$. For many commonly used parametric distributions, entropy and variance agree with each other, *i.e.* an increase in one of them implies so for the other. But this is not always true and a general closed form relationship between variance and entropy does not exists. Variance is more popular in practice because of its simplicity.

Although generally, in the image restoration context, R is estimated by just applying F once, a natural question is what will happen if we use the operator F repeatedly? *i.e.* let $R^{(k+1)}=(r_{ij}^{(k+1)})=F(R^{(k)})=E(R\mid R^{(k)})$ for $k\geq 0$. To investigate this question, we impose the model

$$r_{ij}^{(k)}=r_{ij}+\varepsilon^{(k)}{}_{ij},\quad \varepsilon^{(k)}{}_{ij}\ \sim\ N(0,\sigma^{2(k)}),\ (1\leq i<j\leq n) \tag{6}$$

The estimators $r_{ij}^{(k)}$'s are obtained by minimizing

$$\frac{2}{n(n-1)}\sum_{1\leq i<j\leq n}E[(\hat{r}_{ij}-r_{ij})^2\mid R^{(k)}]$$

and are given by

$$r_{ij}^{(k)}=E(r_{IJ}\mid R_{ij}^{(k)}).$$

similarly $\sigma^{2(k)}$ is estimated by

$$\hat{\sigma}^{2(k)}=\frac{2}{n(n-1)}\sum_{(i,j)\in S}(r_{ij}^{(k)}-\bar{r}^{(k)})^2,$$

$$\bar{r}^{(k)}=\frac{2}{n(n-1)}\sum_{(i,j)\in S}r_{ij}^{(k)}.$$

Since n is usually large, $\hat{\sigma}^{2(k)}$ is a good estimator of $\sigma^{2(k)}$. Corresponding to (5), we have

$$r_{ij}^{(k+1)}=E(r_{IJ}^{(k)}\mid R_{ij}^{(k)})=$$

$$\frac{\sum_{(u,v)\in S_{ij}}r_{uv}^{(k)}\varphi(r_{uv}^{(0)}-r_{ij}^{(0)}\mid\sigma^2)}{\sum_{(u,v)\in S_{ij}}\varphi(r_{uv}^{(0)}-r_{ij}^{(0)}\mid\sigma^2)},\ (i,j)\in S_{ij},\ k\geq 1 \tag{8}$$

$$\approx\frac{\sum_{(u,v)\in S_{ij}}r_{uv}^{(k)}\varphi(r_{uv}^{(0)}-r_{ij}^{(0)}\mid\hat{\sigma}^{2(k)})}{\sum_{(u,v)\in S_{ij}}\varphi(r_{uv}^{(0)}-r_{ij}^{(0)}\mid\hat{\sigma}^{2(k)})}$$

In the above we do not replace the $r_{ij}^{(0)}$'s by the $r_{ij}^{(k)}$'s in $\varphi(\cdot\mid\cdot)$ but with $\sigma^{2(0)}$ replaced by the step k estimator $\sigma^{2(k)}$, only for the reason of simplicity in the proof of the Proposition below. Finally, $\sigma^{2(k)}$ is replaced by $\hat{\sigma}^{2(k)}$ in actual computation.

Although few density functions are convex, many of them are log-convex. For example, the normal, exponential (in fact any quadratic exponential families), Gamma, Beta, chisquare, triangle, uniform distributions. But some are not, such as the T and Cauchy distributions. Condition A) does not require all the $p^{(k)}(\cdot)$'s to belong to the same parametric family, nor even to be parametric. Condition B) is satisfied for almost all parametric families as few parametric families require more than the first two moments to determine. The only restriction we make is that all the $p^{(k)}(\cdot)$'s belong to the same parametric family.

View $r^{(k)}$ as a random realization of the $r_{ij}^{(k)}$'s and as of $R^{(0)}$, let $p^{(k)}(\cdot)$ be the density function of $r^{(k)}$. To study the property of the algorithm, we say a non-negative function $f(\cdot)$ is log-convex if $\log f(\cdot)$ is convex, and assume the following conditions

A) $p^{(k)}(\cdot)$ is log-convex for all k.

B) All the $p^{(k)}(\cdot)$'s belong to a parametric family which is determined by the fist two moments.

Our algorithm has the following desirable property (see Appendix for the proof)

Proposition. 1) Assume either A) or B), then

$$H(p^{(k+1)})\leq H(p^{(k)}),\quad k\geq 0.$$

2) $\sigma^{2(k+1)}\leq\sigma^{2(k)}$, $k\geq 0$.

3) As $k\to\infty$, the table $R^{(k)}$ converges in the component wise sense:

$$R^{(k)}\longrightarrow R^*$$

for some stationary array $R^*=R^*(R^{(0)},F)$.

This Proposition tells us that, if the assumption of neighboring similarity is valid for $R^{(0)}$, then the estimates $R^{(k)}$ become more and more clear (less entropy), and more and more accurate as an estimator of R (less variance). So $R^{(*)}$ is the sharpest picture the data $R^{(0)}$ provide and can be restored by the filter F, the innate regulatory relationships among the genes can be recovered by filter F and provided by the data $R^{(0)}$ under the ideal situation of no noise. Intuitively, this picture has some close relationship with the haplotype block structures.

As of small sample size (mk) and large number ($n(n-1)/2$) of parameters, there is no way of talking about the consistency of R to R. So in general $R^{(*)}$ and R may not equal, however our algorithm enable us to do the best effort we can. Convergence of $R^{(k)}$ can be accessed by the distance criteria: for a given > 0 (usually =1/100 or 1/1000)

$$d_1(R^{(k+1)},R^{(k)})=\frac{2}{n(n+1)}\sum_{i<j}|\,r_{ij}^{(k+1)}-r_{ii}^{(k)}\,|\leq\varepsilon$$

or

$$d_2(R^{(k+1)},R^{(k)})=\frac{2}{n(n+1)}\Big(\sum_{i<j}(r_{ij}^{(k+1)}-r_{ii}^{(k)})\Big)^{1/2}\leq\varepsilon.$$

Network at each time. We may also investigate the problem at each different time point t. In this case (1) is replaced by

$$r_{ij}^{(o)} = \frac{1}{m}\sum_{r=1}^{m} \frac{(x_{ri}(t)-x_i(t))(x_{rj}(t)-x_j(t))}{\sqrt{Var(x_i(t))Var(x_j(t))}}, (1 \le i < j \le n)$$

where, $x_i(t) = \frac{1}{m}\sum_{r=1}^{m} x_{ri}(t)$,

$Var(x_i(t)) = \frac{1}{m}\sum_{r=1}^{m}(x_{ri}(t)-x_i(t))^2$, ($i$ = 1,...,n; t = 1,...,k)

and $R^{(0)}(t) = (r_{ij}^{(0)}(t): 1 \le i < j \le n)$ be the corresponding initial table at each t, and the neighborhood for $r_{ij}^{(0)}(t)$ is $R_{ij}^{(0)}(t) = \{ r_{ab}^{(0)}: |a-i|\le 1, |b-j|\le 1\}$. In this case (6) is

$r_{ij}^{(k)}(t) = r_{ij}(t) + \varepsilon^{(k)}{}_{ij}(t)$, $\varepsilon^{(k)}{}_{ij}(t) \sim N(0, \sigma^{2(k)}(t))$, $(1 \le i < j \le n)$

and $\hat{r}_{ij}^{(k)}(t) = E(r_{IJ}^{(k)}(t) \mid R_{ij}^{(k)}(t))$.

let $\hat{\sigma}^{2(k)}(t) = \frac{2}{n(n-1)}\sum_{(i,j)\in S}(r_{ij}^{(k)}(t)-\bar{r}^{(k)}(t))^2$,

$\bar{r}^{(k)}(t) = \frac{2}{n(n-1)}\sum_{(i,j)\in S} r_{ij}^{(k)}(t)$.

(8) is now $r_{ij}^{(k+1)}(t) = E(r_{IJ}^{(k)}(t) \mid R_{ij}^{(k)}) =$

$$\frac{\sum_{(u,v)\in S_{ij}} r_{uv}^{(k)}(t)\varphi(r_{uv}^{(0)}(t)-r_{ij}^{(0)}(t) \mid \sigma^2)}{\sum_{(u,v)\in S_{ij}} \varphi(r_{uv}^{(0)}(t)-r_{ij}^{(0)}(t) \mid \sigma^2)}, (i,j) \in S_{ij},$$

$$\approx \frac{\sum_{(u,v)\in S_{ij}} r_{uv}^{(k)}(t)\varphi(r_{uv}^{(0)}(t)-r_{ij}^{(0)}(t) \mid \hat{\sigma}^{2(k)}(t))}{\sum_{(u,v)\in S_{ij}} \varphi(r_{uv}^{(0)}(t)-r_{ij}^{(0)}(t) \mid \hat{\sigma}^{2(k)}(t))}$$

$k \ge 1$

The matrix $R^{(k)}(t) = (r^{(k)}{}_{ij}(t))$ is the k-step restored estimate of the genetic correlation network $R(t) = (r_{ij}(t))$ at time t. The proposition is then hold for each fixed t.

3. SIMULATION STUDY

We simulate 40 genes over 12 time conditions at time (hour) points $(t_1,...,t_{12})$ = (1, 2, 3, 4, 5, 6, 7, 8, 9, 10, 11, 12) for 6 individuals by mimicking the setting of the data analyzed in Iyer *et al*. [17]. We simulate the genes from 6 clusters, the numbers of genes in each cluster are given by the vector $(n_1,...,n_6)$ = (8, 6, 4, 4, 6, 12). The baseline values of the gene expressions over time $t \in [0,12]$ in cluster k are generated by functions of the form

$h_k(t) = a_{k1}\sin(t) + a_{k2}\sin(t/2) + a_{k3}\sin(t/3)$, (k = 1,....,6).

Let $h(t)$ be the vector of length 40, with first n_1 components given by $h_1(t)$, second n_2 components by $h_2(t)$,...., last n_6 components by $h_6(t)$. Denote $a_k = (a_{k1}, a_{k2}, a_{k3})$. We arbitrarily choose the a_k's as a_1 = (0.54, –0.18, 1.23), a_2 = (–0.12, –0.25, 0.45), a_3 = (1.0, –0.55, –0.15), a_4 = (–0.32, –0.15, –0.65), a_5 = (0.15, 0.25, 0.35) and a_6 = (–0.52, –0.45, –0.55). First we need to simulate the r_{ij}'s with coordinated patterns. We divide the 40 genes into the 6 clusters, and assume independence among the clusters.

Then for given a covariance matrix $\Omega = \Omega_1 \oplus \cdots \oplus \Omega_6$ we generate the data using this Ω and the time conditions, where Ω_k is the covariance matrix for the genes in cluster k. Directly specifying a high dimensional positive matrix is not easy, we let each Ω_k has the structure $\Omega_k = Q'_k Q_k$, for some Q_k non-singular, so that Ω_k is positive definite. Note that the $Q'_k Q_k$'s may not be correlation matrices, but they are covariance matrices, so is Ω. Let Q_k be upper diagonal with dimension n_k. The non-zero elements of Q_1 are drawn from U(0.5,0.8); those for Q_2 from U(0.2,0.4); those for Q_3 from U(0.2,0.6), those for Q_4 from U(–0.3, –0.1); those for Q_5 from U(0.6,0.9); and those for Q_6 from U(–0.8, –0.6). Then let $\Omega^{1/2} = Q_1 \oplus \cdots \oplus Q_6$. The 6 individuals are i.i.d, so we only need to describe the simulation of observation $x_1 = \{x_{1j}(t): j = 1,...,40; t = 1,...,12\}$ of the first individual. Note for each fixed t, $x_1(t) = (x_{11}(t),..., x_{1,40}(t))$ has covariance matrix Ω. We first generate $y = (y_1,...y_{40})$ with the components i.i.d. N(0,1), then $x_1(t) = h(t) + \Omega^{1/2} y + \varepsilon(t)$ is the desired sample, where for each fixed t, $\varepsilon(t) = (\varepsilon_1(t),..., \varepsilon_{40}(t))$ is the noise, with the $\varepsilon_i(t)$'s i.i.d N(0,1) and independent over t. Convert the covariance matrix $\Omega = (\omega_{ij})$ to a correlation matrix $R = (r_{ij})$ as $r_{ij} = \omega_{ij}/\sqrt{\omega_{ii}\omega_{jj}}$ only for $i < j$. Using the data $X = (x_{ij}(t))$, we compute the $R^{(k)}$'s from (8) then use perspective plots to compare the restored correlations after convergence at step k, $R^{(k)}$, the one-step restored $R^{(1)}$, the initial estimated $R^{(0)}$ and the true simulated correlations R.

After computation, the algorithm meets the convergence criterion at iteration 14 with = 10^{-4}. The distances between the observed, first step estimate and last step estimate are: $d_1(R^{(0)}, R)$ = 0.125, $d_1(R^{(1)}, R)$ = 0.108 and $d_1(R^{(14)}, R)$ = 0.094. We see that the estimate after convergence is closest to the true correlations. The results are displayed in Figure 1 below. We only display the correlations r_{ij} for $j > i$. Those values for r_{ij} is 1's, and those for r_{ij} ($i > j$) are set to zero's, which can be obtained by symmetry.

From this figure we see that the correlations computed from the raw data, panel (b), are very noisy, the true pattern, panel (a), in the network is messed up. The one-step estimate, panel (c), gives some limited sense, while the final estimates, panel (d), recover the true picture with reasonably well. Considering the large number of 40(40+1)/2 = 820 parameters and the small number of 15 individuals on 40 genes, the last step estimates are quite a success. Large number of simulations yield similar results, the convergence criterion is met with 10 to 15 iterations.

Note we only used networks of 40 genes, as large networks are not easy to display graphically. The computations of a network with n genes is in the order $n(n\text{-}1)/2$, so there should be no computational problem for ordinary computer using this method to restore even the whole genome.

4. RESULTS

We use the proposed method to analyze the data with 30 microarray chips from the Stanford microarray database: http:// smd.stanford.edu/cgi-bin/search/QuerySetup.pl. The Category is Normal tissue and the subcategory is PBMC, the following 30 files are the Raw data in the database: 19430.xls, 19438.xls, 19439.xls, 19446.xls, 19447.xls, 19448.xls, 19449.xls, 19450.xls, 19451.xls, 19500.xls, 19505.xls, 19506.xls, 19507.xls, 21407.xls, 21408.xls, 21409.xls, 21410.xls, 21411.xls, 21412.xls, 21413.xls, 21414.xls, 21415.xls, 21416.xls, 21424.xls, 21425.xls, 21426.xls, 21427.xls, 21428.xls, 21429.xls, 21430.xls. The data we used are the overall intensity (mean), the 67th column in the 30 excel files. We choose three subsets of genes on the 30 arrays: set I is genes 0-49, set II is genes 1000-1049 and set III is genes 5000-5049 from the original data set. There are 80 variable for each array. We choose the intensity from normal people for our analysis. The initial correlation coefficients among the genes computed from the raw data in each set, and those estimated after convergence by our algorithm are shown in **Figures 2-4**. Clearly the initial

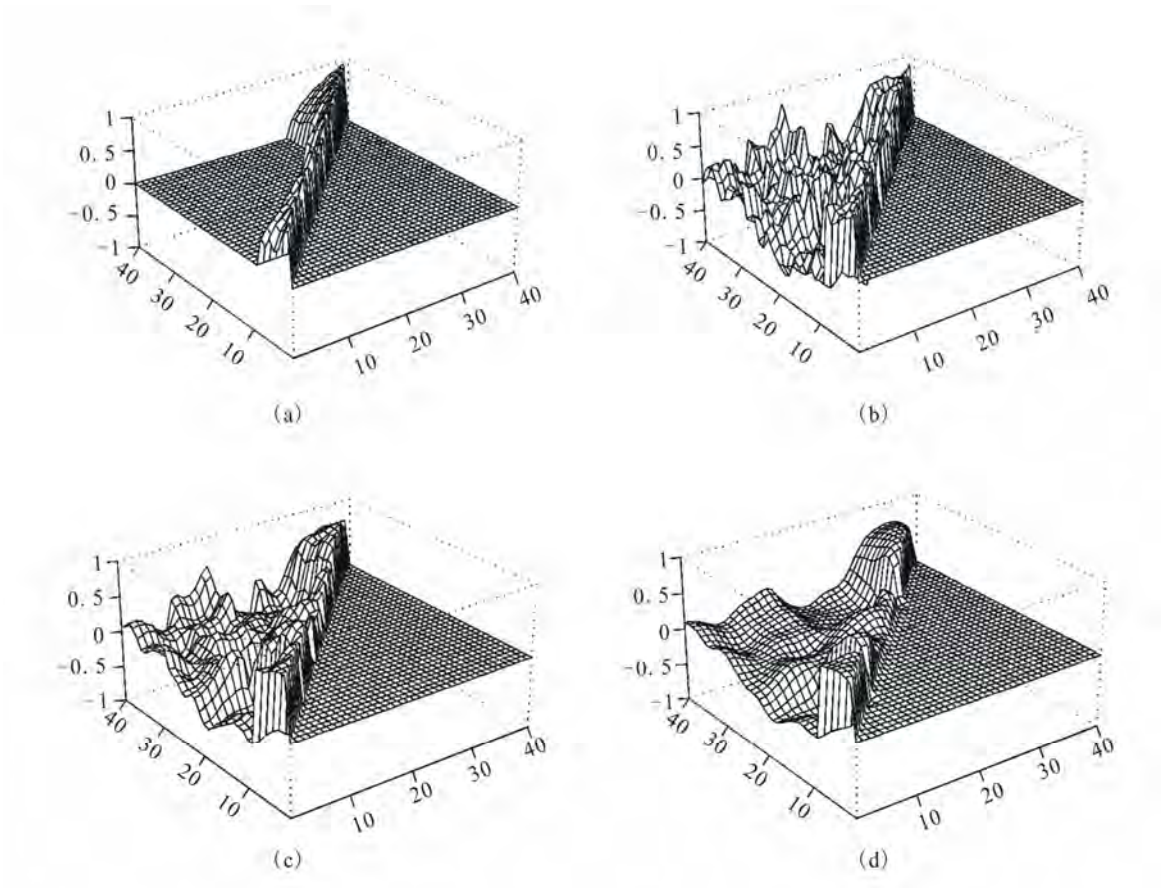

Figure 1. Network Correlations: (a). Simulated R , (b) Initial $R^{(0)}$, (c) One-step Restored $R^{(1)}$, (d) k-step Converged $R^{(k)}$

correlations are noisy and difficult to see any patterned relationships among the genes. In contrast, the restored pictures are quite clear. For set I, the coefficients are rather homogeneous with values around 0.5, but there is a clear boundary around gene 43, which suggests that most of the genes in this set have similar relationships, or functions. But gene 43 seems to have its own separate mechanism. Genes 38 and 29 also have weak relationships with the other genes. For set II, the relationships among the genes are not so homogeneous. The genes are moderately correlated with coefficients around 0.5, some genes around positions 10, 16, 24, 30, and 38 have weak interactions with the other genes. For set III, there is moderate coordinating pattern among the genes, but three genes, around positions 15, 29, and 40, appears to have relatively independent patterns of regulatory functioning.

5. CONCLUDING REMARKS

We considered a image restoration method for genetic network analysis. This method gives unique solution, the results are easy to interpret and computationally simple. We may implement the genetic distances among the genes into the updating system given in (8). The method is not confined to correlation coefficients among genes, other measures of gene-gene relationships can be considered analogously. Very large networks can be analyzed in principle, the only challenge is how to display the results. We found when the number of genes exceeds 50, the figure is difficult to distinguish visually. The computation for a network of size 40 takes about a couple of minutes using the Splus software. It will be much faster using the C program, and there should be no problem to analyze the whole genome by this method. The only requirement is that the data be arranged in their chromosomal order, otherwise the results may not easy to interpret.

The method can also be used for other analysis purposes and data types, such as cluster analysis. Cluster objects by pattern similarities, *etc*. It can be used to analyze qualitative data type such as haplotype analysis.

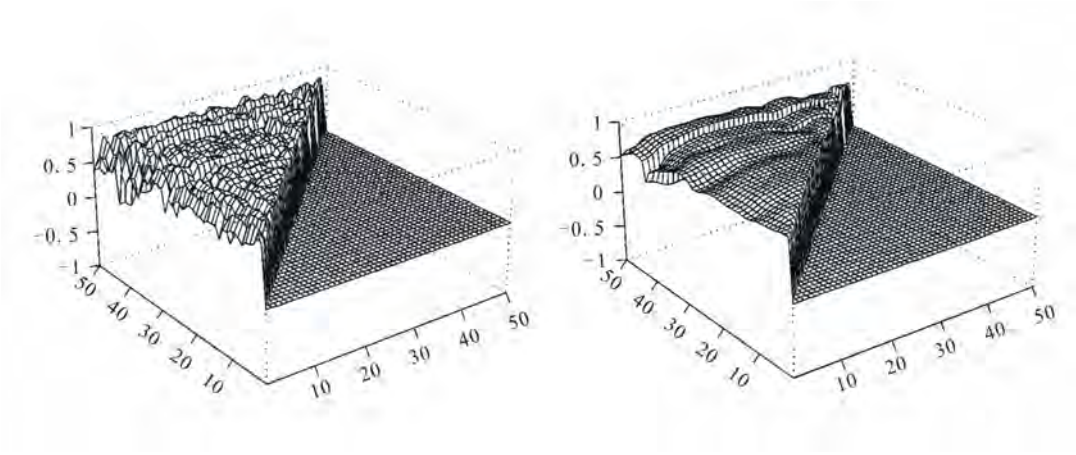

Figure 2. Real data I: initial (left panel) and restored (right panel) correlations.

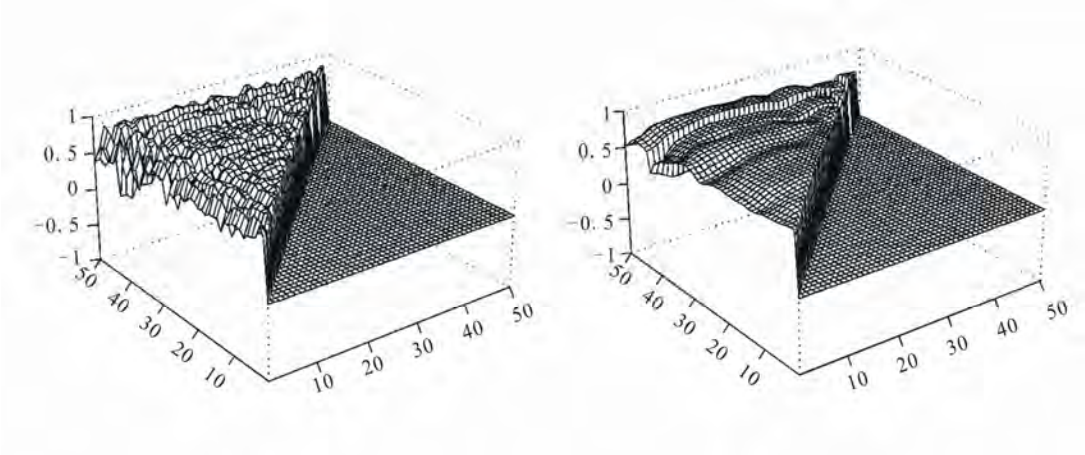

Figure 3. Real data II: initial (left panel) and restored (right panel) correlations.

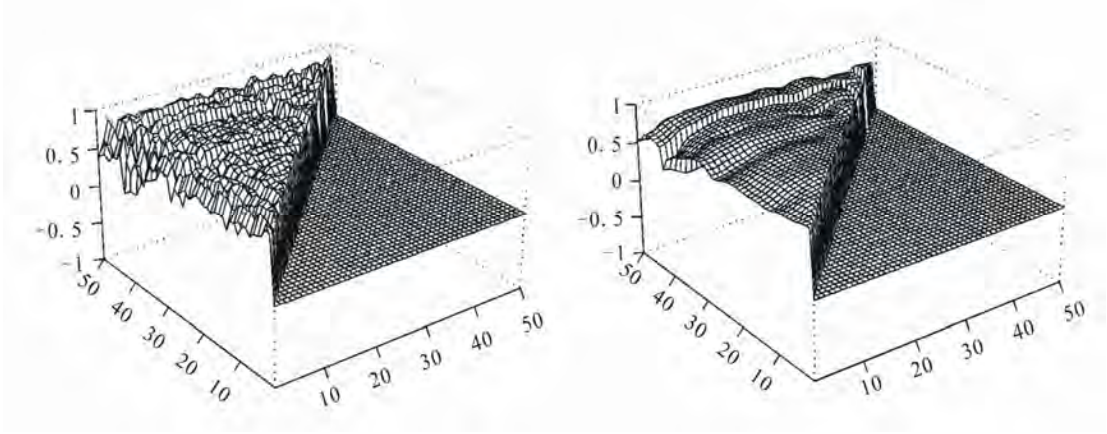

Figure 4. Real data III: initial (left panel) and restored (right panel) correlations.

6. ACKNOWLEDGEMENTS

The research has been supported in part by the National Center for Research Resources at NIH grant 2G12 RR003048.

REFERENCES

[1] Goodwin, B.C. (1965) Oscillatory behavior in enzymatic control processes. In Weber, G., Ed. *Advances in Enzyme Regulation*, Pergamon Press, Oxford, 425-438.

[2] Tyson, J.J. and Othmer, H.G. (1978) The dynamics of feedback cellular control circuits in biochemical pathways. *Progress in Biophysics*, Academic Press, New York, **(5)**, 1-62.

[3] Reinitz, J., Mjolsness, E. and Sharp, D.H. (1995) Model for cooperative control of positional information in Drosophila by bicoid and maternal hunchback. J*ournal of Experimental Zoology*, **271**, 47-56.

[4] Wessels, L.F.A., Van Someren, E.P. and Reinders, M.J.T. (2001) A comparison of genetic network models. *Pacific Symposium on Biocomputing*, **6**, 508-519.

[5] D'haeseleer, P., Liang, S. and Somogyi, R. (1999) Gene expression data analysis and modeling. Pacific Symposium on Biocomputating, Hawaii, USA.

[6] Savageau, M.A. (1976) Biochemical System Analysis: A Study of Function and Design in Molecular Biology. Addison-Wesley, Reading, Massachusetts.

[7] Friedman, N., Linial, M., Nachman, I. and Pe'er, D. (2000) Using Bayesian network to analyze expression data. *Journal of Computational Biology*, **7**, 601-620.

[8] Zhang, B.T. and Hwang, K.B. (2003) Bayesian network classifiers for gene expression analysis. In Berrar D.P., Dubitzky W. and Granzow M. Ed., *A Practical Approach to Microarray Data Analysis*, Kluwer Academic Publishers, Netherlands, 150-165.

[9] Chen, L. and Zhao, H. (2005) Gene expression analysis reveals that histone deacetylation sites may serve as partitions of chromatin gene expression domains. *BMC Genetics*, **6**, 44.

[10] Meloche, J. and Zammar, R. (1994) Binary-image restoration. *Canadian Journal of Statistics*, **22**, 335-355. -0.3cm \item Owen, A. (1984). A neighborhood based classifier for LANDSAT data. *Canadian Journal of Statistics*, **12**, 191-200.

[11] Ripley, B.D. (1986) Statistics, images, and pattern recognition. *Canadian Journal of Statistics*, **14**, 83-111.

[12] Besag, J. (1986) On the statistical analysis of dirty pictures. *Journal of the Royal Statistical Society*, **48**, 259-302.

[13] Cohen, B.A., Mitra, R.D., Hughes, J.D. and Church, G.M. (2000) A computational analysis of whole-genome expression data reveals chromosomal domains of gene expression. *Nature Genetics*, 26(2), 183-186.

[14] Caron, H., Schaik, B., Mee, M., Baas, F., Riggins, G., Sluis, P., Hermus, M.C., Asperen, R., Boon, K., Voute, P.A., *et al*. (2001) The human transcriptome map: clustering of highly expressed genes in chromosomal domains. *Science*, **291**, 1289-1292.

[15] Lercher, M.J., Urrutia, A.O. and Hurst, L.D. (2002) Clustering of housekeeping genes provides a unified model of gene order in the human genome. *Nature Genetics*, **31(2)**, 180-183.

[16] Spellman P.T., Rubin G.M. (2002) Evidence for large domains of similarly expressed genes in the Drosophila genome. *Journal of Biology*, **1(1)**, 5.

[17] Iyer, V.R., Eisen, M.B., Ross, D.T., Schuler, G., Moore, T., Lee, J.C., Trent, J.M., Staudt, L.M., Hudson J.J., Boguski, M.S., Lashkari, D., Shalon, D., Botstein, D. and Brown, P.O. (1999) The transcriptional program in the response of human fibroblast to serum. *Science*, **283**, 83-87.

[18] Ebrahimi, N., Maasoumi, E. and Soofi, E. (1999) Ordering univariate distributions by entropy and variance. *Journal of Econometrics*, **90**, 317-336.

[19] Bar, J.Z, Gerber, G., Gifford, D.K. (2007) Continuous representations of time series gene expression data. Manuscript.

[20] Someren, E.P., Wessels, L.F.A., Reinders, M.J.T. (2000) Linear modeling of genetic networks from experimental data. American Association for Artificial Intelligence. http://www.aaai.org

[21] Voit, E.O. (2000). Computational Analysis of Biochemical Systems, Cambridge University Press, Cambridge.

Appendix

Proof of the Proposition. Recall $r^{(k+1)} = r_{IJ}{}^{(k+1)} = r_{IJ}{}^{(k+1)}(R^{(k)})$ is random in (I,J) and $R^{(k)}$; for fixed $(I,J)=(i,j)$, $r_{ij}{}^{(k+1)} = r_{ji}{}^{(k+1)}(R^{(k)})$ is random in $R^{(k)}$; $r_{IJ}{}^{(k+1)} = r_{IJ}{}^{(k+1)}(R^{(k)} \mid R^{(0)})$ is random in (I,J) (discrete); also $r^{(k+1)} = E(r^{(k)} \mid R_{IJ}{}^{(k)}) = E[r_{UV}{}^{(k)} \mid R_{IJ}{}^{(k)}]$ for random index $(I,J) \in S$ and random index $(U,V) \in S_{IJ}$.

1) We first prove the result under condition A). We have

$$E\log p^{(k+1)}(r^{(k+1)}) - E\log p^{(k)}(r^{(k+1)})$$
$$= \int p^{(k+1)}(r)\log\frac{p^{(k+1)}(r)}{p^{(k)}(r)}dr = D(p^{(k+1)} \,||\, p^{(k)}) \geq 0,$$

which is the relative entropy between $p^{(k+1)}(\cdot)$ and $p^{(k)}(\cdot)$. It is known that $D(p^{(k+1)} \,||\, p^{(k)}) \geq 0$ with "=" if and only if $p^{(k+1)}(\cdot) = p^{(k)}(\cdot)$. Note log-convexity of $p^{(k)}(\cdot)$ imply, for each given $R_{IJ}{}^{(k)}$,

$$\log p^{(k)}(E[r^{(k)} \mid R_{IJ}{}^{(k)}]) \geq E[\log p^{(k)}(r^{(k)}) \mid R_{IJ}{}^{(k)}].$$

Thus by the above two inequalities we get

$$H(p^{(k+1)}) = -E\log p^{(k+1)}(r^{(k+1)}) \leq -E\log p^{(k)}(r^{(k+1)})$$
$$= -E\log p^{(k)}(E[r^{(k)} \mid R_{IJ}{}^{(k)}]) \leq E(E[\log p^{(k)}(r^{(k)} \mid R_{IJ}{}^{(k)}])$$
$$= -E\log p^{(k+1)}(r^{(k)}) = H(p^{(k)}).$$

Under condition B), the result in Ebrahimi *et al.* [18] states that entropy and variance agree each other. *i.e.* one increase/decrease implies the other. Now the conclusion is immediate from 2).

2) By the total variance formula, we have

$$\sigma^{(k)} = Var(r_{UV}{}^{(k)})$$
$$= E[Var(r_{UV}{}^{(k)} \mid R_{IJ}{}^{(k)})] + Var(E[r_{UV}{}^{(k)} \mid R_{IJ}{}^{(k)}])$$
$$= E[Var(r_{UV}{}^{(k)} \mid R_{IJ}{}^{(k)})] + Var(r_{IJ}{}^{(k)})$$
$$= E[Var(r_{UV}{}^{(k)} \mid R_{IJ}{}^{(k)})] + \sigma^{(k+1)} \geq \sigma^{(k+1)},$$
$$(k = 0,1,2,\ldots). =$$

3) We only need to prove the convergence of the component $r_{ij}{}^{(k)}$ for any fixed (i,j). In fact from (8), for any integer m and k we have

$$r_{ij}{}^{(k+m)} = \frac{\sum_{(u,v)\in S_{ij}} r_{uv}{}^{(k-1+m)}\varphi(r_{uv}^{(0)} - r_{ij}^{(0)} \mid \sigma^{2(k-1+m)})}{\sum_{(u,v)\in S_{ij}} \varphi(r_{uv}^{(0)} - r_{ij}^{(0)} \mid \sigma^{2(k-1+m)})} :,$$
$$= F(R_{ij}{}^{(k-1+m)})$$

$(i,j) \in S$, $k,m = 0,1,2\ldots$

Since $\sigma^{(0)} \prec \infty$ and $\sigma^{(k)} \geq 0$, by ii), we have $\sigma^{(k)} \longrightarrow \sigma^*$ for some $0 \leq \sigma^* < \infty$. So if we let

$$\tilde{r}_{ij}{}^{(k+m)} = \frac{\sum_{(u,v)\in S_{ij}} \tilde{r}_{uv}{}^{(k-1+m)}\varphi(\tilde{r}_{uv}^{(0)} - \tilde{r}_{ij}^{(0)} \mid \sigma^{2^*})}{\sum_{(u,v)\in S_{ij}} \varphi(\tilde{r}_{uv}^{(0)} - \tilde{r}_{ij}^{(0)} \mid \sigma^{2^*})} :,$$
$$= \tilde{F}(R_{ij}{}^{(k-1+m)})$$

$(i,j) \in S$, k,m=0,1,2...

then $r_{ij}{}^{(k+m)} = \tilde{r}_{ij}{}^{(k+m)} + o(1)$ as $k \to \infty$, thus we only need to prove the convergence of $\{\tilde{r}_{ij}{}^{(k+m)}\}$.

Note

$$\frac{\partial\tilde{F}(R_{ij}{}^{(k-1+m)})}{\partial\tilde{r}_{ij}{}^{(k-1+m)}} = \frac{\varphi(0 \mid \sigma^{2^*})}{\sum_{(u,v)\in S_{ij}} \varphi(\tilde{r}_{uv}{}^{(0)} - \tilde{r}_{ij}{}^{(0)} \mid \sigma^{2^*})} := C_{ij},$$

We have $0 < C_{ij} < 1$, and for all m,

$$|\tilde{r}_{ij}{}^{(l+1)} - \tilde{r}_{ij}{}^{(l)}| = C_{ij}\,|\tilde{r}_{ij}{}^{(k-1+m)} - \tilde{r}_{ij}{}^{(k-1)}| = \cdots = C^k{}_{ij}\,|\tilde{r}_{ij}{}^{(m)} - \tilde{r}_{ij}{}^{(0)}|$$
$$\leq C^k{}_{ij}\sum_{l=0}^{m-1}|\tilde{r}_{ij}{}^{(l+1)} - \tilde{r}_{ij}{}^{(l)}| \leq C^k{}_{ij}\sum_{l=0}^{m-1}C^l{}_{ij}\,|\tilde{r}_{ij}{}^{(1)} - \tilde{r}_{ij}{}^{(0)}|$$
$$\leq \frac{C_{ij}{}^k}{1-C_{ij}}\,|\tilde{r}_{ij}{}^{(1)} - \tilde{r}_{ij}{}^{(0)}|,$$

thus $\{\tilde{r}_{ij}{}^{(k+m)}\}_{k=1,2,\ldots}$ is a Cauchy sequence, and the convergence follows.

J. Biomedical Science and Engineering, 2010, 3, 987-1001 **JBiSE**
doi:10.4236/jbise.2010.310129 Published Online October 2010 (http://www.SciRP.org/journal/jbise/).

Extending cell cycle synchrony and deconvolving population effects in budding yeast through an analysis of volume growth with a structured Leslie model

Chris C. Stowers[1], Erik M. Boczko[2]

[1]Bioprocess R&D Division, Dow AgroSciences LLC, Indianapolis, USA;
[2]Department of Biomedical Informatics, Vanderbilt University, Nashville, USA.
Email: erik.boczko@vanderbilt.edu

Received 22 June 2010; 12 July 2010; 26 July 2010.

ABSTRACT

Budding yeast are a fundamental organism at the center of systems biology research. Understanding the physiology and kinetics of their growth and division is fundamental to the design of models of gene regulation and the interpretation of experimental measurements. We have developed a Leslie model with structured volume and age classes to understand population growth and cell cycle synchrony in budding yeast. The model exhibits broad agreement with a variety of experimental data. The model is easily annotated with volume milestones and cell cycle phases and at least three distinct goals are realizable: 1) One can investigate how any single cell property manifests itself at the population level. 2) One can deconvolve observed population averages into individual cell signals structured by volume and age. 3) One can investigate controllability of the population dynamics. We focus on the latter question. Our model was initially designed to answer the question: Can continuous volume filtration extend synchrony? To date, most general experimental methods can produce an initially synchronous population whose synchrony decays rapidly over three or four cell cycles. Our model predicts that continuous volume filtration can extend this maintenance of synchrony by an order of magnitude. Our data inform the development of simple fluidic devices to extend synchrony in continuous culture at all scales from nanophysiometers to bioreactors.

Keywords: Quantitative Biology, Systems Biology, Volume Filtration, Cell Cycle

1. INTRODUCTION

Unlike the simple volume symmetric division of E. Coli [1], an initially synchronous culture of budding yeast become asynchronous and stationary very rapidly. While stable, synchronous, autonomous oscillations have been observed and are of enormous interest, they do not occur generically and are far from understood [2-5]. Population synchrony is often monitored by tracking the percent of a culture that is budded as a function of time. The physiological factors influencing the rapid decay of cell cycle synchrony in budding yeast were investigated three decades ago. It was found that new daughter cells take longer to traverse the mitotic cycle than their mothers because of a volume asymmetry at division. That is, daughter cells at the time of division, are smaller in volume than their mothers. Furthermore as mothers age they give rise to progressively smaller daughters on average [6], compounding the problem. Currently there is renewed interest in the physiology of replication in relation to aging and the asymmetric partitioning of biomolecules between mother and daughter [1,7,8].

As yeast are now routinely the subject of expression analysis, synchronous growth and division has important and largely unexplored implications for attaching meaning to commonly measured population signals [5,9]. Our interest in developing a model for the volume growth and population synchrony of budding yeast stems from our previous work on an ostensibly simple gene regulatory circuit involved in nitrogen catabolite repression (NCR). An analysis of a minimal model of the NCR-circuit indicates that the components of the system oscillate in phase with the cell cycle [10,11]. In order to understand how a cellular oscillation is observable at the population level, and further, how one could engineer an experiment to convincingly demonstrate periodic oscillation at the cellular level from a population measurement, we undertook the development of a structured population model of yeast growth and division to be described.

The central observations of this study are theoretical

in nature and can be summarized as follows. Theoretically, volume symmetric division leads to persistent synchrony. Each strain of budding yeast has a characteristic mean daughter—mother division volume asymmetry, some more and some less pronounced. Parenthetically, this asymmetry is a function of growth rate and has been shown to be inversely proportional to it [12]. As the asymmetry between mother and daughter division volume increases, synchrony decays in a predictable way. For a given strain of yeast, growing exponentially in a bioreactor, our model predicts that continuously filtering out the smallest and largest cells extends the synchrony of the system. Our model predicts that with judicious choices of filtration cutoff volumes, synchrony can be extended by an order of magnitude. Given strain specific measurements our model can be used to predict design parameters such as the filtration cutoff volumes. The filtration process can be conceived of, in a way that we shall make precise, as a means to restore partial symmetry. While it is true that continuous filtration will skew the population of cells under observation, it can be accomplished without inducing a generic stress response within the yeast. This trade off may for certain experiments be useful.

The cell cycle synchrony of a population of yeast, its persistence, decay and control are essentially an ontologically dynamical systems phenomena. There is a long and fruitful history associated with the modeling of population growth. Budding yeast and their mitotic cell cycle continue to be an interesting and important area of mathematical cell biology. We make no formal attempt to review this enormous literature but restrict our attention to those models of which we are aware have dealt with volume growth and the effects of a mixed population of cells growing with potentially different growth rates. The mixed mother-daughter model [13] was developed based on the mathematical results of branching processes [14,15] to explain the variations in the G_1 phase of the cell cycle. This model was used to derive a stationary distribution of mothers and daughters as a function of the cell cycle. A model developed in [16] and expanded on by [12] considered the properties of an asynchronous population growing exponentially. A central result of their pioneering work was to derive a formula for the replicative age distribution at stationarity that depends on only two parameters, the culture growth rate and the parental doubling time. The formulas and analysis derived by Lord and Wheals have continued to underpin current models of cell cycle dynamics and division [17, see for instance the reset rule at the bottom of **Table 1**]. An admitted limitation of their work however is that it explicitly assumes that the growth rates among the age classes are the same. Their paper presented compelling evidence to support this claim. There is also a wealth of evidence to the contrary [6,18], and evidence that older mothers grow larger with each division. Age structured models that take into account this finer but important level of detail were proposed and utilized to analyze population signals of a critical protein [19], in search of the still elusive link between size control and division [20].

Population balance models that extend that of Hartwell and Unger have been proposed to explore the links between metabolism and the cell cycle during asynchronous as well as synchronous growth. These models are extensively reviewed in [2]. Recently, sophisticated population balance models have been constructed that take into account the mass changes that accompany growth and division and that can vary among distinct age classes [21]. The Leslie model that we present is a discrete version of the continuous population balance model, although our focus is explicitly on volume as opposed to mass. The obvious advantage of this class of model is that it naturally allows one to describe any variation among age classes since they are explicitly represented. An important reason for utilizing and exploring a volume and age structured model is that it captures the effects that influence synchrony and, because it is a dynamical systems model, it can directly be used to examine the dynamical phenomena of synchrony and the effects of filtration as a control mechanism. That is the goal of this paper.

There is a long history of elutriation as a means of preparing and examining yeast sub-populations in the biological literature [22]. There is also a long history in the chemical engineering literature of filtration and sedimentation as a means to separate and control the growth of micro-organisms [23-25]. These two literatures are now converging as systems biology has hit its stride and seeks to leverage every available technology to

Table 1. A glossary of milestones and their meaning.

Symbol	Definition
k	Denotes replicative age.
$\underline{V}_k$	The minimal volume of yeast cell of age k.
$\overline{V}_k$	The maximal volume of yeast cell of age k.
λ_k	The exponential growth rate of a yeast cell of age k.
k--MDV	The expected volume at which a yeast cell of age k will divide.
k--MEDV	The expected volume of a daughter born from a division in age class k.
k--MEPV	The expected volume of a mother immediately after a division event in age class k.
k--BE	The expected volume at which a cell of age k begins to bud.

examine and understand the physiology of networks. As described in this paper, the main result of our modeling work suggests that continuous volume filtration can maintain the synchrony of an initially synchronous population for 20 to 30 cycles: An order of magnitude improvement. This theoretical result can be put into practice utilizing current microfluidic techniques at every population scale of investigation from the nanophysiometer up to the bioreactor.

2. THE LESLIE MODEL

In a culture of budding yeast, the mitotic cell cycles of distinct cells need not be in phase with each other. We want to model the dynamics of the mitotic cell cycles of a population of budding yeast growing in a bioreactor. A description of the dynamics requires a model describing the rate at which single cells progress through the mitotic cell cycle. The vital rates correspond to growth, division, aging and death. We describe the vital rates through a consideration of two variables, cell volume and replicative age, with the aid of a Leslie matrix. Leslie models are an important and well studied class of structured population models. Structured population models are commonly used to describe the life cycle of an organism or process. A comprehensive review of their mathematical properties can be found in [26]. While we wish to highlight certain aspects of the model for its utility we in no way want to obscure or jeopardize the biological punchline: Continuous volume filtration can extend cell cycle synchrony. A heuristic understanding of our model can be obtained without recourse to equations through the process flow diagram in **Figure 1**. **Figure 1** is analogous, but not identical, to those described in [19, **Figure 5**] and [21, **Figure 3**].

2.1. Variables

The model is organized around two variables:

1) *Replicative cell age.* As a yeast cell buds during the mitotic cell cycle, a chitinous bud scar is permanently formed on the mother cell. The bud scars can be visualized with calcoflour white staining [27], and like the rings of a tree, can be used to determine a replicative age. Each generation can be quantitatively identified with the equivalence class of those yeast that carry precisely the

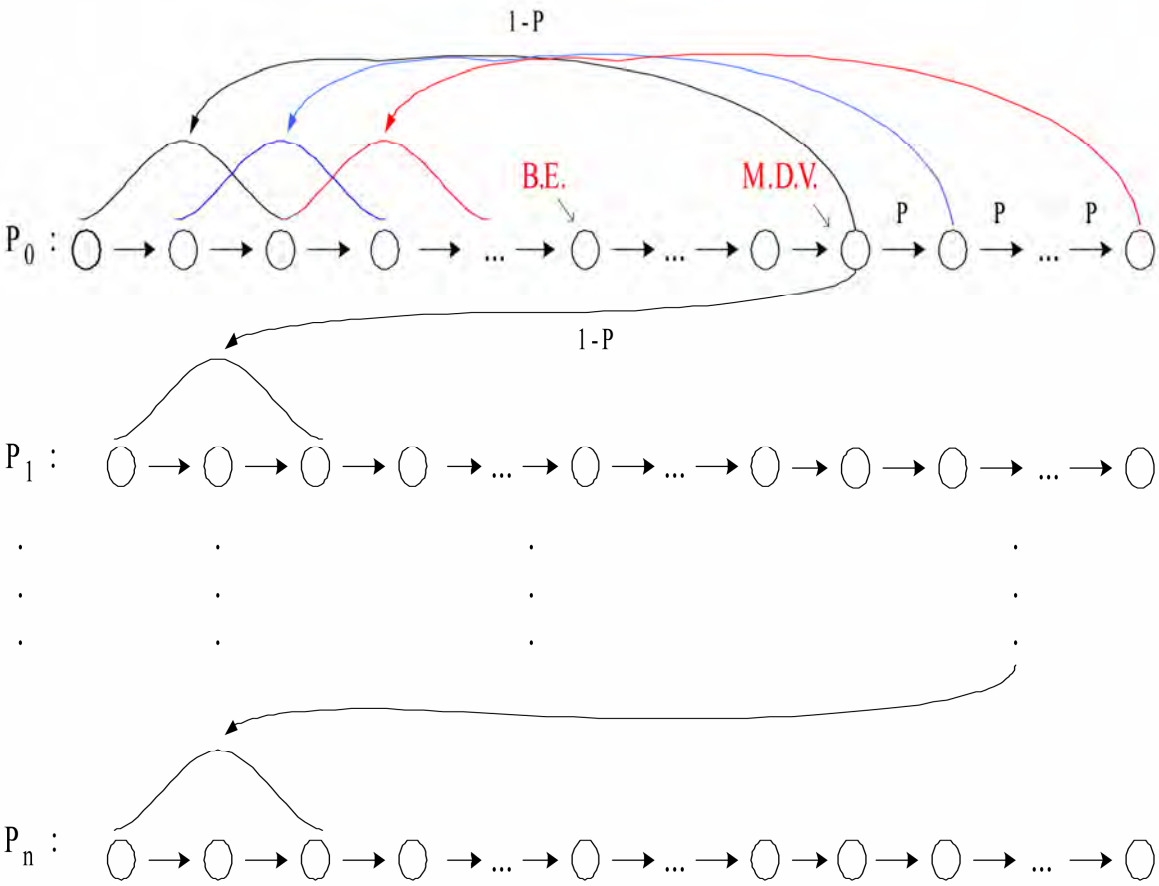

Figure 1. The Leslie model. volume intervals are open circles. Arrows indicate growth or division.

same number of bud scars. Traditionally generations, or bud scar equivalence classes, have been denoted by $P_0, P_1, P_2 \ldots, P_k \ldots, P_n$. Replicative age has been identified as a variable that directly impacts synchrony [6]. Replicative age is properly a discrete variable that we will index by k, the number of bud scars.

2) *The volume of an individual yeast cell.* Cell volume has been observed to increases monotonically with time until division, within a given age class, and thus is often used as a proxy for progression through the mitotic cell cycle. The volume of a budded cell is taken as the total volume of both the mother cell and the bud, until division at which point they become distinct. The results of this paper confirm that volume is intimately connected with synchrony. Volume is consistently expressed in units of cubic microns throughout.

2.2. Volume Intervals and Time

Yeast cells of a given replicative age k, are observed to grow in volume between well defined limits. The minimum and maximum cell volumes observed from experiment are random variables that naturally delimit and define intervals, $\mathcal{I}(k) := [\underline{V}_k, \overline{V}_k]$. We consider the temporal evolution of the system at a sequence of equally spaced times, $t_s := t_o + s\Delta t$. The volume intervals, $\mathcal{I}(k)$, are partitioned into subintervals $I(i,k) := \left(V(i,k), V(i+1,k)\right) \subset \mathcal{I}(k)$, with $\mathcal{I}(k) = \cup_i I(i,k)$, $i = 0,1,...n_k$, where $V(0,k) := \underline{V}_k$, and $V(n_k+1,k) := \overline{V}_k$. The partitions are chosen according to the growth law, within each age class, such that any cell with volume in the interval $I(i,k)$ now, would have a volume in $I(i+1,k)$, precisely Δt later. The unit of time is minutes and we have taken $\Delta t = 1$ throughout. The choice of the time step was chosen based on experimental time series observations of yeast growth and model stability. The number of time intervals n_k is determined from the choice of time step and the experimental values of the volume limits and the growth rate equation relating them. The state of the yeast population at time t_s is described by a vector,

$\rho(i,k)(t_s)$:
$= number\ of\ cells\ of\ generation\ k\ with\ volume$
$v \in I(i,k).$

Each of the $\rho(i,k)(t_s)$ cells living in $I(i,k)$ at time t_s are faced with the following possibilities:

1. The cell dies
2. The volume of the cell increases
3. The cell divides

Each individual yeast does not die or divide at exactly the same volume and age. The population distributions governing each of these possibilities are functions of our independent variables namely volume and age, and are indexed by *i* and *k*. We describe the relevant details of these events and their distributions in the following sections.

2.3. Cell Death

The probability that cell death occurs is denoted by $d_{i,k}$. Mortality curves have been measured for several strains of yeast under a variety of conditions [18,28,29](In particular see **Table 1** of the latter). These data can be used to determine an age class specific death rate. In [12] the authors observe that the death rate on average amounts to $10^{-10}/(cell \cdot generation)$.

2.4. Volume Growth

The probability that growth occurs is denoted by $g_{i,k}$, and the fraction of cells that survive and grow is $\kappa_{i,k} := g_{i,k}(1-d_{i,k})$. Volume growth has been measured and is generally considered to increase exponentially with time. For all of the experiments and analysis in this paper we have considered exponential volume growth. Let λ_k denote the age class specific growth rate. Then, the volume intervals are conveniently described by

$$\begin{aligned} I(0,k) &= \left[\underline{V}_k, \underline{V}_k e^{\lambda_k \Delta t}\right) \\ &\vdots \\ I(i,k) &= \left[V(i,k), V(i,k) e^{\lambda_k \Delta t}\right) \\ &\vdots \\ I(n_k,k) &= \left[V(n_k,k), \overline{V}_k\right) \end{aligned}$$

2.5. Cell Division

All cells do not divide precisely at the same volume. The probability that a division occurs, at a given volume indexed by i, within a given age class indexed by k, is denoted $c_{i,k} := 1 - \kappa_{i,k}$. The importance of including *sloppy size control* in models of growth and division is discussed in [30]. We have implemented a variety of distributions. Two of the most natural are a Poisson process [31] to model division as time to failure, and second a Brownian process using a normal distribution. As will be described in the results section, qualitatively this choice makes little or no difference. The conditional mean volume at which a division happens, with respect to the distribution $c_{i,k}$ for fixed k(age), is referred to as the k--mean division volume and denoted as k--MDV.

We assume that the division of a cell of volume v in age class P_k results in a cell of age class P_0 with volume v' and a cell of age class P_{k+1} with volume v''. Furthermore, $v = v' + v''$. We sometimes denote the division process as $P_k \to P_{k+1}$. It has been experimentally observed [6] that after a cell has budded,

the ensuing volume growth is concentrated almost entirely in the bud. This implies that there is a conditional probability distribution for v' that depends on the size and age of the mother. Let $\mu_{i,j,k}$ be the probability that after a cell division, $P_k \to P_{k+1}$, we get a cell of age class P_0 with volume in $I(i,0)$ from a dividing cell in $I(j,k)$. The conditional expected volume, conditioned on a fixed k, with respect to the distribution $\mu_{i,j,k}$ is referred to as the mean emergent daughter volume and denoted k--MEDV. Let, $\nu_{i,j,k}$ represent the probability that a parent cell of volume $I(j,k+1)$ emerges from a division event in $I(i,k)$. The conditional expected volume of the parent after division is denoted k--MEPV. Generally, the distribution of division volumes has been observed to be normal [32,33].

Given these definitions we can present the projection formula that updates the population in time.

$$\rho(l,0)(t_{s+1}) = \kappa_{l-1,0}\rho(l-1,0)(t_s) + \sum_{k,i}\mu_{l,i,k}c_{i,k}\rho(i,k)(t_s) \quad (1)$$

$$\rho(l,m)(t_{s+1}) = \kappa_{l-1,m}\rho(l-1,m)(t_s) + \sum_{i}\nu_{l,i,m-1}c_{i,m-1}\rho(i,m-1)(t_s); \quad (2)$$

$$m > 0$$

$$\rho(l,m)(t_0) = \rho_0(l,m) \quad (3)$$

The first summand in each equation represents the volume growth contribution while the second summation term represents the density coming from division. The term $c_{i,k}\rho(i,k)(t_s)$ represents the fraction of dividing cells in volume interval $I(i,k)$ and $\mu_{l,i,k}c_{i,k}\rho(i,k)(t_s)$ is the fraction of those that end up in the volume interval $I(l,0)$. The first equation represents daughters and is distinguished because every division results in a daughter. In the higher age classes, $m > 0$, density from division arrives from only one source, namely the age class P_{m-1}.

2.6. Milestones

The parameters of the model that we have described in the previous three subsections such as $\underline{V}_k$, λ_k, $d_{i,k}$, $g_{i,k}$, k--MDV, k--MEDV, and k--MEPV are experimentally measurable quantities associated to a particular strain of yeast that often depend on growth conditions. We refer to these parameters as general volume milestones. For convenience a glossary is provided in **Table 1**.

An experimentally important measure of cell cycle synchrony is the percent of cells in the culture that are budded, also known as the bud index. This quantity can be computed from $\rho(i,k)(t_s)$, given an age class dependent, bud emergence cumulative distribution function, $B_{i,k}$. That is, $0 \le B_{i,k} \le 1$, is a monotonically increasing function of i, for each k, and describes the probability that the cells in $I(i,k)$ are budded. The function is monotone because once a cell has budded it remains that way until it divides. The mean of the bud emergence distribution, for fixed k, is denoted as k--BE. The bud index at time t_s is the normalized inner product:

$$BI(t_s) := \frac{\sum_{i,k}\rho(i,k)(t_s)B_{i,k}}{\sum_{i,k}\rho(i,k)(t_s)}$$

Careful measurements of bud emergence have been made [45] and reveal that the cumulative distribution function of the fraction budded cells relative to volume derives from an underlying normal distribution.

Bud emergence is also a hallmark at the end of the G_1 phase and the beginning of the S-phase of the cell cycle. Likewise, other cell cycle phases can be demarcated within each age class. This annotation enhances the power and utility of the Leslie model. As discussed above the general outline of the process flow in the Leslie model is similar to that outlined in [19,21] although there are some qualitative differences. In their process it is tacitly assumed that the k--MEDV form a monotone increasing series as a function of k. We make no such assumptions. The model can be implemented with measured or arbitrary values. In fact the data described in [6] indicate that in fact the k--MEDV form a monotone decreasing series as a function of age class k.

We have utilized the volume milestones of two strains in this work. To the best of our knowledge the most comprehensive set of milestones have been measured in the diploid strain X2180. For this strain the model was parameterized with yeast physiology data derived from experiments performed over the past four decades [6,13,16,33-38]. Among these the data of Woldringh *et.al.* [6] are particularly comprehensive, and well suited for our modeling. A list of the volume milestones and their description are summarized in **Table 2**.

Additionally we have utilized the haploid, α-factor sensitive strain LHY3865, which is much larger than X2180, and for which we have measured many, but not all, of the volume milestones, see **Table 3**.

The behavior of the model can be investigated with arbitrary parameters. For instance we were interested to examine how the mother daughter volume asymmetry impacts synchrony, all other factors being equal. For this part of the study we used a data set that has no analog in nature that we are aware of, but was constructed to coincide with realistic volume values and exponential growth rates, see **Table 4**.

Table 2. A list of volume milestones and growth parameters for the strain X2180.

Age(k)	$\underline{V}_k$	$\overline{V}_k$	λ_k	BE	MDV	MEDV.
0	14	75	0.0062	38.5	70.7	28.5
1	40	85	0.0061	46.8	75	24.4
2	48	87	0.0044	56.1	82.4	24.2
3	56	94	0.0047	63.9	88.9	22.3
4-13	64	125	0.0047	76.3	95	22.2

Table 3. A list of volume milestones and growth parameters for the strain LHY3865.

Age(k)	$\underline{V}_k$	$\overline{V}_k$	λ_k	BE	MDV	MEDV
0	30	105	0.0054	59.0	98.0	46.0
1	45	105	0.0049	69.5	97.5	43.0
2	53	104	0.0049	68.9	96.6	36.5
3	60	115	0.0049	78.8	110.4	36.5
4	73	140	0.0049	95.7	134.1	36.5
5	97	185	0.0049	155.0	179.1	36.5
6-13	129	190	0.0049	155.0	179.1	36.5

Table 4. A list of growth parameters to study the impact of the daughter to mother volume asymmetry on the decay of synchrony.

Age(k)	$\underline{V}_k$	$\overline{V}_k$	λ_k	BE	MDV	MEDV
0-13	40	110	0.0047	60	100	50

2.7. Initial Conditions

In order to compare the dynamics of our model with data we considered several natural initial conditions for our computational work. For instance, most experiments that follow the bud index oscillations are performed starting from an initially synchronized population of cells. Historically, several different experimental methods have been used to synchronize yeast. These include metabolic starvation, elutriation, and pheromone blocks. These are described in [22]. Perhaps the most common of these is the use of mating pheromones like α-factor, that arrests cells in G_1 prior to the cdc28 delimited start. Computationally we created an initial condition to mimic this population of cells by pruning the time invariant population density of each class such that no cells exist outside of the terminal 20% of the G_1 volume intervals prior to the mean bud emergence. The pruned population density was then renormalized. Correspondingly, we will refer to this distribution as the α-factor initial condition.

In the late 1960's Helmstetter [39] had the ingenious insight to create what is now referred to as the *baby machine*. The concept can be made to work with virtually any dividing cells, but was conceived for yeast. Cells are adhered to a membrane and perfused with media. As the cells divide the daughters fall into a receptacle. The collected P_0 cells can be re-adhered to a fresh membrane and the process iterated, with or without pheromones, limited only by imagination. In this way one can experimentally create and subsequently analyze coherent populations. Other clever ways of preparing and separating cells also exist [29,40].

With the help of a baby machine we have collected coherent P_0 cells and run these cells through a Coulter counter to measure their volume distribution. Such distributions are easy to import into the computer and in this way we have created what we will refer to as a baby initial condition.

2.8. Filtration

The main objective of this study was to observe the behavior of a computational population of yeast undergoing continuous filtration. Here we wish to formally define what we mean by filtration. **Figure 2** depicts how the process works. Two volumes are specified, V_* and V^*, and together these define a volume interval, $\mathcal{F} := (V_*, V^*) \subset \cup_k \mathcal{T}(k)$. In **Figure 2**, the vertical red lines indicate the volumes V_* and V^* and how they intersect the various intervals $\mathcal{T}(k)$. All cells, regardless of age, whose volume lies outside of $\mathcal{F}$ are removed from the system at every timestep.

$$V(i,k) \le V_* \text{ or } V(i,k) \ge V^* \rho(i,k)(t_s) = 0$$

This is intended to mimic what one imagines a perfect volume filter might do to a real yeast culture. In engineering practice this would be called a two stage filtration because each of the two defining inequalities would be implemented by a separate filter and the process carried out in series.

3. LABORATORY MATERIALS AND METHODS

Yeast cells of *Saccharomyces cerevisiae* strain LHY3865 (mat a-URA, LEU, bar1Δ) were grown in YNB media without ammonia or amino acids and with 100 mg/L leucine, 20 mg/L uracil, 0.2% glutamine, and 2% glucose at 30℃. Batch shake flask cultures were grown with an agitation of 225 rpm in a New Brunswick Scientific Innova 44 orbital incubator/shaker. 1.5 L bioreactor cultures were grown in a 3 L New Brunswick Scientific bioreactor with a dilution rate of D = 0.35 hr^{-1}, air was sparged through the reactor at a rate of 500 mL/min, and the culture was agitated with two Rushton-type impellers ran at 225 rpm.

3.1. Cell Cycle Synchronization

A 750 mL yeast culture was arrested at a cell density of

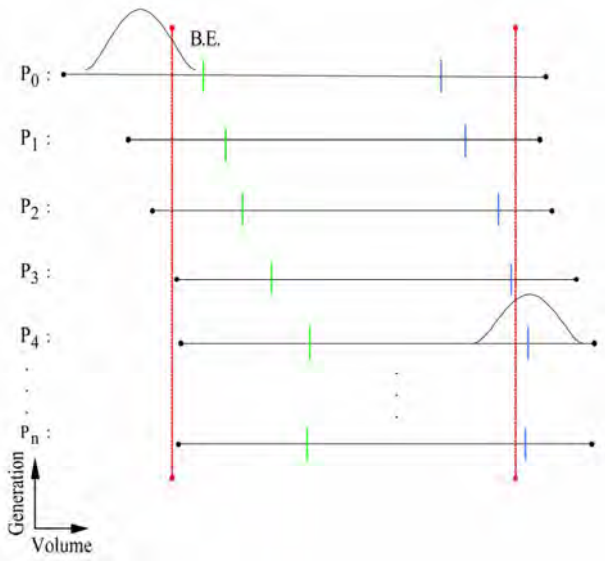

Figure 2. Volume filtration process. The vertical red lines indicate volume filters. Cells below the lower or above the upper filters are moved from the system.

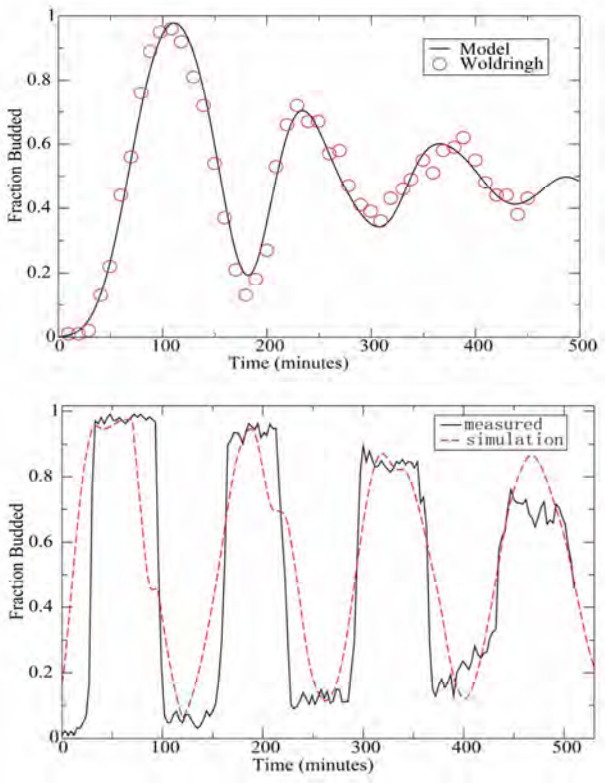

Figure 3. Experimental measurements of bud index synchrony and comparison with simulation. Top bud index oscillations of the X2180 strain in a shake flask [10]. Bottom is LHY3865 strain, grown in a bioreactor and synchronized with α-factor.

OD = 0.8 through the addition of 3×10^{-5} M α-factor mating pheromone (Sigma # 63591) and were incubated for 3 hours. Cells were subsequently released from arrest by pelleting followed by three washes with fresh preconditioned media, free of α-factor, containing 0.1 mg/mL Pronase E (Sigma # P-6911). The preconditioned media was prepared by allowing LHY3865 yeast cells to grow within the media for 4 hours at $OD_{600} = 0.4$ before being removed by a 0.2 μm filter. The synchronized cells were then resuspended in 1.5 L of preconditioned media and grown in the bioreactor as described above. 0.5 mL samples were taken from the bioreactor at a time interval of 3 minutes and were immediately frozen in 50% glycerol by the addition to an ethanol-dry ice bath. For batch experiments, samples were taken at a time interval of 10 minutes for the first 90 minutes of the experiment and then every 20 minutes for the remainder of the experiment duration.

3.2. Bud Index Analysis

Samples were analyzed using a conventional microscope for bud index. Each data point consisted of more than 100 different analyzed cells. Samples were vortexed briefly and then sonicated for 1 minute prior to analysis to minimize cell clumping to ease analysis. 10 μL of each sample was then pippetted onto a glass slide to be analyzed with the microscope. Cells were individually interrogated using multiple focal planes and a 100X objective. Yeast cells were only considered budded if a septum did not separate the mother from the daughter cells.

4. RESULTS

When the model is parameterized with the experimentally determined volume milestones we observe excellent agreement between the output of the model and experiment for both time invariant properties such as the age distribution as well as dynamical properties such as the bud index oscillations. This congruence provides confidence in our main result: The synchrony of an initially synchronous population can be extended by at least an order of magnitude through continuous volume filtration. We define synchrony as the number of consecutive bud index oscillations whose amplitude is at at least 60% of maximum, that is, varies between less than 20% budded and greater than 80% budded.

4.1. Comparison with Experiment

4.1.1. Bud Index Dynamics

The Leslie model produces good agreement with measured experimental time series. The Leslie model qualitatively as well as quantitatively captures the dynamics of two different yeast strains with very different volume milestones.

Figure 3 shows the good agreement between the Leslie model and the experiments described in [6] with strain X2180. We have made careful measurements of the bud index oscillations for the α-factor sensitive strain LHY3865, both in a batch and continuously operated bioreactor. The data shown in **Figure 3** are typical of those described in the literature over the past 4 decades, see for instance [41]. The LHY3865 cells are initially synchronized with the mating pheromone α-factor that arrests unbudded cells in G_1. The agreement of fine structural features between the experiment and simulation, such as the breadth at the top of the oscillation, indicates that the model is capturing the essential features of budding yeast volume growth and division.

Using the bud index experimental data we have performed a sensitivity analysis to determine how the individual milestones affect the congruence between model and system dynamics. The results indicate that the milestones of the daughter generation are the most sensitive and the sensitivity decays monotonically with age. How well the model dynamics fit the data is most sensitive to the mean division volume of the daughter generation, followed by the mean bud emergence milestone. In general a 10% change in the milestones produced less than a 10% change in the overall fit between model dynamics and experimental time series. This indicates that the basic processes of the model robustly capture the dynamical phenomena associated with bud index oscillations.

4.1.2. Stationary Properties

The model parameterized with the X2180 milestones reproduces the measured stationary values within the measured deviations where available, see **Table 5**. The measured quantities were the fractions(F) of daughters (D), parents(P), budded(B) and unbudded(U). It was observed in [13] that a quantitative relationship exists of the form $(1-P(G_1))\tau_D = k$, where $P(G_1)$ is the percentage of cells in the G_1 phase, τ_D is the observed population doubling time and k is a constant. This would be unremarkable save for the fact that $k = 1.1$ hrs was observed over a wide range of growth rates, suggesting some universality. The observed population doubling time is in reality a population weighted average over all the generations and we have computed this quantity from the model using two natural ensemble averages that produce the same value of $k = 1.2$ hrs that is in close agreement with the experimental value for which no standard deviation was reported.

4.2. Decay of Synchrony with Division Asymmetry

As described in the introduction, it has been well known that the volume asymmetry between mothers and daughters has a profound effect on the decay of synchrony of initially synchronized populations of budding yeast. Since budding yeast display a bewildering array of strain variation we felt it legitimate and interesting to ask how the amplitude of the bud index oscillation decays as a function of inherent volume asymmetry between mothers and daughters at division. This volume asymmetry has a constant mean value for each strain of yeast. Essentially this value is $MEPV - MEDV$, when it does not vary with k. From the bud index curve we have computed the envelope of the oscillation and fit the amplitude decay. As expected from the theory, see for instance [26] (subsection 4.7), the decay is exponential. The initial rates of decay are described in the top panel of **Figure 4**, while the number of corresponding synchronous cycles are shown in the bottom panel. The computational results show that as expected the number of cycles of synchrony declines dramatically with volume asymmetry. When the daughter to mother volume ratio is 80% the number of synchronous cycles has decayed from infinity to one for the X2180 milestones.

4.3. Volume Filtration

We have examined two filtration strategies computationally. **Figure 2** describes the general filtering scheme. In a two stage filtration we impose both an upper and a lower volume limit. All cells whose volume lies in between are retained in the system, a bioreactor, and the rest are continuously removed. In a single stage filtration there is only a lower volume limit, and all cells smaller than this are removed, those that are larger remain.

The main two stage filtration results of this paper are presented in **Figures 5** and **6**. After inspecting the volume-time diagram constructed in [6], we conjectured that it would be possible to emulate the symmetry of

Table 5. Comparison of stationary properties of the model with experiment for the X2180 strain. The experimental data are reproduced from table 1 of [47] with the exception of the last two entries that are taken from [36]. F(D),F(P),F(B),F(U) are the fractions of daughters, parents, budded and unbudded respectively.

Property	Model prediction	Experiment
F(D)	61.0	60.3 ±1.8
F(P)	39.0	39.7 ±1.7
F(B)	63.0	66.9 ±4.0
F(U)	37.0	33.1
F(B) $\langle\tau\rangle$	1.2	1.1
$\langle F(B)\tau\rangle$	1.2	1.1

near equal volume division by filtering out cells that were too small or too large. We reasoned that this would have the abstract effect of making all the age class grids nearly the same. In large part this hypothesis was born out as the data show that by a judicious choice of filtration parameters we can extend the synchrony from 1 cycle to close to 20 cell cycles in the X2180 strain and from 3 to 30 in the LHY3865 strain. **Figure 7** shows the bud index profiles associated with several of the filtration parameters that describe the range from no filtering to the best that we have been able to observe at 17 cycles for the X2180 milestones.

Equivalently **Figure 8** shows the bud index osci- llations of the LHY3865 milestones subject to single and double stage filtration. The upper panels show the results of single stage filtration. **Figure 9** codifies the behavior of the single stage filtration of the LHY3865 milestones. This figure is annotated with the k-mean daughter emergence volumes. It is clear from the computational data that the position of these milestones relative to the

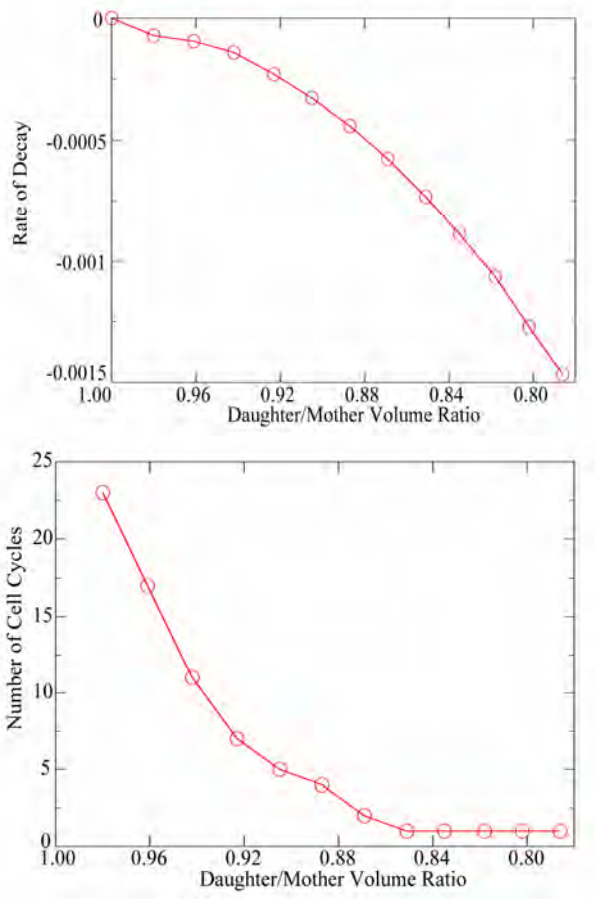

Figure 4. Decay of synchrony as a function of daughter:mother volume ratio. Synchrony is computed from bud index oscillations. Starting from unimodal population of daughter cells distributed in G1.

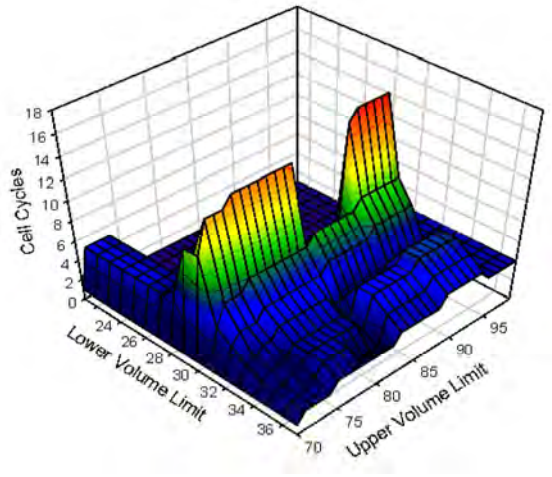

Figure 5. Synchrony computed as a function of two stage filtration for strain X2180 milestones. The data indicate that there is an optimal ridge of values that produce extended synchrony.

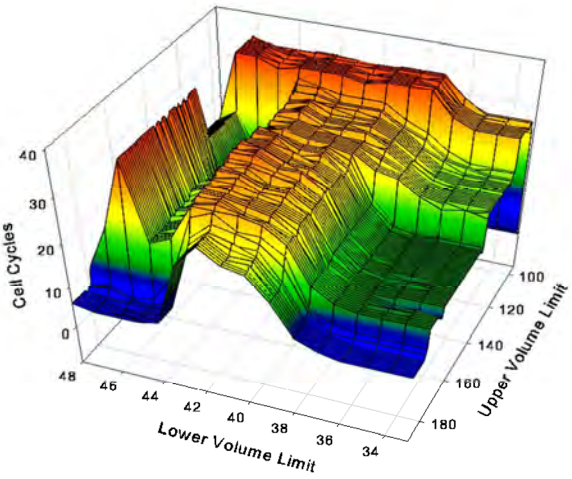

Figure 6. Synchrony computed as a function of two stage filtration for strain LHY3865 milestones.

filtration volume limit determines the range of extended synchrony. The fact that there exists a broad volume range near the top of the peak ensures that the single stage filtration should in practice produce robust results.

4.4. Invariant Density

For the general volume parameters and growth kinetics of budding yeast, like those detailed in [6], and summarized in **Tables 2** and **3**, the population density generically reaches a unique, non trivial stationary state [43]. This behavior is observed experimentally. As a consequence of the primitivity of the Leslie Matrix and the Perron-Frobenious theorem the invariant density can be recovered from the model as the L^1-normalized eigenvector corresponding to the unique largest eigenvalue of the matrix. The state of the system at

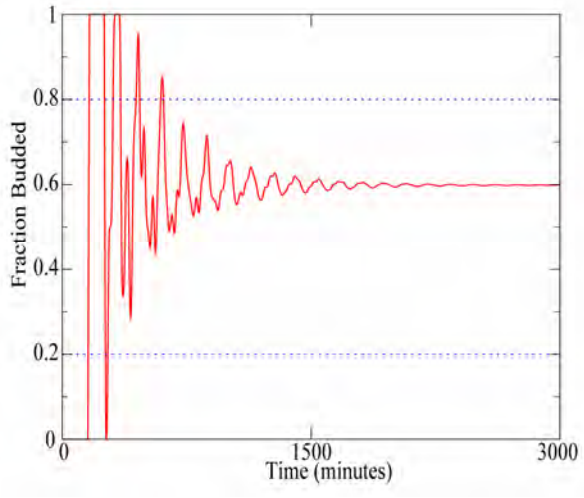

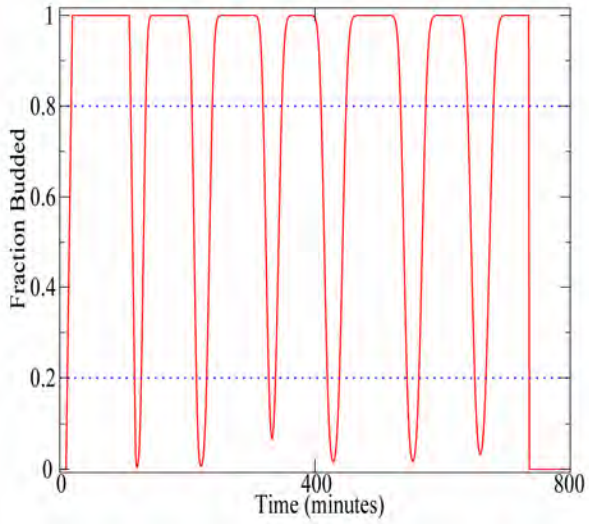

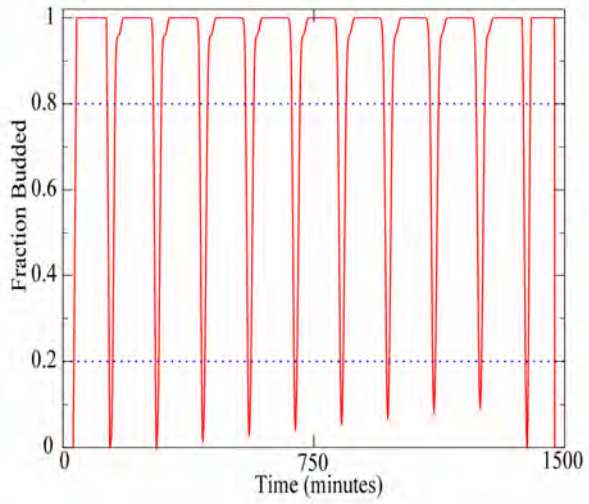

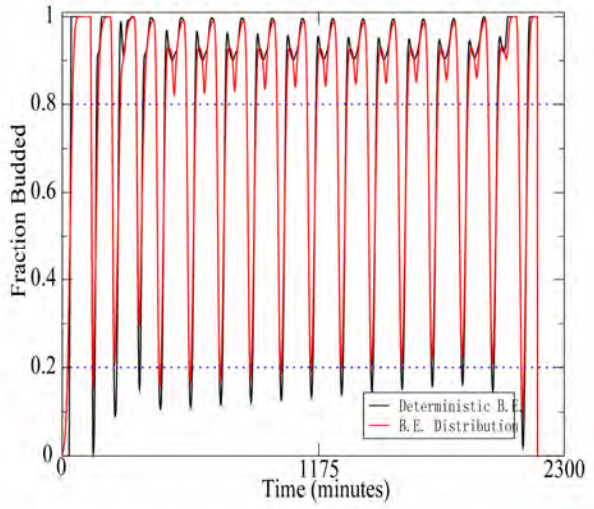

Figure 7. Bud Index oscillations of strain X2180 milestones for various filtration parameters. Top left unfltered system, clockwise limits, in units of cubic microns: [34; 91], [30; 90], and [30; 71] respectively.

asynchronous exponential growth and is described by $\rho(t) = e^{\alpha t} X$, where α is the population growth rate, and X is the eigenvector that, when normalized in the L_1 norm, represents the time invariant probability density of observing a yeast cell of a given volume and age. **Figure 10** describes the properties of the invariant density, X computed for the X2180 milestones. As the figure shows, the invariant population distribution within each age class are smoothed through the use of a distribution of emergent parent and daughter volumes upon division. We examined a family of normal distributions and the qualitative features are insensitive to the specific details, such as the value of σ.

The stationary daughter distribution exhibits an inflection point at the population weighted average of the k--MEDV from all age classes with $k > 0$. Because of the birth of new daughters coming from all age classes, the daughter distribution is the only generation to exhibit bimodality. A local maximum appears just ahead of the 0-MEDV milestone that result from the $P_0 \to P_1$ division. The daughter density distribution decays with increasing volume after the global maximum as a linear combination of two exponentials. The structure of the invariant density is similar to those hypothesized in earlier works [3,29,35,40]. The invariant density within the parent age classes, P_k for $k > 0$ are similar to each other in that they achieve a global maximum that decays exponentially with increasing volume. For all age classes other than the daughter generation, the invariant density is indistinguishable from the function $A2^{1-\theta}$, where the constant A is arbitrary and the simple linear function

$\theta = (v - v_0)/(v_1 - v_0)$ rescales the volume interval into the unit interval. This agrees well with the theory described previously [3,29,35,40].

4.5. Age Distribution

Since replicative age can be distinguished through bud scar analysis it is possible to determine the age distribution of a culture of yeast. For instance, if we select a cell at random from a culture of X2180 cells during asynchronous, exponential growth in a bioreactor we will have a less than 1 in 3 chance of observing a P_1 and about a 1 in 6 chance of finding a P_2.

It is of interest to understand how each age class is weighted during oscillations as well as once the density becomes stationary [12,19,43,44]. The age distribution of a symmetrically dividing organism decays like the geometric series $(\frac{1}{2})^{k+1}{}_{k=0}$. For budding yeast the age distribution is more complicated. Lord and Wheals [12] derived a parsimonious formula based on the culture doubling time and the doubling time of the parents, P.

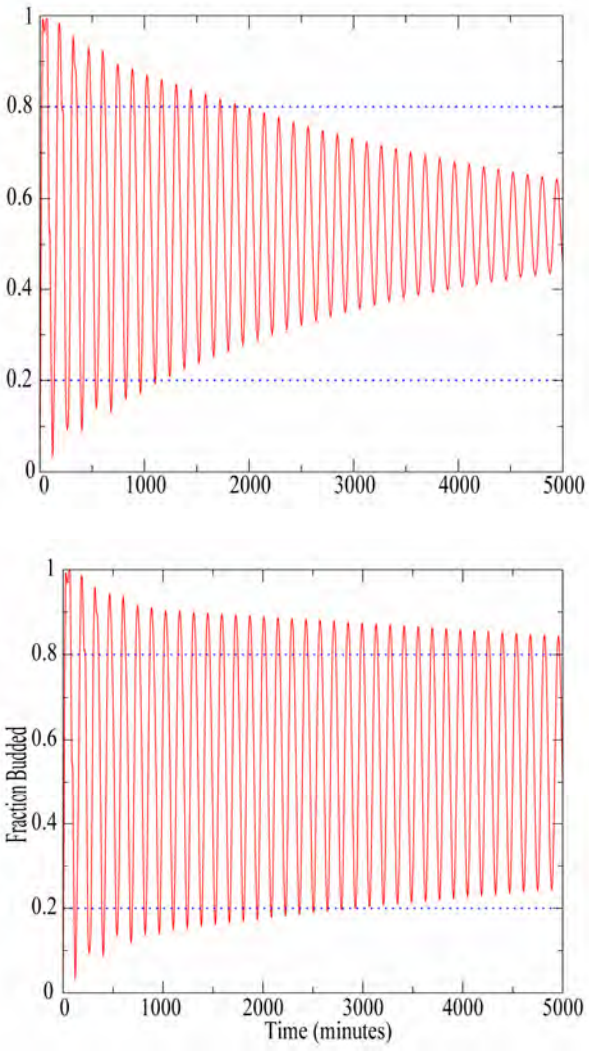

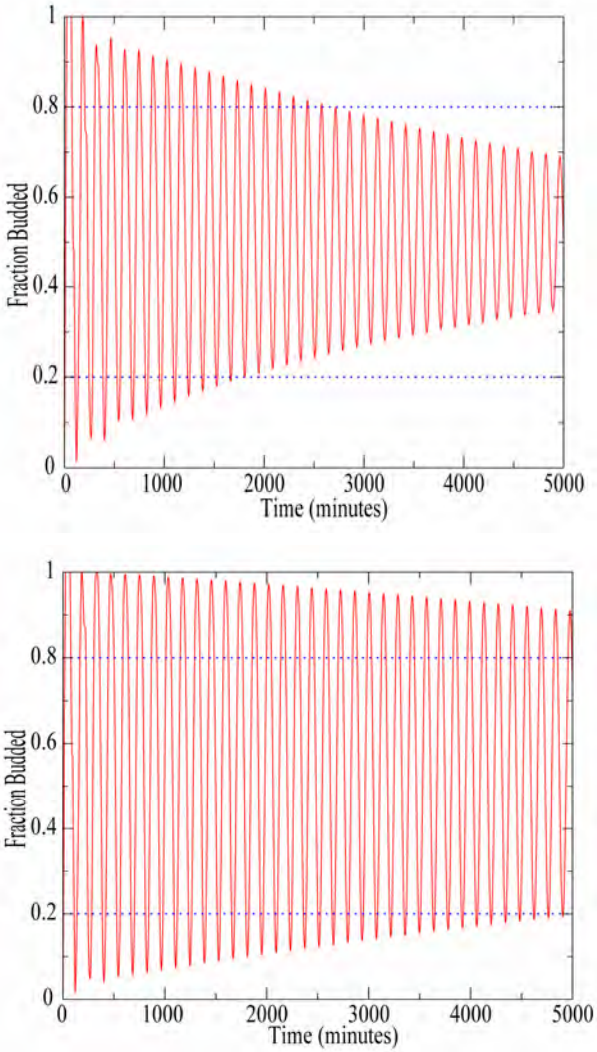

Figure 8. Bud index oscillations of LHY3865. Top panels single stage, bottom are two stage filtration. Right panels are best achievable. Parameters cubic microns are clockwise from top right: 39, 42, [37; 100] and [33; 178].

The age distribution computed using the X2180 milestones, shown at lower left in **Figure 10** shows excellent, agreement with the experimental data of Beran *et al.* [43] for a strain of *Saccharomyces cerevisiae* grown in a bioreactor at comparable dilution rates. The formula of Lord and Wheals was fit by least squares to the Leslie model data through the variable P. The best fit value of $P = 88.3$ minutes is however uninterpretable in relation to the X2180 parameters. For instance the average, maximum doubling time of the parent generations is calculated as 136.6 minutes, while the average minimum doubling time time is 96.8

minutes. These latter two values should realistically bookend the mean doubling times.

Based on a consideration of population flux and flux transit time we have been able to derive a recurrence relation that explains the observed non-geometric decay of the age distribution in terms of the growth parameters that extends previous works [12,44]. This analysis is to be presented elsewhere.

Given the general exponential decay of the age distribution we have contented ourselves to represent 14 generations computationally. Experimentally mortality curves for replicative age has been measured for some strains of budding yeast [18,29,30]. It has been observed

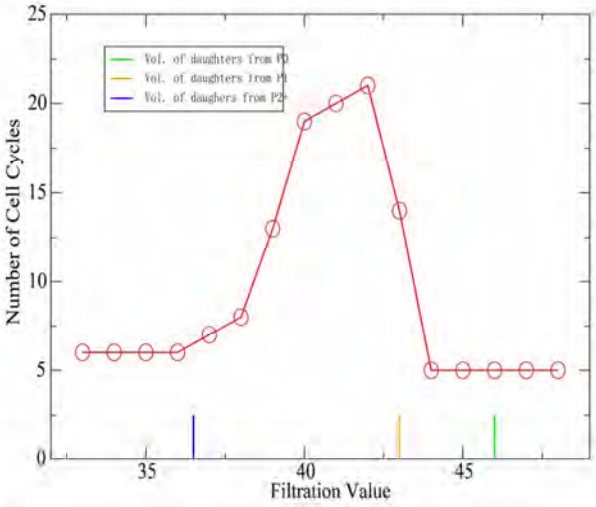

Figure 9. Single stage filtration for LHY3865. Cells below cutoff continuously removed. Synchrony measures successive cycles of Bud index oscillation that maintains at least 60% of its total amplitude.

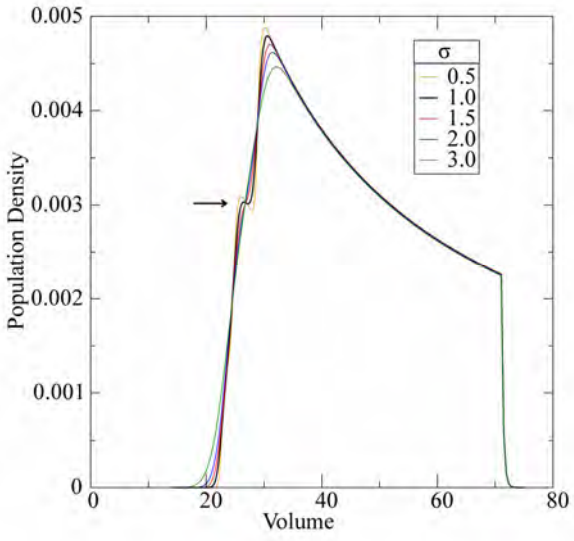

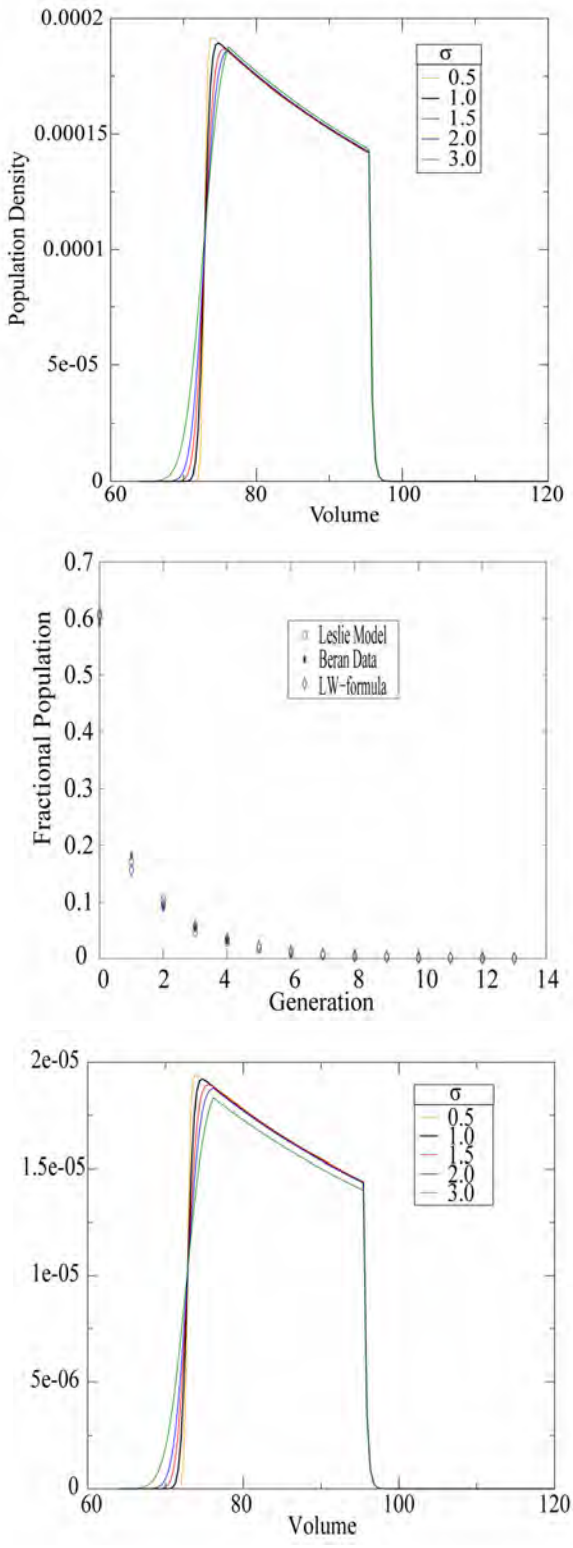

Figure 10. Invariant density for X2180. Clockwise from upper: P0, P6 and P13 distributions. Lower left compares model age distribution with data of Beran *et al.* [43] and formula of Lord and Wheals [24].

there that some yeast can survive upwards of 60 divisions. From the decline in the age distribution we have observed that practically, 20,30,40 generations or more, need not be represented in the model to precisely capture the dynamics of the system. We know of no experimental data sets that have completely characterized more than the first 8 age classes. The precise connection between senescence and replicative aging is currently undecided and is an interesting area of intense activity.

5. DISCUSSION

The Leslie model captures the dynamics of bud index oscillations and their decay. We have shown that there is good agreement between measured data and the predicted bud index oscillations for two different sets of strain milestones, one haploid and one diploid, of different volume extents and growth rates. The different strains of yeast display quantitatively different behavior with regard to their decay of synchrony as we have defined it. The X2180 strain exhibits 1 synchronous cycle while the LHY3865 strain displays 3. The model captures this difference. This instills confidence in the model predictions of synchrony. The strain milestones in both cases contain measurement error and are incomplete especially in generations higher than the fourth age class. The agreement of the model and the experimental data, despite these errors, exposes the robustness of the processes and the ability of the Leslie model to capture the essentials of the asymmetric growth and division process. These claims are supported by the results of a sensitivity analysis.

It is well known that theoretically volume symmetric division is a degenerate case that leads to persistent synchrony [31,42]. Several well known avenues allow the manipulation of the division volume asymmetry. Lord and Wheals observed [12], as have many others, that age class growth rates depend linearly on the culture doubling time and estimated that there exists a growth rate that if achievable would produce balanced and presumably synchronous growth. Growth rates are most typically affected through variation of nitrogen or carbon source. It has also been observed that drugs such as hydroxyurea can induce nearly symmetric division [39]. It is well known that strain variations influence division volume asymmetry. We have explicitly examined the relationship between division volume asymmetry and the number of synchronous cycles of bud index oscillations. Our intentions in doing so are two fold. First, we imagine that if a legitimate relationship exists then it may be possible through a judicious mutation to create strains of yeast with predefined synchrony. Second, we see a direct relationship between the control of synchrony through continuous volume filtration and the natural synchrony that results from volume symmetric division. What this means is that a volume filter is seen in the abstract as a mechanism for restoring partial symmetry to an underlying volume asymmetric system. For instance, consider **Figure 2**. The volume grids of the different generations are not a priori commensurate, however the volume grids that live between the filter cutoffs are more so. Those cells that are far from the symmetry conditions are removed from the system, leaving the remainder more synchronous. The intrinsic asymmetry that volume filtration cannot influence are the volume milestones such as k-MEDV, k-BE and k-MDV. These however can be influenced by mutation and or nutrients. The combination of mutation, media composition and continuous volume filtration is therefore expected to be able to produce budding yeast that are remain synchronous for long periods of time starting from a homogeneous initial condition.

We have explored both single and double stage filtration. We explored single stage filtration and present it here because it is far easier to implement in practice and it appears to produces results that could be observed with even a crude device. The results indicate that there exist robust windows of volume that can be used to control synchrony. An example can be seen in the single stage results, **Figure 9**. There is a broad peak around $41\mu m^3$, approximately $4\mu m^3$ in width that produces a roughly 4 fold extension in synchrony. This result if correct implies that even a crude filtration device should produce observable changes. We are currently exploring design equations for such a device.

Continuous filtration is a control mechanism that will alter the population structure relative to a unfiltered population. A population structure that will be altered in the filtered population are the volume distributions and the overall age distribution. How, and to what extent the age distribution is affected can be analyzed with the model. The results of this analysis are to appear elsewhere. Continuous filtration, we think, can be accomplished experimentally without inducing a general stress response in the individual cells of the population.

We observe that while we have explored here the very specific application of volume filtration, the Leslie model can be used to explore a much broader range of questions that are of continuing interest in yeast physiology and in the larger picture of systems biology. For instance, as has been observed previously [19,22], it is possible to use the model to investigate how signals from single cells manifest themselves at the populations level. With the addition of volume filtration it will be possible to study cell cycle dependent protein expression

more extensively.

A use that has been little explored to date is how a signal, periodic in the cell cycle, such might be conceived for a gene expression, manifests itself at the population level. When signals are routinely evaluated by grinding up large numbers of cells and pooling their mRNA for instance, such questions seem reasonable. We have previously observed that how one grinds up the cells in such a situation has quantifiable effects that depend on the cell cycle [45]. Any extensive quantity that varies in a single cell with the cell cycle can be examined with this model. For example oxygen consumption, glucose uptake, or mRNA production of the population can be studied given measured or putative data from single cells. Conversely, it is also possible to use the model to deconvolve population ensemble averages into individual cell signals.

Finally, a physiological component that has not been included into the current model are the putative asymmetric effects that are now emerging in the study of chronological aging and senescence [7]. It is well known that aging occurs in organisms such as *Escherichia coli* and fission yeast that undergo morphogenically symmetric division [1]. Given the success of the Leslie model in matching the dynamics of the bud index oscillations for a few cell cycles, it is tempting to suggest that deviations between the Leslie model and the dynamics of yeast with a variety of aging phenotypes may provide new and otherwise difficult to attain insight into the rate and effects of senescence.

6. ACKNOWLEDGMENTS

We thank Linda Breeden for the gift of the LHY3865 strain. We thank Konstantin Mischaikow for coding an early version of the model and helpful discussions. EMB, and CS, were partially supported through NSF-DMS 0443855.

REFERENCES

[1] Stewart, E.J., Madden, R., Paul, G. and Taddei, F. (2005) Aging and death in an organism that reproduces by morphologically symmetric division. *PLoS Biology*, **3**, 295-300.

[2] Bellgardt, K.H. (1994) Analysis of synchronous growth of bakers yeast. Part I: Development of a theoretical model for sustained oscillations. *Journal of Biotechnology*, **35**, 19-33.

[3] Keulers, M., Sazuki, T., Satroutdinov, A.D., Kuriyama, H. (1996) Autonomous metabolic oscillations in continuous culture of saccharomyces cerevisiae grown on ethanol, *FEMS Micro Letters*, **142**, 253-258.

[4] Murray, D.B., Klevecz, R.R. and Lloyd, D. (2003) Generation and maintenance of synchrony in saccharomyces cerevisiae continuous culture. *Experimental Cellular Research*, **287**, 10-15.

[5] Tu, B.P., Kudlicki, A., Rowicka, M. and McKnight, S.L. (2006) Logic of the yeast metabolic cycle: Temporal compartmentalization of cellular processes. *Science*, **310**, 1152-1158.

[6] Woldringh, C.L., Huls, P.G. and Vischer, N. (1993) Volume growth of daughter and parent cells during the cell cycle of saccharomyces cerevisiae a/α as determined by image cytometry. *Journal of Bacteriology* **175**, 3174-3181.

[7] Ackerman, M., Chao, L., Berstrom, C. and Doebeli, M. (2007) On the evolutionary origin of aging. *Aging Cell*, **6**, 235-244.

[8] Agilaniu, H., Gustafsson, L., Rigoulet, M. and Nystrom, T. (2003) Asymmetric inheritance of oxidatively damaged proteins during cytokinesis, *Science*, **299**, 1751-1753.

[9] Eisen, M.B., Spellman, P.T., Brown, P.O. and Botstein, D. (1998) Cluster analysis and display of genome-wide expression patterns. *Proceedings of National Academy Sciences*, **95**, 14863-14868.

[10] Boczko, E.M., Cooper, T.G., Gedeon, T., Mischaikow, K., Murdock, D.G., Pratap, S. and Wells, K.S. (2005) Structure Theorems and the Dynamics of Nitrogen Catabolite Repression in Yeast. *Proceedings of National Academy Sciences*, **102**, 5647-5652.

[11] Boczko, E.M., Gedeon, T. and Mischaikow, K. (2007) Dynamics of a simple regulatory switch. *Journal of Mathematical Biology*, **55(5-6)**, 679-719.

[12] Lord, P.G. and Wheals, A.E. (1980) Asymmetrical division of saccharomyces cerevisiae. *Journal of Bacterial* **142**, 808-818.

[13] Slater, M.L., Sharrow, S.O. and Gart, J.J. (1977) Cell cycle of saccharomyces cerevisiae in populations growing at different rates. *Proceedings of National Academy Sciences*, **74**, 3850-3854.

[14] Harris, T.E. (1967) The theory of branching processes. *Die Grundlehren der Mathematischen Wissenschaften* **119**, Springer-Verlag, Berlin; Prentice-Hall, Inc., Englewood Cliffs, New Jersey.

[15] Kimmel, M. and Axelrod, D.E. (2002) Branching processes in biology. *Interdisciplinary Applied Mathematics*, **19**, Springer-Verlag, New York.

[16] Hartwell, L.H. and Unger, M.W. (1977) Unequal division in saccharomyces Cerevisiae and its implications for the control for the cell division. *Journal of Cellular Biology*, **75**, 422-435.

[17] Chen, K.C., Calzone, L., Ccikasz, N.A., Cross, F.R., Novak, B. and Tyson, J.J. (2004) Integrative analysis of cell cycle control in budding yeast. *Molecular Biology Cellular*, **15**, 3841-3862.

[18] Egilmez, N.K. and Jazwinski, S.M. (1989) Evidence for the involvement of a cytoplasmic factor in the aging of the yeast saccharomyces cerevisiae. *Journal of Bacteriology*, **171**, 37-42.

[19] Vanoni, M., Vai, M., Popolo, L. and Alberghina, L. (1983) Structural heterogeneity in populations of the budding yeast saccharomyces cerevisiae. *Journal of Bacteriology*, **156**, 1282-1291.

[20] Jorgensen, P. and Tyers, M. (2004) How cells coordinate growth and division. *Current Biology*, **14**, R1014-R1027.

[21] Hatzis, C. and Porro, D. (2006) Morphologically structured models of growing budding yeast populations. *Journal of Biotechnology*, **124**, 420-438.
[22] Walker, G. (1999) Synchronization of yeast cell populations. *Methods in Cell Science*, **21**, 87-93.
[23] Davis, R.H. and Gecol, H. (1996) Classification of concentrated suspensions using inclined settlers. *International Journal of Multiphase Flow*, **22**, 563-574.
[24] Walsh, T.J. and Bungay, H.R. (1979) Shallow depth sedimentation of yeast cells. *Biotechnology and Bioengineering*, **21**, 1081-1084.
[25] Wickramasinghe, S.R., Lin W.C. and Dandy D.S. (2001) Seperation of different sized particles by inertial migration. *Biotechnical Letters*, **23**, 1417-1422.
[26] Caswell, H. (2001) Matrix Population Models. 2nd Edition, Sinauer Associates Inc. Sunderland.
[27] Pringle, J.R. (1991) Staining of bud scars and other cell wall chitin with calcoflour. *Methods in Enzymology*, **194**, 732-735.
[28] Pohley, H.J. (1987) A formal mortality analysis for populations of unicellular organisms (saccharomyces cerevisiae). *Mech. Ageing Dev.*, **38**, 231-243.
[29] Sinclair, D., Mills, K. and Guarente, L. (1998) Aging in saccharomyces cerevisiae. *Annual Revised Microbiology*, **52**, 533-560.
[30] Tyson, C.B., Lord, P.G. and Wheals, A.E. (1979) Dependency of size in saccharomyces cerevisiae cells on growth rate. *Journal of Bacteriology*, **138**, 92-98.
[31] Smith, J.A. and Martin, L. (1973) Do cells cycle? *Proceedings of National Academy Sciences*, **70**, 1263-1267.
[32] Hersh, R.T. and Kitos, P.A. (1980) Is G_1 normally distributed? *Journal of Theoretical Biology*, **86**, 117-122.
[33] Wheals, A.E. (1982) Size control models of saccharomyces cerevisiae cell proliferation. *Mollecular and Cellular Biology*, **2**, 361-368.
[34] Barford, J.P. and Hall, R.J. (1976) Estimation of the length of cell cycle phases from asynchronous cultures of saccharomyces Cerevisiae, *Experimental Cell Research*, **102**, 276-284.
[35] Brewer, B.J., Chlebowicz, S.E. and Fangman, W.L. (1984) Cell cycle phases in the unequal mother/daughter cell cycles of saccharomyces Cerevisiae. *Molecular and Cellular Biology*, **4(11)**, 2529-2531.
[36] Johnston, G.C., Pringle, J.R. and Hartwell, L.H. (1977) Coordination of growth with cell division in the yeast Saccharomyces Cerevisiae. *Experimental Cellular Research*, **105**, 79-98.
[37] Johnston, G.C., Ehrhardt, C.W., Lorincz, A. and Carter, B.L.A. (1979) Regulation of cell size in the yeast Saccharomyces Cerevisiae. *Journal of Bacteriology*, **137**, 1-5.
[38] Singer, R.A. and Johnston, G.C. (1981) Nature of the G1 phase of the yeast saccharomyces cerevisiae. *Proceedings of National Academy Sciences*, **78**, 3030-3033.
[39] Helmstetter, C. A. (1991) Description of a baby machine for Saccharomyces cerevisiae. *The New Biologist*, **3**, 1089-1096.
[40] Koshwanez, J., Holl, M., Marquardt, B., Dragavon, J., Burgess, L. and Meldrum, D. (2004) Identification of budding yeast using a fiber-optic imaging bundle. *Revised Scientific Instruction*, **75**, 1363-1365.
[41] Breeden, L.L. (1997) α -Factor synchronization of budding yeast. *Methods in Enzymology*, **283**, 332-342.
[42] Diekmann, O., Heijmans, H.J.A.M. and Thieme, H.R. (1984) On the stability of the cell size distribution. *Journal of Mathematical Biology*, **19**, 227-248.
[43] Beran, K., Malek, I., Steiblova, E. and Lieblova, J. (1967) The distribution of the relative age of cells in yeast populations. *Microbial physiology and continuous culture : Third international symposium held at the Microbiological Research Establishment (Ministry of Defense)*, Porton Down, Salisbury, Wiltshire.
[44] Gover, N.B. and Woldringh, C.L. (1995) Relationship between the fraction of cell of different genealogical ages and their cycle times in saccharomyces Cerevisiae: A theoretical analysis. *Journal of Theoretical Biology*, **174**, 223-225.
[45] Stowers, C. and Boczko, E.M. (2007) Reliable Cell Disruption in Yeast. *Yeast*, **24**, 533-541.
[46] Johnston, G.C. and Singer R.A. (1983) Growth and the cell cycle of the yeast saccharomyces Cerevisiae. *Experimental Cellular Research*, **149**, 1-13.
[47] Kaeberlein, M. (2005) Regulation of yeast replicative life span by TOR and Sch9 in response to nutrients. *Science* **310**, 1193-1196.

J. Biomedical Science and Engineering, 2010, 3, 1002-1006 **JBiSE**
doi:10.4236/jbise.2010.310130 Published Online October 2010 (http://www.SciRP.org/journal/jbise/).

Different initial conditions in fuzzy Tumor model

Somayeh Saraf Esmaili[1], Ali Motie Nasrabadi[2]

[1]Dept. Biomedical engineering, Science and Research Branch, Islamic Azad University, Tehran, Iran
[2]Dept. Biomedical engineering, Engineering Faculty, Shahed University, Tehran, Iran
Email: Somayeh_saraf83@yahoo.com; nasrabadi@shahed.ac.ir

Received 26 July 2010; revised 18 August 2010; accepted 25 August 2010.

ABSTRACT

One of the best ways for better understanding of biological experiments is mathematical modeling. Modeling cancer is one of the complicated biological modeling that has uncertainty. Therefore, fuzzy models have studied because of their application in achievement uncertainty in modeling. Overall, the main purpose of this modeling is creating a new view of complex phenomena. In this paper, fuzzy differential equation model consisting of tumor, the immune system and normal cells has been studied. Model derived from a classical model DePillis in 2003, which some parameters from a clinical point of view can be described in the region. In this model, by considering fuzzy parameters from clinical point of view, the three-dimensional fuzzy tumor cells in terms of time and membership function are pictured and region of uncertainties are determined. To access the uncertainty area we use fuzzy differential inclusion method that is one of the including methods of solving differential equations. Also, different initial conditions on the model are inserted and the results of them are analyzed because tumor has different treatment in different initial conditions. Results show that fuzzy models in the best way justify what happens in the reality.

Keywords: Tumor Cells; Mathematical Modeling; Fuzzy Parameters; Fuzzy Differential Equation

1. INTRODUCTION

R Using mathematical models is one of the techniques stricken with cancer for finding appropriate treatment and low risk of it. In this way, models of diversity in to different factors such as competition in tumor cells with normal cells over food sources and effects of the immune system on the growth of tumor cells and in some cases different ways of treatment such as chemotherapy have been presented [1-6]. These models often based on biological principles and by using the parameters as obtained from experiment or estimated investment are originated. Thus always to determine these parameters, there are some uncertainties [7,8].

Therefore, because of uncertainty in the parameters of models, using of differential equations and definite tendency in some of artificial systems don't have efficiency to analyze the behavior of living systems, and all the reality not be said by these models. More generally, there are two major reasons for using fuzzy systems in modeling uncertainties. The first reason is being fuzzy measurements. Modeling phenomena are always come from observations and measurements, and these measurements are always exposed to errors and errors from the physical and biological processes with uncertainty are natural. Any numeric measurements that can be extracted also affected by measurement tools and are also influenced by the observer to understand. The second reason is due to be qualitative model. Each of the mathematical variables of model is a sign and the desired quantity, which in turn is a matter of quality. Characters and relationships in the analysis of phenomena common to the process (recognition condition), all those answers are generating subsets acceptable answers and because of that they are accepted in daily applications [9]. There are many different viewpoints for modeling uncertainty. Use of fuzzy differential equations is one of these viewpoints. When these uncertainties in the modeling are combined with differential equation, they are caused fuzzy differential equations in the modeling that can be kept ambiguity in the phenomena. Recent years, fuzzy differential equations have been proposed as a tool for modeling in non-deterministic systems. The main goal of a fuzzy differential equation estimates further conformity with reality in comparison with ordinary differential equations. There have been many different methods for solving fuzzy differential equations that across them fuzzy differential inclusion (FDI) because having the ability to prevent and eliminate the production and dissemination of uncertainty in the problem solving process to occur, is suitable for all types of equations including

Responsiveness is the linear and nonlinear [10-12].

For the first time in 2004, K. Kumar Majumdar and D. Dutta Majumder in one grade differential equation tumor model proposed the idea of using fuzzy differential equations and the advantages of its use in modeling [10,11,13]. In 2009, we simulated and analyzed that model by using fuzzy differential inclusion method [14].

In this paper, a model of third degree consists of tumor cells, immune system cells and normal cells are used and method of solving fuzzy differential inclusion are expressed and all areas of response three-dimensional figures using the above method are determined. The purpose of this article is entering uncertainty into tumor model by considering fuzzy model parameters. Fuzzy parameters change crisp system into fuzzy system. Areas of uncertainty for the number of tumor cells in terms of membership function and time are determined. Also in this model, different initial conditions are evaluated by their results of simulation. The main purpose of this article is creation a new view of cancer noted that simulation could be stomata for complex phenomena to determine the uncertainty area. This paper is organized as follows. In Section 2, the model from Depillis in 2003 and its mathematical equations are presented. In Sections 3 and 4 the fuzzy model-based and the method reached the fuzzy surfaces is described, and then simulation results of the different initial conditions are evaluated. Section 5 presents some conclusions.

2. TUMOR MODEL AND ITS MATEMATICAL EQUATIONS

Mathematical model presented in this paper based on the Depillis model [15]. Since the clinical observations, some parameters of the model with uncertainty and range are acceptable, so in this paper these parameters based on clinical observations and based on the possibility of its occurrence are considered fuzzy. In this paper, for the first time, the uncertainty range of tumor cells in terms of time and membership function is drawn and behavior in terms of its possible occurrence is determined.

In this model, T is the population of tumor cells, N is the total population of healthy cells and I the total population of immune cells. The dynamic model of three populations as well as the drug concentration in the blood has been written.

Equations of model are presented as follow:

$$\begin{aligned}
\dot{N} &= r_2 N(1-b_2 N) - c_4 TN - a_3(1-e^{-u})N \\
\dot{T} &= r_1 T(1-b_1 T) - c_2 TI - c_3 TN - a_2(1-e^{-u})T \\
\dot{I} &= s + \frac{\rho IT}{\alpha + T} - c_1 TI - d_1 I - a_1(1-e^{-u})I \\
\dot{u} &= v(t) - d_2 u
\end{aligned} \tag{1}$$

Range of parameters was introduced as follows [15] (see Table I):

- a_1 , a_2 and a_3 are fraction cell kill with $a_3 \le a_1 \le a_2$ and high bandwidth is not more than 0.5.
- $b_1^{-1} = b_2^{-1} = 1$ are carrying capacities.
- c_4, c_3, c_1, c_2 are completion terms.
- s is immune source rate; in our experiments $0 \le s \le 0.5$.
- d_1 and d_2 are death rate of immune cells and death rate of drug, respectively.
- α is immune threshold rate.
- ρ is immune response rate; a clinical range of ρ is the interval (0, 2.5).

3. CONSIDERING FUZZY PARAMETERS

According to the parameters described in the previous section, can be concluded that some model parameters such as s , a_1 , a_2 , a_3 and ρ are non-deterministic and uncertain in model. Thus, for entering the uncertainty in model, these parameters are considered fuzzy. Trapezoidal fuzzy number is written as a/b/c/d, where [a d] defines the support and [b c] is the vertex (or core) that is used in the model. The parameters in the peril immune system disease, are in the area with membership function is equaled one (vertex) and minimum and maximum value of described parameters are on the base and their membership functions are zero (trapezoid fuzzy number). Values of parameters are in **Table 1**. Functions of fuzzy parameters such as s , a_1 , a_2 , a_3 and ρ in term of $\mu(x)$ are located in **Table 2**. Figures of membership functions of $\mu_s(x)$, $\mu_{a_1}(x)$, $\mu_{a2}(x)$, $\mu_{a3}(x)$ and $\mu_\rho(x)$ are shown in **Figure 1**.

4. SIMULATION OF TUMOR MODEL USING FDI

Fuzzy differential inclusion (FDI) is one of the new solving methods. Five parameters are fuzzy parameters and other parameters have precise amount. For modeling the system using FDI method in MATLAB command

Table 1. Fuzzy functions of rigght and left supports of parameters.

parameter	Crisp value	parameter	Crisp and fuzzy value
d_1	**0.2**	ρ	**0/0.009/0.011/2.5**
d_2	**1**	s	**0/0.32/0.34/0.5**
r_1	**1.5**	a_1	**0/0.19/0.21/0.5**
r_2	**1**	a_2	**0/0.29/0.31/0.5**
$c_4 = c_3 = c_1$	**1**	a_3	**0/0.09/0.11/0.5**
c_2	**0.5**	a_2	**1**
α	**0.5**	a_1	**1**

Table 2. Fuzzy and crisp value parameters.

Description	Fuzzy function
Left supprot of (s) parameter	$0.32\mu(x)$
Right supprot of (s) parameter	$-0.16\mu(x)+0.5$
Left supprot of (a_1) parameter	$0.19\mu(x)$
Right supprot of (a_1) parameter	$-0.29\mu(x)+0.5$
Left supprot of (a_2) parameter	$0.29\mu(x)$
Right supprot of (a_2) parameter	$-0.19\mu(x)+0.5$
Left supprot of (a_3) parameter	$0.09\mu(x)$
Right supprot of (a_3) parameter	$-0.39\mu(x)+0.5$
Left supprot of (ρ) parameter	$0.0099\mu(x)$
Right supprot of (ρ) parameter	$-2.489\mu(x)+2.5$

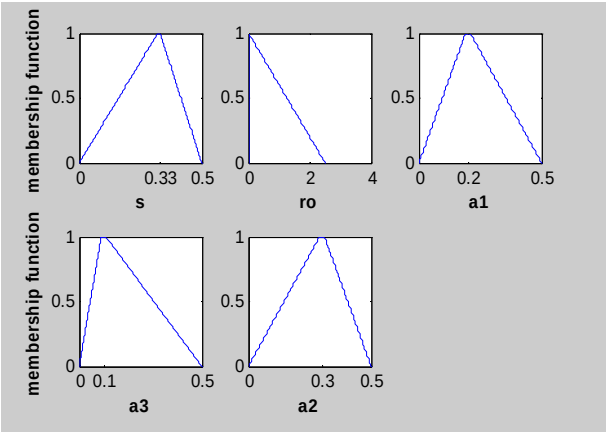

Figure 1. Trapezoidal fuzzy numbers of s, a_1, a_2, a_3 and ρ parameters.

file, the five parameters with regard to fuzzy membership functions are written (analysis with fuzzy numbers is based on using intervals after taking α-cuts), then low and high and middle support of each of the five parameters are considered by low and high and middle support of other five parameters. The figures have been specially created which are computed from all left and right supports of parameters with left and right supports of other parameters, and left and right supports of other parameters with middle supports of other parameters.

There are 32 (2^5 = 32) figures for upper and lower supports of each parameter with other parameters and 80 ($5\times2^{5-1}$=80) figures for each parameter bound middle with upper and lower support of other parameters (In total there are 112 figures). The fuzzy differential equation solutions by the program per membership function from zero to one are found. A total 112 figures per level from zero to one membership function is created. Maximum and minimum of three dimensional fuzzy figures, respectively as the upper bound and lower bound of the final model are considered. The general uncertainties by using fuzzy parameters are into the model. Fuzzy parameters change crisp system to fuzzy system. Upper and lower supports of model are come from maximum and minimum of 112 figures. Thereby uncertainty in the system can be modeled (high and low figures of three dimensional fuzzy figures).

Two different initial conditions of tumor size will insert in the model because the size of recognition of tumor by immune system is a serious element in early disappearance of tumor or in tumor regression.

4.1. Results of Simulation in Large Initial Conditions of Tumor

First, assume that tumor is identified in large size; *i.e.* the initial condition is as follow: $N(0)=1$, $I(0)=0.15$ and $T(0)=0.25$, (this corresponds to a tumor with 0.25×10^{11} cells and $T(0)=0.25$ is normalized value) and in no treatment conditions we found the area of the tumor cells response. Early recognition of tumor by immune system is a serious element in early disappearance of tumor as the tumor obviation will occur if the immune cells can identify the tumor in small size. The clinical detection threshold for a tumor is generally 10^7 cells [16], so the initial tumor volume of 0.25 normalized units is above clinical detection levels and we will expect growth on tumor.

The number of tumor cells based on time and membership function is shown in **Figure 2**. Considering **Figures 2** and **3**, in the case without treatment, the number of cells will increase in the high possibility (membership function = 1). The number of tumor cells will be in the normalized range of 0.53 to 0.59. As shown in the **Figure 2** where the membership function is equaled to zero, number of cancer cells is near zero in on a lower bound and it is one in upper bound, this means that the event can reach tumor cells to zero is zero or on a very low possibility. **Figure 2** is good confirming by the reality. In the reality, due to immune cells, the possibility that the number of cells reaches its maximum value on the whole body is very low, and in this status the possibility that the number of tumor cells to zero, is also very low. It is confirming the fact that decreasing the number of normal cells due to increasing of tumor cells is possible. Since the figures created are occurred by combining uncertainty of all the fuzzy parameters together, so all shapes have as well as confirmation of what happens in the real world.

4.2. Results of Simulation in Small Initial Conditions of Tumor

In different initial condition, assume that tumor is identified in small size; *i.e.* the initial condition is as follow: $N(0)=1$, $I(0)=0.15$ and $T(0)=10^{-5}$, (relatively very small tumor volume in normalized value). Again by using the above method, uncertainty region of

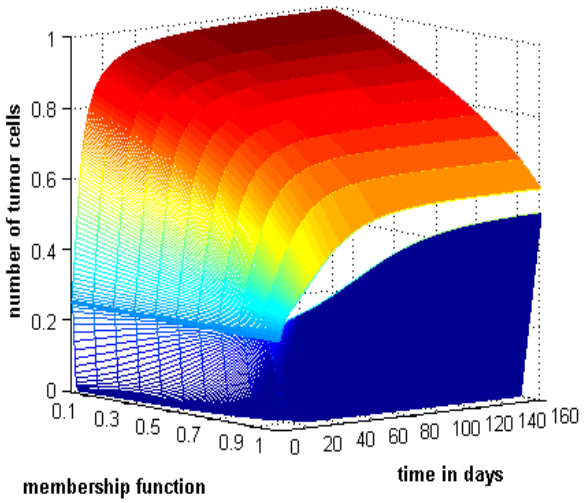

Figure 2. Fuzzy number of tumor cells with respect to time and membership function in tumor identification in small size.

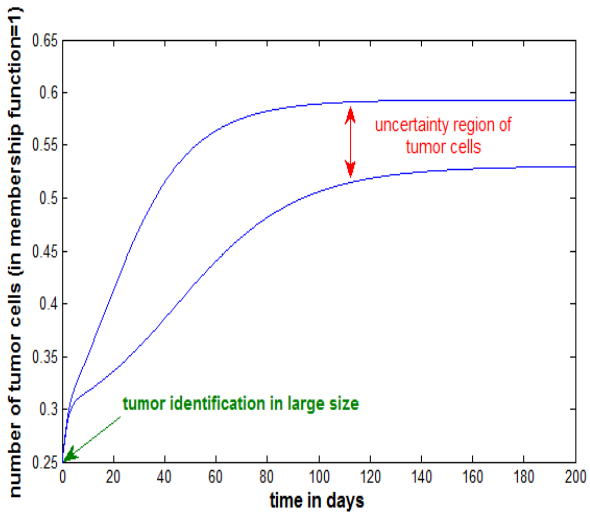

Figure 3. Uncertainty region of tumor cells in membership function=1 and in tumor identification in large size.

tumor cells are found. As later noted, the clinical detection threshold for a tumor is generally 10^7 cells, so the initial tumor volume of $T(0)=10^{-5}$ normalized units is below clinical detection levels and we will expect disappearance of tumor ($T(0)=10^{-5}$ is equivalent to 10^6 cells).

As can be seen in **Figure 4** and **5**, in the highest possibility (membership function = 1) the tumor is disappeared, so population of cells will reduce and there is the chance of death to escape because the immune system cells identify tumor in small size. In addition, **Figure 4** indicates that the number of tumor cells can be increased, and it can be reduced in very low possibility, but the possibility of tumor growth is enormous Although the tumor is in small size, sometimes for unknown reasons, the immune cells can't remove the tumor cells and this is coordinate with unusual events in the reality. For model validation, the information has been used in articles [5,15,16]. According to data from the study of articles and the ways you can get that model in the most possibility (membership function = 1) acts properly and in the less possibility (less membership function), events which may live for each system occur and may well be expected to explain.

5. DISSCUSSIONS AND CONCLUSIONS

This paper by considering fuzzy parameters in the model from the view point of clinical, the uncertainty was entered in to the model, and three-dimensional figures for number of tumor cells based on membership function

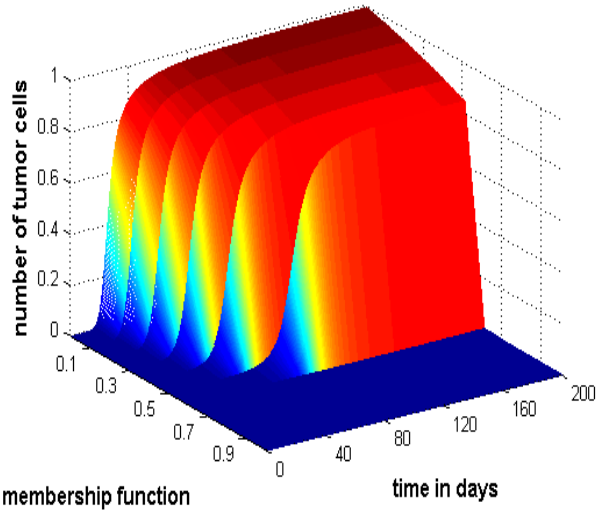

Figure 4. Fuzzy number of tumor cells with respect to time and membership function in tumor identification in small size.

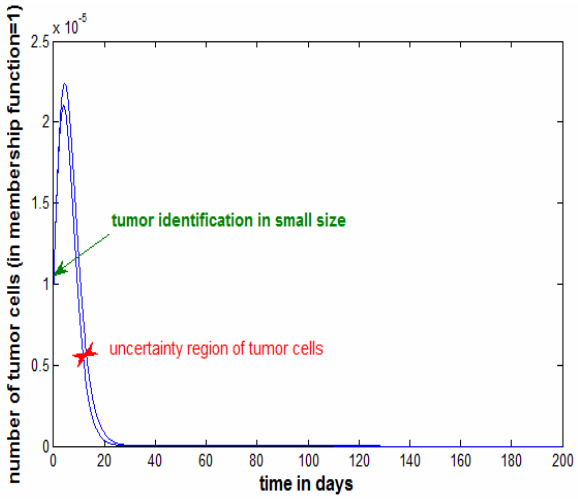

Figure 5. Uncertainty region of tumor cells in membership function=1 and in tumor identification in small size.

and time were figured.

Considering the simulated results, without treatment in large initial condition of tumor, the number of tumor cells is increased, but there is possible to reduce the number of tumor cells in the presence of the immune system, and this possibility with regard to its membership function is very low. The simulations show that in small initial condition of tumor, in regions of possible high, the number of tumor cells is reduced to zero. In areas, that the possible occurrence is low, even in small size of tumor, reduce the number of tumor cells is not possible, and immune system cells can't remove the tumor that this is by considering the complex system of the body being very close to reality. This case may be occurred sometimes for unknown reasons due to different patient conditions, including the power of being different immune system, its ability to be different in the development of tumor cells, and etc. Therefore from the observations obtained that the models based on fuzzy differential equations in three dimensions in term of time and number of cells are appropriate model because of considering the uncertainty in model parameters. It should be noted in the modeling using fuzzy differential equations; the figures created are occurred by combining uncertainty of all the fuzzy parameters together, so all shapes have as well as confirmation of what happens in the real world.

Consequently, the theory of fuzzy differential equations is considered as suitable tool for modeling complex phenomena. By using fuzzy differential equations, the ambiguity in the phenomena can be kept and also behaviors of tumors without the experiment can be predicted.

REFERENCES

[1] Kirschner, D., Panetta, J.C. (1998) Modeling immunotherapy of the tumor–immune interaction. Journal of Mathematical Biology, **37(3)**, 235-252.

[2] Pillis, L.G., Gua, W., Radunskaya, A.E, (2006) Mixed immunotherapy and chemotherapy of tumors: modeling, applications and biological interpretations. *Journal of Theoretical Biology*, **238(4)**, 841-862.

[3] Onofrio, A. (2006), Tumor–immune system interaction: Modeling the tumor-stimulated proliferation of effectors and immunotherapy. *Mathematical Models and Methods in Applied Sciences*, **16(8)**, 1375-1401.

[4] Pillis, L.G., Radunskaya and A.E. (2003) Immune response to tumor invasion, In: Bathe, K. (Ed.), Computational Fluid and Solid Mechanics, **2**. MIT Press, Cambridge, MA, 1661-1668.

[5] Pillis, L.G., Radunskaya and A.E. (2001) A mathematical tumor model with immune resistance and drug therapy: an optimal control approach. *Journal of Theoretical Medicine*, **3(2)**, 79–100.

[6] Derbel, L. (2004) Analysis of a new model for tumor–immune system competition including long time scale effects. Math. Mod. Meth. Appl. S. **14(11)**, 1657-1681.

[7] Jowers, L.J., Buckley, J.J., Reilly, K.D. (2008) Simulating continuous fuzzy systems for fuzzy solution surfaces. *Soft Computer*, **12(3)**, 235-241.

[8] Jowers, L.J., Buckley, J.J., Reilly, K.D. (2007) Simulating continuous fuzzy systems. *Information Sciences*, **177(2)**, 436-448.

[9] Bezdek, J.C. (1993) Fuzzy models, what are they and why? *Transcation of Fuzzy Set and Systems*, **1(1)**.

[10] Majumdar, K.K. (2002/2003) One dimensional fuzzy differential inclusions. *Journal of Intelligent & Fuzzy Systems*, **13(1)**, 1-5.

[11] http://www.cancer.org/Research/CancerFactsFigures/cancer-facts-figures-2006

[12] Zuchowski, T.R. and Wasowski1, J. (2001) Differential equations with fuzzy parameters via differential inclusions. *Journal of Mathematical Analysis and Applications*, **255(1)**, 177-194.

[13] Majumdar, K.K., Majumder, D.D. (2004) Fuzzy differential inclusions in atmospheric and medical cybernetics. *IEEE Transaction on Systems, MAN, and Cybernetics*, **34(2)**.

[14] Esmaili, S.S., Nasrabadi, A.M. (2009) Uncertainty analysis in tumor model with fuzzy parameter. *Proceedings of the CiSENG Conference*, China.

[15] Pillis, L.G., Radunskaya, A.E. (2003) The Dynamics of an optimally controlled tumor model. *A Case Study, Mathemaics and Computer Modeling*, **37(1)**, 1221-1244.

[16] Pillis, L.G., Gua, W., Radunskaya, A.E., (2006) Mixed immunotherapy and chemotherapy of tumors: modeling, applications and biological interpretations. *Journal of Theoretical Biology*, **238(4)**, 841-862.

[17] Majumdar, K.K., Majumder, D.D. (2004) Some studies on uncertainty management in dynamical systems using cybernetic approaches and fuzzy techniques with applications. *International Journal of Systems Science*, **35(15)**, 889-901.

J. Biomedical Science and Engineering, 2010, 3, 1007-1013 **JBiSE**
doi:10.4236/jbise.2010.310131 Published Online October 2010 (http://www.SciRP.org/journal/jbise/).

Immunohistochemical characterization of the rabbit tracheal cartilages

Richard D. Wemer[1], Michael Detamore[2], Robert A. Weatherly[3]

[1]Department of Otolaryngology-Head and Neck Surgery, Park Nicollet Clinics, St. Louis Park, USA
[2]Department of Chemical and Petroleum Engineering, University of Kansas, Kansas City, USA
[3]Department of Otolaryngology-Head and Neck Surgery, University of Kansas, Kansas City, USA
Email: wemerr@parknicollet.com; detamore@ku.edu; rweatherly@kumc.edu

Received 5 August 2010; revised 18 August 2010; accepted 27 August 2010.

ABSTRACT

The objective of this study was to immunohistochemically elucidate the major extracellular matrix constituents of rabbit tracheal cartilage. The impetus for this project is the need for crucial design and validation criteria for tissue engineering juxtaposed with the conspicuous lack of trachea extracellular matrix data in the literature. Tracheal tissue specimens were harvested from New Zealand White rabbits, and were immunostained for collagen I, collagen II, aggrecan and decorin; and a Verhoeff-Van Gieson stain was performed to visualize elastin. The most striking result was the highly organized relationship between distinct fibrous (containing collagen I, decorin and elastin) and hyaline-like (containing collagen II and aggrecan) regions of the tracheal wall. The tracheal cartilage stained strongly with collagen II throughout, with periodic bands of aggrecan in the tracheal arches, meaning that there were areas void of aggrecan immunostaining alternating with areas with strong aggrecan immunostaining. In contrast, the periphery of the cartilage and the perichondrium itself exhibited strong collagen I staining and no collagen II staining. Elastin fibers and decorin were also detected along the periphery of the cartilage in the perichondrium and corresponded highly with the distribution of collagen I staining. The body of the rabbit trachea is therefore composed of a hyaline-cartilage structure primarily made of collagen II and bands of aggrecan, surrounded by a fibrous region composed of elastin and collagen I, indicative of a flexible tissue with distinct regions of compressive integrity. This information will be a valuable reference to future tissue engineering efforts in the creation of a biosynthetic substitute for laryngotracheal reconstruction.

Keywords: Trachea; Collagen; Aggrecan; Decorin; Elastin.

1. INTRODUCTION

The treatment of subglottic stenosis is a difficult clinical problem that may require invasive measures at both primary and donor sites. After failure of more conservative measures, open airway surgery is often performed, which requires donor cartilage tissue to be harvested, usually a segment of autologous costal cartilage. Such procedures are complicated by long healing times, donor site complications including pain and pneumothorax, size and shape mismatches, and prolonged hospital stays.

Tissue-engineered cartilage offers a viable alternative to these highly morbid procedures. Donor site complications could be eliminated, and tissue could be shaped appropriately for specific defects in the tracheal wall. Tissue engineering attempts for the trachea are still preliminary, from a clinical perspective, at this time. Nevertheless, tracheal tissue engineering is a burgeoning field [1-13], and the level of urgency is high for providing crucial characterization data for tissue engineers, both to develop new ideas for design strategies for recapitulating the native tracheal structure, and to elucidate validation criteria.

We have used rabbits in previous tracheal defect reconstruction studies [14-16], as rabbits are an ideal animal model for early-stage *in vivo* investigations. A review of animal models for trachea research suggested that large animals such as goats and sheep should be used for tracheal tissue engineering based on size and cell number [17]. However, the rabbit has heretofore been a more commonly used animal model for tracheal tissue engineering and is a logical stepping stone en route to larger animal models. For this reason, we have selected the rabbit for our immunohistochemical charac-

terization of the trachea.

In contrast to the trachea, the extracellular matrix of the vocal folds of the larynx (which lie just superior to the trachea) continues to be a popular research topic, including studies of collagen types, elastin, and proteoglycans [18-36]. However, despite the wide variety of trachea characterization efforts, ranging from camel trachea dimensions [37] to dolphin trachea biomechanics [38], and even speculation of airflow in dinosaur tracheas [39], very little is known about the distribution of key extracellular matrix components of the trachea.

Evans and colleagues presented a nice series of matrix studies on the basement membrane zone associated with the trachea in monkeys and rats [40-42]. However, only a handful of studies have begun to elucidate the collagen and/or elastin content of the trachea in guinea pigs, mice and rats [43-47], in pigs [48, 49], and in humans [50, 51]. It is known that collagen fibers in the trachea run obliquely and are intermingled [43, 51, 52], that collagen I appears predominately in the perichondrium and collagen II appears predominately in the cartilaginous tracheal body [45-47, 50]. It is also known that elastic fibers may be abundant in the perichondrium of the trachea [36, 43, 44], forming an extensive network that extends into the posterior membranous tracheal wall [36]. With regard to elastin, it is noteworthy that a pair of studies found trappin-2 (also known as elafin), an elastase inhibitor, in the trachea [48, 49].

In addition, specific glycosaminoglycans (GAGs) were identified immunohistochemically in rat tracheas, although the heterogeneous distributions of chondroitin-4-sulfate and chondroitin-6-sulfate were not in agreement [47]. Toluidine blue O staining in humans also revealed a heterogeneous GAG distribution [51], although the distributions of specific proteoglycans was not identified. It is also known that regions of the trachea are calcified, although there is a debate as to whether the tissue is commonly ossified [46, 47, 50, 53].

What was not known prior to the current study was the distribution of key proteoglycans, which have important functional roles, and whether their distribution coincided with the distribution of collagen types I and II. Moreover, it was unknown whether the distribution of collagens I and II observed in the trachea of rats [45-47] and humans [50] would be observed in the rabbit trachea as well. Therefore, the objective of the current study was to identify the distributions of elastin, collagen I, and collagen II; as well as two key proteoglycans (aggrecan and decorin) in the rabbit trachea. These matrix components were chosen based on their relevance to tissue engineering, implications for mechanical performance, and to establish relative distribution and abundance for validation of engineered constructs. Given that collagen II and aggrecan are associated with hyaline cartilage, whereas elastin, collagen I and decorin are associated primarily with fibrous tissues [54], we hypothesized that aggrecan would coincide with collagen II distribution, and that decorin would coincide with collagen I and elastin distribution. The relative distributions of these key extracellular matrix components will be crucial to tissue engineering efforts that address surgical repair of laryngotracheal stenosis.

2. METHODS

2.1. Specimen Preparation

Four New Zealand White rabbits were obtained and sacrificed at adult age. All rabbits were male and weighed approximately 9 lbs. They were sacrificed after undergoing a single cardiovascular physiology experiment not relevant to tracheal protein structure or synthesis. Immediately after sacrifice, the larynx-trachea complexes were collected and stored in PBS-saturated gauze at –20˚C prior to sectioning. Serial 10 μm frozen sections were taken from each of the samples. Sections were mounted on slides, fixed in chilled acetone for 20 min, and then stored at –20˚C until further use.

2.2. Verhoeff-Van Gieson Elastic Tissue Stain

Fixed rabbit tissue samples were stained for elastin. The samples were first placed in an iron hematoxylin solution for 10 min and then rinsed in distilled water and differentiated in 2% ferric chloride. After rinsing in distilled water and placing in 95% alcohol, the samples were counterstained with Van Gieson's solution (Sigma Aldrich; St. Louis, MO) for 4 min. The samples were then dehydrated in graded alcohol and then cleared in xylene and mounted.

2.3. Immunohistochemistry

Slides were placed in a Biogenex i6000 (San Ramon, CA) autostainer and rehydrated for 5 min in PBS. Endogenous peroxidase activity was quenched with 1% hydrogen peroxide in methanol for 30 min. Specimens were blocked with serum from the secondary antibody host for 20 min and followed by incubation with the primary antibody for 60 min (dilutions provided in **Table 1**). Mouse monoclonal IgG anti-collagen I and mouse monoclonal IgG anti-collagen II antibodies were obtained from Accurate Chemical and Scientific (Westbury, NY) and Chondrex, LLC (Redmond, WA), respectively. Mouse monoclonal IgG anti-aggrecan and sheep polyclonal IgG anti-decorin were obtained from Abcam (Cambridge, MA). Negative controls were assessed by omission of the primary antibody, and the absence of non-specific staining was verified.

The specimens were then incubated with the appro-

Table 1. Immunohistochemistry primary antibody dilutions.

ECM Constituent	*Primary Antibody Dilution*
Collagen I	1,500
Collagen II	1,000
Decorin	100
Aggrecan	50

priate secondary antibody for 30 min (1:300 dilution), followed by an avidin-biotinylated enzyme complex for 30 min and then 3,3'-diaminobenzidine for 4 min. Avidin-biotin complex kits were obtained from Vector Laboratories (Burlingame, CA). The kits consisted of a biotinylated secondary antibody (horse anti-mouse IgG, or rabbit anti-sheep IgG), the corresponding host animal serum, and an avidin-biotinylated enzyme complex. Slides were removed from the autostainer, counterstained with hematoxylin, dehydrated in graded ethanol and mounted.

3. RESULTS

3.1. Collagen II and Aggrecan

The tracheal hyaline cartilage stained strongly with collagen II throughout the body of the cartilage ring. Outside of the cartilage ring, no collagen II staining was detected **Figure 1(a)**. Also, within the tracheal body, we did observe staining for aggrecan. Aggrecan, however, had a different staining pattern within the tracheal body. The body of the cartilage exhibited a striped effect where there were areas void of aggrecan immunostaining, alternating with areas displaying strong aggrecan immunostaining. This was observed throughout all sections of the tracheal cartilage, on multiple slides, and from all observed animal specimens. There was also some aggrecan staining in the surrounding tissues outside of the cartilage ring **Figure 1(b)**.

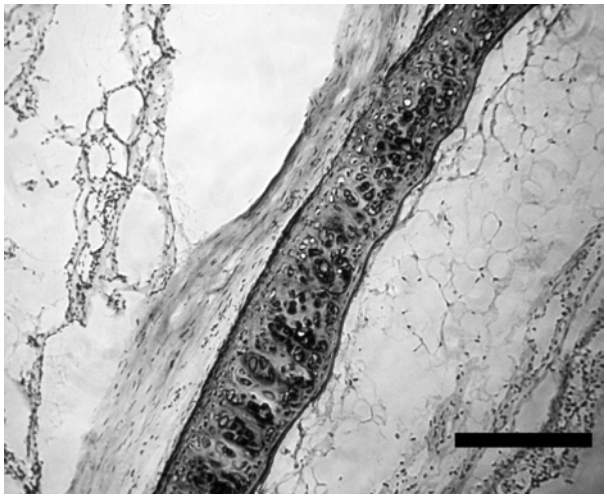

(a)

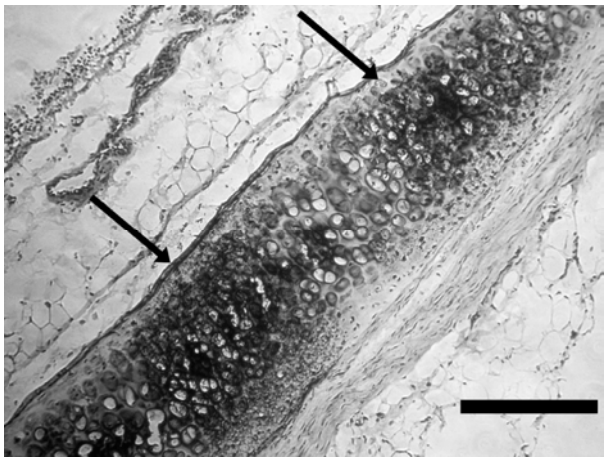

(b)

Figure 1. Collagen II and Aggrecan Localization. Tracheal cartilage with collagen II (brown immunostain) demonstrated throughout the tracheal arch (a). A striped effect (arrows) was observed in the tracheal arch with aggrecan immunostaining (b). Hematoxylin counterstain. Scale bars are 50 μm (a) and 100 μm (b).

3.2. Collagen I, Decorin, and Elastin

Collagen I immunostaining was observed around the periphery of the tracheal body cartilage. There was no immunostaining in the cartilage body itself **Figure 2(a)**. Decorin staining was also identified in the tracheal cartilage samples. Decorin was seen in the periphery of the cartilage and perichondrium, as well as the surrounding soft tissues. This distribution was very similar to the distribution seen with collagen I staining **Figure 2(b)**, with no decorin staining being observed in the hyaline cartilage itself.

Elastin fibers, detected with the Verhoeff-Van Gieson stain, were also located along the periphery of the cartilage within the perichondrium. No staining was seen in the pericellular areas or in within the cartilage extracellular matrix. Elastin staining corresponded highly with the distribution of collagen I and decorin staining **Figure 2(c)**.

4. COMMENT

To the best of our knowledge, the current study is the first to describe the extracellular matrix of the rabbit trachea, and more importantly, the first to investigate the distribution of key proteoglycans in the trachea and correlate their distribution with collagens I and II. The current study was in agreement with previous findings in other species that found collagens I and II in mutually exclusive regions [45-47, 50], with the former present in only the surrounding perichondrium and the latter present in only the body of the tracheal cartilage. Further-

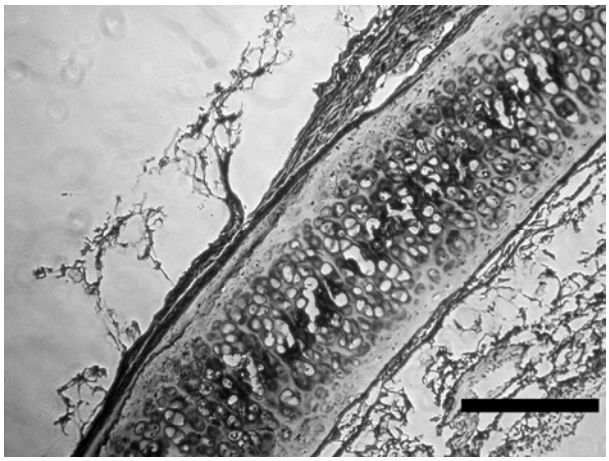

(a)

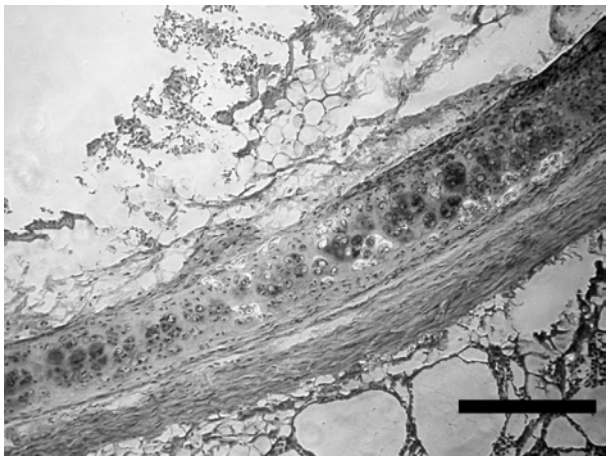

(b)

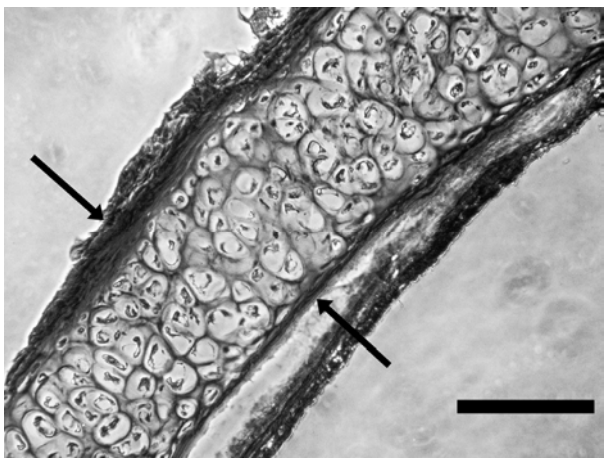

(c)

Figure 2. Collagen I, Decorin and Elastin Localization. Collagen I was peripheral to the tracheal arch (a). Decorin was also peripheral to the tracheal arch (b). Verhoeff-Van Gieson stain for elastin (black bands marked by arrows) (c). Counterstain for (a) and (b) was hematoxylin. Scale bars are 100 μm (a, c) and 50 μm (b).

more, the current study was in agreement with a previous study in guinea pigs that found elastin in the tracheal periphery [43].

Although the distributions of three specific GAGs (most likely chondroitin-4-sulfate, chondroitin-6 sulfate and keratan sulfate) were elucidated in rats [47], the relevant and functionally more significant distribution of proteoglycans in the trachea was heretofore unknown. As hypothesized, aggrecan and collagen II distribution coincided, and decorin distribution was consistent with collagen I and elastin. However, an interesting and unexpected finding was the observation of a striped or "layered" effect with regard to the staining pattern of aggrecan (**Figure 3**). This observation is the first of its kind and its significance is not yet clear. Nevertheless, it is likely that this pattern of aggrecan distribution may have an important functional role. For example, periodic regions of increased compressive integrity, interspersed with regions of more flexibility, may provide the tracheal cartilaginous arch with a balance of flexibility and rigidity. The need for aggrecan to promote such a balance in a tissue engineered construct is a hypothesis worth exploring in the future.

Both collagen I and elastin were found to stain around the periphery of the tracheal body. Decorin, which has been described to "decorate" collagen, was also found in the extracellular matrix surrounding the tracheal body. Previous studies have demonstrated a decorin-collagen interaction, concluding that decorin plays a role in regulating collagen fiber formation [55]. One study demonstrated a decrease in collagen fiber diameter, as well as altered collagen morphology in decorin-deficient mice [56]. It may, therefore, be possible that the close alliance of decorin and collagen I are necessary for structural integrity of the tracheal arches, while the relationship of aggrecan and collagen II are primarily responsible for optimal flexibility of the tracheal cartilages.

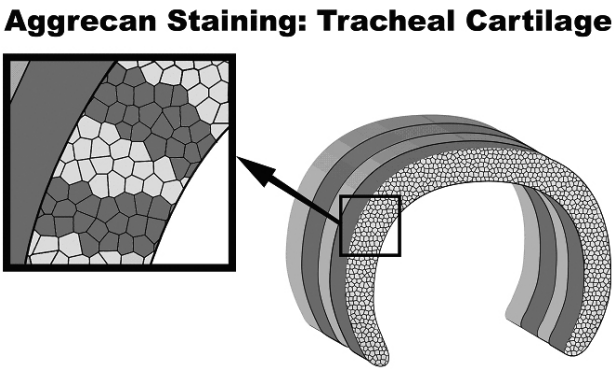

Figure 3. Schematic of Aggrecan Staining in Tracheal Cartilage. Aggrecan was located in such a way as to demonstrate a "layered" or "striped" appearance within the body of the tracheal cartilagenous arch. See also **Figure 1(b)**.

The biochemical characterization of the rabbit trachea is an important step for a tissue engineering solution to the treatment of airway stenosis. This animal model has been employed for reasons presented earlier, as well as for the rabbit laryngotracheal segment's size closely approximating that of a young pediatric population, of high relevance to tissue engineering for use in treating human disease. In demonstrating the composition of a portion of the laryngotracheal complex, we can then attempt to engineer a tissue that possesses properties similar to that of the native tissue. Future studies will be required to elucidate whether any part of the tracheal body possesses an osseous character (*e.g*., alkaline phosphatase activity and collagen I in addition to calcium) [46, 47, 50, 53]. Moreover, other trachea characterization efforts will be crucial for construct design and analysis, in particular, studies of the biomechanics of the trachea [51, 57-59], the fluid dynamics of air flow through the trachea [60-65], and characterization of surrounding tissues such as the tracheal smooth muscle.

The identification of native tracheal proteins and proteoglycans is critical to the actual construction of tissue-engineered implants. The identification of proteins such as collagen I and II, as well as proteoglycans like decorin and aggrecan, may ultimately lend information as to what substrates are required to produce a suitable cartilage graft. We must, however, remain cautious when considering the need to replicate native tracheal cartilage. The biochemical composition of cartilage is complex, and an exact reproduction of the structure may be neither feasible nor warranted to successfully reconstruct the trachea after injury to a tracheal segment. For example, a newly formed cartilage segment may merely need to possess rigidity, but not maximal flexibility, depending on the size and length of the diseased tracheal segment to be replaced. Additional aspects of tracheal reconstruction such as mucosal resurfacing and vascular supply to large segments, as highlighted by the Leuven Tracheal Transplant Group from Belgium [66], will also need to be addressed as the process of engineered cartilage replacement for tracheal defects becomes more clearly defined.

In the current study, we have demonstrated that the body of the tracheal ring is composed of collagen II and bands of aggrecan (hyaline-like tissue), surrounded by a supporting matrix composed of collagen I, elastin, and decorin (fibrous-like tissue). Looking forward, the information obtained in the current study can be applied to the construction of a bioengineered tracheal graft. In an endeavor to replicate the tracheal cartilage ultrastructure, an ideal graft would possess enough rigidity to withstand stresses, but remain flexible enough to allow for motion and other functional measures. Future studies as described above will be required to correlate the structure of the tracheal cartilage to its function (fluid mechanics of airflow and biomechanical integrity).

5. ACKNOWLEDGMENTS

All of the authors in this study had full access to all the data in the study and take responsibility for the integrity of the data and the accuracy of the data analysis.

REFERENCES

[1] Tan, Q., Steiner, R., Hoerstrup, S.P and Weder, W. (2006) Tissue-engineered trachea: History, problems and the future**.** *Eur J Cardiothorac Surg*, **30**, 782-786.

[2] Kojima, K. and Vacanti, C.A. (2004) Generation of a tissue-engineered tracheal equivalent**.** *Biotechnol Appl Biochem*, **39**, 257-262.

[3] Bucheler, M. and Haisch, A. (2003) Tissue engineering in otorhinolaryngology. *DNA Cell Biol*, **22**, 549-564.

[4] Grillo, H.C. (2002) Tracheal replacement: a critical review. *Ann Thorac Surg*, **73**, 1995-2004.

[5] Grillo, H.C. (2003) Tracheal replacement. *J Thorac Cardiovasc Surg*, **125**, 975.

[6] Grillo, H.C. (2005) Bioengineered airway tissue**.** *J Thorac Cardiovasc Surg*, **129**, 1208.

[7] Birchall, M. and Macchiarini, P. (2008) Airway transplantation: a debate worth having? *Transplantation*, **85**, 1075-1080.

[8] Doss, A.E., Dunn, S.S., Kucera, K.A., Clemson, L.A. and Zwischenberger, J.B. (2007) Tracheal replacements: Part 2. *ASAIO J*, **53**, 631-639.

[9] Kucera, K.A., Doss, A.E., Dunn, S.S., Clemson L.A. and Zwischenberger J.B. (2007) Tracheal replacements: Part 1**.** *ASAIO J*, **53**, 497-505.

[10] Macchiarini, P., Jungebluth, P., Go, T., Asnaghi, M.A., Rees, L.E., Cogan, T.A., Dodson, A., Martorell, J., Bellini, S., Parnigotto, P.P., Dickinson, S.C., Hollander, A.P., Mantero, S., Conconi, M.T. and Birchall, M.A. (2008) Clinical transplantation of a tissue-engineered airway. *Lancet*.

[11] Steger, V., Hampel, M., Trick, I., Muller, M. and Walles, T. (2008) Clinical tracheal replacement: transplantation, bioprostheses and artificial grafts. *Expert Rev Med Devices*, **5**, 605-612.

[12] Asnaghi, M.A., Jungebluth, P., Raimondi, M.T., Dickinson, S.C., Rees, L.E., Go, T., Cogan, T.A., Dodson, A., Parnigotto, P.P., Hollander, A.P., Birchall, M.A., Conconi, M.T., Macchiarini, P. and Mantero, S. (2009) A double-chamber rotating bioreactor for the development of tissue-engineered hollow organs: from concept to clinical trial. *Biomaterials*, **30**, 5260-5269.

[13] Jungebluth, P., Go, T., Asnaghi, A., Bellini, S., Martorell, J., Calore, C., Urbani, L., Ostertag, H., Mantero, S., Conconi, M.T. and Macchiarini, P. (2009) Structural and morphologic evaluation of a novel detergent-enzymatic tissue-engineered tracheal tubular matrix. *J Thorac Cardiovasc Surg*, **138**, 586-593.

[14] Grimmer, J.F., Gunnlaugsson, C.B., Alsberg, E., Murphy, H.S., Kong, H.J., Mooney, D. J. and Weatherly, R.A. (2004) Tracheal reconstruction using tissue-engineered cartilage. *Arch Otolaryngol Head Neck Surg*, **130**, 1191-

1196.
[15] Robey, T.C., Eiselt, P.M., Murphy, H.S., Mooney, D.J. and Weatherly, R.A. (2000) Biodegradable external tracheal stents and their use in a rabbit tracheal reconstruction model. *Laryngoscope*, **110**, 1936-1942.
[16] Robey, T.C., Valimaa, T., Murphy, H.S., Tormala, P., Mooney, D.J. and Weatherly, R.A. (2000) Use of internal bioabsorbable PLGA "finger-type" stents in a rabbit tracheal reconstruction model. *Arch Otolaryngol Head Neck Surg*, **126**, 985-991.
[17] Hallers, E.J., Rakhorst, G., Marres, H.A., Jansen, J.A., Kooten, T.G., Schutte, H.K., Loon, J.P., Houwen, E.B. and Verkerke, G.J. (2004) Animal models for tracheal research. *Biomaterials*, **25**, 1533-1543.
[18] Buhler, R.B., Sennes, L.U., Mauad, T., Melo, E.C., Silva, L.F. and Saldiva, P.H. (2008) Collagen fiber and versican distribution within the lamina propria of fetal vocal folds. *Laryngoscope*, **118**, 371-374.
[19] Butler, J.E., Hammond, T.H. and Gray, S.D. (2001) Gender-related differences of hyaluronic acid distribution in the human vocal fold. *Laryngoscope*, **111**, 907-911.
[20] Hammond, T.H., Gray, S.D. and Butler, J.E. (2000) Age- and gender-related collagen distribution in human vocal folds. *Ann Otol Rhinol Laryngol*, **109**, 913-920.
[21] Gray, S.D., Titze, I.R., Alipour, F. and Hammond, T.H. (2000) Biomechanical and histologic observations of vocal fold fibrous proteins. *Ann Otol Rhinol Laryngol* **109**, 77-85.
[22] Gray, S.D., Titze, I.R., Chan, R. and Hammond, T.H, (1999) Vocal fold proteoglycans and their influence on biomechanics. *Laryngoscope*, **109**, 845-854.
[23] Hammond, T.H., Zhou, R., Hammond, E.H., Pawlak, A. and Gray, S.D. (1997) The intermediate layer: a morphologic study of the elastin and hyaluronic acid constituents of normal human vocal folds. *Journal of Voice*, **11**, 59-66.
[24] Pawlak, A.S., Hammond, T., Hammond, E. and Gray, S.D. (1996) Immunocytochemical study of proteoglycans in vocal folds. *Ann Otol Rhinol Laryngol*, **105**, 6-11.
[25] Chan, R.W., Fu, M., Young, L. and Tirunagari, N. (2007) Relative contributions of collagen and elastin to elasticity of the vocal fold under tension. *Ann Biomed Eng*, **35**, 1471-1483.
[26] Melo, E.C., Lemos, M., Aragao, X.F.J., Sennes, L.U., Nascimento, S.P.H. and Tsuji, D.H. (2003) Distribution of collagen in the lamina propria of the human vocal fold. *Laryngoscope*, **113**, 2187-2191.
[27] Sivasankar, M. and Ivanisevic, A. (2007) Atomic force microscopy investigation of vocal fold collagen. *Laryngoscope*, **117**, 1876-1881.
[28] Tateya, T., Tateya, I. and Bless, D.M.(2006) Collagen subtypes in human vocal folds. *Ann Otol Rhinol Laryngol*, **115**, 469-476.
[29] Tateya, T., Tateya, I. and Bless, D.M. (2007) Immuno-scanning electron microscopy of collagen types I and III in human vocal fold lamina propria. *Ann Otol Rhinol Laryngol*, **116**, 156-159.
[30] Sakae, F.A,, Imamura, R., Sennes, L.U., Mauad, T., Saldiva, P.H. and Tsuji, D.H. (2008) Disarrangement of collagen fibers in Reinke's edema. *Laryngoscope*, **118**, 1500-1503.
[31] Sato, K., Hirano, M. and Nakashima, T. (2003) 3D structure of the macula flava in the human vocal fold. *Acta Otolaryngol*, **123**, 269-273.
[32] Sato, K., Hirano, M. and Nakashima, T. (2002) Age-related changes of collagenous fibers in the human vocal fold mucosa. *Ann Otol Rhinol Laryngol*, **111**, 15- 20.
[33] Sato, K. and Hirano, M. (1995) Histologic investigation of the macula flava of the human vocal fold. *Ann Otol Rhinol Laryngol*, **104**, 138-143.
[34] Hirano, S., Minamiguchi, S., Yamashita, M., Ohno, T., Kanemaru, S.I. and Kitamura, M. (2008) Histologic characterization of human scarred vocal folds. *Journal of Voice*, **Epub**.
[35] Ximenes, F.J.A, Tsuji, D.H., Nascimento, P.H. and Sennes, L.U. (2003) Histologic changes in human vocal folds correlated with aging: A histomorphometric study. *Ann Otol Rhinol Laryngol*, **112**, 894-898.
[36] Kamel, K.S., Beckert, L.E. and Stringer, M.D. (2009) Novel insights into the elastic and muscular components of the human trachea. *Clin Anat*, **22**, 689-697.
[37] Al-Zghoul, M.F., Ismail, Z.B., Al-Rukibat, R.K. and Al-Majali, A.M. (2006) A quantitative study on the trachea of young Arabian camels (Camelus dromedarius). *J Camel Pract Res*, **13**, 129-133.
[38] Cozzi, B., Bagnoli, P., Acocella, F. and Costantino, M.L. (2005) Structure and biomechanical properties of the trachea of the striped dolphin Stenella coeruleoalba: evidence for evolutionary adaptations to diving. *Anat Rec A Discov Mol Cell Evol Biol*, **284**, 500-510.
[39] Pierson, D.J. (2009) The physiology of dinosaurs: circulatory and respiratory function in the largest animals ever to walk the earth. *Respir Care*, **54**, 887-911.
[40] Evans, M.J., Fanucchi, M.V., Baker, G.L., Winkle, L.S., Pantle, L.M., Nishio, S.J., Schelegle, E.S., Gershwin, L.J., Miller, L.A., Hyde, D.M. and Plopper, C.G. (2004) The remodelled tracheal basement membrane zone of infant rhesus monkeys after 6 months of recovery. *Clin Exp Allergy*, **34**, 1131-1136.
[41] Evans, M.J., Winkle, L.S., Fanucchi, M.V., Toskala, E., Luck, E.C., Sannes, P.L. and Plopper, C.G. (2000) Three-dimensional organization of the lamina reticularis in the rat tracheal basement membrane zone. *Am J Respir Cell Mol Biol*, **22**, 393-397.
[42] Evans, M.J., Fanucchi, M.V., Baker, G.L., Winkle, L.S., Pantle, L.M., Nishio, S.J., Schelegle, E.S., Gershwin, L.J., Miller, L.A., Hyde, D.M., Sannes, P.L. and Plopper, C.G. (2003) Atypical development of the tracheal basement membrane zone of infant rhesus monkeys exposed to ozone and allergen. *Am J Physiol Lung Cell Mol Physiol* , **285**, L931-939.
[43] Amiri, M.H. and Gabella, G. (1988) Structure of the guinea-pig trachea at rest and in contraction. *Anat Embryol (Berl)*, **178**, 389-397.
[44] Maki, J.M., Sormunen, R., Lippo, S., Kaarteenaho, W.R, Soininen, R. and Myllyharju, J. (2005) Lysyl oxidase is essential for normal development and function of the respiratory system and for the integrity of elastic and collagen fibers in various tissues. *Am J Pathol*, **167**, 927-936.
[45] Sasano, Y., Takahashi, I., Zhu, J.X., Ohtani, H., Mizoguchi, I. and Kagayama, M. (2001) Gene and protein expressions of type I collagen are regulated tissue-specifically in rat hyaline cartilages in vivo. *Eur J*

Morphol, **39**, 149-154.

[46] Sasano, Y., Takahashi, I., Mizoguchi, I., Kagayama, M., Takita, H. and Kuboki, Y. (1998) Type X collagen is not localized in hypertrophic or calcified cartilage in the developing rat trachea. *Anat Embryol (Berl)*, **197**, 399-403.

[47] Sasano, Y., Mizoguchi, I., Furusawa, M., Aiba, N., Ohtani, E., Iwamatsu, Y. and Kagayama, M. (1993) The process of calcification during development of the rat tracheal cartilage characterized by distribution of alkaline phosphatase activity and immunolocalization of types I and II collagens and glycosaminoglycans of proteoglycans**.** *Anat Embryol (Berl)*, **188**, 31-39.

[48] Tamechika, I., Itakura, M., Saruta, Y., Furukawa, M., Kato, A., Tachibana, S. and Hirose, S. (1996) Accelerated evolution in inhibitor domains of porcine elafin family members. *J Biol Chem*, **271**, 7012-7018.

[49] Suzuki, Y., Furukawa, M., Abe, J., Kashiwagi, M. and Hirose, S. (2000) Localization of porcine trappin-2 (SKALP/elafin) in trachea and large intestine by in situ hybridization and immunohistochemistry. *Histochem Cell Biol*, **114**, 15-20.

[50] Kusafuka, K., Yamaguchi, A., Kayano, T. and Takemura, T. (2001) Ossification of tracheal cartilage in aged humans: A histological and immunohistochemical analysis. *J Bone Miner Metab*, **19**, 168-174.

[51] Roberts, C.R., Rains, J.K., Pare, P.D., Walker, D.C., Wiggs, B. and Bert, J.L. (1998) Ultrastructure and tensile properties of human tracheal cartilage. *J Biomech*, **31**, 81-86.

[52] Rao, R.A., Mehta, M.R. and Toussaint, K.C. (2009) Fourier transform-second-harmonic generation imaging of biological tissues. *Opt Express*, **17**, 14534-14542.

[53] Maki, K., Hayashi, S., Nishioka, T., Kimura, M. and Noguch, T.: A new type of matrix vesicles is found in fetal bovine tracheal cartilage. *Connect Tissue Res*, **41**, 109-115.

[54] Detamore, M.S. and Athanasiou, K.A. (2003) Structure and function of the temporomandibular joint disc: implications for tissue engineering. *J Oral Maxillofac Surg*, **61**, 494-506.

[55] Poole, A.R., Webber, C., Pidoux, I., Choi, H. and Rosenberg, L.C. (1986) Localization of a dermatan sulfate proteoglycan (DS-PGII) in cartilage and the presence of an immunologically related species in other tissues. *J Histochem Cytochem*, **34**, 619-625.

[56] Danielson, K.G., Baribault, H., Holmes, D.F., Graham, H., Kadler, K.E. and Iozzo, R.V. (1997) **T**argeted disruption of decorin leads to abnormal collagen fibril morphology and skin fragility. *Journal of Cell Biology*, **136**, 729-743.

[57] Teng, Z., Ochoa, I., Li, Z., Lin, Y., Rodriguez, J.F., Bea, J.A. and Doblare, M. (2008) Nonlinear mechanical property of tracheal cartilage: A theoretical and experimental study. *J Biomech*, **41**, 1995-2002.

[58] Miller, T.L., Altman, A.R., Tsuda, T. and Shaffer, T.H. (2007) An ultrasound imaging method for in vivo tracheal bulk and Young's moduli of elasticity. *J Biomech*, **40**, 1615-1621.

[59] Rains, J.K., Bert, J.L., Roberts, C.R. and Pare, P.D. (1992) Mechanical properties of human tracheal cartilage. *J Appl Physiol*, **72**, 219-225.

[60] Jayaraju, S.T., Paiva, M., Brouns, M., Lacor, C. and Verbanck, S. (2008) Contribution of upper airway geometry to convective mixing. *J Appl Physiol*, **105**, 1733-1740.

[61] Russo, J., Robinson, R. and Oldham, M.J. (2008) Effects of cartilage rings on airflow and particle deposition in the trachea and main bronchi. *Med Eng Phys*, **30**, 581-589.

[62] Rakesh, V., Rakesh, N.G,. Datta, A.K., Cheetham, J. and Pease, A.P. (2008) Development of equine upper airway fluid mechanics model for Thoroughbred racehorses. *Equine Vet J*, **40**, 272-279.

[63] Nazridoust, K. and Asgharian, B. (2008) Unsteady-state airflow and particle deposition in a three-generation human lung geometry. *Inhal Toxicol*, **20**, 595-610.

[64] Isaacs, K.K., Schlesinger, R.B. and Martonen, T.B. (2006) Three-dimensional computational fluid dynamics simulations of particle deposition in the tracheobronchial tree. *J Aerosol Med*, **19**, 344-352.

[65] Martonen, T.B., Zhang, Z., Yu, G. and Musante, C.J. (2001) Three-dimensional computer modeling of the human upper respiratory tract. *Cell Biochem Biophys*, **35**, 255-261.

[66] Delaere, P., Vranckx, J., Verleden, G., Leyn, P. and Raemdonck, D. (2010) Tracheal allotransplantation after withdrawal of immunosuppressive therapy. *N Engl J Med*, **362**, 138-145.

J. Biomedical Science and Engineering, 2010, 3, 1014-1021 **JBiSE**
doi:10.4236/jbise.2010.310132 Published Online October 2010 (http://www.SciRP.org/journal/jbise/).

Foetal heart rate variability frequency characteristics with respect to uterine contractions

Mario Cesarelli*, Maria Romano, Mariano Ruffo, Paolo Bifulco, Giulio Pasquariello

DIBET - University "Federico II", Naples, Italy;
*Corresponding author.
Email: cesarell@unina.it; mariarom@unina.it; mariano.ruffo@libero.it; pabifulc@unina.it; giulio.pasquariello@unina.it

Received 6 August 2010; revised 9 September 2010; accepted 13 September 2010.

ABSTRACT

Monitoring foetal health is important to appropriately plan pregnancy management and delivery. Cardiotocography (CTG) is one of the most employed diagnostic techniques. Because CTG interpretation still lacks of complete reliability, new methods of interpretation and parameters are necessary to further support physicians' decisions. To this aim, indexes related to variability of foetal heart rate (FHRV) are particularly studied. Frequency components of FHRV and their modifications can be analysed by applying a time-frequency approach, which allows for a distinct understanding of the spectral components related to foetal reactions to internal and external stimuli and their change over time. Being uterine contractions (UC) strong stimuli for the foetus and his autonomic nervous system (ANS), it is worth exploring the FHRV response to UC. This study analysed modifications of FHRV frequency characteristics with respect to 108 UC (relative to 35 healthy foetuses). Results showed a statistically significant (*t*-test, $p < 0.01$) power increase of the FHRV in both LF and HF bands in correspondence of the contractions. Moreover, we observed a shift to higher values of the maximum frequency contained in the signal corresponding to the power increase. Such modifications of the FHRV power spectrum can be a sign of ANS reaction and therefore represent additional, objective information about foetal reactivity and health during labour.

Keywords: Foetal Heart Rate, Uterine Contractions, Foetal Monitoring

1. INTRODUCTION

Cardiotocography (CTG) is one of the most diffused, non-invasive pre-natal diagnostic techniques, in clinical practice, to monitor foetal health, both in ante partum (third trimester of pregnancy) and intra partum period. It can be used from the 24th week of gestation to delivery. However, in some countries, in clinical routine, it is generally used from the 35th week and it is a medical report with legal value [1].

In CTG monitoring, foetal heart rate (FHR) and uterine contractions (UC) are simultaneously recorded by means of two probes placed on the maternal abdomen (a US Doppler probe for FHR signal and a pressure transducer for UC signal) [2].

Cardiotocographic data provide physicians information about healthy foetal development. To assess foetal health and reactivity, gynaecologists and obstetrics evaluate specific clinical signs (average value of FHR, number and kind of accelerations and decelerations in FHR signal, intensity, though as relative and not absolute values, and number of UC and their correlation with FHR modifications, etc). Important physiological mechanisms, like thermoregulatory oscillations, maturational changes with advancing gestational age, foetal behavioural states and maternal drugs can influence FHR patterns. In addition, clinicians generally make their evaluation on the basis of an eye inspection of cardiotocographic traces. The validity of the diagnostic procedure is hence still limited by the lack of complete objectivity and reproducibility. Moreover, even if CTG monitoring has been proved to be useful in early detection of foetal distress and, in intra partum period, electronic foetal monitoring led to a considerable reduction of mortality [1,3,4], it is not been found a significant decrease of postnatal injuries, such as cerebral palsy [5]. Besides, some authors state that prenatal stress can provoke changes in foetal endocrine and metabolic processes that can impact the later health of children and adults [6] and that from oxygen deprivation during delivery, a rare but devastating event, lifelong disability can result [7].

Unfortunately, non-invasive methods to measure di-

rectly the foetal acid-base status and cerebral oxygenation do not exist and clinicians have to rely upon indirect measures. Therefore, more detailed information about the foetal status is necessary and can be particularly useful during the last period of gestation and labour.

To achieve this aim, several analysis methodologies have been proposed in recent years [3, 8-10]. In particular, great interest has been dedicated to the analysis of FHR variability (FHRV), which, like so for adults, could be a base for a more powerful, detailed and objective analysis, both in ante partum and in intra partum period [2,11-14]. The study of autonomic rhythms by FHR recordings may provide a sight into the foetal development of autonomic nervous system (ANS) [6].

Changes in FHR control, elicited by the ANS in response to foetal hypoxia, were reported in literature [3, 15]. A UC is a strong compressive stimulus; it provokes an acute hypoxic stress to the foetus and generally elicits reactions in the FHR. It is well known that FHR decelerations are often associated with UC and that their characteristics are of great interest for physicians [4]. Moreover, although the FHR is subject to numerous influences, UC is the only input which can be externally monitored [7]. Interest in studying UC reactions is also outlined by recent studies in which UC were elicited by an oxitocin challenge test to explore the consequent blood flow changes [2,16,17]. In conclusion, it is worth investigating FHRV modifications, which reflect reactions of foetal ANS to UC, in order to have more comprehensive information about the insult and the foetal ability to withstand it. This could provide additional and objective information about foetal health and then support clinical diagnosis.

Concerning FHRV estimation, even if, as it is known, it can be analysed both in time domain and in frequency domain, the power spectral density (PSD) seems to be the index that best recovers all the information present in the heart rate (HR) series [18]. Spectral analysis provides a tool for quantifying rather small changes in FHRV in response to internal or external stimuli that may remain undetected if only visual interpretation of FHR tracings is used. Among most common methods employed to estimate PSD, parametric and non-parametric, we can mention Short-time Fourier transform (STFT); Auto Regressive methods (AR); Fast Recursive least square algorithms (RLS) [2,12,14,19], wavelet transform [20] and Lomb method [21].

Supported by previous results [1, 22], this study aimed to analyse more in depth spectral modifications in the FHRV signal (by means of STFT) in response to UC for healthy foetuses, which may help in the understanding of specific foetal reactivity, capability and modality of foetal compensation to hypoxic stress, by using the natural disturbance caused by UC. In particular, considering physiological cases, we would highlight the specific modification pattern of FHRV power spectrum, here regarded as ANS response. In future works, this pattern could be compared to patterns corresponding to pathological conditions in order to define a new classification criterion.

2. METHODS

2.1. Data Collection

CTG were recorded during routine foetal monitoring, in an Italian public hospital, from 35 healthy pregnant women (singleton pregnancies), close to delivery (33-42 gestation weeks), who did not take drugs and having no known genetic malformations; subjects laid down in a rest position. In line with clinical practice, CTG signals lasting less than 20 min or excessively noisy signals were excluded from our database (at the moment populated by about 600 CTG). 35 CTG recordings were gathered for this study, 3 intra partum and the others with evident UC. On average, CTG recordings have a duration of about 30 minutes. At birth, Apgar scores, birth weights and other information were collected in order to involve in the analysis only CTG regarding healthy foetuses: in particular, enrolled infants had Apgar scores > = 7 at 1st minute and > = 9 at 5th minute, birth weights (ranging from 2.7 to 4.25 Kg) appropriate for the gestational age and no one needed neonatal intensive care unit treatment.

Cardiotocographic signals were acquired using HP-135x or Sonicaid cardiotocographs, equipped with an ultrasound Doppler probe to detect FHR signals (measured in beats per minute-bpm) and a pressure transducer to record UC signals (measured in mmHg). Both probes were placed upon maternal abdomen.

In HP cardiotocographs, FHR and UC signals are internally stored at 4 Hz (corresponding to a sampling interval of 250 ms). On the contrary, in Sonicaid cardiotocograph, FHR and UC signals are unevenly stored. Both devices provide a three-level signal which indicates the 'quality' of the received Doppler signal, which can result optimal, acceptable or insufficient (the latter corresponding to signal loss). In both cases, recorded data are transferred to the output serial port of the device that was connected to a laptop PC through a serial (RS232) connection.

2.2. Signal Selection

CTG recordings with evident UC were chosen for the analysis; as done in previous works of the authors [1, 22]. UC were selected respecting specific criteria in order to reduce the physiological variability and to achieve a sort of uniformity for the UC stimuli. In particular, only

uterine contractions of pronounced amplitude (at least 40 mmHg with respect to the resting tone), isolated (at least 130 s must elapse between the end and the start of two subsequent contractions), corresponding to good FHR and UC signal quality were considered for the analysis. About 100 UC, compliant with the above-mentioned specifications were enrolled in the analysis.

In order to carry out a quantitative comparison between the FHRV power spectrum modifications related to UC with respect to a reference condition, two kinds of time segments of the same length (231 samples, about 57 s) were selected; let us call them: 'reference-segments', chosen before the UC onset and 'UC-segments', chosen in correspondence of the UC (slightly retarded with respect to the UC apex) (please, refer to the previous publication for more detailed information [1]).

Figure 1 offers an example of CTG signals and chosen segments.

2.3. Pre-Processing

Before FHR signal processing, it is worth mentioning that, because CTG is acquired in a clinical setting, it is subject to specific noises; for example, the loss of probe contact can temporarily interrupt the recording. Moreover, FHR signals are intrinsically uneven series; each FHR value is computed as inverse of the time between two consecutive R waves, so that FHR values are available only when new heart beats occur. To obtain evenly sampled series, some commercial cardiotocographs (e.g. HP-135x) use a zero-order interpolation, that is each sample is held constant until the next heart beat occurs. This is an efficient solution for FHR time-domain analyses (accelerations and/or decelerations detection, etc) but can introduce alterations in the FHR power spectrum [18, 22]. To overcome these limitations, CTG recordings were pre-processed, by means of an algorithm previously developed by the authors, in order to select reliable FHR segments, to eliminate possible artifacts related to the Doppler technique and, only when necessary, to get rid of the zero-order interpolation [23- 25].

2.4. FHRV Time-Frequency Analysis

According to literature and previous works [1,7,22], we considered the FHR power spectrum mainly composed of a DC component (average of the FHR), a very low frequency (VLF) band (0-0.03 Hz) and FHR variability (FHRV) at higher frequencies. Therefore, FHRV signals were obtained evaluating (and then subtracting) components at lower frequencies by means of a smoothing cubic spline.

After that, because of the non-stationary behaviour of the FHRV signal, a time-varying frequency analysis by means of STFT had been carried out considering sliding Hamming windows of 128 samples (corresponding to 32 s) and using 99% overlap (window length was chosen according to literature [26]).

Finally, to concisely describe spectral modifications against time, the power associated with LF (0.03-0.2 Hz) and HF (0.2-1 Hz) bands was computed, for each time instant, PLF (t) and PHF(t), as expressed by [1]:

$$P_{LF}(t) = \frac{1}{T}\int_{0.03}^{0.2} |S(f,t)|^2 \, df$$
$$P_{HF}(t) = \frac{1}{T}\int_{0.2}^{1} |S(f,t)|^2 \, df \quad (1)$$

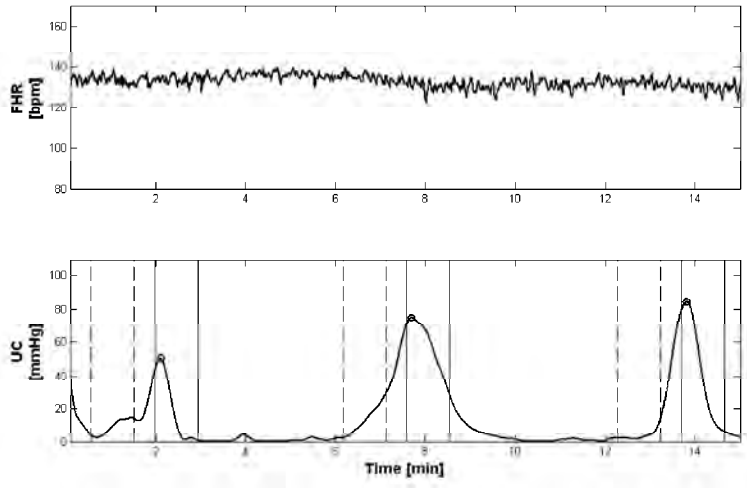

Figure 1. Example of CTG recording (from the top, FHR and UC signals) during labour, subject #12—week 40th. It is possible to recognise three UC, which were selected according to the required criteria. Couples of vertical dashed lines represent start and end of reference segments and vertical solid lines represent start and end of UC segments.

where, S (f, t) represents the time-varying spectral estimation of the FHRV signal and T is the time interval considered [1].

In order to highlight a common foetal ANS response to UC in a physiological situation, we also performed an average of LF and HF power signals (computed both for UC and references segments).

2.5. FHRV Frequency Content

To further characterise PSD modifications of FHRV signals related to UC, we carried out an analysis to detect, at each time instant, the maximum frequency bin contained in the signal's spectrum. To this aim, we used the "Modified Crossing Threshold Method", based on D'Alessio's algorithm [22,27,28]. The method considers that the tail of the spectrum gives information on the level of noise present in the signal, since white noise is equally spread over all frequency. An estimation of the noise made in the tail of the spectrum is then used for setting a threshold. The magnitude of each bin of the spectrum is compared with the threshold and when the magnitudes of two successive bins are higher than the threshold, the first bin is considered as the maximum frequency bin. We evaluated the noise level using the bins from 14 to 32 of a 128 FFT array (corresponding to the frequency range from about 0.4 Hz to 1 Hz). The selected frequency range to evaluate the noise depends on the method used in evaluating the FHR and its spectrum array [27], which could substantially modify the far tail of the spectrum. The algorithm threshold is computed multiplying this estimation of noise for an integer factor; we heuristically chose a value of 5, which means that the probability value for which a sample crosses the threshold is less than 1% in presence of only noise [28].

2.6. Statistic Analysis

A Student's *t*-test was employed to check the statistic separation between the analysed FHRV spectral populations (power in the different bands and frequency content of UC-segments and reference-segments; levels of statistical significance were always set at p value < 0.01).

For power estimation in HF band, we chose the fixed range 0.2-1 Hz, without considering the computed variable maximum frequency bin, in order to take into account noise contribution both for UC and ref segments.

3. RESULTS

As an example, **Figure 2** reports a spectrogram **Figure 2(a)** of a FHRV time-frequency distribution, obtained by STFT method, together with the corresponding CTG signal (FHR in **Figure 2(c)** and UC in **Figure 2(b)**).

As illustrated by **Figure 2(a)** the FHRV power increases in correspondence of UC.

It is worth noting that this increase does not correspond, in the time domain, to a clear modification of the floating-line (id est, in the FHR signal there are no alterations, such as accelerations or decelerations, that could justify the power increase).

Furthermore, to present concise results, obtained average powers of LF and HF bands of FHRV power spectrum, estimated both for selected UC segments and reference segments, are reported in **Table 1**.

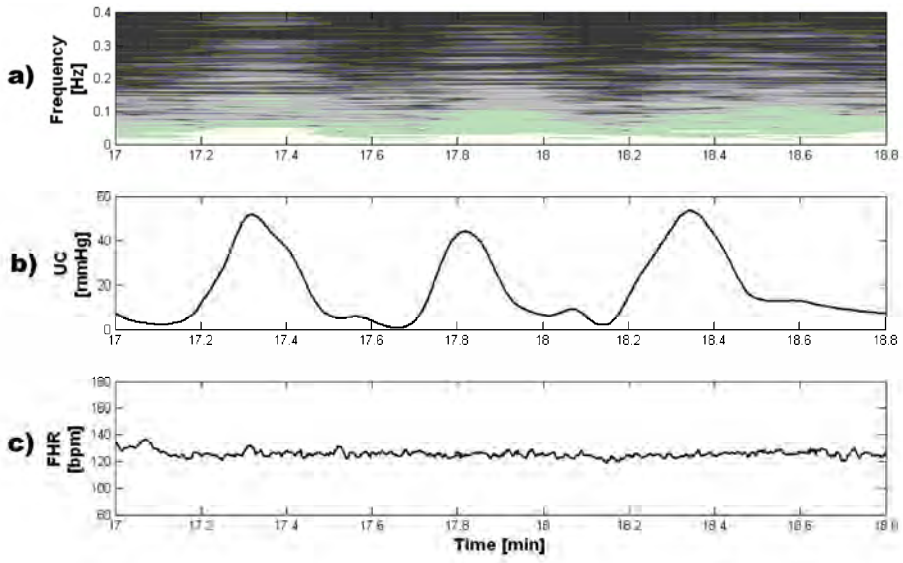

Figure 2. Example of FHRV spectral modifications in correspondence of UC. From the top, spectrogram, evaluated by means of STFT, and CTG signal of the subject #24 (UC in 2(b), FHR in 2(c)).

Table 1. powers in LF and HF bands, computed by means of STFT, are reported for the UC and reference segments in bpm^2. Reported values represent average results computed on 108 segments, in brackets we report the standard deviation.

	UC segments [bpm^2]	REF segments [bpm^2]
Power of LF band	459.44 (205.36)	183.72 (113.94)
Power of HF band	164.15 (85.36)	81.53 (62.15)

It is possible to note that average powers corresponding to UC-segments are higher than average powers corresponding to reference-segments. Moreover, UC-segments population resulted significantly different compared with reference-segments population for both FH RV power spectrum bands (*t*-test).

Concerning the analysis of FHR frequency content, results obtained by means of Modified Crossing Threshold Method highlighted that an enlargement of the band (shift to a higher value of signal maximum frequency bin) corresponds to the power increase of FHRV PSD. The following **Figure 3** shows an example of obtained results about the comparison between the power increase and the correspondent shift of signal maximum frequency bin.

The average behaviour has been studied also in this case and obtained results are reported in **Table 2**.

Our average results highlighted, in correspondence of the UC, a percentage increase of the band, computed as $\frac{\text{UC seg. value - REF seg. value}}{\text{REF seg. value}} \times 100$, of about 27%. Also in this case, UC-segments population resulted significantly different compared with reference-segments population (*t*-test).

4. DISCUSSIONS

Cardiotocography is an established part of daily obstetric practice, to monitor foetal health, mostly in the last weeks of gestation. Clinicians regularly monitor FHR and UC for signs of at-risk (or compromised) foetal conditions. During labour, to assess foetal reactivity, attention is focused on FHR alterations (such as decelerations) in correspondence to UC.

CTG usefulness is undoubted; nevertheless, there is, still nowadays, substantial intra- and inter-observer variation in the assessment of FHR patterns, due mainly to the visual inspection of CTG, which can lead to intervention when it is not required or lack of intervention when it is. Hence, several analysis methodologies (in time domain, in frequency domain, with semi-automatic software which compute specific time-domain parameters, etc.) were proposed in recent years to improve reliability and objectivity of CTG signals interpretation [2,3].

This is still insufficient to certainly identify suspect or ambiguous conditions. So, great interest was dedicated to the FHRV. It is commonly accepted that the use of a convenient technique for measuring and displaying beat to beat fluctuations is of value for estimating the maturation of ANS and the integrity of the nervous control of heart rate [29]. In particular, frequency analysis of FHRV could be a useful, additional tool [8,12,30] both in ante partum and in intra partum period.

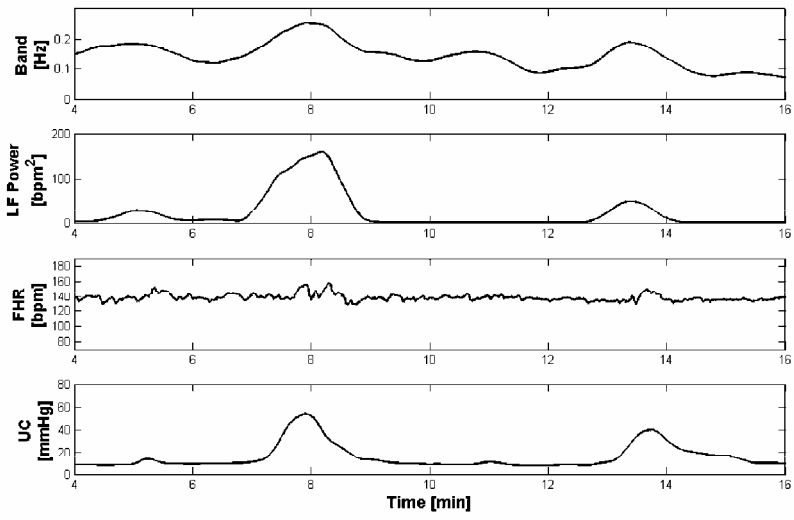

Figure 3. Example of FHRV spectral modifications. From the top, frequency content, evaluated by means of the Modified Crossing Threshold Method, power of the LF band, and CTG signal of the subject #18.

Table 2. maximum frequency bin contained in the analyzed signals both for UC segments and reference segments. Reported values represent average results computed on 108 segments, in brackets we report the standard deviation.

	UC segments [Hz]	REF segments [Hz]
Maximum frequency bin	0.218 (0.064)	0.172 (0.045)

A careful surveillance has to be dedicated to the intra partum period; in fact, while labour is of short duration in comparison to pregnancy, this period is of great risk for the foetus [31]. Intra partum stress can provoke adaptive changes in foetal metabolic process that can impact the future health of newborn. [6]. Therefore, clinicians regularly check FHR and UC to try to identify foetal distress symptoms and adapt the extracting procedure for signs of at risk foetuses. In particular FHR alterations in correspondence to UC are evaluated, to assess foetal reactivity. However, it is well known that there is still controversy over the interpretation of different FHR patterns and that objective clinical criteria to recognise foetal distress by CTG data are still poorly defined, especially during labour [32] and no clear conclusions are available so far. Positive predictive value of abnormal intra partum FHR patterns for foetal acidemia is only around 30% [15], whereas detection of foetal distress, early in labour, may significantly improve newborn's health. Besides, literature regarding intra partum CTG is much less rich than that about ante partum CTG, mainly due to registration difficulties. Therefore, it is important to try to obtain more reliable and objective methods for CTG interpretation and for neonatal outcome prediction [16,17,33-37].

In this scenario, analysis of FHRV can provide additional, useful information related to the foetal ANS control of the heart and its compensation capability. Analogously as for adults, specific stimuli can alter heart autonomic regulation and in turn generate specific modifications in the HR, particularly evident in frequency domain. Indeed, a UC is a strong compressive stimulus [38] (intra-uterine pressure can become four times stronger than basal pressure) that severely solicits the immature foetal ANS. This stress causes reactions in the FHR; one of the most evident is a FHR deceleration that often is associated with a UC, which is an important sign for physicians. Therefore, a more detailed study of the reaction of foetal ANS to UC, such as FHRV spectral modifications analysis, may help in the understanding of specific foetal reactivity, capability and modality of foetal compensation to hypoxic stress.

This work presents a study to investigate spectral modifications of the FHRV in response to the external stimulus represented by UC, for healthy foetuses, in order to find, during labour, possible predictive information about risky foetal conditions, before foetuses become injured.

We did not consider the gestational age (related to ANS maturation), even if it is well known that considerably affects the foetal hemodynamic responses to stimuli and distress, because weeks of gestation, in all our recordings, were in a range where it is possible to disregard this factor as an additional cause of considerable FHR changes [18,39,40].

Clinical intra partum UC and FHR are very noisy signals prone to frequent sensor disturbances; however, despite these conditions, the segment length required for frequency analysis, as proposed in this work, is short enough to overcome this problem.

Our results showed that a FHRV power spectrum modification can be observed in response to UC stimulus. In particular, a significant increase of the average power (confirmed by a *t*-test, $p < 0.01$) during UC-segments with respect to reference-segments is noted.

Moreover, we observed a shift to higher values of the maximum frequency contained in the signal in correspondence of the power increase. So that, we can conclude that the power increase is not due to a specific band enlargement but is spread over all frequencies.

By literature it is known that, in general, a large variability reflects a healthy ANS and also chemoreceptors, baroreceptors and cardiac responsiveness; while foetal hypoxia, congenital heart anomalies and stress, cause a decreased variability [3,4,41]. So, in healthy foetuses, we expected an evident modification in FHRV frequency characteristics corresponding to a good capability of reaction to UC stimulus.

Obtained results, according to that finding, should indicate a foetal reactivity (in terms of FHRV power spectrum modifications with respect to the rest condition) to mechanical compressive stimulus represented by UC for healthy foetuses. Therefore, such spectral modifications, being a sign of ANS reaction, could represent additional, objective information about foetal reactivity and in turn about foetal health during labour.

In a future perspective, it should be very interesting to analyse not only the average behaviour of FHR spectral modifications but also its trend during labour course in order to evaluate the individual status of a foetus and possibly to set an alarm threshold. Since foetal response is probably due to number and frequency as well as intensity of UC, it is important to establish a criterion for an objective and standardised measure of the stimulus intensity. In fact, let us remind that in cardiotocography only a relative measure of UC is known.

However, these issues deserve a more detailed and

exhaustive analysis, mainly involving problematic pregnancies and cases of ascertained foetal distress, in order to, considering foetal health situations as point of reference, to recognise specific spectral characteristics to distinguish foetal well-being and foetal distress in order to propose such methodology in daily clinical practice.

5. CONCLUSIONS

The Variability of the Foetal Heart Rate around its baseline provides extremely significant information concerning the cardiac and ANS activities and their functional development during pregnancy up to labour. Our results demonstrated important modifications in the PSD of FHRV signals related to physiological stimulus represented by UC, both as power and frequency content, proving that the FHRV time-frequency analysis could be a very useful tool for a more objective and depth evaluation of the foetal health. We would not expect to find such modifications in cases of foetal distress; therefore, if these results will be confirmed by the study of FHRV signals recorded during risky pregnancies, information about the capability of a foetus to react to stress during labour course could be obtained by means of this approach.

REFERENCES

[1] Romano, M., Bifulco, P., Cesarelli, M., Sansone, M., and Bracale, M. (2006) Fetal heart rate power spectrum response to uterine contraction. *Medical & Biological Engineerin & Computing*, **44(3)**, 188-201.

[2] Cesarelli, M., Romano, M., Bifulco, P., (2009) Comparison of short term variability indexes in cardiotocographic foetal monitoring. *Computers in Biology and Medicine*, **39(2)**, 106-118.

[3] Signorini, M.G., Magenes, Cerutti, G.S., Arduini, D. (2003) Linear and nonlinear parameters for the analysis of fetal heart rate signal from cardiotocographic recordings. *IEEE Transaction on Biomedical Engineering*, **50(3)**, 365-375.

[4] Sweha, A., Hacker, T.W. (1999) Interpretation of the electronic fetal heart rate during labor. *American Academy of Family Physician*, **59 (9)**, 2487-2500.

[5] Rizzo, N., Accorsi, P., Baronciani, D., *et al.*, "La sorveglianza del benessere fetale in travaglio di parto. *Linea guida basata su prove di efficacia Regione Emilia Romagna*, Progetto n. 3.

[6] Hoyer, D., Heinicke, E., Jaekel, S., Tetschke, F., Paolo, D.P., Haueisen, J., Schleußner, E. and Schneider, U. (2009) Indices of fetal development derived from heart rate patterns. *Early Human Development*, **85**, 379-386.

[7] Philip, A., Warrick, E.F., Hamilton, D.P. and Robert E.K., "Identification of the dynamic relationship between intra-partum uterine pressure and fetal heart rate for normal and hypoxic foetuses", *IEEE Transactions on Bio-Medical Engineering*, **56(6)**, 1587-1597.

[8] Martin, C.B. (1982) Physiology and clinical use of fetal heart rate variability. *Clinics in Perinatology*, **9(2)**, 339-352.

[9] Dawes, G.S., Meir, Y.J., Mandruzzato, G.P. (1994) Computerized evaluation of fetal heart-rate patterns. *Journal of Perinatal Medicine*, **22(6)**, 491-499.

[10] Romano, M., Cesarelli, M., Bifulco, P., Sansone, M. and Bracale, M. (2002) Development of an algorithm for homogeneous FHR signals identification. *Proceedings of Embec*'02 2*nd European Medical and Biological Engineering Conference*, December 2002, Vienna, Austria; II: 1542.

[11] Sibony, O., Fouvillot, J.P., Benaoudia, M., Benhalla, A., Oury, J.F., Sureau, C. and Blot, P. (1994) Quantification of the heart rate variability by spectral analysis of fetal well-being and fetal distress. *European Journal of Obstetrics & Gynecology and Reproductive Biology*, **54(2)**, 103-108

[12] Cerutti, S., Civardi, S., Bianchi, A., Signorini, M.G., Ferrazzi, E. and Pardi, G. (1989) Spectral analysis of antepartum heart rate variability. *Clinical Physics and Physiological Measurement*, **10(Suppl B)**, 27-31.

[13] Divon, M.Y., Muska, Y., Platt, L.D. and Paldi, E. (1984) Increased beat to beat variability during uterine contractions: A common association in uncomplicated labor. *American Journal of Obstetrics and Gynecology*, **149(8)**, 893-896.

[14] Romano, M., Bracale, M., Cesarelli, M., Campanile, M., Bifulco, P., Falco, M.D., Sansone, M., Lieto, A.D. (2005) Antepartum cardiotocography: A study of fetal reactivity in frequency domain. *Computers in Biology and Medicine*, **36 (6)**, 619-633.

[15] Geijn, H.P. (1996) Developments in CTG analysis. *Baillieres Clin Obstet Gynaecol*, **10(2)**, 185-209.

[16] Gudmudsson, S. and Olofsson, P. (2004) Acute changes of cerebral venous blood flow in growth-restricted human fetuses in response to uterine contractions. *Ultrasound Obstet Gynecol*, **24(5)**, 516-521.

[17] Li, H., Gudmundsson, S. and Olofsson, P. (2003) Acute increase of umbilical artery vascular flow resistance in compromised fetuses provoked by uterine contractions. *Early Human Development*, **74(1)**, 47-56.

[18] Laguna, P., Moody, G.B. and Mark, R.G. (1998) Power spectral density of unevenly sampled data by least-square analysis: performance and application to heart rate signals. *IEEE Transactions on Biomedical Engineering*, **45(6),** 698-715.

[19] Pola, S., Macerata, A., Emdin, M. and Marchesi, C. (1996) Estimation of the power spectral density in nonstationary cardiovascular time series: Assessing the role of the time-frequency representation (TFR). I*EEE Transactions on Biomedical Engineering*, **43(1)**, 46-59.

[20] Salamalekis, E., Thomopoulos, P., Giannaris, D., Salloum, I., Vasios, G., Prentza, A., Koutsouris, D. (2002) Computerised intrapartum diagnosis of fetal hypoxia based on fetal heart rate monitoring and fetal pulse oximetry recordings utilising wavelet analysis and neural networks. *BJOG: An International Journal of Obstetrics and Gynaecology*, **109(10)**, 1137-1142.

[21] Cesarelli, M., Romano, M., Ruffo, M., Bifulco, P., Pasquariello, G. and Fratini, A. (2009) PSD modifications of FHRV due to CTG storage rate. *Proceedings of 9th International Conference on Information Technology and*

Applications in Biomedicine, Larnaca, Cyprus.

[22] Romano, M., Cesarelli, M., Bifulco, P., Ruffo, M., Fratini, A. and Pasquariello, G. (2009) Time-frequency analysis of CTG signals. *Current Development in Theory and Applications of Wavelets*, **3(2)**, 169-192.

[23] Cesarelli, M., Romano, M., Bifulco, P., Fedele, F. and Bracale, M. (2007) An algorithm for the recovery of fetal heart rate series from CTG data. *Computers in Biology and Medicine*, **37(5)**, 663-669.

[24] Romano, M., Cesarelli, M., Bifulco, P., Sansone, M. and Bracale, M. (2003) Study of fetal autonomous nervous system's response by means of FHRV frequency analysis. 1*st International IEEE EMBS Conference on Neural Engineering*, Capri, Italy, 399-402.

[25] Hieftje, G.M., Bistroff, R.I. and Lim, R. (1973) Application of correlation analysis for signal-to-noise enhancement in flame spectrometry. *Analytical chemistry*, **45(2)**, 253-258.

[26] Karin, J., Hirsch, M., Sagiv, C. and Akeselrod, S. (1992) Fetal autonomic nervous system activity monitoring by spectral analysis of heart rate variations. *IEEE Proceedings of Conference on Computers in Cardiology*, 479-482.

[27] Moraes, R., Aydin, N. and H. Evans, D. (1995) The performance of three maximum frequency envelope detection algorithms for Doppler signals. *Journal of Vascular Investigation*, **1(3)**, 126-134.

[28] Alessio, T.D., (1985) Objective algorithm for maximum frequency estimation in Doppler spectral analysers. *Medical & Biological Engineering & Computing*, **23(1)**, 63-68.

[29] David, M., Hirsch, M. and Akeselrod, S. (2006) Maturation of fetal cardiac autonomic control as expressed by fetal heart rate variability. *IEEE Proceedings of Conference on Computers in Cardiology*, 901-904.

[30] Oppenheimer, L.W. and Lewinsky, R.M. (1994) Power spectral analysis of fetal heart rate. *Baillère's Clinical Obstetrics and Ginecology*, **8(3)**, 643-661.

[31] Logier, R., jonckheere, J.D., Jeanne, M. and Matis, R. (2008) Fetal distress diagnosis using heart rate variability analysis: design of a high frequency variability index. *IEEE Proceedings of* 30*th Annual International IEEE EMBS Conference Vancouver*, British Columbia, 4728-4731.

[32] Cao, H., Lake, D.E., Chisholm, C.A., Ferguson, J.E., Grifin, M.P. and Moorman, J.R. (2003) Toward quantitative monitoring of human cardiotocography during labor. *Proceedings of the* 25*th Annual International Conference of the IEEE EMBS*, Cancun, Mexico.

[33] Salamalekis, E., Vitoratos, N., Loghis, C., Panayotopoulos, N., Kassanos, D. and Creatsas, G. (1999) Evaluation of fetal heart rate patterns during the second stage of labor through fetal oximetry. *Gynecologic and Obstetric Investigation***, 48**, 151-154.

[34] Zimmer, E.Z., Paz, Y., Copel, J.A. and Weiner, Z. (1998) The effect of uterine contractions on intrapartum fetal heart rate analyzed by a computerized system. *American Journal of Obstetrics and Ginecology*, **178(3)**, 436-440.

[35] Jensen, O.H.R. and Narverud, G. (1994) Fetal heart rate decelerations and umbilical cord blood gas values. *European Journal of Obstetrics & Gynecology and Reproductive Biology*, **53(2)**, 103-106.

[36] Padhye, N.S., Duan, Z. and Verklan, M.T. (2004) Response of fetal heart rate to uterine contractions. *Proceedings of the* 26*th Annual International Conference of the IEEE EMBS, San Francisco*, 3953-3955.

[37] Kodama, Y., Sameshima, H., Ikeda, T. and Ikenoue, T. (2009) Intrapartum fetal heart rate patterns in infants (≥34 weeks) with poor neurological outcome. *Early Human Development*, **85(4)**, 235-238.

[38] Goeschen, K. (1998) Cardiotocografia pratica. Roma, V edizione, CIC Edizioni Internazionali, Roma.

[39] Rantonen, T., Ekholm, E., Siira, S., Metsala, T., Leino, R., Ekblad, U. And Valimaki, I. (2001) Periodic spectral components of fetal heart rate variability reflect the changes in cord arterial base deficit values: A preliminary report. *Early Hum Dev*, **60(3)**, 233-238.

[40] Ohta, T., Okamura, K., Kimura, Y., Suzuki, T., Watanabe, T., Yasui, T., Yaegashi, N. and Yajima, A. (1999) Alteration in the low-frequency domain in power spectral analysis of fetal heart beat fluctuations. *Fetal Diagnosis and Therapy*, **14(2)**, 92-97.

[41] .Geijn, H.P., Jongsma, H.W., Haan, J. and Eskes. T.K. A.B. (1980) Analysis of heart rate and beat-to-beat variability: Interval difference index. American Journal of Obstetrics and Ginecology, **138(3)**, 246-252.

J. Biomedical Science and Engineering, 2010, 3, 1022-1029 **JBiSE**
doi:10.4236/jbise.2010.310133 Published Online October 2010 (http://www.SciRP.org/journal/jbise/).

Ensemble-based active learning for class imbalance problem

Yanping Yang, Guangzhi Ma

School of Computer Science and Technology; Huazhong University of Science and Technology, Wuhan, China
Email: maguangzhi.hust@gmail.com

Received 8 September 2010; revised 20 September 2010; accepted 25 September 2010

ABSTRACT

In medical diagnosis, the problem of class imbalance is popular. Though there are abundant unlabeled data, it is very difficult and expensive to get labeled ones. In this paper, an ensemble-based active learning algorithm is proposed to address the class imbalance problem. The artificial data are created according to the distribution of the training dataset to make the ensemble diverse, and the random subspace re-sampling method is used to reduce the data dimension. In selecting member classifiers based on misclassification cost estimation, the minority class is assigned with higher weights for misclassification costs, while each testing sample has a variable penalty factor to induce the ensemble to correct current error. In our experiments with UCI disease datasets, instead of classification accuracy, F-value and G-means are used as the evaluation rule. Compared with other ensemble methods, our method shows best performance, and needs less labeled samples.

Keywords: Class Imbalance, Active learning, Ensemble, Random Subspace, Misclassification Cost

1. INTRODUCTION

In the medical diagnosis, it is common that there is a huge disproportion in the number of cases belonging to different classes [1]. For example, the number of cancer cases is much smaller than that of the healthy. The traditional classifiers, however, are incapable of countering such class imbalance problem, because they favor the majority class. Moreover, the minority class is much more important in real applications. In addition, in real world, there are abundant unlabeled data but labeled instances are difficult, time-consuming or expensive to obtain. It will in turn make the labeled minority class much fewer further, which often degrades the performance of traditional classifiers greatly. As a result, active learning with unlabeled imbalanced data becomes an important issue in machine learning [3].

To address the class imbalance problem, the direct way is to reduce the imbalance by re-sampling original dataset. Some methods try to under-sampling majority class, like Tomek link [4], condensed nearest neighbor rule [5] and neighborhood cleaning rule [6][7]. In these methods, the majority samples in certain area are considered as useless and can be removed from training dataset. But, there is a risk of missing representative samples. Other methods, like SMOTE [8], try to over-sampling the minority class. In SMOTE method, the artificial datasets are created according to the distribution of the minority class. However, the enhancement will be little, if the created artificial datasets have the same properties as the labeled samples

Finding proper classifier for minority class is another way to counter class imbalance problem. Joshi [9] once modified the Boosting algorithm by assigning the minority class with a weight different from that of the majority class. Akbni [10] adjusted the SVM's decision-boundary by modifying the kernel function. But, the certain classifier is only efficient in countering specific class imbalance, and cannot be extended to other applications. Another trend is to use ensemble of classifiers, which often has better performance than single classifier. But, the performance depends on the diversity of the ensemble [11]. If classifiers in an ensemble have the same property, there will be less improvement of performance even with more classifiers.

Active learning techniques are conventionally used to solve problems where there are abundant unlabeled data but rare labeled ones [3]. Recently, various approaches on active learning from imbalanced datasets have been proposed in literatures [12]. For instance, as a good classifier, support vector machine (SVM) was proposed in active learning for the imbalance problem [14]. To reduce the computational complexity in dealing with large imbalanced datasets, this method was implemented in a random set of training populations, instead of the entire training dataset. In [16], bootstrap-based over- sampling was proposed to reduce the imbalance in the application

of word sense disambiguation. Facing the class imbalance issue, however, both re-sampling and classifier strategy have their own advantage as well as disadvantage. The best way is to combine them together [17]. But progress in this field is little.

In this paper, an ensemble-based active learning with artificial samples is proposed to address class imbalanced problem by using unlabeled data. Different from random sampling, we try to use active selection strategy to label the sample with potential benefit to the ensemble's diversity. In addition, we will create artificial datasets from the distribution as the training dataset. The conversely labeling of each artificial data will bring diversity to the ensemble. Both the training dataset and the artificial dataset will be re-sampled according to random subspace concept. It will release the difficulty of traditional sampling methods while facing with high-dimension data. Further, when choosing member classifiers according to misclassification cost, the minority class is assigned with a higher weight for misclassification cost, and each testing sample has a variable penalty factor to induce the ensemble to correct current error. In the experiments with UCI disease datasets, instead of accuracy, F-value and G-mean are used to evaluate the performance, since they are better for minority classification tasks.

The rest of this paper is organized as follows. In Section 2, the proposed ensemble is described in detail, including the creation of artificial datasets, random subspace re-sampling and misclassification cost estimation. Section 3 introduces how to implement active learning with our proposed ensemble method. In experiment part, the new evaluation rules are introduced. Based on experiments on the UCI datasets, our proposed method is compared with other state-of-art methods.

2. RANDOM SUBSPACE ENSEMBLE WITH ARTIFICIAL DATASETS

In our ensemble-based active learning, the ensemble algorithm is the core. So, in this section, we will introduce our Random Subspace Ensemble with Artificial Data (RSEAD) in detail.

2.1. Overview

Figure 1 is the algorithm of our Random Subspace Ensemble with Artificial Data (RSEAD). Each member classifier in the ensemble is created via the iteration steps in **Figure 1**.

At the beginning of the algorithm, the training dataset *T* will be mapped into another dataset *T*, in a *m*-dimension subspace. Then a classifier will be created based on *T*, and used to initiate the ensemble *C**. Also, the misclassification cost of current ensemble will be calculated. Whereafter, the algorithm will enter following iteration:

1) According to the distribution of the training dataset *T*, an artificial dataset will be generated. The size of the artificial dataset will be in a certain ratio, *Rsize*, to that of training dataset. They will be labeled with a class different from what the ensemble predicts

2) In the *m*-dimension subspace, both *T* and *R* will be re-sampled to *T*, and *R*,.

3) A new classifier *C*, will be learned from both labeled *R*, and *T*,. In order to guarantee the performance of the ensemble when pursuing the diversity, the misclassification cost of the new ensemble with *C*, is calculated. Compared with the previous ensemble, if the new classifier brings more misclassification cost, it will be removed; otherwise, it will be kept in the ensemble;

4) The above steps will be iterated until algorithm returns the expected size of ensemble, or the number of iterations reaches the limited value.

To predict the class of an unlabeled sample *x*, each member classifier C_i in ensemble *C*, will assign *x* with an membership probability, $\hat{P}_{C_i,y}(x)$. Then the ensemble will calculate membership probability of each class *y* for sample *x* via following equation:

Algorithm: The RSEAD ensemble
Input:
BaseLearn – Base Learner
L - Training Set
R - Artificial dataset
m - Dimension of random subspace
Csize - Target size of subspace
Imax - Maximum number of iterations
Rsize - Ratio between the size of dataset *R* and *L*
(1) $i = 1$;
(2) trials = 1 ;
(3) Preprocessing the training set based on *m*-dimension subspace : $T' = RSM - sampling(T)$
(3) $C_i = BaseLearn(T')$
(4) $C^* = \{C_i\}$
(5) Calculate the ensemble error, ε ; $i = i + 1$
(6) While $i < Csize$ and $trials < Imax$
{
(7) Create artificial dataset , the size will be $Rsize \times |T|$;
(8) Assign each artificial sample a label different from *C**'s prediction.
(9) Re-sample the training set and artificial set in m-dimension subspace:
$T' = RSM - sampling(T)$ $R' = RSM - sampling(R)$
(10) $T' = T' \bigcup R'$
(11) $C_i = BaseLearn(T')$ $C^* = C^* \bigcup \{C_i\}$
(12)Calculate the misclassification cost of new ensemble, ε'
(13) If $\varepsilon' \le \varepsilon$ then { $\varepsilon = \varepsilon'$, $i = i + 1$ }
(14) else { $C^* = C^* - \{C'\}$: $trials = trials + 1$}

Figure 1. Algorithm of RSEAD ensemble.

$$\hat{P}_y(x) = \frac{\sum_{C_i \in C^*} \hat{P}_{C_i,y}(x)}{\left|C^*\right|} \quad (1)$$

Equation (1) reflects the probability of x belonging to class y. Therefore, the label with largest membership probability will be assigned to x:

$$C^*(x) = \arg\max_{y \in Y} \hat{P}_y(x) \quad (2)$$

2.2. Creation and Labeling of Artificial Datasets

The diversity is a critical factor for a successful ensemble [11]. An ensemble will have less diversity if its member classifiers have the same property. To bring more diversity, Bagging [19] divides the training set into several smaller one, while Boosting adjusts the distribution of the training dataset according to the chosen classifier [20]. Further, in Random Forest [21], both training dataset and feature space are divided into smaller ones to train different classifiers. However, all these methods depend on the training dataset to induce the diversity. Therefore, if the training dataset is not big enough, the diversity will be limited.

In our active learning method, the RSEAD ensemble's diversity will be guaranteed in three ways: 1) with active learning, the large pool of unlabeled data can be sampled to get good training datasets; 2) besides the training dataset, the artificial data are also created for training classifier; 3) both the original training and the artificial datasets will be re-sampled in subspace to enhance diversity. In this part, we will focus on the creation of artificial dataset and their labeling.

In our method, the artificial data are created by randomly picking data points from an approximation of the training dataset distribution. The numeric attributes are defined according to the mean and the standard deviation of the training dataset, and generated in Gaussian distribution. For a nominal attribute, its value is based on the probability of the occurrence of each distinct value in its domain. The Laplace smoothing is used if a certain nominal attribute is absent in the training dataset. Further, to construct an artificial data, there is a simplifying assumption that the attributes are independent, because it will cost much time and labeled data to accurately estimate the joint probability distribution of these attributes.

In each iteration shown in **Figure 1**, the ensemble will predict the class label for each artificial data x. Firstly, ensemble will give a membership probability of x belonging to certain class y. The zero membership probability will be replaced by a small non-zero value in case that it may act as a denominator. Then the artificial data will be labeled a class that is different from what the ensembles predict. Therefore, if current ensemble predicts the probability of x belonging to y is $\hat{P}_y(x)$, then, the choice of label for x will be based on $\hat{P}_y^{'}(x)$:

$$\hat{P}_y^{'}(x) = \frac{1/\hat{P}_y(x)}{\sum_y 1/\hat{P}_y(x)} \quad (3)$$

Let us show this labeling method with a two-class problem. For instance, for an artificial sample x, the ensemble estimates that it has 20% probability of being a positive sample and 80% probability of being a negative one. In other words, the ensemble believes that x is more likely a negative sample. In our method, to create a new classifier with more diversity, x will be assigned with a positive label, and then used to train a new classifier.

The ensemble often has higher accuracy than single member classifier if each member classifier is not related with others. Therefore, our method of labeling artificial data can reduce the relevancy between classifiers, which will in turn bring the ensemble with higher accuracy and less generalization error.

2.3. Re-Sampling in Subspace

Re-sampling is the popular way to deal with class imbalance problem. However, most of sampling methods, like SMOTE, often work in the whole feature space, which is not efficient in countering high-dimension datasets. In addition, they often try to consider the class imbalance and the properties of the dataset as a whole. The data, however, often exhibit characteristics and properties at a local level, rather than the global level. Hence, it is important to study the dataset in a reduced subspace. Although a certain feature subspace may only lead to a weak classifier, the ensembling of such weak ones can make a strong classifier [22], since it induces higher diversity, which is an important condition for a classifier with good performance.

To this end, we proposed the Random-Subspace-Mapping Sampling (RSM-sampling) algorithm.

Suppose we have a dataset L, which has a n-dimension space: $|L| = 1$, $F = \{F_1, F_2, ..., F_n\}$. Any data $P \in L$ can be represented as $P = \{P_1, P_2, ..., P_n\}$, where P_i is the value of the related feature F_i in the feature space F.

If the dimension of each subspace is set to m, $m<n$, the number of the likely subspace will be $k_{\max} = C_n^m$. When $m = [n/2]$, k_{max} has its biggest value. For our algorithm, each feature subspace will bring a candidate classifier. We often choose $Cszie < k_{max}$ classifiers to construct an ensemble, since not every candidate classifier will help enhance the ensemble,s performance.

Before re-sampling, a subspace S should be randomly selected from the feature space F. $\left|F\right| = m < n$. $S = \{S_1, S_2, ..., S_m\} \subset F$. Then, in the feature subspace,

each data $P \in L$ will be mapped into $P_S = \{P_{s1}, P_{s2}, ..., P_{sm}\}$.

In each iteration step of our algorithm, both the training dataset *L* and the artificial dataset *R* are re-sampled in chosen sub-space.

2.4. Misclassification Cost Estimation

When pursuing the diversity, the performance of ensemble should be guaranteed too. To address the problem of class imbalance, the misclassification cost is used to replace the traditional classification error. A new classifier will be kept in the ensemble if it helps decrease the misclassification cost; otherwise, it will be removed.

In our algorithm, the minority class is assigned with a higher weight of misclassification cost than that of the majority class. Also, each test sample will be assigned with a penalty factor. If current ensemble makes wrong decision on it, its penalty factor will be increased; otherwise, its penalty factor will be decreased. In this way, the ensemble will choose the new classifier that helps to correct the error of current ensemble. Also, since the minority samples have more chance to be misclassified, this penalty factor will bring an ensemble proper for minority class.

Suppose we have *t* samples to evaluate the ensemble based on misclassification cost. Firstly, each sample's penalty factor will be initialized as:

$$d_i^1 = 1/t \quad 1 \le i \le t \tag{4}$$

The misclassification cost of the ensemble gotten in *k*-th iteration can be represented as:

$$\varepsilon_k = \sum_{i=1}^{t} \cos t(y_i, C_k^*(x_i)) \times d_i^k \tag{5}$$

In Equation (5), y_i is the correct class label of testing sample x_i, $C_k^*(x_i)$ is the predicted class of the ensemble for x_i. d_i^k is x_i,s penalty factor for the *k*-th iteration. $\cos t(y_i, C_k^*(x_i))$ is the weight of misclassifying a sample with label y_i as class $C_k^*(x_i)$. When $y_i = C_k^*(x_i)$, there is $\cos t(y_i, C_k^*(x_i)) = 0$ because classification is correct.

If the misclassification cost in the *k*-th iteration is less that that in the (*K*–1)-th iteration, then newly created classifier will be kept in ensemble. There, we have the coefficient of performance enhancing:

$$\alpha_k = \ln((1-\varepsilon_k)/\varepsilon_k)/2 \text{。} \tag{6}$$

Each testing sample's penalty factor will be modified according to current ensemble's prediction. If current ensemble makes correct classification on x_i, its penalty factor d_i^{k+1} will be decreased to:

$$d_i^{k+1} = d_i^k \exp(-a_k) \tag{7}$$

Otherwise, it will be increased to:

$$d_i^{k+1} = d_i^k \exp(a_k) \tag{8}$$

Please note, all samples, new penalty factors will be normalized as following:

$$Z_{k+1} = \sum_{i=1}^{t} d_i^{k+1}$$

$$d_i^{k+1} = d_i^{k+1} / Z_{k+1}. \tag{9}$$

d_i^{k+1} will be used in the (*k* + 1)-th iteration.

The design of misclassification cost weigh $\cos t(y_i, C_k^*(x_i))$ and penalty factor d_i^{k+1} will help the ensemble to pick the classifiers that can better deal with minority class.

3. ACTIVE LEARNING WITH THE ENSEMBLE RSEAD

The ensemble with diversity will be used in active learning for selecting unlabeled data. Like the QBC [23], our proposed active learning method also chooses the unlabeled samples that have the biggest prediction difference among the classifiers in the ensemble. Such prediction difference is often called uncertainty, which is calculated via margin measure in our algorithm. The margin is defined as the difference of membership probability between the sample,s most likely class and second most likely class.

$$Margin(C^*, x) = \hat{P}_{y1}(x) - \hat{P}_{y2}(x) \tag{10}$$

where *y*1 and *y*2 are class labels of unlabeled sample *x* predicted by ensemble C*. *y*1 has the highest membership probability for *x*, while *y*2 is the second highest one. Then, the uncertainty can be represented as:

$$Uncertainty(C^*, x) = \frac{1}{Margin(C^*, x) + \delta} \tag{11}$$

where the δ is a small value in case margin is 0. The smaller margin is, the bigger the uncertainty is. For a two-class task, when $\hat{P}_{y1}(x) = \hat{P}_{y2}(x)$, the margin will be 0, and *x* will have the biggest uncertainty, $Uncertainty(C^*, x) = 1/\delta$

4. EXPERIMENTS

To evaluate our method,s effectiveness for medical diagnosis, eight disease datasets from the UCI machine learning repository [24] are used in experiments. In this section, we will discuss the experiments in detail.

4.1. Evaluation Rule

In a two-class task, a classifier will have four kinds of prediction results [25] for dataset with *N* samples, shown in **Table 1**. *TP* and *FN* responsively mean the number of correctly and wrongly classified positive samples, while

TN and *FP* mean the number of correctly and wrongly classified negative samples.

The classification accuracy is often calculated as :

$$\text{Accuracy} = (TP+FN)/N. \quad (12)$$

The accuracy rule, however, is not a good one for imbalance classification [26], for example, if there are only 1% positive samples but 99% negative samples. Simply classifying all samples as negative class will bring 99% accuracy, but misclassified 1% positive samples will bring enormous cost. Therefore, such 99% accuracy is a disaster for medical diagnosis.

In our proposed method, F-value [27] defined in Equation (13) is used to evaluate the classifier for imbalance class problem.

$$F-value = \frac{(1+\beta^2)\times \text{Precision}\times \text{Recall}}{\beta^2\times \text{Precision}+\text{Recall}} \quad (13)$$

where, Precision = *TP*/(*TP*+*FN*); Recall = *TP*/(*TP*+*FP*). β measures the importance of Precision vs. Recall. In our method, β = 1, which means Precision and Recall is equally important.

In addition, G-Mean [28] is also used in evaluating the performance of our classifier.

$$\text{G-mean}=\sqrt{\text{PositiveAccuracy}\times \text{NegativeAccuracy}} \quad (14)$$

where PossitiveAccuracy = Precision, NegativeAccuracy = *TN*/(*TN*+*FP*). It can be seen that G-mean measure tries to build a balance between positive class and negative class.

4.1. Datasets Description

For testing, eight disease datasets from UCI are chosen. Some basic information about them is summarized in **Table 2**, in which P:N means the number of positive samples via number of negative samples.

4.2. Experiments on the Dimension of Subspaces

As discussed in 2.3, to randomly select a *m*-dimension subspace from a *n*-dimension feature space, the number of choices will be $k_{\max} = C_n^m$. In our algorithm, the *m* is recommended as $m = [n/2]$, since it bring the maxim choice. Even if we choose a *Csize* < K_{max}, bigger value of k_{max} means more chance to get good member classifiers.

Based on dataset *Breast-w*, we test the relation between the dimension of a subspace and the performance of a classifier based on F-value. The result is shown in **Figure 2**. In this experiment, the *Csize* of the ensemble is 30. Since *Breast-W* has 9 features, *m* = 1 and *m* = 9 are meaningless to this experiment. So, the dimension of feature space *m* will be changed from 2 to 8 in experiment. In **Figure 2**, F-value will reach its peak when *m* = 5. The F-value at *m* = 4 is a little less than *m* = 5, although they have the same k_{max}. The reason may be that 5-feature subspace brings more information than 4-feature one. From **Figure 2**, we can see that if *m* is too small, the information in each subspace is too little to train a good classifier; but if *m* is too big, there will be little diversity among different subspace, which is also bad for the performance of the ensemble. This experiment shows that *m* = [*n*/2] is a good setting for dataset *Breast-W*.

4.3. Experiment on the Size of Ensemble

In this experiment, we test the relation between the ensemble's size and its classification performance. The *Breast-W* is still used and the result is shown in **Figure 3**.

Table 1. Classification of a two-class problem.

	#classified as positive	**#classified as negative**	**Total**
Positive sample	*TP*	*FN*	*TP+FN*
Negative sample	*FP*	*TN*	*FP+TN*
Total	*TP+FP*	*FN+TN*	*N*

Table 2. Summary of experimental UCI disease datasets.

Dataset	**#features**	**#instances**	**P：N**
Colic	22	368	136：232
Sick	30	3772	231：3541
Diabetes	8	768	268:500
SAheart	11	462	160:302
Hepatitis	20	155	32:123
mammograph	5	961	445:516
Breast-W	9	699	241:458
Spect	22	267	55:212

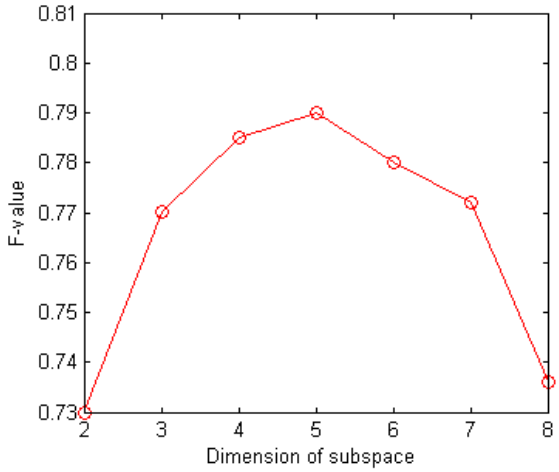

Figure 2. F-value for different dimension of subspace on *Breast-W* dataset.

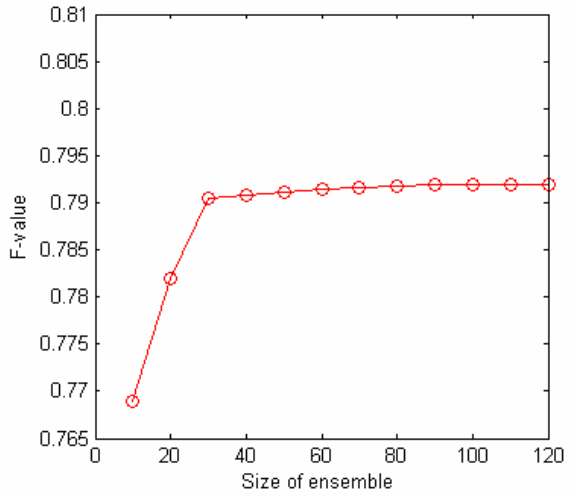

Figure 3. F-Value for different size of an ensemble on *Breast-W* dataset.

In the experiment, the dimension of subspace is fixed as $m=[n/2]=[9/2]=5$. Therefore, there will be $C_9^5=126$ choices of subspaces to train *Csize* classifiers for the ensemble. In **Figure 3**, the F-value increases quickly when *Csize* grows from 10 to 30, but the enhancement is not big when *Csize* is changed from 30 to 120. It shows that for dataset *Breast-W*, 30 subspaces with 5 dimensions are enough to build a good ensemble. The additional subspace will contribute little to the diversity of ensemble, and there will be no much enhancement in performance, though the computation cost grows much. Therefore, 30 is a trade-off between performance and computation cost for dataset *Breast-W*.

4.3. Experiment Result

In this experiment, we firstly test the performance of our proposed RSEAD ensemble algorithm. For comparison, two state-of-art classification algorithms, Bagging and Adaboost, are chosen. For fair comparison, C4.5 is used as base learner, and is configured with the default setting in Weka [29]. In the evaluation of performance, F-value and G-mean are used in experiments with 10-fold cross validation. For RSEAD algorithm, it has a setting with $m=[n/2]$, k = 30, and *Imax* = 50.

Shown in **Table 3** is the F-value for the minority class in each dataset, while **Table 4** is the G-value for every whole dataset. For each dataset, the highest value is marked in bold. For convenience of comparison, the base learner C4.5 is also used as the reference. In the tables, Ada represents the Adaboost algorithm.

In **Table 3** and **4**., all 3 ensembles have good F-value and G-mean than C4.5 on eight datasets. Compared with Bagging and Adaboost, our RSEAD has higher F-value and G-mean on most of dataset. From **Table 3**, it can be concluded that RSEAD has the best performance for minority class on 6 datasets. On dataset *mammograph*, the difference between ensembles is not significant. The reason may be that ratio between the minority and majority classes is near 4:5, which has a very small class imbalance. Also, dataset *mammograph* is defined only by 5 features, which leaves little room for our random subspace re-sampling method to enhance the ensemble's performance. In the evaluation based on G-mean, our RESEAD wins for all 8 datasets. From **Tables 3** and **4**, it can be seen that our ensemble RESEAD has better performance than Bagging and ADABOOST in countering problem of imbalance class. This advantage comes from the unique way of creating each member classifier as well as the misclassification cost based decision in selecting proper classifiers. Compared with Bagging, Adaboost has better performance, because Adaboost introduces different cost weight for different misclassification. It also indirectly proves the correctness of our misclassification cost estimation.

To further test the performance of our active learning method with RSEAD ensemble, the Bagging and Adaboost are also merged into the active learning architecture for comparison. Single RSEAD is tested further as reference. **Table 5** shows how many samples each algorithm needs to get certain F-value on each dataset. Compared with RSEAD, the active learning methods need fewer samples to get the same F-value. Among the three active learning methods, our Active-RSEAD has significant advantage, which benefits from the design of RSEAD ensemble.

Table 3. F-vaule for minority class in each dataset.

Dataset	C4.5	RSEAD	Bagging	Ada
Colic	76.54	**80.97**	79.71	80.03
Sick	87.65	**93.23**	90.44	91.43
Diabetes	61.4	**71.8**	67.9	69.8
SAheart	55.3	**75.2**	67.4	73.1
Hepatitis	52.8	68.4	67.2	**68.5**
mammograph	79.5	81.2	82.1	**83.2**
Breast-W	89.7	**95.6**	92.3	94.0
Spect	73.1	**79.76**	76.6	77.5

Table 4. G-mean for each dataset.

Dataset	C4.5	RSEAD	Bagging	Ada
Colic	81.5	**85.5**	83.4	84.51
Sick	91.2	**95.8**	95.6	95.2
Diabetes	64.3	**76.4**	71.4	74.3
SAheart	60.4	**77.8**	72.3	77.5
Hepatitis	58.4	**76.3**	74.3	73.4
mammograph	88.4	**89.4**	89.1	89.3
Breast-W	94.3	**96.5**	95.3	95.4
Spect	82.3	**85.6**	82.4	83.4

Table 5. Number of sampling for target F-vlalue.

Dataset	RSEAD	Active-RSEAD	Active-Bagging	Active Adaboost	Target F-value
Colic	41	**23**	35	37	85%
Sick	321	**134**	178	165	93%
Diabetes	245	**101**	114	106	75%
SAheart	280	**123**	157	167	60%
Hepatitis	117	**45**	56	54	95%
mammograph	100	**24**	35	30	80%
Breast-W	32	**36**	45	75	95%
Spect	53	**38**	43	39	75%

5. CONCLUSIONS

To address the problem of imbalance class in medical diagnosis, an ensemble-based active learning method is proposed. Our ensemble algorithm, RSEAD, introduces the subspace sampling method to reduce the complexity of computation and bring more diversity together with the creation of artificial datasets. Further, in evaluating the quality of each classifier candidate based on misclassification cost, the minority class is assigned with a higher weight for misclassification costs, while each testing sample has a variable penalty factor to induce the ensemble to correct current classification error.

In above experiments, eight UCI disease datasets are chosen. The F-value and G-mean are used instead of classification accuracy to evaluate the performance of classifiers. The result shows that our proposed ensemble method has better performance than others. Moreover, in active learning experiment, having the same performance with F-value rule, our method needs fewer samples. These experiments show that our ensemble-based active learning method has significant advantage than traditional methods.

Ensemble-based active learning is a promising method to counter the problem of class imbalance in medical diagnosis. But, there are still many issues for further studying. For example, our method only deals with two-class tasks, while the real world has many multi-class tasks. In addition, the noise in a dataset is not considered in current study. Also, the weighting method in our method needs further improvement from both theory and implementation. Therefore, we will focus on these issues to improve our active-RSEAD method in following research work.

REFERENCES

[1] Japkowicz, N. and Stephen, S. (2002) The class imbalance problem: A systematic study. *Intelligent Data Analysis*, **6(5)**, 203-231.

[2] Gustavo, E.A., Batista, P.A., Ronaldo, C., *et a1*. (2004) A study of the behavior of several methods for balancing machine learning training data. *SIGKDD Explorations*, **6(1)**, 20-29**.**

[3] Settles, B. (2009) Active Learning Literature Survey. *Computer Sciences Technical Report* 1648, University of Wisconsin-Madison.

[4] Tomek, I. (1976) Two modifications of CNN. *IEEE Transaction on Systems Man and Communications*, **6**, 769-772.

[5] Hart, P.E. (1968) The condensed nearest neighbor rule. *IEEE Transaction on Information Theory*, **14(3)**, 515-516.

[6] Laurikkala, J. (2001) Improving identification of difficult small classes by balancing class distribution. *Proceedings of the* 8*th Conference on AI in Medicine*, Cascais, Portugal, *Europe*: *Artificial Intelligence Medicine*, 63-66.

[7] Wilson, D.L. (1972) Asymptotic properties of nearest neighbor rules using edited data. *IEEE Transaction on Systems, Man and Communications*, **2(3)**, 408-421.

[8] Chawlan, V., Bowyer, K.W. and Hall, L.O. (2002) SMOTE: Synthetie minority over-sampling technique. *Journal of Aflificial Intelligence Research*, **16**(1), 321-357.

[9] Joshi, M., Kumar, V. and Agarwal, R. (2001) Evaluating boosting algorithms to classify rare classes: Comparison and improvements. *Proceedings of the* 1*st IEEE International Conference on Data Mining.* Washington DC: IEEE Computer Society, 257-264.

[10] Akbani, R., Kwek, S. and Japkowicz, N. (2004) Applying support vector machines to imbalanced datasets. *Proceedings of the* 15*th European Conference on Machines Learning*, Pisa, Italy, 39-50.

[11] Krogh, A. and Vedelsby, J. (1995) Neural network ensembles, cross validation and active learning. *Advances in Neural Information Processing Systems*, **7**, 231-238.

[12] Provost, F. (2000) Machine learning from imbalanced data sets 101. *Invited paper for the AAAI*, Workshop on Imbalanced Data Sets, Menlo Park, CA.

[13] Abe, N. (2003) Invited talk: Sampling approaches to learning from imbalanced datasets: Active learning, cost sensitive learning and beyond. ICML-KDD Workshop: Learning from Imbalanced Data Sets.

[14] Ertekin, S., Huang, J. and Giles, C.L. (2007) Active learning for class imbalance problem. *Proceedings of Annual International ACM SIGIR Conference Research and development in information retrieval*, Amsterdam, Netherlands, 823-824.

[15] Ertekin, S., Huang, J., Bottou, L. and Giles, C.L. (2007) Learning on the border: Active learning in imbalanced

data classification. *Proceedings of the sixteenth ACM conference on Conference on information and knowledge management*, November 6-8, Lisboa, Portugal, 127-136.

[16] Zhu, J. and Hovy, E. (2007). Active Learning for Word Sense Disambiguation with Methods for Addressing the Class Imbalance Problem. *In Proc. Joint Conf. Empirical Methods in Natural Language Processing and Computational Natural Language Learning*, Prague, 783-790.

[17] Chawla, N.V., Lazarevic, A. and Hall, O. (2003) SMOTE-Boost: improving prediction of the minority class in boosting: knowledge discovery in databases. *Proceeding of the 7th European Conference on Principles and Practice of Knowledge Discovery in Databases*. Cavtat Dubrovnik, 107-119.

[18] Veropoulos, K., Campbell, C. and Cristianini, N. (2009) Con- trolling the sensitivity of support vector machines. *Proc of Intemational Joint Confbrence on AI*, 55-60.

[19] Breiman, L. (1996) Bagging predictors. *Machine Learn -ing*, **24(2)**, 123-140.

[20] Abe, N. and Mamitsuka, H. (1998) Query learning strategies using boosting and bagging. *Proceedings of the International Conference on Machine Learning* (*ICML*), *Morgan Kaufmann*, 1-9.

[21] Breiman, L. (2001) Random forests. *Machine Learning*, 2001, **45(1)**, 5-32.

[22] Kleinberg, E.M. (1990) Stochastic discrimination. *Annals of Mathematics and Artificial Intelligence*, **1(1-4)**, 207-239.

[23] Seung, H.S., Opper, M. and Sompolinsky, H. (1992) Query by committee. *In Proceedings of the ACMWorkshop on Computational Learning Theory*, 287-294.

[24] Blake, C., Keogh, E., and Merz, C.J. UCI repository of machine learning databases. http://www.ics.uci.edu

[25] Su, C.T., Chen, L.S. (2006) Knowledge acquisition through information granulation for imbalanced data. *Expert Systems with applications*, **31**, 531-541.

[26] Joshi, M. (2002) On evaluating performance of classifiers for rare classes. *Proceeding of the 2nd IEEE International Conference on Data Mining, Maebishi, Japan*, 641-644.

[27] Kotsiantis, S., Kanellopoulos, D., Pintelas, P. (2006) Handling imbalanced datasets: A review. *GESTS International Transactions on Computer Science and Engineering*, **30(1)**, 25-36.

[28] Guo, H., Viktor, H. (2004) Learning from imbalanced data sets with boosting and data generation: the DataBoost-IM approach. *Sigkdd Explorations*, **6(1)**, 30-39.

[29] Witten, I. H., Frank, E. (2005) Data mining-pracitcal machine learning tools and techniques with JAVA implementations. 2nd Edition, Morgan Kaufmann Publishers.

J. Biomedical Science and Engineering, 2010, 3, 1030-1039 **JBiSE**
doi:10.4236/jbise.2010.310134 Published Online October 2010 (http://www.SciRP.org/journal/jbise/).

The mode of action of electrical high frequency stimulation

Miriam Kammerer, Jonas M. Hebel, Thomas J. Feuerstein

Section of Clinical Neuropharmacology, Department of Neurosurgery, University Hospital, Freiburg, Germany
Email: thomas.feuerstein@uniklinik-freiburg.de

Received 19 March 2010; revised 6 April; accepted 28 July 2010.

ABSTRACT

This article analyses, on the basis of the pathophysiological grounds of various syndromes treated with deep brain stimulation, whether there is a collective explanation of the mode of action of the applied regional stimulations with high frequencies (HFS). This proposed hypothesis assumes that HFS selectively releases GABA. The selective GABA release can explain the efficacy and the side effects of HFS in the various target regions according to the maxim of the philosopher William of Ockham that the simplest explanation is probably the correct explanation.

Keywords: HFS, DBS, Parkinson's disease, Essential tremor, Huntington's disease, Depression

1. INTRODUCTION

Deep brain stimulation (DBS) mostly reflects high frequency stimulation (HFS, > 100 Hz); low frequency stimulation (LFS, < 30 Hz) is rarely linked to the term DBS. Parkinsonian tremor was the first syndrome which was beneficially treated with HFS (130 Hz) in the ventral intermediate thalamic nucleus, in the year 1987 [1]. Today, *i.e*. 22 years after this first application of HFS, its mechanism of action is still unclear [2]. DBS is applied in a multitude of clinical conditions, *e.g*. Parkinson's disease, Chorea Huntington, dystonia, depression, Gilles de la Tourette syndrome, and obsessive compulsive disorder. For the treatment of each disorder a unique target brain area needs to be stimulated. Therefore, many brain target regions exist, *e.g*. the subthalamic nucleus (STN), the globus pallidus medialis (GP_{med}), and the ventral intermediate thalamic nucleus (VIM).

Hitherto, the following assumptions about the mode of action of HFS and their contradictions are discussed:

HFS is thought to inactivate the stimulated structures (see [3]). However, the decreased activity of thalamic neurons upon GP_{med}-HFS [4] (evaluation in awake monkeys) rather goes in the opposite direction. The axon terminals from GABAergic GP_{med} neurons impinge on glutamatergic thalamic neurons. Thus, their decreased activity must be explained by a $GABA_A$ receptor- mediated inhibition due to increased GABA release. The axon terminals of GP_{med} neurons release GABA upon activation, not upon inhibition, by HFS. Thus, HFS may *activate* the neurons of the stimulated structure GP_{med}.

HFS activates the stimulated structures [5]. This is at variance with the increased activity of STN neurons in Parkinson patients [6]. In addition, HFS has been reported to reduce the STN firing rate [7]. An even higher activity due to HFS of subthalamic glutamatergic neurons seems counterproductive pathophysiologically: Even more drive of the basal ganglia output nuclei leads to even stronger retardation of thalamic neurons, being less active in the hypokinetic parkinsonian state anyway (see **Figure 1**). Thus, HFS may *inactivate* the neurons of the stimulated structure STN to alleviate hypokinesia.

2. HFS: EXCITATION OR INHIBITION OF NERVE TERMINALS OR AXONS?

Stimulation of a brain region is normally expected to result in excitatory symptoms (*e.g*. muscle twitchings, flashes of light [8]). But, as Benabid *et al*. [2] have shown, clinical benefits from HFS-DBS often resemble those of earlier therapeutic lesions in the target brain areas. This observation leads to the assumption that HFS —corresponding to a functional removal of active neurons or their effects—may be similar to an inhibition of these neurons. As such a great variety of brain target regions, involved neurons and treated disorders exists, it seems quite impossible to find a single common denominator for a possible mode of action. Nevertheless, one may ask: Are there any mechanistics hints to solve the question of the HFS mechanism of action?

STN, GP_{med} and VIM are the most often targeted DBS regions in advanced Parkinson's disease [9]. Frequency is the most important parameter accounting for the therapeutic effects: Only HFS is efficacious, not low frequency stimulation (LFS, ~20 Hz) [8]. Stimulation at 5-10 Hz even worsens Parkinsonism and no significant

improvement is observed between 10 and 50 Hz [10,11]. In another brain region, the nucleus pedunculopontinus (PPN), only LFS, not HFS, improves parkinsonian posture and gait disturbances (see 3.1). The inhibitory GABAergic neurotransmission, including GABA neurons and receptors, seems to play a predominant role in the mechanism of action of HFS [12]. Dostrovsky *et al.* [8] have proved this involvement, as local injection of the $GABA_A$ receptor agonist muscimol into DBS target regions in animal models imitated the corresponding HFS effect. Consequently, HFS would affect, directly or indirectly, GABAergic terminals, resulting in a local release of GABA. Interestingly, only axons, which represent the most excitable components of neurons [13], react to the widths of electrical pulses used with HFS (60-3000 µs, see [14,15]): Chronaxies of this magnitude are typical for nerve fibers. Compared to that, chronaxies of cell bodies and dendrites (and also of myelin-free synaptosomes) are approximately 10-fold higher, *i.e.* 1-10 ms. Therefore, HFS pulses should mainly affect nerve fibers in areas where HFS is applied, with the subsequent induction of neurotransmitter release from their terminals impinging on postsynaptic cells. Their reaction would then represent the HFS effect. Local axon collaterals around cell bodies in an HFS target region are of course also responding to HFS if this mechanism holds true. In that case, somatodendritic autoreceptors would respond to the transmitter released from endings of axon collaterals. The speciality of the HFS parameter constellation (120 to 180 Hz, 60 to 200 µs pulse duration, current ≤ 1 mA) makes a unique mechanism of action, affecting axons only, at least probable. This is exemplified by our following recent finding using the method of superfusion and electrical depolarization of brain tissue. In this study we investigated, whether it is possible to evoke [^{3}H]-GABA and [^{3}H]-glutamate release from rat and human neocortical synaptosomes, *i.e.* isolated nerve endings, electrically. To this end, synaptosomes were pre-loaded with the triated neurotransmitters and then—after incubation to take up the transmitter to be investigated—superfused and stimulated. Two different stimulation parameter constellations were applied: HFS (130 Hz, 1 mA, puls duration 0.1 ms, for 10 min) and 10 Hz, 10 mA, pulse duration 30 ms, for 1 min. HFS did not evoke the release of [^{3}H]-GABA (**Figure 2**) or [^{3}H]-glutamate (**Figure 3**) from rat neocortical synaptosomes. However, the alternative parameter constellation *e.g.* 10 Hz instead of 130 Hz, 10 mA instead of 1 mA, 30 ms instead of 0.1 ms pulse duration, application for only 1 instead of 10 min, clearly induced the release of both [^{3}H]-glutamate and [^{3}H]-GABA from synaptosomes pre-loaded with these transmitters. Similar results have also been found for human neocortical synaptosomes (data not shown).

Obviously, electrical stimulations typical for HFS did not evoke any transmitter release from neocortical synaptosomes. However, another constellation of electrical parameters, applied for only a tenth of time, clearly evoked the synaptosomal release of [^{3}H]-GABA or [^{3}H]-glutamate. This shows 1) that it is possible, as a matter of principle, to release neurotransmitters from synaptosomes if their higher chronaxy is translated into a much higher duration of electrical pulses and 2) that the minimal pulse width and electrical current together with the typical frequency of HFS do not directly affect syn- aptosomes, *i.e.* nerve endings. Thus, HFS may indeed excite axons exclusively; then, transmitter release occurs not until the axonal depolarization has propagated to the nerve endings. Whether HFS is selective for a certain neurotransmitter system, *e.g.* for

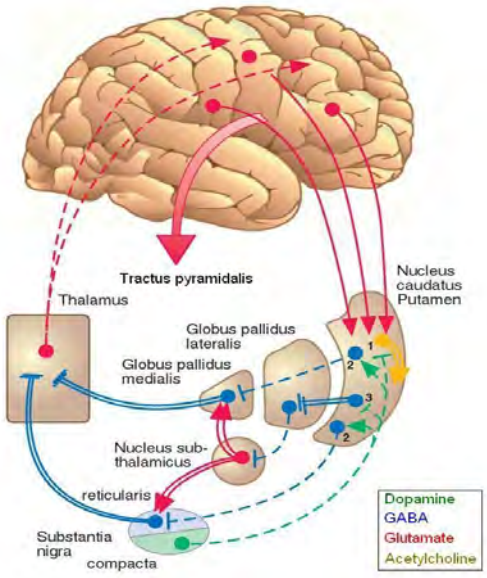

Figure 1. Pathophysiology of Parkinson's disease. This figure (adapted from [16]) illustrates the structural pathophysiologic condition of Parkinson's disease. Degeneration of modulating dopaminergic neurons (dashed green line) originating from the substantia nigra pars compacta (SNC) and projecting to the striatum (caudate nucleus and putamen) mainly entails two consequences: a reduced activity in formerly excited (through dopamine D_1 receptors) GABAergic interneurons (2; dashed blue lines) and an intensified activity in formerly inhibited (through dopamine D_2 receptors) GABAergic interneurons (3; doubled blue line). However, these two obviously oppositional situations finally conclude in an identical effect of intensified thalamic inhibition and a thereby increased filter function of the thalamus. Two different pathways emanating from the striatum and reaching the thalamus explain that. The direct pathway (2) straightly leads from the striatum to the thalamus, either passing the medial globus pallidus (GP_{med}) or the substantia nigra reticularis (SNR), whereas in the indirect pathway (3) additionally the lateral globus pallidus (GP_{lat}) and the glutamatergic (doubled red arrows) subthalamic nucleus (STN) are connected in series.

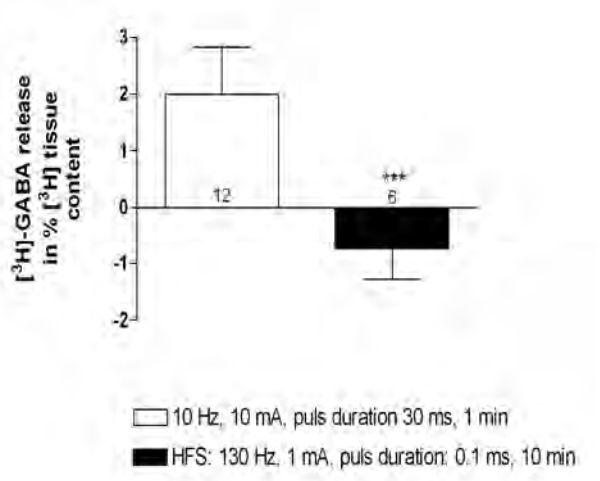

Figure 2. [^{3}H]-GABA release in % of synaptosomal [^{3}H]-content in rat neocortex. Values in the columns represent the number of observations. Stimulation values are given as means with 95% confidence intervals (CI_{95}). The significance of the difference is indicated by asterisks: *** $p < 0.001$.

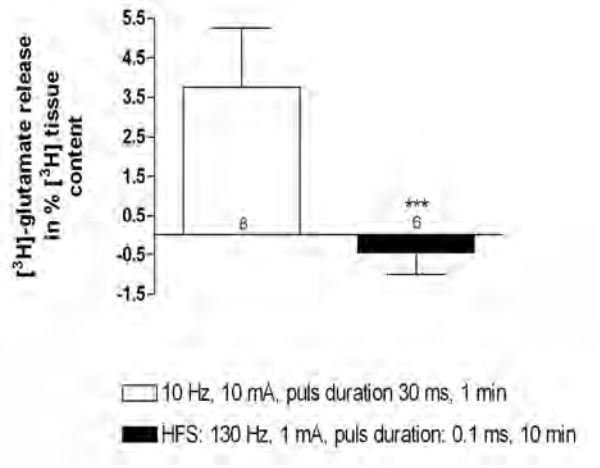

Figure 3. [^{3}H]-glutamate release in % of synaptosomal [^{3}H]-content in rat neocortex. Values in the columns represent the number of observation. Stimulation values are given as means with 95% confidence intervals (CI_{95}). The significance of the difference is indicated by asterisks: *** $p < 0.001$.

GABAergic axons only, cannot be answered with these experiments on synapto- somes.

What considerations on the basis of a selective GABA release as HFS mechanism of action are necessary for the different target regions? Is this unique HFS mechanism of action indeed appropriate to explain consistently and most simply why HFS acts beneficially in so many, pathophysiologically different, syndromes? Are there counterexamples where HFS worsens a clinical condition which would also be worsened by a selective release of GABA? The discussion of all clinical syndromes, which can be successfully treated with HFS without any doubt, in the light of the proposed mechanism of action, may illustrate the dimension of the proposed hypothesis and possible consequences and needs in future research in this matter.

3. HFS APPLIED IN PARKINSON`S THERAPY PROPOSED HYPOTHESIS: HFS IN REGIONS WITH GABAERGIC AXONS SELECTIVELY RELEASES GABA

DBS of the STN using HFS parameters improves the cardinal symptoms of Parkinson´s disease, tremor, rigidity, and bradykinesia [2]. The alleviation of the hypokinetic symptoms, caused by a so-called increased thalamic filter function with decreased output to the neocortex, can be explained comprehensively as follows. According to **Figure 1** the STN contains glutamatergic neurons projecting to both GP_{med} and SNR, and further GABAergic axon terminals originating from the GP_{lat}. A selective GABA release upon HFS from these fibers impinging on glutamatergic neurons may explain the beneficial outcome in hypokinetic patients. The released GABA activates $GABA_A$ receptors on glutamatergic STN neurons, resulting in a renormalization of the beforehand—because of a deficient GABAergic inhibition—disinhibited glutamatergic neurotransmission from STN to GP_{med} and SNR (doubled red arrows). The assumption of a non-selective neuronal excitation by HFS, *i.e.* of GABAergic and glutamatergic fibers, would also bring about an increased release of glutamate in the basal ganglia output nuclei. However, this makes no sense, as an increased glutamatergic transmission in GP_{med} and SNR would finally increase the thalamic suppression and therefore worsen hypokinetic symptoms.

The recently published findings of Mantovani *et al.* [17] show that HFS of human neocortical slices selectively induces the release of GABA, involving facilitatory $GABA_A$ autoreceptors may serve as an *in vitro* backup for the proposed hypothesis of the mechanism of action of DBS-HFS. Note in this context that Mantovani *et al.* excluded a release of glutamate. Although the existence of a glutamate outflow due to HFS of the ventrolateral thalamus has been published lately [18], does this not deductively signify an annulment of the proposed GABA-selective action of HFS, as the reported elevation of extracellular glutamate was not shown to reflect release from glutamatergic neurons.

Therapeutically, the most effective site for STN-HFS is located just dorsal/dorsomedial to the STN in the area of the pallidofugal fibers [19]. This location may contain GABAergic fibers from the GP_{lat} to the STN (which

should be activated by STN-HFS to induce the release of GABA within the STN).

It is possible to reduce the levodopa dosage of parkinsonian patients treated with STN-HFS by more than 50% and to accomplish an alleviation of levodopa-induced hyperkinesias with this reduction [20]. Without lowering the administered levodopa dose, STN-HFS even worsens the dyskinesias [20-22], which can be ascribed to a decreased filter function of the thalamus, as both levodopa and STN-HFS may diminish the eventual GABAergic neurotransmission to the thalamus. Levodopa should renormalize the patho-physiological condition in the striatum (see **Figure 1**; dashed green pathways). Concomitantly, and in accordance with our hypothesis, STN-HFS may throttle the glutamatergic output of the STN. Ultimately, an additionally reduced activation of the output nuclei, GP_{med} and SNR, results.

3.1. LFS Treatment of Postural Imbalance and Gait Disturbance

Postural instability and gait disturbance are two very handicapping symptoms in Parkinson's disease, but can be markedly ameliorated by applying LFS to the pedunculopontine nucleus (PPN) [23,24]. In contrast to this, DBS of the cholinergic and glutamatergic PPN with a frequency of 100 Hz (approaching HFS) induced Parkinson-like akinesia and postural imbalance in non-human primates [25]. The described impairment may be attributed to a GABAergic inhibition of excitatory PPN neurons. This assumption is reinforced by the fact that in a monkey model of Parkinson's disease PPN lesioning also induced akinesia and postural instability [24]. This lesioning presumably means a withdrawal of PPN projection fibers; this would correspond with a HFS-induced local GABAergic inhibition of cholinergic and glutamatergic PPN neurons. Further, both local application of bicucullin—a $GABA_A$ receptor antagonist—into the PPN and stimulation of the PPN with low frequency (~20 Hz) annihilated the previous HFS-induced symptoms [24]. Summing up, the effects of HFS and LFS seem to be antithetic. LFS may coincide with the expected effects of electrical stimulation of brain structures, *i.e.* in case of the PPN an augmentation of excitatory neuron activity, whereas HFS would abolish these effects, most likely through selective GABA release and activation of $GABA_A$ receptors on cholinergic and glutamatergic PPN neurons. Altoghether, this is an example for an *in vivo* correlation between HFS and $GABA_A$ receptor agonism (see [17] for an *in vitro* correlate). Note that PPN-LFS primarily leads to a melioration of the parkinsonian symptoms gait disturbance and postural instability, but rarely of other typical parkinsonian symptoms like rigidity or bradykinesia [23,26]. The last-mentioned authors recommended a combination of bilateral STN-HFS and PPN-LFS in appropriate Parkinson patients.

3.2. Diversity of Effects of HFS in the GP_{med}

The GABAergic GP_{med} projection neurons send their axons to the ventral tier thalamic nuclei and to the PPN; some of these GP_{med} "motor" neurons additionally project to the CM/Pf thalamic complex [27]. The axons of other GP_{med} neurons, termed "limbic" neurons by Parent and Parent (2002), arborize principally within the lateral habenular nucleus (LHb) with some collaterals to the anterior thalamic nuclei. Afferents to the GP_{med} include the GABAergic direct striato-pallidal monosynaptic pathway and the glutamatergic subthalamo-pallidal part of the indirect polysynaptic pathway. In addition, a majority of GABAergic GP_{lat} efferents have been shown to project through the GP_{med} en route to the STN [27,28].

According to the literature, HFS of various GP_{med} targets may induce different and even contrary clinical effects. Unintentional co-stimulation of GP_{lat} areas may play a role here.

GP_{med}-HFS is reported to alleviate *hypo*kinesias as well as *hyper*kinesias [29,30]. GP_{med}-HFS improves abnormal involuntary movements, though without the possibility to reduce the dosage of levodopa essentially, in contrast to the case of STN-HFS [31]. When the GP_{lat} is stimulated instead of the GP_{med}, HFS usually does not improve abnormal involuntary movements [32]. When, however, GP_{lat}-HFS affects axons of striatal neurons of the indirect pathway to the GP_{lat}, HFS may increase a too low GABAergic impulse flow in the hyperkinetic state to improve hyperkinesias (see below). Bejjani *et al.* [33] and Krack *et al.* [34] reported that GP_{med}-HFS within the most *ventral* contacts, lying at the ventral margin of, or just below, the GP_{med}, led to a pronounced improvement in rigidity and a complete arrest of levodopa-induced abnormal involuntary movements. The anti-akinetic effect of levodopa, however, was blocked and the patients became severely akinetic. Stimulation of the most *dorsal* contacts, lying at the dorsal border of the GP_{med} or inside the GP_{lat}, usually led to moderate improvement of off-drug akinesia and induced dyskinesias in some patients. Tronnier *et al.* [35] reported a reduction of dyskinesias, but a worsening of hypokinetic parkinsonian symptoms upon GP_{med}-HFS, in contrast to other studies (see [29]). Thus, multiple sites, possibly not confined to the GP_{med}, but involving also the GP_{lat}, seem to be responsible for partly contrasting clinical effects [33].

Obviously, the GP_{med} does not represent a uniform HFS object. Two GP_{med}-HFS target regions have been distinguished by Bejjani *et al.* [33] and by Krack *et al.*

[34]. There may be even more HFS targets within, and in the close vicinity of, the GP_{med}:

1) HFS may affect *thalamopetal axons* of GP_{med} neurons and thereby improve a *hyper*kinetic syndrome.

2) Alternatively, HFS can reach the *pallidopetal fibers* of striatal neurons of the *direct pathway* to increase their too low GABAergic impulse flow in the hypokinetic state; in this case, it alleviates *hypo*kinesia.

3) At a still other site within the GP_{med}, HFS may stimulate the *en route fibers from* GP_{lat} *to STN* running within the GP_{med}. Then, GP_{med}-HFS mirrors STN-HFS and also improves *hypo*kinesia.

4) Further, GP_{med}-HFS may (also) affect nearby *pallidopetal fibers* of striatal neurons of the *indirect pathway* to the GP_{lat}. In this last case, HFS increases the too low GABAergic impulse flow in the hyperkinetic state and improves *hyper*kinesia.

The pathophysiological assumptions behind (A)—(D) are the following:

(a) HFS of *thalamopetal axons*

Abnormal involuntary movements, *i.e*. *hyper*kinesias, of the original *hypo*kinetic Parkinson syndrome correspond with a *reduced filter* function of the thalamus, *i.e.* an insufficient GABAergic inhibition of thalamic neurons. Accordingly, a reduced neuronal activity in GP_{med} during levodopa-induced dyskinesia has been shown in parkinsonian monkeys [36]. Thus, GP_{med}-HFS diminishes the abnormal involuntary movements in advanced Parkinson's disease if the HFS-mediated selective GABA release is paralleled by a less diminished, *i.e.* normalized, GABAergic projection to the thalamus.

It was shown in human neocortex slices that HFS induces action potentials in GABAergic fibers and subsequent terminal release of GABA with subsequent activation of facilitatory $GABA_A$ autoreceptors. $GABA_A$ receptor blockade, changing the plasmalemmal chloride gradient of $GABA_A$ receptor channels and tetrodotoxin (which abolishes action potentials) antagonized this HFS-evoked GABA release [17,37]. Thus, orthodromic action potentials may be induced in thalamopetal GABAergic axons by HFS within the GP_{med} with subsequent release of GABA from their thalamic terminals; even more GABA release is due to activation by released GABA of facilitatory $GABA_A$ autoreceptors on these terminals. In addition, one can suppose antidromic action potentials due to HFS. These antidromic action potentials excite the soma of the GP_{med} neuron or travel backwards to reach recurrent axon collaterals with subsequent release of GABA in the somatodendritic region of the GABAergic cell. GABA may increase the firing rate of the GABAergic neuron through facilitatory somatodendritic $GABA_A$ autoreceptors. These $GABA_A$ autoreceptors have been demonstrated in human neocortical slices [17]. Whether these somatodendritic autoreceptors are facilitatory, like those on GABAergic terminals, or inhibitory, as usual for $GABA_A$ receptors, depends on the local somatodendritic chloride gradient. Using the pharmacological tool furosemide to change the plasmalemmal chloride gradient, Mantovani *et al*. [17] did not differentiate between the involvement of somatodendritic and/or terminal autoreceptors in the mode of action of HFS. In any case, the overall effect of altering the chloride gradient was a decrease of HFS-induced GABA release. The terminal $GABA_A$ autoreceptors were clearly facilitatory (as shown on isolated nerve endings, see [17]); it may well be that the *facilitatory* terminal autoreceptors have overridden *inhibitory* somatodendritic autoreceptors of minor importance for the overall HFS-induced GABA release. Possibly, also both terminal and somatodendritic $GABA_A$ autoreceptors are facilitatory and cooperate to realize the HFS-induced GABA release. Regardless of the somatodendritic autoreceptor being inhibitory or excitatory, the facilitatory feature of the terminal $GABA_A$ autoreceptors enabled HFS to induce an increased release of GABA. In the case of GP_{med}-HFS the increase in GABA release from terminals in the thalamus may either be the positive net effect of facilitatory terminal and inhibitory somatodendritic $GABA_A$ autoreceptors or the sum of the effects of facilitatory terminal and facilitatory somatodendritic receptors. Boraud *et al*. [38] found that GP_{med}-HFS reduced the firing frequency of GP_{med} neurons in the N-methyl-4-phenyl-1, 2, 3, 6-tetrahydropyridine (MPTP)-treated parkinsonian monkey; this would correspond to the combination of facilitatory terminal and inhibitory somatodendritic $GABA_A$ autoreceptors.

(b) HFS of *pallidopetal fibers*

HFS in the *dorsal* GP_{med} and/or inside the GP_{lat} may activate the GABAergic fibers from striatum through GP_{lat} to GP_{med} of the direct pathway (see **Figure 1**; dashed blue projection from the striatum to the GP_{med}). Then, the striato-pallidal GABAergic transmission of the direct pathway is strengthened, $GABA_A$ receptors on GP_{med} projection neurons are activated, *i.e*. the pallido-thalamic neurotransmission is diminished, the filter function of the thalamus decreases, and *hypo*kinesia improves. In the end, activating these striato-pallidal fibers of the direct pathway should correspond to STN-HFS.

(c) HFS of *en route fibers from* GP_{lat} *to STN*

GP_{med}- or GP_{lat}-HFS matches STN-HFS when axons from GP_{lat} neurons with terminals in the STN are stimulated (see **Figure 1**; dashed blue projection within the GP_{lat} to the STN). Then, GABAergic axon terminals within the STN will release more GABA, the glutamatergic subthalamo-pallidal and -nigral neurotransmissions decrease, the firing rate of the basal ganglia output

nuclei is less activated, and *hypo*kinetic parkinsonian symptoms improve as the filter function of the thalamus decreases.

(d) HFS of *pallidopetal fibers* of striatal neurons of the *indirect pathway*

GP_{lat}-HFS may, either intentionally or not in the course of GP_{med}-HFS, target the GABAergic striato-pallidal fibers of the indirect pathway (see **Figure 1**; doubled blue projection (3) from striatum to GP_{lat}).

In the *hypo*kinetic parkinsonian condition these over-active striato-pallidal fibers strongly decelerate the pallido-subthalamic neurons. Then, the axons of these striato-pallidal neurons either may react to HFS with even more increased GABA release from their terminals or the increased GABA release is already maximal without a further deceleration of the pallido-subthalamic neurons. Again, also antidromic action potentials due to HFS must be supposed; they excite the soma of the striatal GABAergic neuron or reach recurrent axon collaterals which subsequently release GABA in the somatodendritic region in the striatum.

In *hyper*kinesia, the inhibition by the GABAergic output nuclei GP_{med} and SNR of the thalamus is mediated through the too strong dopamine D_1 receptor-driven GABAergic transmission in the monosynaptic direct striato-pallidal and striato-nigral pathway. The resulting reduction of the *filter* function of the thalamus is intensified by the D_2 receptor-initiated decrease in the activity of the polysynaptic indirect pathway to the output nuclei with an increased GABA release in the STN and, subsequently, a reduced subthalamic drive of GP_{med} and SNR.

The proposed hypothesis predicts an increased release of GABA upon HFS: Indeed, GP_{med}-HFS enhanced the concentration of GABA in the ventricular cerebrospinal fluid during stimulation. In addition, the GABA level correlated with the degree of HFS-induced clinical effects against tremor, rigidity, and drug-induced dyskinesia [39].

3.3. HFS in the Treatment of Parkinsonian Tremor

Parkinsonian tremor can be treated by HFS in the ventral intermediate thalamic nucleus (VIM, see 4.) and by STN-HFS. An even better anti-tremor efficacy in Parkinson patients seems to result from HFS in the centrum medianum and parafascicularis thalamic nucleus (CM/Pf) [40]. The thalamic neurons of the CM/Pf are retarded by both GABAergic afferents from the GP_{med} and axon collaterals of GABAergic interneurons and activated by glutamatergic afferents, e.g. from the cerebellum. According to these circumstances, a selective GABA release due to HFS in the CM/PF either inhibits a tremor-transmitting cerebellar projection and/or local glutamatergic tremor cells.

Dyskinesias can also be improved using CM/Pf-HFS, as shown by Krauss *et al*. [41], reminding of earlier antidyskinetic outcomes of medial thalamotomies [42]. Also in this case, a local inhibition of glutamatergic neurons due to a selective GABA release may explain the HFS mode of action.

4. HFS IN THE TREATMENT OF ESSENTIAL TREMOR

Excitatory afferences from the deep cerebellar nuclei project to the VIM, which is their thalamic relay. Parkinsonian tremor [1] as well as essential tremor [43] is improved due to the application of HFS to the VIM. Essential tremor can also be improved by local injection of the $GABA_A$ receptor agonist muscimol into the VIM, as shown by Pahapill *et al*. [43]. VIM-HFS as well as the application of muscimol results in improvement of tremor; this leads us to presume that the selective GABA release is the most likely HFS mode of action also in this target area. In the VIM, a selective GABA release from axon terminals of thalamic reticular neurons and VIM interneurons inhibits the thalamic relay cells which are driven by cerebellar afferents (for anatomical connections see [44]). Consequently, released GABA seems to activate inhibitory $GABA_A$ receptors on glutamatergic cerebellar afferents and on glutamatergic thalamic relay neurons.

5. HFS IN THE TREATMENT OF DYSTONIA AND HUNTINGTON'S DISEASE

A similar reasoning as for the therapy of hyperkinesias in Parkinson's disease, *i.e.* a strengthening of the GABAergic pallido-thalamic projection, explains hypothetically the efficacy of GP_{med}-HFS on other hyperkinesias, *e.g.* on dystonia and Huntington´s disease. One, or even the most important, pathophysiological basis of these hyperkinesias is also a reduced filter function of the thalamus, to be reversed therapeutically. Besides using HFS to treat chorea of a Huntington patient, Moro *et al*. [45] also applied 40 Hz. 130 Hz improved choreatic symptoms more than 40 Hz; the concomitant bradykinesia, however, was rarely affected. The bradykinesia ameliorated with 40 Hz, admittedly at the expense of the chorea reduction. A corresponding clinical difference between HFS and 40 Hz-stimulation was also observed by Fasano *et al*. [46]. Thus, 40 Hz induce other, possibly opposed, effects as the HFS-typical 130 Hz.

6. HFS IN DEPRESSION

6.1. HFS in the Treatment of Major Depression

In depression the subgenual gyrus cinguli (Brodman area

25) is metabolically overactive. This overactive metabolism is being decreased due to antidepressant medication [47]. HFS of the white matter of the subgenual gyrus cinguli was applied to reduce this elevated activity and successfully improved treatment-resistant major depression. Therefore white matter of the subgenual gyrus cinguli-HFS may lead to an increased release of GABA from axon terminals in the Brodman area 25. GABA then activates inhibitory $GABA_A$ receptors on overactive postsynaptic neurons which calms these neurons.

6.2. Suicidality as Side-effect of STN-HFS

A depression-like behaviour is aggravated in the forced swim test due to STN-HFS; the forced swim test is a widely used and validated rodent model of depression. On the level of neuronal activities, the firing rate of 5-HT neurons in the dorsal raphe nucleus (NDR) of rats is inhibited following STN-HFS [48]. Muscimol, being infused into the STN, imitated the effects of STN-HFS on the firing rate of 5-HT- neurons. Voon *et al*. [49] have recently confirmed that suicide is one of the most important risks for mortality following STN-HFS in advanced Parkinson's disease. This serious adverse effect's pathophysiology may allow us to draw conclusions about the mode of action of HFS.

Anatomically, the following connections between STN and the 5-HT neurons of the NDR exist (see [50,51]; →: excitation, ┤: inhibition, ncl. habenulae lateralis: LHb, GABA interneurons of NDR: NDR_{GABA}, 5-HT neurons of NRD: $NDR_{5\text{-}HT}$):

The physiological condition is reflected by the following chain of neuronal impacts:

STN → GP_{med} ┤ LHb → NDR_{GABA} ┤ $NDR_{5\text{-}HT}$.

The condition in patients suffering from Parkinson's disease, however is different. In the hypokinetic state the STN is disinhibited, which changes the above-mentioned chain.

(→→ means increased, (→) decreased, excitation; ╟ means increased, (┤) decreased, inhibition):

STN →→ GP_{med} ╟ LHb (→) NDR_{GABA} (┤) $NDR_{5\text{-}HT}$.

A reduced inhibition of NDR 5-HT neurons is the result of the disinhibited STN.

The condition after STN-HFS, however, may vary as follows:

STN-HFS (→) GP_{med} (┤) LHb →→ NDR_{GABA}╟ $NRD_{5\text{-}HT}$.

Obviously, STN-HFS increases the inhibition of 5-HT neurons of the NDR which results in a lowering of the serotonergic neurotransmission to cortical areas. Deficiencies in the monoamine neurotransmission is the current hypothesis underlying major depression. Consequently, this decrease may explain the increased suicidality of Parkinson patients after STN-HFS.

Not only 5-HT neurons in the NDR, but also noradrenergic neurons in the locus coeruleus (LC), which project to the cortical areas, are influenced by STN-HFS.

Pathophysiological condition in the hypokinetic Parkinson syndrome:

STN →→ GP_{med} ╟ LHb (→) LC_{GABA} (┤) LC_{NA}.

Condition in Parkinson patients after STN-HFS:

STN-HFS (→) GP_{med} (┤) LHb →→ LC_{GABA} ╟ LC_{NA}.

An increased inhibition due to a lowered noradrenergic neurotransmission also promotes the occurrence of depression [52].

Note that the coincidence of a decrease of the serotonergic as well as the noradrenergic neurotransmission may lead to a substantially increased risk of the occurrence of depression.

GP_{med}-HFS is also used in the treatment of Parkinson's disease. Does suicidality also occur in GP_{med}-HFS as an adverse effect? Rodriguez-Oroz *et al.* [53] have compared the clinical occurence of depression in Parkinson patients treated with these two different HFS methods, *i.e.* STN-HFS and GP_{med}-HFS. A lower rate of depressions after GP_{med}-HFS compared to STN-HFS was found. This could be the result of a decreased inhibition of $NDR_{5\text{-}HT}$ after GP_{med}-HFS which ends in an undiminished serotonergic neurotransmission to cortical areas. Therefore, depression is not likely to occur after GP_{med}-HFS.

Condition of Parkinson patients after GP_{med}-HFS:

GP_{med}-HFS ╟ LHb (→) NDR_{GABA} (┤) $NRD_{5\text{-}HT}$.

7. HFS IN THE GILLES DE LA TOURETTE SYNDROME

According to Servello *et al*. [54] it is possible to successfully treat patients suffering from Tourette syndrome by applying HFS to the centrum medianum/ parafascicular nucleus (CM/Pf) of the thalamus and to the ventral oral anterior thalamic nucleus (Voa). Although the pathophysiological knowledge about the exact network of neurotransmitters acting in the Gilles de la Tourette syndrome is limited, one may assume a GABAergic inhibition of glutamatergic (CM/Pf and Voa) and cholinergic (CM/Pf) neurons through $GABA_A$ receptors. The GABAergic afferents in this case come from the GP_{med}. While applying HFS to the CM/Pf and Voa, a terminal release of GABA is induced in afferent fibers to these nuclei and, by this, neurons in the HFS target structures are inhibited. Thus, the above stated assumption leads to the proposal that CM/Pf- and Voa-efferents, projecting to both striatum and neocortex, there may trigger the Gilles de la Tourette syndrome.

8. HFS IN OBSESSIVE COMPULSIVE DISORDER

Corresponding to a recent publication by Greenberg *et al*. [55] DBS of the ventral internal capsule (VC) and the

ventral striatum (VS) with HFS parameters meliorates the symptoms of patients with Obsessive Compulsive Disorder. Also here the particular pathophysiology is unclear, but, in compliance with our hypothesis of the mode of functioning of HFS, GABA release in the VS as well as from VC fiber endings would take place. Now, on the one hand, axon collaterals from GABAergic inter or projection neurons of the VS could be excited by HFS and, on the other hand, postsynaptic neurons in target areas of VC fibers could be influenced in an inhibitory manner by the released GABA.

9. HFS IN EPILEPSIES

Various human epilepsies have also been experimentally treated with DBS and by subdural neocortical stimulation (target regions: hippocampus, cerebellum, thalamus, STN, neocortex; see [56]). Comparing the efficacies, a higher rate of electrical stimulation approaches in animal models of epilepsies than of the corresponding clinical applications have displayed anticonvulsant properties (*e.g.* STN-HFS against absence-like seizures, cortex piriformis-LFS in kindled animals, hippocampus-HFS and -LFS). Taken together, electrical stimulation methods in the treatment of epilepsies seem to be more remote from a common clinical application than the other clinical syndromes mentioned above. Mechanistically, however, just epilepsies could offer interesting aspects for the implementation of HFS inducing selective GABA release, as regards the pathophysiological role of the opponents GABA and glutamate in these disorders.

10. WHAT IS THE OVERALL IMPACT OF THE HYPOTHESIS OF A SELECTIVE GABA RELEASE BY HFS?

Various treatment locations and options for HFS against different neurological and psychiatric syndromes are discussed above; there are detailed pathophysiological conceptions for most of these syndromes and, additionally for the suicidality following STN-HFS [49]. The hypothesis of a selective GABA release due to HFS is in line with these conceptions (see underlined pathophysiological basis in the following) by explaining the efficacies and side effects of HFS according to the stimulated regions. (A) Augmented filter function of the thalamus (see 3.): GABA, released in the STN from axon terminals of neurons from the GP_{lat}, reduces the disinhibition of the glutamatergic neurotransmission from STN to GP_{med} and to SNR and thus (re-) normalizes their thalamopetal projections. (B) Reduced filter function of the thalamus (see 3.2, 5.): GP_{med}-HFS increases the GABAergic transmission of projection neurons to the thalamus. (C) In contrast to STN-HFS, GP_{med}-HFS is not depressiogenic, according to the pathophysiological conception of the transmission from GP_{med} to LHb to both NDR and LC. (D) In opposition to PPN-LFS (3.1), PPN-HFS impairs gait disturbance and postural instability of the Parkinson syndrome, as HFS induces a GABAergic inhibition of excitatory PPN neurons. (E) CM/Pf-HFS and VIM-HFS are effective against tremor and dyskinesias (3.3, 4.) by a GABAergic inhibition of glutamatergic thalamic neurons. (F) HFS in the subgenual gyrus cinguli inhibits through GABAergic axon terminals overactive neurons of the Brodmann area 25 in depression.

The error probability of a correct explanation of the overall mechanism of action of HFS (selective GABA release) with regard to its clinical effects may be assessed as follows: Together, six independent arguments have been listed (A-F). If this independence of the six arguments is accepted, then a single probability of only 39.5% has to be assumed: The validity of the hypothesis "a selective GABA release explains argument (A) or (B) or … or (F)" corresponds to a significant collective explanation for the mode of action of HFS. The error probability for this collective explanation is in that case $p = 0.049 = (1 - 0.395)^6$. Thus, we can state that a selective GABA release significantly explains the mode of action of HFS. The proposed hypothesis corresponds to an optimal simplicity in explaining the observed clinical effects since the collective explanation is in any case simpler than another one which assumes different modes of actions of HFS in different target regions.

We should add that the individual evidence of the selective GABA release following HFS in the various conditions should be separately demonstrated in spite of the present consideration of a collective explanation.

Disclosure/Conflict-of-Interest Statement: This research was conducted in the absence of any commercial or financial relationships that could be construed as a potential conflict of interest.

REFERENCES

[1] Benabid, A.L., Pollak, P., Louveau, A., Henry, S. and Rougemont, J.D. (1987) Combined (thalamotomy and stimulation) stereotactic surgery of the VIM thalamic nucleus for bilateral Parkinson disease. *Applied Neurophysiology*, **50(1-6)**, 344-346.

[2] Benabid, A.L., Chabarde, S., Mitrofanis, J. and Pollak, P. (2009) Deep brain stimulation of the subthalamic nucleus for the treatment of Parkinson disease. *Lancet Neurology*, **8(1)**, 67-81.

[3] Beurrier, C., Bioulac, B., Audin, J. and Hammond, C. (2001) High-frequency stimulation produces a transient blockade of voltage-gated currents in subthalamic neurons. *Journal of Neurophysiology*, **85(4)**, 1351-1356.

[4] Anderson, M.E., Postupna, N. and Ruffo, M. (2003) Effects of high-frequency stimulation in the internal globus pallidus on the activity of thalamic neurons in the awake

monkey. *Journal of Neurophysiology*, **89(2)**, 1150-1160.
[5] Montgomery, E.B. and Baker, K.B. (2000) Mechanisms of deep brain stimulation and future technical developments. *Neurological Research*, **22(3)**, 259-266.
[6] Levy, R., Ashby, P., Hutchison, W.D., Lang, A.E., Lozano, A.M. and Dostrovsky, J.O. (2002) Dependence of subthalamic nucleus oscillations on movement and dopamine in Parkinson's disease. *Brain*, **125**, 1196-1209.
[7] Meissner, W., Leblois, A., Hansel, D., Bioulac, B., Gross, C.E., Benazzouz, A. and Boraud T. (2005) Subthalamic high frequency stimulation resets subthalamic firing and reduces abnormal oscillations. *Brain*, **128**, 2372-2382.
[8] Dostrovsky, J.O. and Lozano, A.M. (2002) Mechanisms of deep brain stimulation. *Movement Disorders*, **17(3)** S63-S68.
[9] Garcia, L., Allesandro, G.D., Bioulac, B. and Hammond, C. (2005) High-frequency stimulation in Parkinson's disease: More or less? *Trends in Neuroscience*, **28(4)**, 209-216.
[10] Moro, E., Esselink, R.J., Xie, J., Hommel, M., Benabid, A.L. and Pollak, P. (2002) The impact on Parkinson's disease of electrical parameter settings in STN stimulation. *Neurology*, **59(5)**, 706-713.
[11] Rizzone, M., Lamotte, M., Bergamasco, B., Tavella, A., Torre, E., Faccani, G., Melcarne, A. and Lopiano, L. (2001) Deep brain stimulation if the subthalamic nucleus in Parkinson's disease: Effects of variation in stimulation parameters. *Journal of Neurology, Neurosurgery, and Psychiatry*, **71(2)**, 215-219.
[12] Benabid, A.L., Benazzous, A. and Pollak, P. (2002) Mechanisms of deep brain stimulation. *Movement Disorders*, **17(3)**, S73-S74.
[13] Nowak, L.G. and Bullier, J. (1998) Axons, but not cell bodies, are activated by electrical stimulation in cortical grey matter. I. evidence from chronaxie measurements. *Experimental Brain Research*, **118(4)**, 477-488.
[14] Holsheimer, J., Demeulemeester, H., Nuttin, B. and Sutter, P.D. (2000) Identification of the target neuronal elements in electrical deep brain stimulation. *European Journal of Neuroscience*, **12(12)**, 4573-4577.
[15] Holsheimer, J., Dijkstra, E.A., Demeulemeester, H. and Nuttin, B. (2000) Chronaxie calculated from current-duration and voltage-duration data. *Journal of Neuroscience Methods*, **97(1)**, 45-50.
[16] Feuerstein, T.J. (2009) Antiparkinsonmittel. Pharmakotherapie des morbus Parkinson. In: Aktories, K., Förstermann, U., Hofmann, F., Starke, K., Eds., *Allgemeine und Spezielle Pharmakologie and Toxikologie*, Urban & Fischer, München, 299-305.
[17] Mantovani, M., Moser, A., Haas, C.A., Zentner, J. and Feuerstein, T.J. (2009) $GABA_A$ autoreceptors enhance GABA release from human neocortex: towards a mechanism for high-frequency stimulation (HFS) in brain? *Naunyn-Schmiedeberg's Archives of Pharmacology*, **380 (1)**, 45-58.
[18] Chang, S., Shon, Y.M., Agnesi, F. and Lee, K.H. (2009) Microthalamotomy effect during deep brain stimulation: Potential involvement of adenosine and glutamate efflux. *Conference Proceedings:* 31*st Annual International Conference of the IEEE EMBS*, 3294-3297.
[19] Plaha, P., Shlomo, Y.B., Patel, N.K. and Gill, S.S. (2006) Stimulation of the caudal zona incerta is superior to stimulation of the subthalamic nucleus in improving contralateral Parkinsonism. *Brain*, **129**, 1732-1747.
[20] Moro, E., Scerrati, M., Romito, L.M., Roselli, R., Tonali, P. and Albanese, A. (1999) Chronic subthalamic nucleus stimulation reduces medication requirements in Parkinson's disease. *Neurology*, **53(1)**, 85-91.
[21] Krack, P., Pollak, P., Limousin, P., Hoffman, D., Xie, J., Benazzouz, A. and Benabid, A.L. (1998) Subthalamic nucleus or internal pallidal stimulation in young onset Parkinson's disease. *Brain*, **121**, pp. 451-457.
[22] Limousin, P., Pollak, P., Hoffmann, D., Benazzouz, A., Perret, J.E. and Benabid, A.L. (1996) Abnormal involuntary movements induced by subthalamic nucleus stimulation in parkinsonian patients. *Movement Disorders*, **11(3)**, 231-235.
[23] Plaha, P. and Gill, S.S. (2005) Bilateral deep brain stimulation of the pedunculopontine nucleus for Parkinson's disease. *Neuroreport*, **16(17)**, 1883-1887.
[24] Pereira, E.A., Muthusamy, K.A., Pennington, N.D., Joint, C.A. and Aziz, T.Z. (2008) Deep brain stimulation of the pedunculopontine nucleus in Parkinson's disease. Preliminary experience at Oxford. *British Journal of Neurosurgery*, **22(1)**, S41-S44.
[25] Nandi, D., Liu, X., Winter, J.L., Aziz, T.Z. and Stein, J.F. (2002) Deep brain stimulation of the pedunculopontine region in the normal non-human primate. *Journal of Clinical Neuroscience*, **9(2)**, 170-174.
[26] Stefani, A., Lozano, A.M., Peppe, A., Stanzione, P., Galati, S., Tropepi, D., Pierantozzi, M., Brusa, L., Scarnati, E. and Mazzone, P. (2007) Bilateral deep brain stimulation of the pedunculopontine and subthalamic nuclei in severe Parkinson's disease. *Brain*, **130**, 1596-1607.
[27] Parent, M. and Parent, A. (2002) Axonal collateralization in primate basal ganglia and related thalamic nuclei. *Thalamus & Related systems*, **2(1)**, 71-86.
[28] Sato, F., Lavallée, P., Lévesque, M. and Parent, A. (2000) Single-axon tracing study of neurons of the external segment of the globus pallidus in primate. *Journal of Comparative Neurology*, **417(1)**, 17-31.
[29] Volkmann, J. (2004) Deep brain stimulation for the treatment of Parkinson's disease. *Journal of Clinical Neurophysiology*, **21(1)**, 6-17.
[30] Siegfried, J. and Lippitz, B. (1994) Bilateral chronic electrostimulation of ventroposterolateral pallidum: A new therapeutic approach for alleviating all parkinsonian symptoms. *Neurosurgery*, **35(6)**, 1126-1129.
[31] Perlmutter, J.S. and Mink, J.W. (2006) Deep brain stimulation. *Annual Review of Neuroscience*, **29**, 229-257.
[32] Peppe, A., Pierantozzi, M., Altibrandi, M.G., Giacomini, P., Stefani, A., Bassi, A., Mazzone, P., Bernardi G. and Stanzione, P. (2001) Bilateral GPi DBS is useful to reduce abnormal involuntary movements in advanced Parkinson's disease patients, but its action is related to modality and site of stimulation. *European Journal of Neurology*, **8 (6)**, 579-586.
[33] Bejjani, B., Damier, P., Arnulf, I., Bonnet, A.M., Vidailhet, M., Dormont, D., Pidoux, B., Cornu, P., Marsault C. and Agid, Y. (1997) Pallidal stimulation for Parkinson's disease. Two targets? *Neurology*, **49(6)**, 1564-9156.
[34] Krack, P., Pollak, P., Limousin, P., Hoffman, D., Benazzouz A. and. Bas, J.F.L., Koudsie, A. and Benabid, A.L. (1998) Opposite motor effects of pallidal stimulation in

Parkinson's disease. *Annals of Neurology*, **43(2)**, 180-192.

[35] Tronnier, V.M., Fogel, W., Kronenbuerger, M. and Steinvorth, S. (1997) Pallidal stimulation: an alternative to pallidotomy? *Journal of Neurosurgery*, **87(5)**, 700-705.

[36] Papa, S.M., Desimone, R., Fiorani, M. and Oldfield, E.H. (1999) Internal global pallidus discharge is nearly suppressed during levodopa-induced dyskinesias. *Annals of Neurology*, **46(5)**, 732-738.

[37] Mantovani, M., Velthoven, V.V., Fuellgraf, H., Feuerstein, T.J. and Moser, A. (2006) Neuronal electrical high frequency stimulation enhances GABA outflow from human neocortical slices. *Neurochemistry International*, **49(4)**, 347-350.

[38] Boraud, T., Bezard, E., Bioulac, B. and Gross, C. (1996) High frequency stimulation of the internal Globus pallidus (GPi) simultaneously improves parkinsonian symptoms and reduces the firing frequency of GPi neurons in the MPTP-treated monkey. *Neuroscience Letters*, **210(1)**, 17-20.

[39] Ogura, M., Nakao, N., Nakai, E., Uematsu, Y. and Itakura, T. (2004) The mechanism and effect of chronic electrical stimulation of the globus pallidus for treatment of Parkinson disease. *Journal of Neurosurgery*, **100(6)**, 997-1001.

[40] Peppe, A., Gasbarra, A., Stefani, A., Chiavalon, C., Pierantozzi, M., Fermi, E., Stanzione, P., Caltagirone, C. and Mazzone, P. (2008) Deep brain stimulation of CM/PF of thalamus could be the new elective target for tremor in advanced Parkinson's Disease? *Parkinsonism & Related Disorders*, **14(6)**, 501-504.

[41] Krauss, J.K., Pohle, T., Weigel, R. and Burgunder, J.M. (2002) Deep brain stimulation of the centre median-parafascicular complex in patients with movement disorders. *Journal of Neurology, Neurosurgery and Psychiatry*, **72(4)**, 546-548.

[42] Ohye, C. and Shibazak, T. (2001) Lesioning the thalamus for dyskinesia. *Stereotactic and Functional Neurosurgery*, **77(1-4)**, 33-39.

[43] Pahapill, P.A., Levy, R., Dostrovsky, J.O., Davis, K.D., Rezai, A.R., Tasker, R.R. and Lozano, A.M. (1999) Tremor arrest with thalamic microinjections of muscimol in patients with essential tremor. *Annals of Neurology*, **46(2)**, 249-252.

[44] Strafella, A., Ashby, P., Munz, M., Dostrovsky, J.O., Lozano, A.M. and Lang, A.E. (1997) Inhibition of voluntary activity by thalamic stimulation in humans: relevance for the control of tremor. *Movement Disorders*, **12(5)**, 727-737.

[45] Moro, E., Lang, A.E., Strafella, A.P., Poon, Y.Y., Arango, P., Dagher, A., Hutchison, W.D. and Lozano, A.M. (2004) Bilateral globus pallidus stimulation for Huntington's disease. *Annals of Neurology*, **56(2)**, 290-294.

[46] Fasano, A., Mazzone, P., Piano, C., Quaranta, D., Soleti F. and Bentivoglio, A.R. (2008) GPi-DBS in Huntington's disease: Results on motor function and cognition in a 72-year-old case. *Movement Disorders*, **23(9)**, 1289-1292.

[47] Mayberg, H.S., Lozano, A.M., Voon, V., McNeely, H.E., Seminowicz, D., Hamani, C., Schwalb, J.M. and. Kennedy, S.H. (2005) Deep brain stimulation for treatment-resistant depression. *Neuron*, **45(5)**, 651-660.

[48] Temel, Y., Boothman, L.J., Blokland, A., Magill, P.J., Steinbusch, H.W., Vandewalle, V.V. and Sharp, T. (2007) Inhibition of 5-HT neuron activity and induction of depressive-like behavior by high-frequency stimulation of the subthalamic nucleus. *Proceedings of the National Academy of Sciences of the United States of America*, **104(43)**, 17087-17092.

[49] Voon, V., Krack, P., Lang, A.E., Lozano, A.M., Dujardin, K., Schüpbach, M., Ambrosia, J.D., Thobois, S., Tamma, F., Herzog, J., Speelman, J.D., Samanta, J., Kubu, C., Rossignol, H., Poon, Y.Y., Cyr, J.A.S., Ardouin, C. and Moro, E., (2008) A multicentre study on suicide outcomes following subthalamic stimulation for Parkinson's disease. *Brain*, **131**, 2720-2728.

[50] Ferraro, G., Montalbano, M.E., Sardo, P. and Grutta, V.L., (1996) Lateral habenular influence on dorsal raphe neurons. *Brain Research Bulletin*, **41(1)**, 47-52.

[51] Smith, Y., Bevan, M.D., Shink, E. and Bolam, J.P. (1998) Microcircuitry of the direct and indirect pathways of the basal ganglia. *Neuroscience*, **86(2)**, 353-387.

[52] Sartorius, A. and Henn, F.A. (2007) Deep brain stimulation of the lateral habenula in treatment resistent major depression. *Medical Hypotheses*, **69(6)**, 1305-1308.

[53] Oroz, M.C.R., Obeso, J.A., Lang, A.E., Houeto, J.L., Pollak, P., Rehncrona, S., Kulisevsky, J., Albanese, A., Volkmann, J., Hariz, M.I., Quinn, N.P., Speelman, J.D., Guridi, J., Zamarbide, I., Gironell, A., Molet, J., Sedano, B. P., Pidoux, B., Bonnet, A.M., Agid, Y., Xie, J., Benabid, A.L., Lozano, A.M., Cyr, J.S., Romito, L., Contarino, M.F., Scerrati, M., Fraix, V. and Blercom, N.V. (2005) Bilateral deep brain stimulation in Parkinson's disease: a multicentre study with 4 years follow-up. *Brain*, **128**, 2240-2249.

[54] Servello, D., Porta, M., Sassi, M., Brambilla, A., Robertson, M.M., (2008) Deep brain stimulation in 18 patients with severe Gilles de la Tourette syndrome refractory to treatment: The surgery and stimulation. *Journal of Neurology, Neurosurgery and Psychiatry*, **79(2)**, 136-142.

[55] Greenberg, B.D., Gabriels, L.A., Jr, D.A.M., Rezai, A.R., Friehs, G.M., Okun, M.S., Shapira, N.A., Foote, K.D., Cosyns, P.R., Kubu, C.S., Malloy, P.F., Salloway, S.P., Giftakis, J.E., Rise, M.T., Machado, A.G., Baker, K.B., Stypulkowski, P.H., Goodman, W.K., Rasmussen, S.A. and Nuttin, B.J. (2010) Deep brain stimulation of the ventral internal capsule/ventral striatum for obsessive-compulsive disorder: worldwide experience. *Molecular Psychiatry*, **15(1)**, 64-79.

[56] Gubellini, P., Salin, P., Goff, L.K.L. and Baunez, C. (2009) Deep brain stimulation in neurological diseases and experimental models: from molecule to complex behaviour. *Progress in Neurobiology*, **89(1)**, 79-123.

